Advanced Detection in Lorentz Microscopy

Pixelated Detection in Differential Phase Contrast Scanning Transmission Electron Microscopy

Matúš Krajňák, M.Sc., Bc.

Materials and Condensed Matter Physics Group
School of Physics and Astronomy
University of Glasgow

Submitted in fulfilment of the requirements for the Degree of
Doctor of Philosophy

February 2017

Abstract

Modern devices require fundamental length scales to be analysed in a maximum detail to enable research of new types of phenomena and design new materials. In this thesis, an advancement in Lorentz microscopy will be presented where the focus was placed not only onto resolution in spatial space but also onto resolution in reciprocal space. This allows greater sensitivity to measurements of the integrated magnetic induction within thin samples. This was achieved by a novel approach to the data acquisition, where instead of a segmented (annular) detector, a pixelated detector was used to measure the deflection of the scanning transmission microscopy (STEM) probe due to the in-plane integrated magnetic induction.

Computer vision algorithms were researched to find an efficient, noise-robust way to register the deflection of the STEM probe. This enabled a novel approach to data analysis, where a scatter of the 2D integrated induction (a bivariate histogram) is used to show the distribution of the magnetic induction vector. The experimental results are supported by simulations, where a model of a thin polycrystalline sample causes a shift of the simulated beam due to phase modulations. The results of the detection in both the simulation and experiment showed that cross-correlation based processing can efficiently separate the low spatial frequencies (from the in-plane magnetic induction), and high spatial frequencies (from the structure of the polycrystalline sample).

This work will enable quantitative analysis of a greater number of thin magnetic samples, for which the current methods are hampered by the diffraction contrast. This will be particularly helpful for the study low moment, out of plane, magnetised thin films. Currently such systems are of great interest due to the tunability of their magnetic properties and the novel magnetic structures present within them. This work also provides an important step for computational methods in transmission electron microscopy, as this is one of the first examples of 4D data acquisition of processing in STEM (where two dimensions represent the spatial scanning dimensions and other two the reciprocal space).

Imaging methods developed in this thesis were applied to the topic of skyrmions in a thin layer of a *FeGe* cubic helimagnet, where the very fine detail of the structure of their in-plane integrated magnetic induction was shown to contain a distorted modulations of its profile. This was compared to a simple three harmonic frequency model, which was altered to fit some characteristics of the imaged magnetic skyrmions.

In this work, for the first time, a direct comparison of differential phase contrast and electron holography will be shown for a simple experiment in which the integrated electric field between two needles was measured in free space in the same microscope. Although it was concluded that both methods are equivalent, some small discrepancies of measured values were present due to a long range electric field in electron holography and/or drift of the beam in between scans in STEM.

Dedicated to my family...

"When you come out of the storm, you won't be the same person who walked in. That's what this storm's all about."

— *Haruki Murakami*
Kafka on the Shore

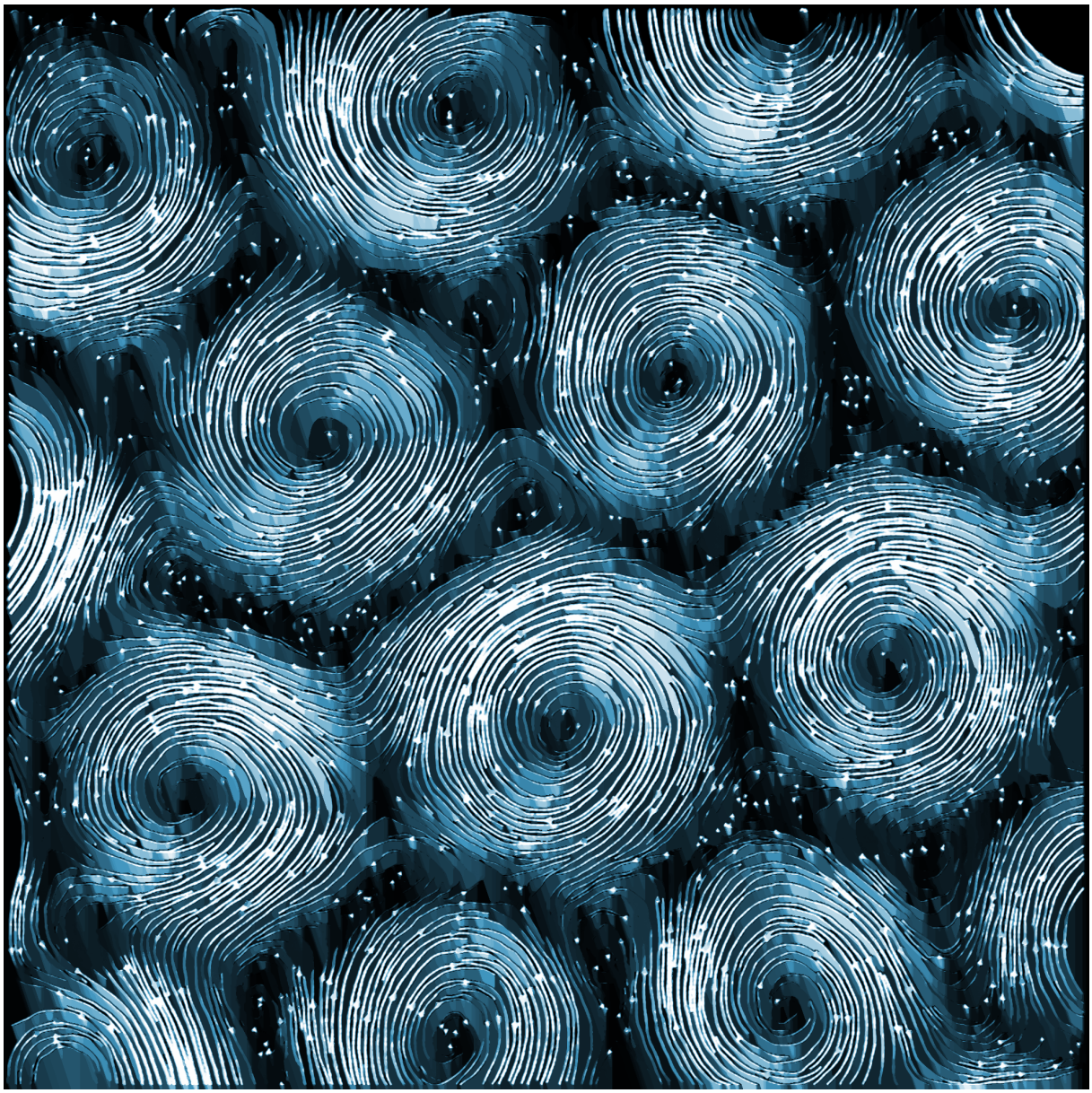

Artistic view on magnetic skyrmions

Declaration

This thesis is a record of research carried out by myself at the Materials and Condensed Matter Physics group, School of Physics and Astronomy at The University of Glasgow from 2012-2016. The work described herein is my own, except where specific reference is made to the work of others. The contents of this dissertation are original and have not been submitted in whole or in part for consideration for any other degree or qualification in this, or any other university.

Matúš Krajňák, M.Sc., Bc.
February 2017

Some of the work reported in this thesis is a part of following publications:

Pixelated Detectors and Improved Efficiency for Magnetic Imaging in STEM Differential Phase Contrast, M. Krajnak, D. McGrouther, D. Maneuski, V. O' Shea, S. McVitie, Ultramicroscopy, 165, 2016, 42-50,

Chiral surface twists and skyrmion stability in nanolayers of cubic helimagnets, A. O. Leonov, Y. Togawa, T. L. Monchesky, A. N. Bogdanov, J. Kishine, Y. Kousaka, M. Miyagawa, T. Koyama, J. Akimitsu, Ts. Koyama, K. Harada, S. Mori, D. McGrouther, R. Lamb, M. Krajnak, S. McVitie, R. L. Stamps, and K. Inoue, Physical Review Letters, 117, 2016, 5,

Internal structure of hexagonal skyrmion lattices in cubic helimagnets, D. McGrouther, R. Lamb, M. Krajnak, S. McVitie, R. L. Stamps, A. O. Leonov, A. N. Bogdanov, and Y. Togawa, New Journal of Physics, Special Edition: Focus on Magnetic Skyrmions, 18, 2016, 095004

Imaging electric fields in free space - comparing off-axis electron holography and scanned electron diffraction, I. MacLaren, M. Krajnak, V. Migunov, S. McVitie, R. E. Dunin-Borkowski, Submitted to Ultramicroscopy (Sept 2016)

Acknowledgements

I would like to acknowledge Dr Stephen McVitie, for his kind support and supervision. I would also like to acknowledge Prof Bob Stamps, and The University of Glasgow who funded my PhD studentship.

Much of this work would not be possible without the support of Dr Damien McGrouther, who introduced me to experimental TEM microscopy. Special thanks needs to be given to Dr Sam McFadzean for his technical support and hard drive space, which this project required. I would like to say thanks to Dr Donald MacLaren for his valuable suggestions in colloquia, which allowed this work to pace much faster. I would like to say cheers to Scott, who has been my office companion for some years and who has been through this with me. The same applies to Rob, who has been a great companion for the years in Glasgow. And very special thanks to Kayla for proof reading and help with finalising of this thesis.

Other people should not be missed including, Dr Aleš Hrabec, for valuable samples which were the base of this thesis; Dr Maria Jose Benitez Romero, who introduced me to the ARM/T20; and Prof Yoshihiko Togawa for his support and enthusiasm for my work. I would also like to thank Dr Bernhard Schaffer for a recourceful DM scripting guide which was invaluable, and last but not least Colin and Billy for their technical support.

Table of contents

List of figures

List of tables

Abbreviations

TEM ..... transmission electron microscopy

DMI ..... Dzyaloshinskii-Moriya interaction

STEM ..... scanning transmission electron microscopy

DPC ..... differential phase contrast

CTEM ..... conventional transmission electron microscope

CCD ..... charge-coupled device

DF ..... dark field

ADF ..... annular dark field

BF ..... bright field

FT ..... Fourier transform

FFT ..... Fast Fourier transform

CTF ..... contrast transfer function

TIE ..... transport of intensity equation

FE ..... field emission

FEG ..... field emission gun

CFEG ..... cold field emission gun

SAD ..... selected area diffraction

DM ..... Digital Micrograph®

MagTEM .... Jeol ARM 200 CFEG at The University of Glasgow specialised in

..... magnetic imaging

HAADF ..... high angle annular dark field

COM ..... centre of mass

CrossCorr .... cross-correlation

FWHM ..... full width half maximum

EFTEM ..... energy filtered transmission electron microscopy

STDEV ..... standard deviation

CPU ..... central processor unit

GPU ..... graphical processor unit

EELS ..... electron energy loss spectroscopy

FIB ..... focused ion beams

SPM ..... scanning probe microscopy

CHAPTER 1

Magnetism of thin films

1.1 Introduction

The technological applications of magnetism of thin films are wide ranging. They have fuelled much of the success of modern technology - mainly in data storage [1–4]. Other applications can include the biological application of magnetic nanoparticles in drug delivery or cancer treatment [5, 6].

The properties of magnetic films and nanostructures can change significantly when the dimensions start to approach fundamental length scales. The ferromagnetic exchange length defines the largest length for which a magnetic configuration of the sample can be assumed uniform. The theory of ferromagnetism is well established in physics, however, some new interesting phenomena were observed recently. The antisymmetric Dzyaloshinskii-Moriya interaction is of considerable interest and can be observed in helical magnets [7], that can support the formation of skyrmions [8–10] which will be studied in this thesis in Chap. 5.

Study of magnetism on nanometre scales requires state of the art instrumentation. In this thesis, a new development in magnetic imaging using a scanning transmission electron microscope will be introduced. It is based on an enhanced detection method in which instead of standard, quadrant based detection fuller information about the diffraction pattern will be acquired. This new type of dataset can be then analysed computationally which enhances the efficiency of the imaging and, therefore, enables the study of a broader range of materials.

1.2 Ferromagnetism in thin films

Magnetic fields arise from electrical currents (moving charges) and from intrinsic magnetic moments within fundamental particles (spins). Particles with spin can produce magnetic dipole moments, similar to a rotating charge body in classical electrodynamics. In most of the materials, these magnetic moments are randomly oriented and cancel each other out. Materials in which magnetic moments align locally can produce macroscopic magnetic field.

If a material does not spontaneously align its magnetic moments, it can either be paramagnetic or diamagnetic. The induced moment of a paramagnet is in the direction of the external field, whereas a diamagnet has the induced moment in the opposite direction.

A measure of the magnetic configuration of a material is described by magnetisation, which is defined as the magnetic moment per unit volume. The response of material to an external field can be characterised by its susceptibility χ:

$$\mathbf{M} = \chi \mathbf{H}, \tag{1.1}$$

where $\mathbf{M}$ is magnetisation and $\mathbf{H}$ is magnetic field. The material is paramagnetic if $\chi > 0$ and diamagnetic if $\chi < 0$. The values of susceptibility can be typically 10^{-5} – 10^{-4} for paramagnets and -10^{-5} for diamagnets. Many materials, however, do not fit this

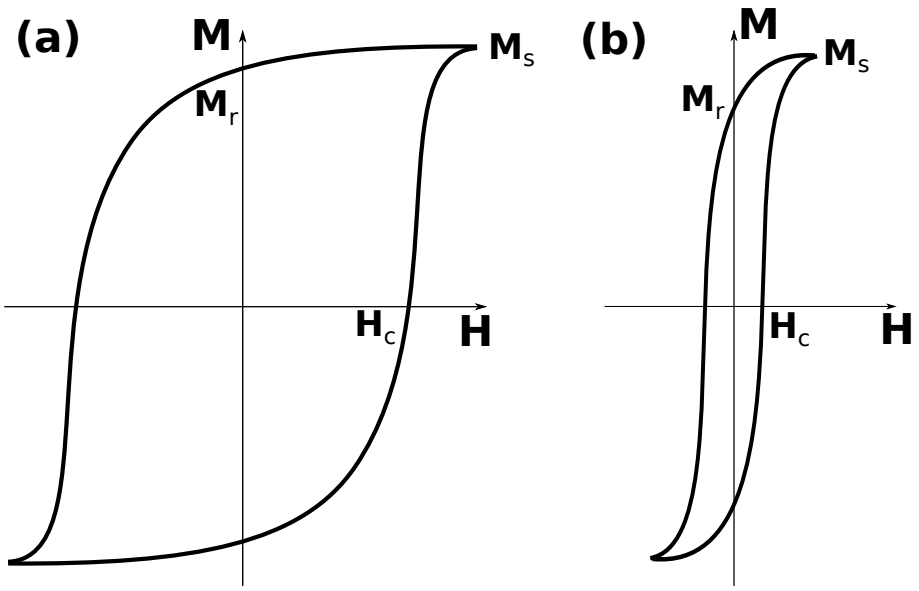

Fig. 1.1 *Schematic of a hysteresis loop for a hard (a) and soft (b) ferromagnetic material showing a response of magnetisation* $\mathbf{M}$ *to the applied field* $\mathbf{H}$*,* $\mathbf{M}_S$ *saturation magnetisation,* $\mathbf{M}_r$ *is a remanent magnetisation present in a sample when field is switched off,* $\mathbf{H}_c$ *is a coercive field*

classification because the magnetisation,$\mathbf{M}$, can be not linear to $\mathbf{H}$ and they can even have non zero $\mathbf{M}$ at $\mathbf{H} = 0$.

Ferromagnetic materials can magnetise spontaneously by aligning their atomic or molecular magnetic moments. The response of the magnetisation of a ferromagnet can be schematically shown in a hysteresis loop, as is shown in Fig. 1.1. The magnetic field, $\mathbf{H}$, can be used to saturate the sample, this means that the magnetisation of the sample will reach its maximum value, saturation magnetisation, $\mathbf{M}_s$. If the field is switched off, the magnetisation will stay at remanent value, $\mathbf{M}_r$. The magnetisation can be reversed by the application of the coercive field, $\mathbf{H}_c$. Ferromagnetic materials can be divided into two groups: hard ferromagnets (Fig. 1.1(a)), which have a large coercive field $\mathbf{H}_c$ and large saturation magnetisation $\mathbf{M}_s$ (Fig. 1.1(b)) and do not allow movements of domain wall (which will be described later in this chapter); and soft ferromagnets which are easier to demagnetise and allow relatively easy movement of domain walls.

Werner Karl Heisenberg explained ferromagnetic ordering by an exchange interaction, the Hamiltonian of which can be written as [11]:

$$H_{ex} = -2 \sum_{i<j} J_{ij}\, \mathbf{S_i} \cdot \mathbf{S_j}, \tag{1.2}$$

where J_{ij} is material dependant exchange constant (its unit is Joule per meter) and $\mathbf{S_i}$ and $\mathbf{S_j}$ are neighbouring spins (dimensionless unit vectors of the directions of magnetic moments). This interaction fundamentally arises due to an overlap interaction between the wavefunctions of neighbouring electrons. Due to $\mathbf{S_i} \cdot \mathbf{S_j}$ operation, energy is minimised when the two spins are parallel. Ferromagnetic materials have a positive exchange energy ($J > 0$) (their spins align parallel to their neighbours) and antiferromagnetic materials have a negative exchange energy ($J < 0$) (antiparallel spin alignment).

Ferromagnetic properties also depend on temperature. Curie temperature T_C is a limit above which spontaneous ordering is suppressed by thermal fluctuations. This is

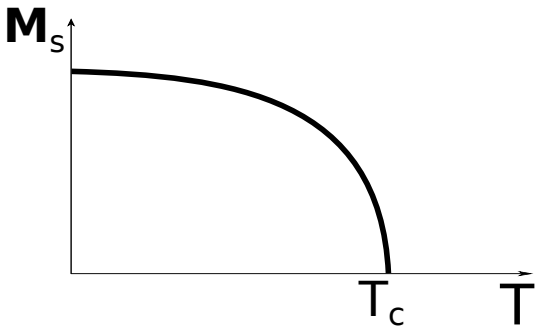

Fig. 1.2 *Schematic of the dependence of the saturation magnetisation* $\mathbf{M}_s$ *on temperature. For temperatures larger than* T_c *ferromagnetic ordering is suppressed by thermal fluctuations in the sample*

effectively due to the chaotic orientation of spins with higher thermal energy in the system. Schematic of the dependence of saturation magnetisation on temperature is shown in Fig. 1.2. Examples of the Curie temperature can be given for Iron - 1043 K [12] or permalloy ($Ni_{80}Fe_{20}$) - 553 K – 872 K [13] in which T_c depends on the structure.

Another type of exchange interaction, which will also be experimentally studied in this thesis, is the Dzyaloshinskii-Moriya interaction. It favours an anti-symmetric orientation of the spins. Hamiltonian for DMI is given by:

$$H_{DMI} = -\sum_{i<j} \mathbf{D}_{ij} \cdot (\mathbf{S_i} \times \mathbf{S_j}), \tag{1.3}$$

where $\mathbf{D}_{ij}$ is Dzyaloshinskii-Moriya vector (in Joule per meter squared) and $\mathbf{S_i}$ and $\mathbf{S_j}$ are neighbouring spins. This interaction arises in magnets with a lack of inversion symmetry in their atomic structure. Magnetic materials with broken inversion symmetry are also called chiral. The DMI interaction favours perpendicular alignment of neighbouring spins and competes with ferromagnetic exchange. A schematic of a three site atomic unit is shown in Fig. 1.3, where the spin orientation of two ferromagnetic atoms is affected by strong spin-orbit coupling from a third atom. The DMI vector is pointing out of the plane defined by the three atoms.

There are two types of DMI interaction: interfacial and bulk DMI. Interfacial DMI arises due to the presence of metal atoms with large spin orbit coupling at the interface of the material [10, 14–17]. Bulk DMI is caused by broken internal symmetry of a crystal with spin orbit coupling [8, 9, 18, 19]. The DMI exchange results in different magnetic structures depending on the direction of the **D** vector. Some of these structures will be introduced later in the chapter and also studied experimentally in Chap. 5.

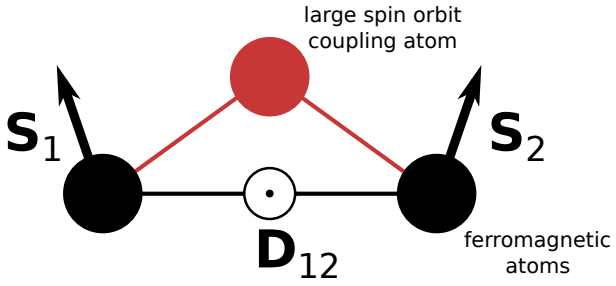

Fig. 1.3 *Schematic of DMI interaction between three atoms. DMI vector is pointing out of plane of three atoms and causes miss-alignment between two spins of ferromagnetic atoms.*

1.3 Energy terms in micromagnetics

The magnetic configuration of a sample is the result of competing forces and interactions. The two types of exchange interactions mentioned already are between neighbouring spins. The ferromagnetic exchange interaction favours a simple single domain structure within a sample, for which the exchange energy (Eq. 1.2) is minimised. If the DMI term is also considered, the spins in such a material favour rotation to their neighbours and the resulting magnetic structure of the sample can be more complicated. We will discuss ferromagnetic exchange first and then consider the DMI interaction.

Micromagnetics will be explained here as a competition between different energy terms. A total energy can be assigned to the static magnetic sample:

$$E_{tot} = E_{ex} + E_m + E_\alpha + E_z. \tag{1.4}$$

Local energy minima of this equation will give stable magnetic configurations. The energies are: exchange energy, E_{ex}, magnetostatic energy, E_m, anisotropy, E_α and Zeeman energy, E_z. The origins of magnetic energy terms will be discussed individually in the following sections before discussing domain the formation.

1.3.1 Exchange energy

The Hamiltonian for exchange energy in Eq. 1.2 can be rewritten to:

$$H_{ex} = -2JS^2 \sum_{ij} cos(\phi_{ij}), \tag{1.5}$$

where ϕ_{ij} is the angle between neighbouring spins, i and j. This energy will be minimised if ϕ is zero for a ferromagnet ($J > 0$) and ϕ is 180∘ for antiferromagnet ($J < 0$). The exchange interaction is a local, atomic scale interaction which can be characterised by exchange length parameter, l_{ex}, defined as:

$$l_{ex} = \sqrt{\frac{2A}{\mu_0 M_s^2}}, \tag{1.6}$$

where A is the exchange stiffness (unit J/m) and μ_0 is the permeability of vacuum ($\mu_0 = 4\pi \times 10^{-7}\, H/m$). This depends on the material and an example can be given for polycrystalline permalloy ($Ni_{80}Fe_{20}$), for which $A = 1.3 \times 10^{-11}\, J/m$ and $M_s = 860\, kA/m$, this gives an exchange length of $l_{ex} = 5.3\, nm$ [20–22]. The ferromagnetic exchange energy is minimised when the spins in the sample point in the same direction (schematic is shown in Fig. 1.4(a)).

Dzyaloshinskii-Moriya interaction

Dzyaloshinskii-Moriya interaction is an antisymmetric interaction which gives rise to exciting phenomena in the magnetism of thin films. Contrary to the Heisenberg exchange interaction, this energy term is minimised for spins with a 90° angle between neighbouring spins. Therefore, these interactions compete locally. The Hamiltonian for the DMI interaction was given in Eq. 1.3.

In this thesis, a thin sample of single crystal *FeGe* will be imaged by Lorentz microscopy and the results of enhanced detection of bulk magnetic skyrmions will be shown (details about helical magnets and skyrmions will be given later in the chapter). The ratio of the ferromagnetic exchange and the Dzyaloshinskii-Moriya constant defines another length-scale in helical magnets known as helical periodicity, J/D [23].

1.3.2 Magnetostatic energy

Magnetostatic energy stems from a dipole interaction which creates a field opposing the magnetisation. This can be in the form of an internal (demagnetising) field or an external (stray) field. The magnetostatic field, $\mathbf{H_d}$, can be calculated as the gradient of a scalar magnetostatic potential, ϕ_M, [24]:

$$\begin{aligned} \mathbf{H_d} &= -\nabla\phi_M, \\ \phi_M(\mathbf{r}) &= \frac{1}{4\pi}\left[\int_V \frac{-\nabla\cdot\mathbf{M}}{|\mathbf{r}-\mathbf{r}'|}dV' + \int_S \frac{\mathbf{M}\cdot\hat{n}}{|\mathbf{r}-\mathbf{r}'|}dS'\right], \end{aligned} \tag{1.7}$$

where ϕ_M essentially shows bulk (first integral) and surface (second integral) forms of magnetostatic charges. These charges interact with the magnetisation of the sample as dipoles and is termed magnetostatic energy [24]:

$$E_{mstat} = -\frac{\mu_0}{2}\int_V \mathbf{H_d}\cdot\mathbf{M}\,dV, \tag{1.8}$$

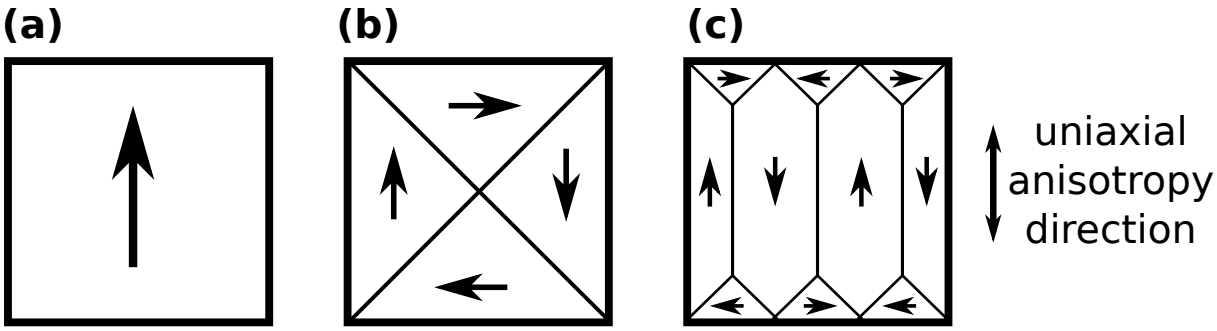

Fig. 1.4 *Comparison of effects on domain structure for (a) only ferromagnetic exchange present, (b) with magnetostatic energy, (c) with uniaxial magnetocrystalline anisotropy in a thin ferromagnetic square particle*

where μ_0 is permeability of vacuum. Magnetostatic energy is effectively responsible for the alignment of magnetisation with sample edges in thin films. This is schematically shown in Fig. 1.4(b).

1.3.3 Magnetocrystalline anisotropy

Magnetocrystalline anisotropy causes directional dependence of the magnetisation due to crystal structure. The preferred direction, easy axis, gives the lowest anisotropy energy (E_α), therefore magnetisation is likely to align itself with this axes. If it is forced to be misaligned (by an external field or a magnetostatic energy at the interfaces), this comes with an energy cost, which is the largest for a hard axis in the crystal. An example of the domain configuration with uniaxial anisotropy is shown in Fig. 1.4(c). Polycrystalline films weaken the anisotropy because of random orientation of crystallites. This is the case in permalloy, which is studied in this thesis (unless the material was deposited under a constant magnetic field).

1.3.4 Zeeman energy

By the application of an external field, Zeeman energy is introduced into the micromagnetic system. It is defined as:

$$E_z = -\mu_0 \int_V \mathbf{M} \cdot \mathbf{H_a}\, dV, \tag{1.9}$$

where $\mathbf{M}$ is magnetisation of the sample and $\mathbf{H_a}$ is applied magnetic field (external). The Zeeman energy favours the alignment of the magnetisation with the external field.

1.4 Micromagnetic structures

1.4.1 Magnetic domains and domain walls

Magnetic domains form in ferromagnets due to the exchange interaction. If the magnetisation of the sample was aligned in a single direction, the exchange energy would be minimised. However, unless the sample is very small (on the order of the exchange length), this is very unlikely due to other terms in Eq. 1.4 (mainly the magnetostatic energy). For larger samples, multiple domains will exist due to the minimisation of the total energy of the sample. Magnetic domains will then be separated by domain walls, which also have their own energetic cost [25]. Domain walls have an assigned angle, which depends on the orientation of the magnetisation in the two domains, between which the domain wall is formed. In the continuous layer of ferromagnetic material domain wall widths are typically

around 1–100 nm. There are two main types of domain wall in continuous films - Bloch and Néel walls which are distinguishable by the orientation of the magnetisation in the wall relative to the orientation within the domains. An example for an in-plane magnetic materials is shown in Fig. 1.5. A Néel wall (Fig. 1.5(a)) has magnetisation rotating in plane, where magnetic charges are created at the edge of it (+ and − signs). On the contrary, the magnetisation of a Bloch wall (Fig. 1.5(b)) goes out of plane and magnetic charges are created at the surfaces of the sample (divergence of magnetisation is zero for a Bloch wall).

In a given material, the existence of Bloch and Néel walls depends on its thickness. This can be simply argued by considering the width of the wall. If the sample thickness is larger than the characteristic width of the wall the configuration will be Bloch, whereas for thinner samples it will be Néel wall. An example can be given in permalloy in which a 180° domain wall in a $> 30\,nm$ thick sample will lead to a Bloch wall. For thinner permalloy samples surface charges, which build in the centre of the wall and on the top and bottom of the sample, make an in-plane magnetisation vector rotation favourable hence domain walls will be of a Néel type [26].

In this thesis, Néel domain walls in a $20\,nm$ thick polycrystalline permalloy sample will be used for the development of imaging in Lorentz microscopy in particular quantitative imaging in differential phase contrast [27–30]. Such a system is problematic to image, because diffraction contrast from randomly oriented grains swamps contrast from the magnetic induction of the sample in Lorentz STEM imaging, this will be explained in detail in the following chapters.

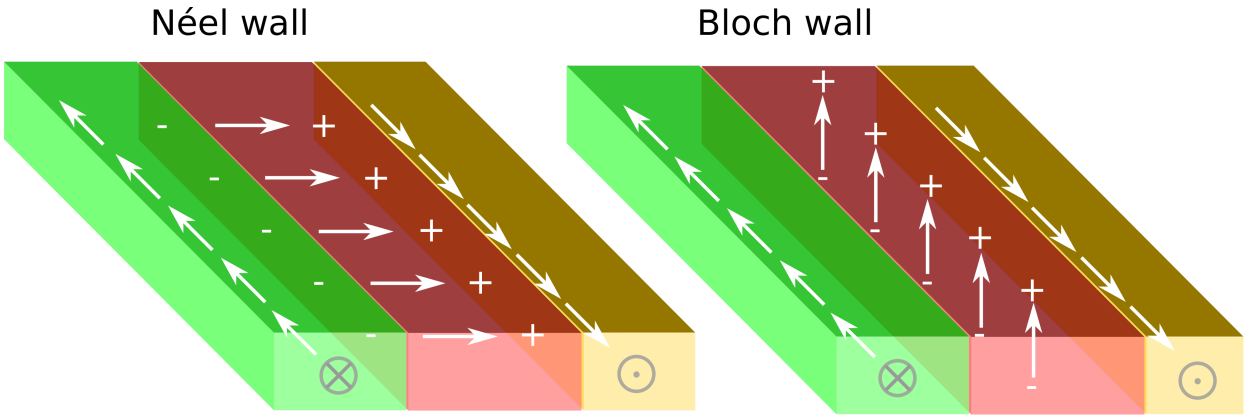

Fig. 1.5 *Schematic of (a) Néel domain wall and (b) Bloch domain wall in in-plane magnetised sample, '+' and '−' signs show position of magnetostatic charges.*

1.4.2 Chiral magnets and skyrmions

As mentioned earlier in this chapter, the competition between the Dzyaloshinskii-Moriya interaction and Heisenberg exchange can lead to novel states in thin layers of magnetic materials. The Bulk DMI interaction can be present in materials which lack inversion symmetry in their crystal lattice. An example of such a material is *FeGe*, which will be studied later in this thesis. *FeGe* is a chiral magnet, in which various magnetic phases can be present for certain range of temperature, applied field and thickness of the sample. An example of a phase diagram for a thin film of *FeGe* is shown in Fig. 1.6[1]. This diagram shows four different phases in bulk helical *FeGe*. A helical phase is present if no or a small magnetic field is applied perpendicular to the plane of the sample (which is oriented in $\langle 110 \rangle$). A schematic of helical magnetic ordering is shown in Fig. 1.7(a), where spins alternate periodically along the sample (schematic shows a planar view of the magnetic spin configuration). A Fresnel TEM image of helical order in *FeGe* is shown in Fig. 1.7(b), where helical stripes are oriented according to the thickness variation of the sample (which is schematically shown by the blue inset). A skyrmion lattice can be created by the application of a perpendicular field at the right temperature, which is schematically shown in the phase diagram in Fig. 1.6. A schematic of the spin configuration of a Bloch type

[1] thickness of the sample in the schematic is smaller than helical magnetic ordering - which is about 70 nm in *FeGe*[32]

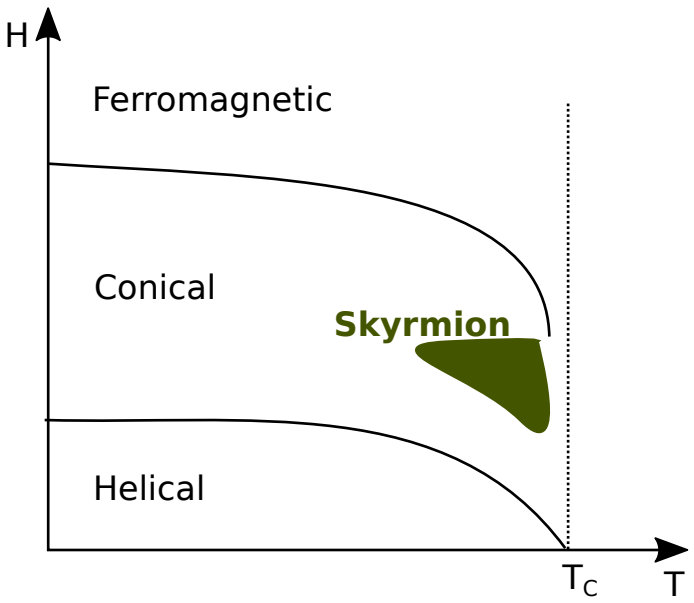

Fig. 1.6 *Phase diagram for magnetic structures in thin helical magnets. Four different types of phases (helical, conical, skyrmion and ferromagnetic) are present at the temperatures bellow the T_C. Their schematics and examples imaged by Lorentz microscopy are shown in the following figure (Fig. 1.7).*

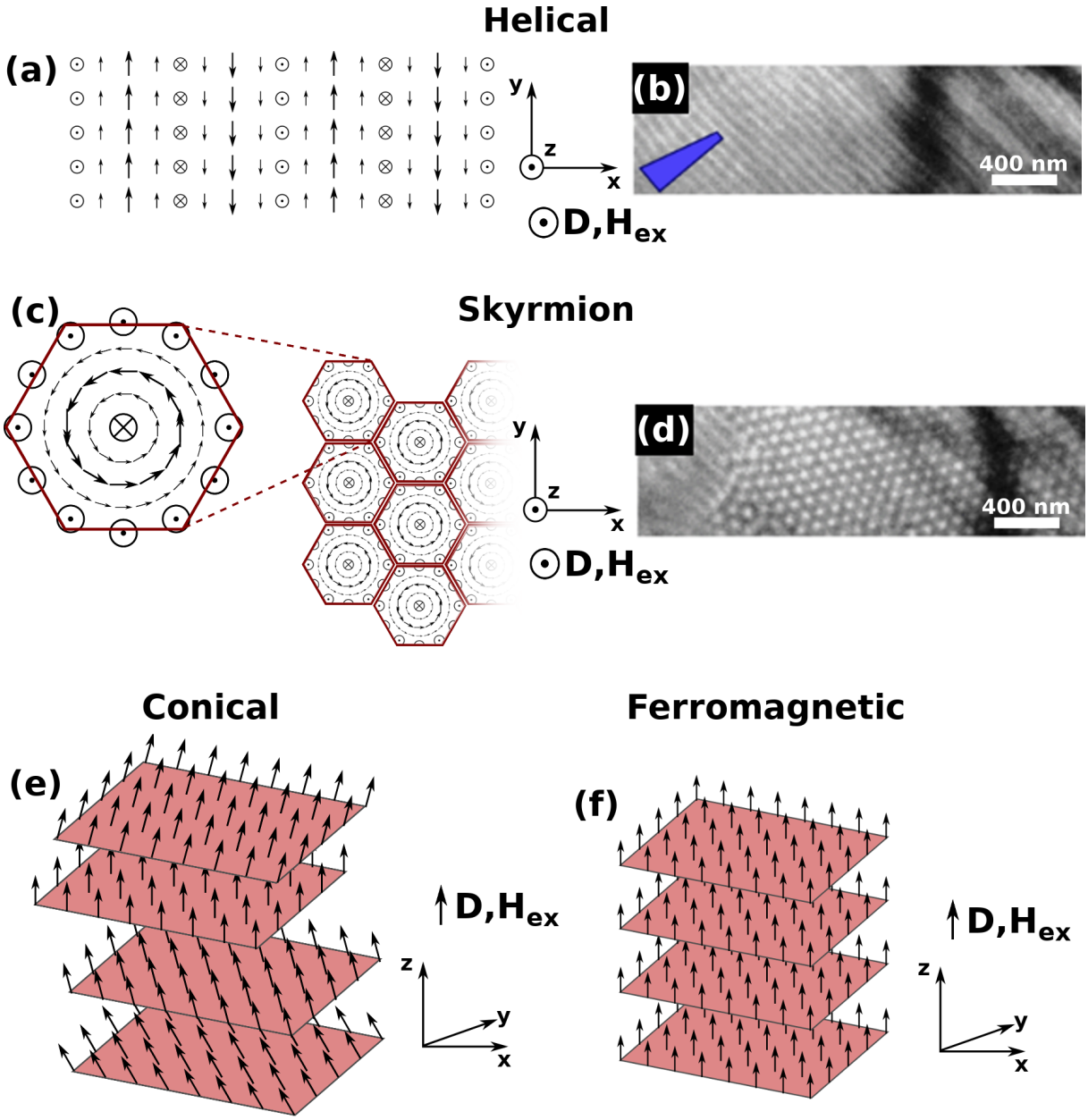

Fig. 1.7 *Phase diagram for magnetic structures in helical magnets. Orientations of* $\boldsymbol{D}$ *vector and external applied field are noted. (a) is a schematic of helical phase present when no or a small perpendicular field is applied . (b) is a Lorentz microscopy image (Fresnel) of helical order in FeGe (inset blue rectangle indicates orientation of the wedge sample). (c) is a schematic of a skyrmion in skyrmions lattice in helical magnets. (d) is a Lorentz microscopy image (Fresnel) of skyrmion lattice in FeGe. (e) is a schematic of conical phase and (f) ferromagnetic phase with no chiral structure present. FeGe crystal was oriented* $\langle 110 \rangle$ *orientation normal. Images (b) and (d) were obtained under Creative Commons 3.0 licence from [31].*

of skyrmion (again from a planar view) is shown in Fig. 1.7(c). Skyrmion configuration will be studied in detail later in the chapter. In thin *FeGe*, skyrmions form an ordered hexagonal lattice. A Fresnel TEM image of a skyrmion lattice in *FeGe* is shown in Fig. 1.7(d), which clearly shows a highly ordered hexagonal lattice of Bloch skyrmions. A schematic of the conical phase is shown in Fig. 1.7(e). This configuration contains constant spins within layers of the sample, which are slowly rotating through the thickness of the sample. Fig. 1.7(f) shows the saturated electromagnetic phase, where spins are aligned due to the external magnetic field and no DMI effect is present.

Bloch skyrmions are easy to image in TEM because their configuration is similar to Bloch walls. The detail of the configuration is shown in Fig. 1.8(a). In systems with the interfacial DMI, a different configuration of the skyrmion exists - Néel skyrmion. A schematic of their spin configuration is shown in Fig. 1.8(b). Imaging an out of plane Néel walls requires a tilt of the sample in a TEM [33], which is also the case for Néel skyrmions.

Bloch skyrmions were observed in a range of chiral crystals including *MnSi* [35], $Fe_{0.5}Co_{0.5}Si$ [8], and *FeGe* [9]. The stabilisation of a skyrmion lattice is to this date a question [31], but there are two proposed mechanisms. The first is based on an induced uniaxial anisotropy, which could stem from a lattice mismatch between the substrate and the helical magnet [36–38] and is shown in Fig. 1.9(a). The second is due to twists of chiral states near the top and bottom surfaces of cubic helimagnet crystals [39–41], which are similar to the Néel configuration and are shown in Fig. 1.9. It should be possible to examine the surface twist configuration by quantitative imaging methods in Lorentz microscopy, where a clear difference in a lowered magnetic moment should be present for the surface twist configuration compared to the bulk skyrmion configuration in helical magnets.

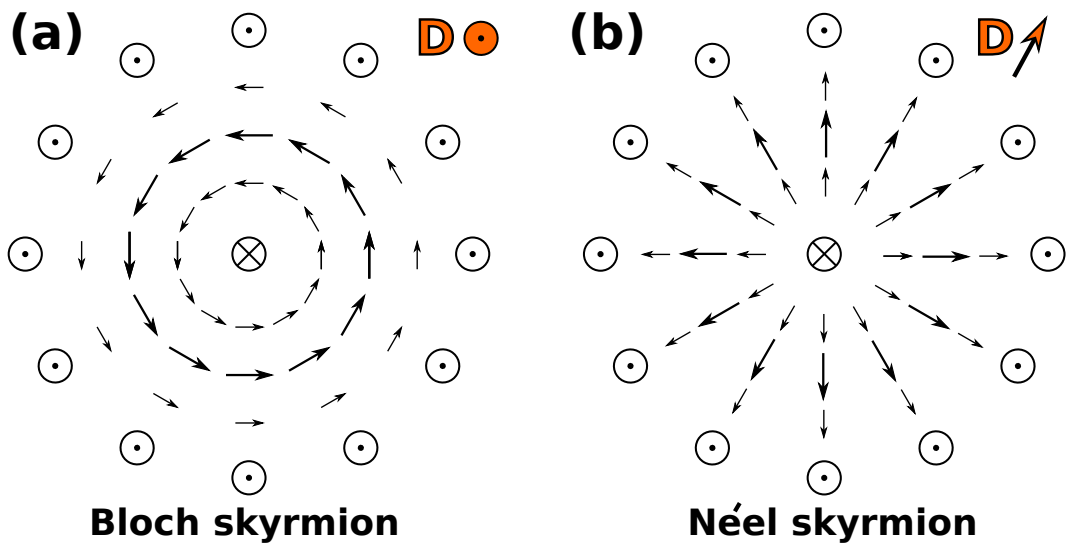

Fig. 1.8 *(a) Bloch and (b) Néel skyrmion spin configuration with the direction of* **D** *vector noted*

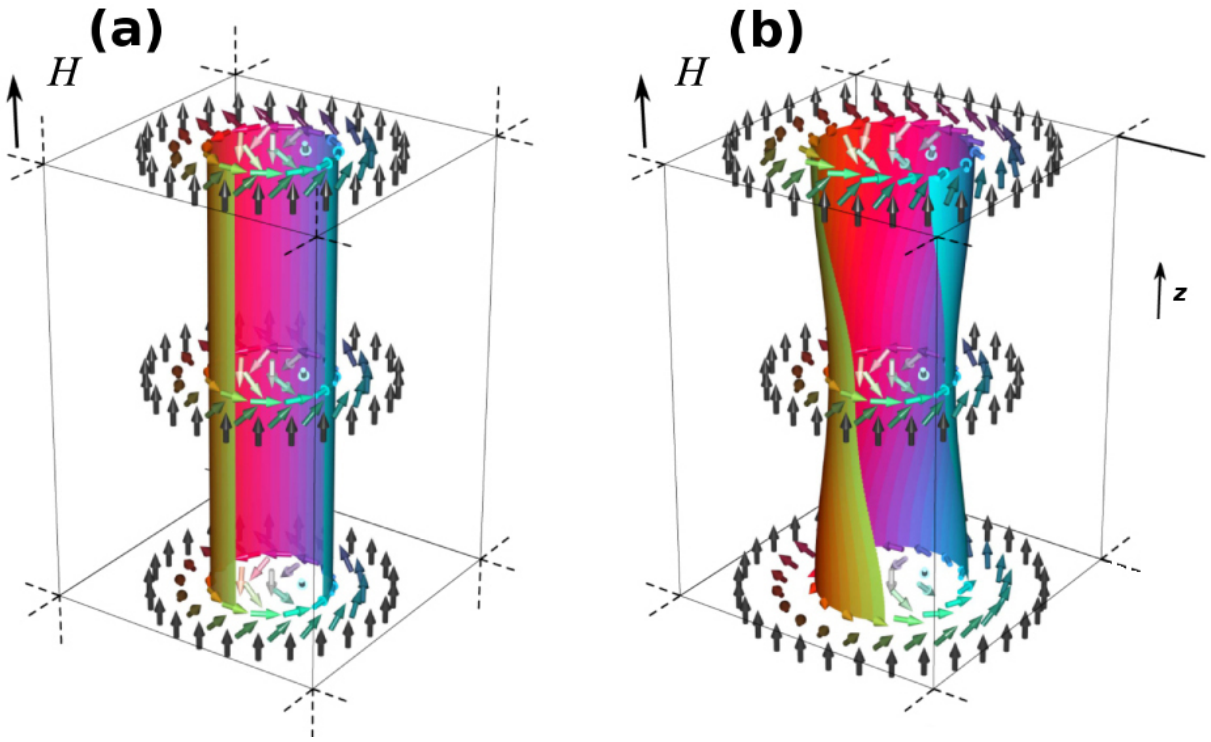

Fig. 1.9 *Possible configuration of a skyrmion in helical magnets (a) a pure Bloch skyrmion (b) a configuration changing through the thickness of the sample, where Néel like skyrmion twist is present at surfaces and Bloch configuration is in the bulk of the sample. Image was altered under Creative Commons 3.0 licence from [34]*

In this thesis, high resolution Lorentz microscopy [30] will be used to image detailed internal structure of magnetic skyrmion within a skyrmion lattice in a thin film of *FeGe*. Methods of statistical analysis will used to compare the internal structure to a 3Q model for magnetic bubble domains [42], which will be also described later in Chap. 5. The 3Q model is based on an assumption that the lattice of skyrmions can be created by a combination of three helical phases oriented 120° to each other. This model is, however, a first approximation but it can be used to argue a simple case for expected characteristics of magnetic skyrmions. The details of the model, together with state of art images of skyrmions within a skyrmion lattice, will be given in Chap. 5.

1.5 Micromagnetic simulations

In this thesis, micromagnetic simulations will be provided by $MuMax^3$ software [43]. It is a multipurpose micromagnetic simulator, with CUDA graphic card acceleration. $MuMax^3$

uses a phenomenological model based on the Landau-Lifshitz-Gilbert equation [44]:

$$\frac{\partial \mathbf{M}}{\partial t} = -\gamma\, \mathbf{M} \times \mathbf{H_{eff}} - \frac{\gamma\, \alpha}{|\mathbf{M}|}\, \mathbf{M} \times (\mathbf{M} \times \mathbf{H_{eff}}), \tag{1.10}$$

where $\mathbf{M}$ is the magnetisation, t is the time, γ is the gyromagnetic ratio, α is the damping coefficient and $\mathbf{H}_{eff}$ is the effective field defined by:

$$\mathbf{H_{eff}} = -\frac{1}{\mu_0}\frac{\partial E_{tot}}{\partial \mathbf{M}} \tag{1.11}$$

where E_{tot} is the total energy functional. The Landau-Lifshitz-Gilbert equation describes the gyroscopic precession of a magnetic moment due to the applied field and damping. This is schematically shown in Fig. 1.10. The magnetisation $\mathbf{M}$ will precess due to damping, α, and align with effective field, $\mathbf{H}_{eff}$.

MuMax^3 simulations are based on a finite difference method, where the geometry is split into cubic cells. A necessary condition for a valid simulation is to keep the size of the cell smaller than exchange length of the simulated material. Simulations shown in this thesis are also made at zero temperature.

An example of a magnetisation configuration for a hexagonal ferromagnetic particle is shown in Fig. 1.11. Simulated magnetisation maps will be used to simulate Lorentz microscopy images by algorithm described in [45], the details of which will be given at the end of the following chapter.

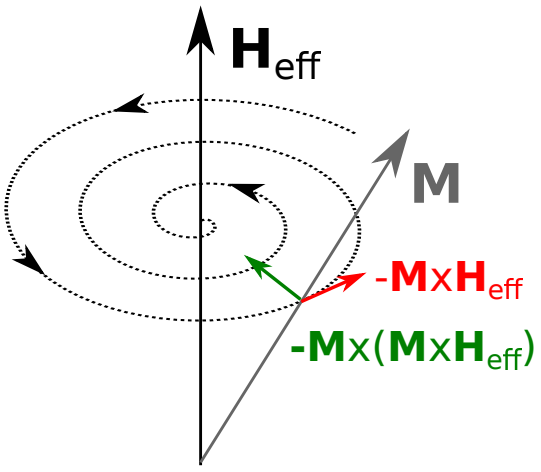

Fig. 1.10 *Schematic of Landau-Lifshitz-Gilbert precession used in micromagnetic simulations.* $\mathbf{M}$ *is precessing around* H_{eff} *field with applied dumping. Two terms of Eq. 1.10 are highlighted in colour*

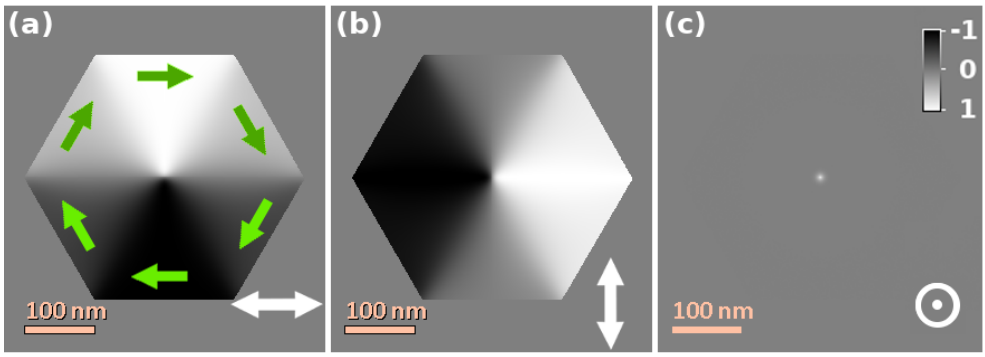

Fig. 1.11 *Mumax*^{3} *simulation of a* 20 *nm thick ferromagnetic hexagonal particle,* m_x*,* m_y *and* m_z *components of magnetisation are in (a), (b) and (c) respectively. The size of a cell was* $1.6 \times 1.6 \times 20\,nm^3$*, the exchange stiffness was* $A = 13 \times 10^{-12}\,J/m$ *and the saturation magnetisation was* $M_s = 860 \times 10^3\,A/M$*.*

Thesis outline

In this thesis Lorentz microscopy will be studied in the terms of wave optical formulation in **Chapter 2**. It will be shown how phase contrast can be imaged by different methods within TEM, especially focusing on quantitative imaging of integrated magnetic induction in thin samples.

The theory of differential phase contrast scanning transmission electron microscopy will be given in **Chapter 3**, where a wave-optical simulation of STEM DPC imaging will be introduced. This will be used to show the response of different detection algorithms for theoretically created complex transmission function representing polycrystalline magnetic sample.

In **Chapter 4**, experimental DPC imaging will be introduced where a pixelated detector will be used to acquire image of central diffraction disk in STEM. Algorithms introduced in Chap. 3 will be used to find the deflection of the beam. It will be demonstrated how this variation to detection of DPC can enhance the imaging where strong diffraction contrast is present for polycrystalline thin films in standard segmented detector method.

Chapter 5 will present imaging of the structure of skyrmions within skyrmion lattice in FeGe helical magnet. It will be shown how can the enhanced imaging scheme introduced in this work reveal fine details of in-plane integrated magnetic induction of skyrmions.

A comparison of electron holography and differential phase contrast will be presented in **Chapter 6**. The methods will be compared for a simple imaging of integrated electric field present between two biased needles within TEM. It will be successfully shown that both methods provide quantitative imaging of integrated fields and their advantages and disadvantages will be discussed.

In the final chapter, **Chapter 7**, the results of this thesis are analysed and their significance is discussed. An outline of future research stemming from this thesis is given.

References

[1] E. Grochowski and R. D. Halem, "Technological impact of magnetic hard disk drives on storage systems," *IBM Systems Journal*, vol. 42, no. 2, p. 338, 2003.

[2] S. Schmaus, A. Bagrets, Y. Nahas, T. K. Yamada, A. Bork, M. Bowen, E. Beaurepaire, F. Evers, and W. Wulfhekel, "Giant magnetoresistance through a single molecule," *Nature nanotechnology*, vol. 6, no. 3, pp. 185–189, 2011.

[3] S. Mao, Y. Chen, F. Liu, X. Chen, B. Xu, P. Lu, M. Patwari, H. Xi, C. Chang, B. Miller, *et al.*, "Commercial TMR heads for hard disk drives: characterization and extendibility at 300 gbit/in^2," *IEEE transactions on magnetics*, vol. 42, no. 2, pp. 97–102, 2006.

[4] J. Daughton, "GMR applications," *Journal of Magnetism and Magnetic Materials*, vol. 192, no. 2, pp. 334–342, 1999.

[5] Y. Bao, T. Wen, A. C. S. Samia, A. Khandhar, and K. M. Krishnan, "Magnetic nanoparticles: material engineering and emerging applications in lithography and biomedicine," *Journal of materials science*, vol. 51, no. 1, pp. 513–553, 2016.

[6] Q. A. Pankhurst, J. Connolly, S. K. Jones, and J. Dobson, "Applications of magnetic nanoparticles in biomedicine," *Journal of physics D: Applied physics*, vol. 36, no. 13, p. R167, 2003.

[7] Y. Togawa, T. Koyama, K. Takayanagi, S. Mori, Y. Kousaka, J. Akimitsu, S. Nishihara, K. Inoue, A. Ovchinnikov, and J. Kishine, "Chiral magnetic soliton lattice on a chiral helimagnet," *Phys. Rev. Lett.*, vol. 108, no. 10, p. 107202, 2012.

[8] X. Yu, Y. Onose, N. Kanazawa, J. Park, J. Han, Y. Matsui, N. Nagaosa, and Y. Tokura, "Real-space observation of a two-dimensional skyrmion crystal," *Nature*, vol. 465, no. 7300, pp. 901–904, 2010.

[9] X. Yu, N. Kanazawa, Y. Onose, K. Kimoto, W. Zhang, S. Ishiwata, Y. Matsui, and Y. Tokura, "Near room-temperature formation of a skyrmion crystal in thin-films of the helimagnet FeGe," *Nature materials*, vol. 10, no. 2, pp. 106–109, 2011.

[10] A. Fert, V. Cros, and J. Sampaio, "Skyrmions on the track," *Nature nanotechnology*, vol. 8, no. 3, pp. 152–156, 2013.

[11] A. Aharoni, *Introduction to the Theory of Ferromagnetism*. Clarendon Press, 1996.

[12] C. Kittel, *Introduction To Solid State Physics*. John Wiley & Sons, 1996.

[13] P. Yu, X. Jin, J. Kudrnovskỳ, D. Wang, and P. Bruno, "Curie temperatures of fcc and bcc nickel and permalloy: Supercell and Green's function methods," *Physical Review B*, vol. 77, no. 5, p. 054431, 2008.

[14] M. Belmeguenai, J.-P. Adam, Y. Roussigné, S. Eimer, T. Devolder, J.-V. Kim, S. M. Cherif, A. Stashkevich, and A. Thiaville, "Interfacial Dzyaloshinskii-Moriya interaction in perpendicularly magnetized Pt/Co/AlO x ultrathin films measured by Brillouin light spectroscopy," *Phys. Rev. B*, vol. 91, no. 18, p. 180405, 2015.

References

[15] S. Rohart and A. Thiaville, "Skyrmion confinement in ultrathin film nanostructures in the presence of Dzyaloshinskii-Moriya interaction," *Phys. Rev. B*, vol. 88, no. 18, p. 184422, 2013.

[16] A. Hrabec, N. Porter, A. Wells, M. Benitez, G. Burnell, S. McVitie, D. McGrouther, T. Moore, and C. Marrows, "Measuring and tailoring the Dzyaloshinskii-Moriya interaction in perpendicularly magnetized thin films," *Phys. Rev. B*, vol. 90, no. 2, p. 020402, 2014.

[17] K. Di, V. L. Zhang, H. S. Lim, S. C. Ng, M. H. Kuok, J. Yu, J. Yoon, X. Qiu, and H. Yang, "Direct observation of the Dzyaloshinskii-Moriya interaction in a Pt/Co/Ni film," *Phys. Rev. Lett.*, vol. 114, no. 4, p. 047201, 2015.

[18] S. Huang and C. Chien, "Extended skyrmion phase in epitaxial FeGe (111) thin films," *Phys. Rev. Lett.*, vol. 108, no. 26, p. 267201, 2012.

[19] Y. Onose, Y. Okamura, S. Seki, S. Ishiwata, and Y. Tokura, "Observation of magnetic excitations of skyrmion crystal in a helimagnetic insulator Cu_2OSeO_3," *Phys. Rev. Lett.*, vol. 109, no. 3, p. 037603, 2012.

[20] Z. Wang, V. Zhang, H. Lim, S. Ng, M. Kuok, S. Jain, and A. Adeyeye, "Observation of frequency band gaps in a one-dimensional nanostructured magnonic crystal," *Applied Physics Letters*, vol. 94, no. 8, p. 083112, 2009.

[21] Y. Nakatani, A. Thiaville, and J. Miltat, "Faster magnetic walls in rough wires," *Nature materials*, vol. 2, no. 8, pp. 521–523, 2003.

[22] R. Hertel, W. Wulfhekel, and J. Kirschner, "Domain-wall induced phase shifts in spin waves," *Phys. Rev. Lett.*, vol. 93, no. 25, p. 257202, 2004.

[23] Y. Tokunaga, X. Yu, J. White, H. M. Rønnow, D. Morikawa, Y. Taguchi, and Y. Tokura, "A new class of chiral materials hosting magnetic skyrmions beyond room temperature," *Nature communications*, vol. 6, 2015.

[24] A. Aharoni, *Introduction to the Theory of Ferromagnetism*. Clarendon Press, 2000.

[25] D. Jiles, *Introduction to magnetism and magnetic materials*. CRC press, 2015.

[26] S. McVitie and J. Chapman, "Measurement of domain wall widths in Permalloy using Differential Phase Contrast imaging in STEM," *Journal of Magnetism and Magnetic Materials*, vol. 83, no. 1, pp. 97–98, 1990.

[27] J. Chapman, P. Batson, E. Waddell, and R. Ferrier, "The direct determination of magnetic domain wall profiles by Differential Phase Contrast electron microscopy," *Ultramicroscopy*, vol. 3, no. 0, pp. 203–214, 1978. http://www.sciencedirect.com/science/article/pii/S0304399178800278.

[28] J. Chapman, "The investigation of magnetic domain structures in thin foils by electron microscopy," *Journal of Physics D: Applied Physics*, vol. 17, p. 623, 1984.

[29] J. Chapman, I. McFadyen, and S. McVitie, "Modified differential phase contrast Lorentz microscopy for improved imaging of magnetic structures," *Magnetics, IEEE Transactions on*, vol. 26, pp. 1506–1511, sep 1990.

[30] M. Krajnak, D. McGrouther, D. Maneuski, V. O'Shea, and S. McVitie, "Pixelated detectors and improved efficiency for magnetic imaging in STEM differential phase contrast," *Ultramicroscopy*, vol. 165, pp. 42–50, 2016.

[31] A. O. Leonov, Y. Togawa, T. L. Monchesky, A. N. Bogdanov, J. Kishine, Y. Kousaka, M. Miyagawa, T. Koyama, J. Akimitsu, T. Koyama, K. Harada, S. Mori, D. McGrouther, R. Lamb, M. Krajnak, S. McVitie, R. L. Stamps, and K. Inoue, "Chiral Surface Twists and Skyrmion Stability in Nanolayers of Cubic Helimagnets," *Phys. Rev. Lett.*, vol. 117, p. 087202, Aug 2016.

[32] D. McGrouther, R. J. Lamb, M. Krajnak, S. McFadzean, S. McVitie, R. L. Stamps, A. O. Leonov, A. N. Bogdanov, and Y. Togawa, "Internal structure of hexagonal skyrmion lattices in cubic helimagnets," *New Journal of Physics*, vol. 18, no. 9, p. 095004, 2016.

[33] M. J. Benitez, A. Hrabec, A. P. Mihai, T. A. Moore, G. Burnell, D. McGrouther, C. H. Marrows, and S. McVitie, "Magnetic microscopy and topological stability of homochiral Neel domain walls in a Pt/Co/AlOx trilayer," *Natre Communicatins*, vol. 6, DEC 2015.

[34] F. N. Rybakov, A. B. Borisov, S. Blügel, and N. S. Kiselev, "New spiral state and skyrmion lattice in 3D model of chiral magnets," *New Journal of Physics*, vol. 18, no. 4, p. 045002, 2016.

[35] S. Mühlbauer, B. Binz, F. Jonietz, C. Pfleiderer, A. Rosch, A. Neubauer, R. Georgii, and P. Böni, "Skyrmion lattice in a chiral magnet," *Science*, vol. 323, no. 5916, pp. 915–919, 2009.

[36] A. Butenko, A. Leonov, U. Rößler, and A. Bogdanov, "Stabilization of skyrmion textures by uniaxial distortions in noncentrosymmetric cubic helimagnets," *Phys. Rev. B*, vol. 82, no. 5, p. 052403, 2010.

[37] M. Wilson, A. Butenko, A. Bogdanov, and T. Monchesky, "Chiral skyrmions in cubic helimagnet films: The role of uniaxial anisotropy," *Phys. Rev. B*, vol. 89, no. 9, p. 094411, 2014.

[38] E. Karhu, S. Kahwaji, T. Monchesky, C. Parsons, M. Robertson, and C. Maunders, "Structure and magnetic properties of MnSi epitaxial thin films," *Phys. Rev. B*, vol. 82, no. 18, p. 184417, 2010.

[39] M. Wilson, E. Karhu, D. Lake, A. Quigley, S. Meynell, A. Bogdanov, H. Fritzsche, U. Rößler, and T. Monchesky, "Discrete helicoidal states in chiral magnetic thin films," *Phys. Rev. B*, vol. 88, no. 21, p. 214420, 2013.

[40] F. Rybakov, A. Borisov, and A. Bogdanov, "Three-dimensional skyrmion states in thin films of cubic helimagnets," *Phys. Rev. B*, vol. 87, no. 9, p. 094424, 2013.

[41] F. N. Rybakov, A. B. Borisov, S. Blügel, and N. S. Kiselev, "New type of stable particlelike states in chiral magnets," *Phys. Rev. Lett.*, vol. 115, no. 11, p. 117201, 2015.

[42] T. Garel and S. Doniach, "Phase transitions with spontaneous modulation-the dipolar Ising ferromagnet," *Phys. Rev. B*, vol. 26, no. 1, p. 325, 1982.

[43] A. Vansteenkiste, J. Leliaert, M. Dvornik, M. Helsen, F. Garcia-Sanchez, and B. Van Waeyenberge, "The design and verification of MuMax^3," *Aip Advances*, vol. 4, no. 10, p. 107133, 2014.

[44] T. L. Gilbert, "A phenomenological theory of damping in ferromagnetic materials," *IEEE Transactions on Magnetics*, vol. 40, no. 6, pp. 3443–3449, 2004.

[45] M. Mansuripur, "Computation of electron diffraction patterns in Lorentz electron microscopy of thin magnetic films," *Journal of Applied Physics*, vol. 69, pp. 2455–2464, feb 1991.

CHAPTER 2

Methods and theory of transmission electron microscopy and Lorentz microscopy

Introduction

In this chapter, basic methods of transmission electron microscopy will be discussed. Image formation of the TEM will be explained. Methods of Lorentz microscopy of magnetic samples will be described together with their advantages and limits. This will help to understand the particular approach of the development of DPC STEM imaging, which will be introduced in this work.

2.1 Transmission Electron Microscopy

The resolution of microscopic imaging is ultimately limited by the size or wavelength of used radiation (photons/electrons/ions). Diffraction limits the resolution d of an optical microscope system which can be described by Abbe's limit as [1]:

$$d = \frac{\lambda}{2\,n\,sin(\theta)}, \tag{2.1}$$

where λ is the wavelength of the radiation and $n\,sin(\theta)$ is the numerical aperture of the instrument. Due to Abbe's limit, standard optical microscopy can only resolve details of about $200\,nm$.

Higher resolution can be achieved by radiation with smaller wavelengths. In 1924, Louis de Broglie postulated that matter can have wave-like behaviour and that the wavelength

of a particle depends on its momentum, in the non-relativistic regime as:

$$\lambda = \frac{h}{p}, \tag{2.2}$$

where h is Planck's constant and p is the momentum of the particle. De Broglie's postulate has given an important advantage to microscopy: matter particles can be accelerated to achieve much smaller wavelengths than those of visible light. For example, an electron and a Helium ion travelling at $50000\,ms^{-1}$ will have wavelengths $\lambda_e = 14.5\,nm$ and $\lambda_{He^+} = 2\,pm$ respectively. Electrons are enormously practical for this purpose, as they are easy to generate and their momentum and trajectories can be changed by the application of electric and magnetic fields, because they are charged particles.

The history of electron microscopy started with Ernest Ruska and his colleagues in the early 1930s. They proved that a magnetic coil can act as an electron lens and constructed the first prototype of a transmission electron microscope (CTEM). In 1937, Manfred Von Ardenne created the first scanning transmission electron microscope (STEM). Decades of developments improved not only the resolution but also the functionality and vast aspects of science of the TEM. Advances in specimen preparation, vacuum systems, environmental stability, high voltage circuitry, electron sources and others are a crucial part of the development of the TEM. In modern, aberration corrected, TEM instruments resolution of tens of picometers is possible in high resolution mode [2–4], allowing routinely accessible atomic resolution [5]. It is also important to mention that the resolution of the TEM is not diffraction limited (this is the main limiting factor in optical microscopy).

The majority of TEM instruments operate with accelerating voltages of 80–300 kV. The momentum of such highly accelerated electrons is in the relativistic regime. Therefore the wavelength of an electron is described by [6]:

$$\lambda = \frac{h}{\left[2\,m_e\,eV\left(1 + \frac{eV}{2\,m_e\,c^2}\right)\right]^{\frac{1}{2}}}, \tag{2.3}$$

where eV is the kinetic energy of an electron, c is the speed of light and m_e is the rest mass of an electron. For an instrument using $200\,kV$ electron acceleration, the difference of non-relativistic $\lambda_c = 2.71\,pm$ and relativistic $\lambda_r = 2.51\,pm$ wavelengths is considerable. The graph of electron wavelength against its kinetic energy is shown in Fig. 2.1.

The resolution of the TEM can be enhanced by two different approaches. The first option is to increase the electron acceleration voltage. There are a small number of instruments with $> 1\,MV$ acceleration. Such specialised instruments are at the forefront of electron microscopy, however their cost is enormous. Furthermore, as electrons interact with a specimen and deposit energy into it, imaging with very highly energetic electrons can

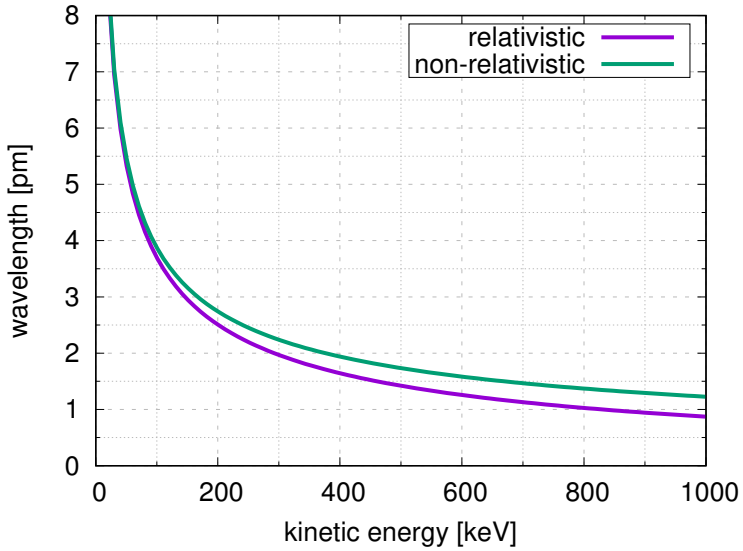

Fig. 2.1 *The wavelength of accelerated electron as a function of its kinetic energy for the relativistic and non-relativistic calculations*

cause damage to the atomic structure of the specimen [7], therefore very high acceleration voltages can be impractical. The second option to achieve higher resolution is to improve the electro-optical system of the instrument. Electron lenses are not perfect and their aberrations limit the resolution of the TEM. As mentioned before, the wavelength of the $200\,kV$ electron is $\lambda_r = 2.51\,pm$, however the resolution of the modern, aberration corrected TEMs is larger by a factor of 20 at best [3]. This massive improvement, compared to the past is allowed by the introduction of sophisticated aberration correctors. Such corrections are based on the creation of negative aberrations in specialised, multi-pole magnetic lenses which largely cancel aberrations produced by the imaging lenses of the instrument. A description of the common aberrations will be provided in Sec. 2.2.3.

Specimens imaged by the TEM are required to be electron-transparent, usually less than $100\,nm$ thick. Specimen preparation techniques, such as manual polishing and grinding, were mostly replaced by the FIB thin film creation. This technique is based on ion milling of the specific site of a bulk sample to create a thin, electron-transparent lamella which is attached to the specimen holder. The other option is to deposit a material of interest on the top of an electron transparent membrane, which can be mounted directly on the rod and imaged in the TEM.

TEM can be divided into 2 main categories - CTEM and STEM. The main difference is that, in CTEM, the area of the specimen to be imaged is illuminated by an electron beam in parallel condition and works in a similar manner to an optical microscope. The resolution of CTEM is mainly dependent on the quality of the objective lens, the main imaging lens of CTEM. In STEM, a focused electron beam is used to scan the specimen. The detected signal is only ever related to the spot of the specimen which was illuminated,

therefore the final image has to be built pixel by pixel. The objective lens use differs in STEM where it is used to focus the beam. The size of the focused beam, limited by aberrations and diffraction, is the main limit to the resolution of STEM [6].

A schematic of a CTEM instrument is shown in Fig. 2.2. In a very simplistic description, an electron beam is generated in an electron gun at the top of the instrument, after which it travels down the column. The electron beam is then accelerated by an electrostatic field to achieve the selected energy/momentum/wavelength. Condenser lenses prepare the beam for transmission through the specimen (which is mounted on a rod). After transmission, the objective lens magnifies the image of the specimen and projector lenses project the image onto a viewing screen. The column of the TEM is kept under vacuum for multiple reasons: it maximises the free electron path in the instrument, helps to prevent the arc of the high voltage acceleration coil with the ground, and minimises contamination of the specimen.

A description of the wave-optical imaging process of CTEM and STEM is given in following sections.

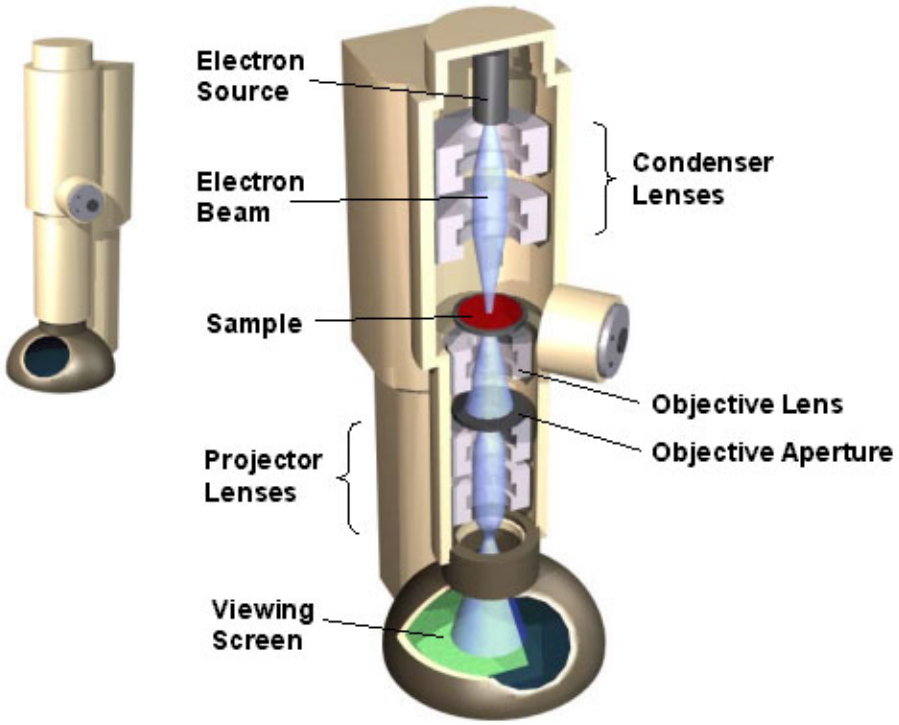

Fig. 2.2 *A simplified schematic of the TEM column showing a setup for CTEM imaging. The schematic shows the most common configuration of the CTEM. This image was taken from the Barrett Research Group webpage [8]*

2.2 Image formation of CTEM and STEM

Although modern TEM instruments are highly sophisticated machines consisting of numerous parts, the standard CTEM and STEM imaging process can be simplified to the diagrams shown in Fig. 2.3(a) and (b) respectively.

In standard CTEM, the specimen is illuminated by a parallel electron beam which travels in the positive z direction, a schematic of which is shown in Fig. 2.3(a). The electron beam scatters from the material of the specimen and the objective lens images the scattered beams. The image of the specimen formed by the objective lens is magnified as is shown, but not to the scale, in Fig. 2.3(a). The objective aperture restricts the maximum scattering angle α of the electronsthat are allowed to form the image. Projector lenses follow after the objective aperture, which magnify the image further. Aberrations of projector lenses are small compared to the objective lens because the angles involved are much smaller (electrons travel closer to ideal optical path). The image is formed in the image plane which can be projected onto the microscope viewing screen, the CCD camera or an other detector.

It is important to mention that if the objective lens were ideal and no objective aperture is used, there would be no signal visible in the CTEM image for a pure phase object. Assuming uniform transmission (no change of the amplitude of the transmitted beam), the ideal objective lens would image all the scattered electrons travelling along the different

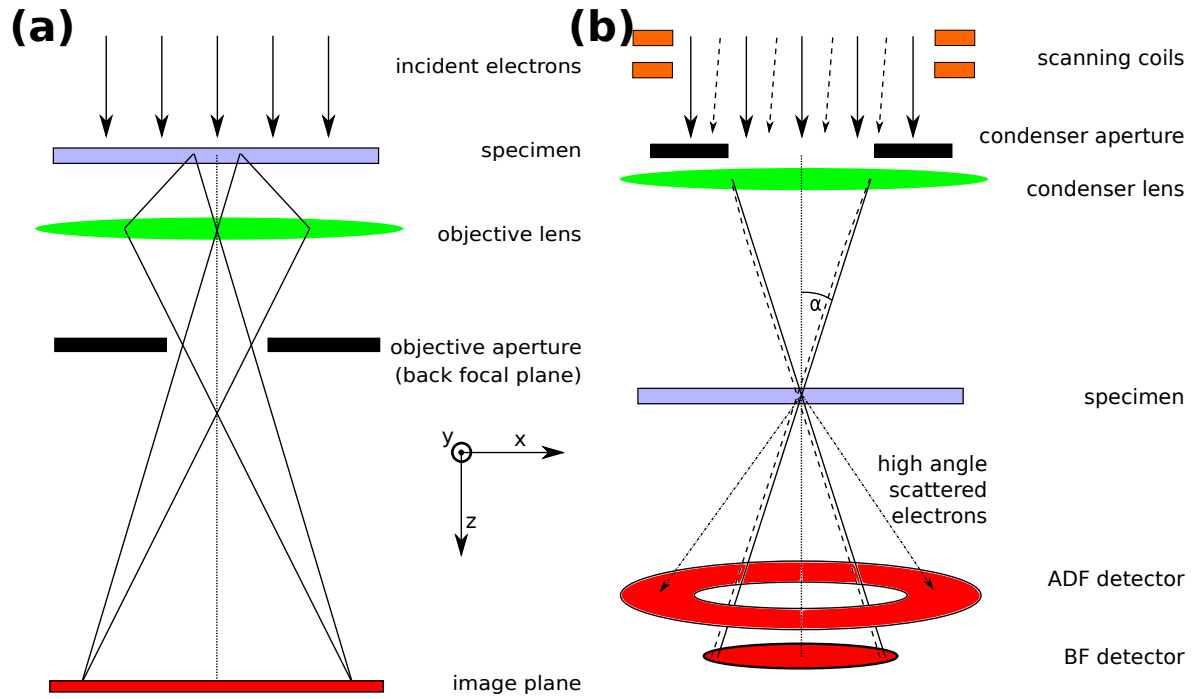

Fig. 2.3 *Diagrams of (a) CTEM image formation (b) STEM image formation. Optical paths and component sizes in schematic are not to scale*

optical paths to the same spots in the image that they were generated from, albeit magnified. This is important for the Fresnel type of imaging magnetic specimens where magnetic contrast is phase contrast, therefore not visible in the focused TEM image. This point will become clearer after the explanation of the imaging formation and importance of aberrations in Secs 2.2.1 and 2.2.3.

Projector lenses can also be set to project the back focal plane (diffraction pattern) onto the viewing screen of the CTEM. Such an image can be used for analysis of the structure of the specimen, or it can be used for the setup of the dark field imaging. In dark field imaging only selected spots of the diffraction pattern are allowed to form the image. This is achieved with use of an objective aperture or SAD aperture in the back focal plane, which masks unwanted scattering signals. An example of a bright field CTEM image and a dark field CTEM image (formed from the same field of view of crystalline specimen) is shown in Fig. 2.4, and shows the types of expected contrast. Fig 2.4(a) is the bright field image formed by the unscattered beam, where the darker areas correspond to material in which electrons are strongly scattered. The dark field image in Fig. 2.4(b) shows brighter areas that correspond to stronger scattering - in this case from the [002] diffraction point index. Fig. 2.4(c) shows which spots were used to form CTEM the images.

As previously mentioned, the STEM imaging is based on focusing of the electron beam to a fine spot and scanning over the specimen, a schematic of which is shown in Fig. 2.3(b).

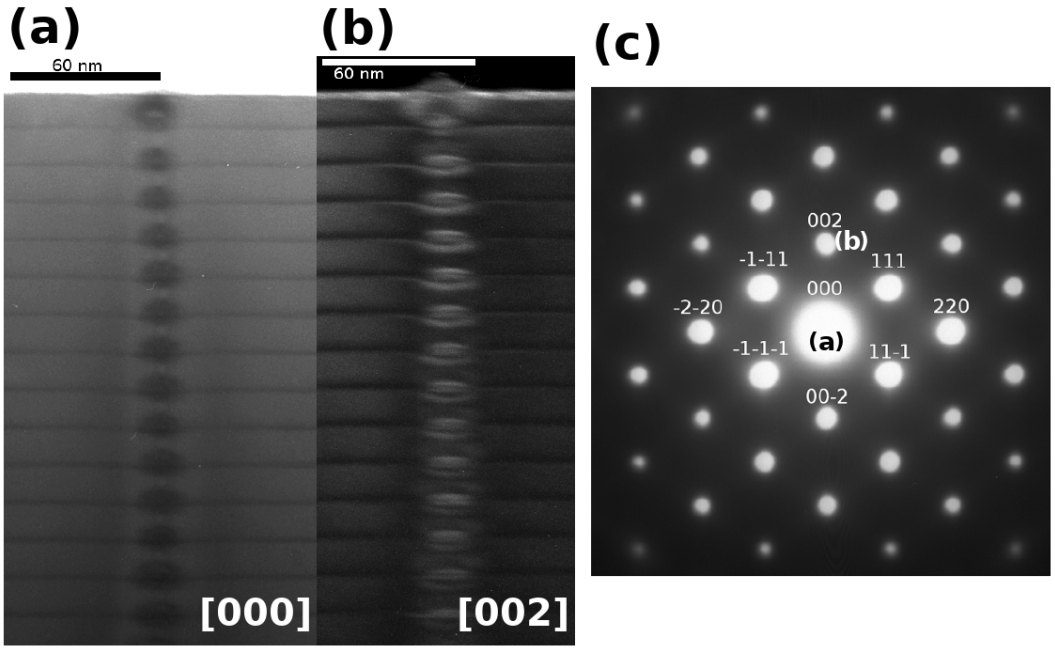

Fig. 2.4 *An example of (a) a bright field and (b) a dark field TEM images of InGaAs quantum dwells grown within GaAs stacks, (c) shows contrast forming spots in the diffraction pattern. The dark field image in (b) was created from* (002) *spot. (used with permission of Dr Magnus Nord)*

The circular probe is formed by a pre-specimen aperture, which is then focused to a spot by the condenser lens. Scanning coils deflect the beam over the specimen. The schematic in Fig. 2.3(b) shows the two principal imaging modes of STEM. The mode, in which the intensity of the central spot/disk is measured by a bright field detector is mostly equivalent to the bright field CTEM imaging. If only scattered electrons are observed by an annular dark field detector (central beam passes through a hole in the detector), ADF images can be formed. This allows for a large improvement to the image contrast as ADF signals and mainly high angle HAADF signals[1] contain intensity information from inelastically scattered electrons which depends on $\sim Z^2$, where Z is the atomic number [9]. Examples

[1]HAADF signals contain only a little information from Bragg diffraction

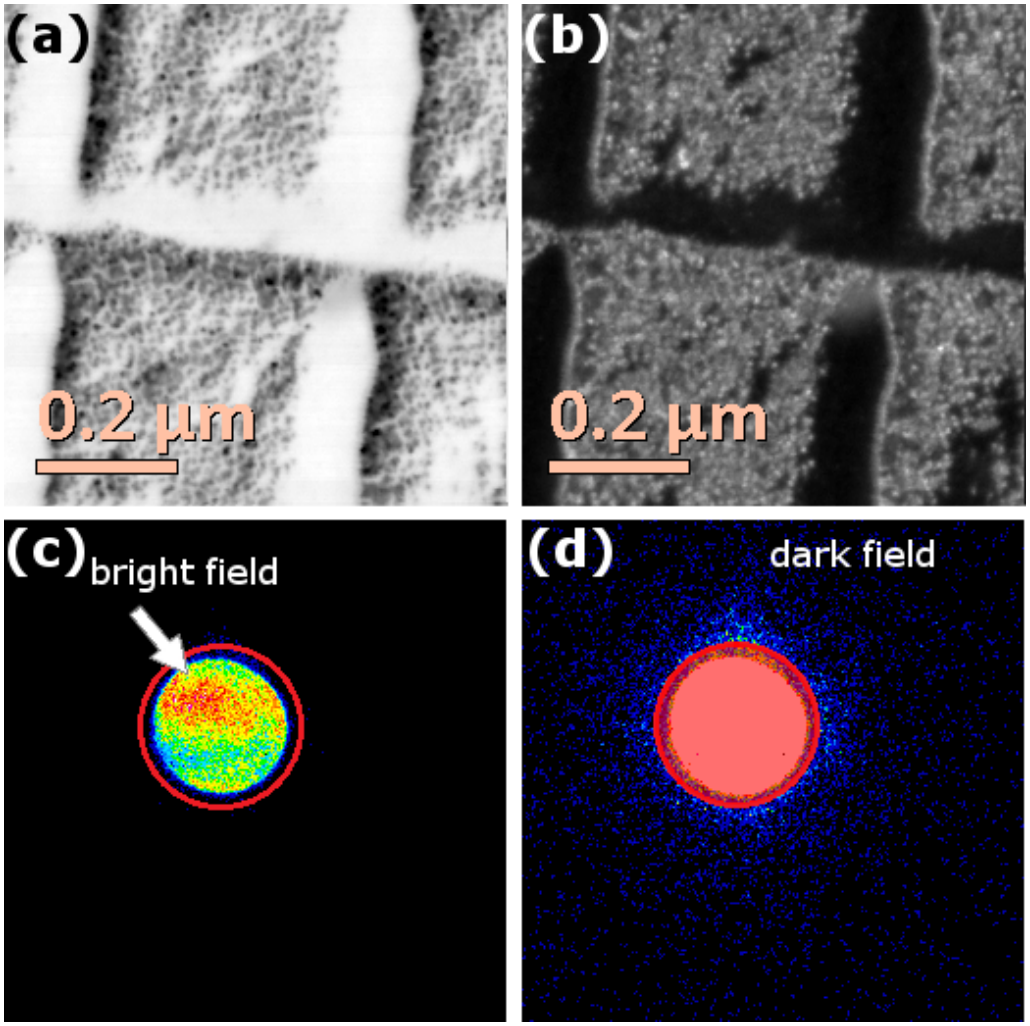

Fig. 2.5 *An example of (a) the bright field and (b) dark field STEM images of gold nanoparticle cross-grating, image forming signal for (c) bright field, within the highlighted area containing central disk and (d) dark field, outside of highlighted area containing only scattered information. Contrast for both diffraction patterns was altered to show the variation of the signal. Images were generated from pixelated STEM experiment allowing post processing of the datasets*

of BF and ADF STEM images acquired simultaneously are shown in Fig. 2.5. The contrast in the two imaging modes is inverted, as electrons which are scattered to larger angles do not contribute to BF image and vice versa. They are however not inverse to each other, as the angles into the detectors are not simply inverted (ADF detector will have a maximal angle).

For thin specimens, a mathematical description of the TEM imaging can be provided by wave-optics. Imaging can be approximated as a linear convolution of the specimen image and a point spread function of the microscope. Wave optical explanation of TEM imaging will be used to simulate imaging magnetic materials with STEM DPC in the following chapter.

2.2.1 CTEM linear imaging approximation

The schematic of the wave-optical description of CTEM is shown in Fig. 2.6, which includes the notation of important positions and forms of wave functions along the optical path.

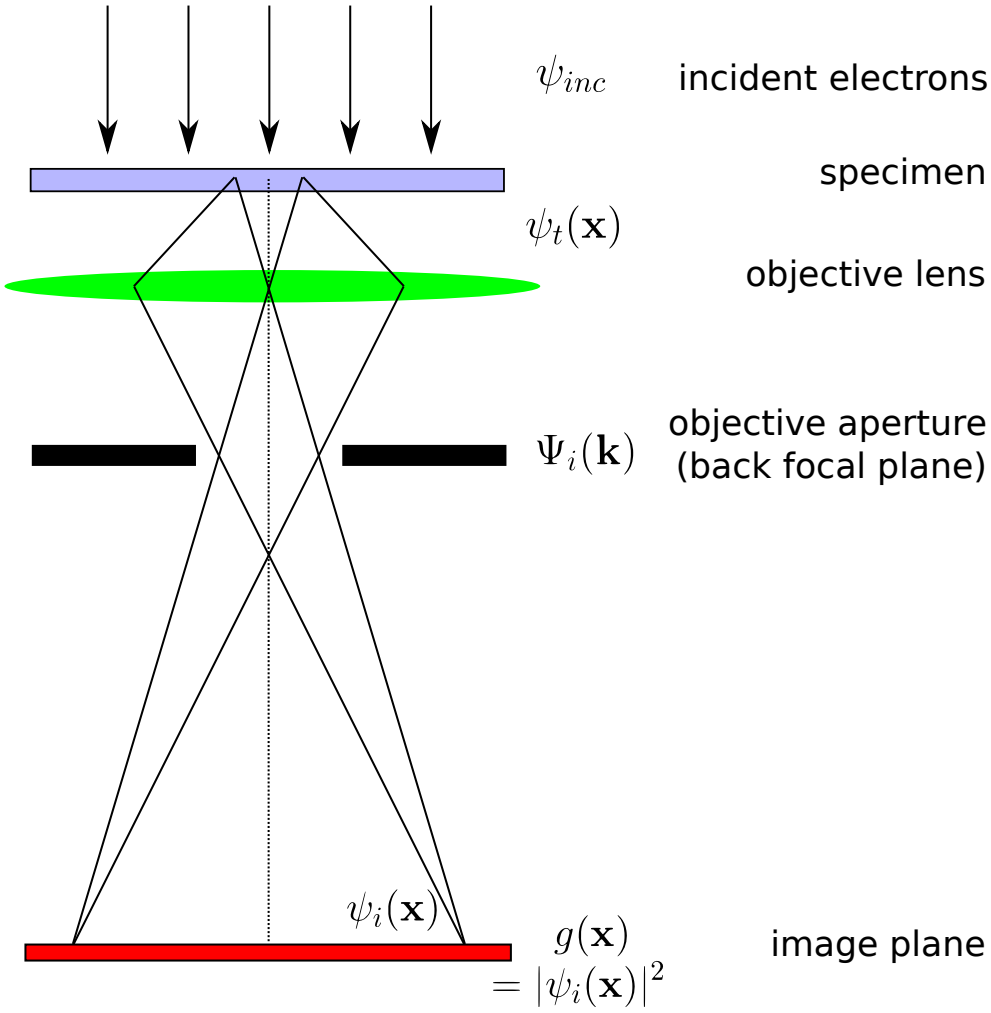

Fig. 2.6 *Schematic of wave optical description of CTEM linear imaging approximation*

Incident electrons can be approximated as plain Bloch waves, $\psi_{inc} \approx 1$. If the specimen can be represented by a multiplicative transmission function ψ_t, then ψ_t can be simply given as a multiplication of the incident electron wave with the complex specimen transmission function $t(\mathbf{x})$, which can be split into an amplitude $S(\mathbf{x})$ and a phase $\phi(\mathbf{x})$ [10] function:

$$\psi_t(\mathbf{x}) = \psi_{inc}\, t(\mathbf{x}) = \psi_{inc}\, S(\mathbf{x})\, e^{\imath\phi(\mathbf{x})}. \tag{2.4}$$

The diffraction causes a change of the amplitude and phase of the transmitted beam $\psi_t(\mathbf{x})$. The aberrations of the objective lens will cause a change of the phase of the transmitted beam. The aberration function can be expressed as a complex exponential function $exp[-\imath\chi(\mathbf{k})]$, where $\chi(\mathbf{k})$ is a phase shift caused by aberrations. If $\Psi_t(\mathbf{k})$ is the Fourier transform of the transmission wave function $\psi_t(\mathbf{x})$, then the effect of the aberrations on the electron wave in the back focal plane $\Psi_i(\mathbf{k})$ will be given by:

$$\Psi_i(\mathbf{k}) = \Psi_t(\mathbf{k})\, exp[-i\chi(\mathbf{k})] = FT[\psi_t(\mathbf{x})]\, exp[-i\chi(\mathbf{k})]. \tag{2.5}$$

An image of the sample is created in the image plane of the objective lens. The wave function of the electron beam just before the detector is equivalent to the inverse Fourier transform of $\Psi_i(\mathbf{k})$. The effect of magnification can be ignored in a mathematical description because the coordinates refer to the dimensions of the specimen. The electron wave function at the detector can be described as:

$$\psi_i(\mathbf{x}) = FT^{-1}[\Psi_i(\mathbf{k})], \tag{2.6}$$

where FT^{-1} is an inverse Fourier transform. This function, however, is not what the detector will image. The recorded image $g(\mathbf{x})$ will be equivalent to the intensity of the wave function $\psi_i(\mathbf{x})$:

$$g(\mathbf{x}) = |\psi_i(\mathbf{x})|^2, \tag{2.7}$$

which can also be expressed as:

$$g(\mathbf{x}) = |\psi_t(\mathbf{x}) \otimes h_0(\mathbf{x})|^2, \tag{2.8}$$

where $h_0(\mathbf{x})$ is an inverse Fourier transform of the aberration function of the objective lens (point spread function): $h_0(\mathbf{x}) = FT^{-1}[exp[-i\chi(\mathbf{k})]]$ and $\otimes$ is a convolution operator. The influence and importance of the aberration function $\chi(\mathbf{k})$ will be discussed further in Sec. 2.2.3.

2.2.2 STEM linear imaging approximation

As mentioned before, STEM imaging is based on the focusing of the fine probe and subsequent scanning of the specimen. A schematic of the image formation process of the STEM is shown in Fig. 2.7, which again includes important wave functions along the optical path. The probe function is defined by [11]:

$$\psi_p(\mathbf{x}) = A_p \int_0^{k_{max}} exp[-\imath\chi(\mathbf{k}) - 2\pi\imath\mathbf{k}\cdot\mathbf{x}]d^2\,\mathbf{k}, \tag{2.9}$$

where $\chi(\mathbf{k})$ is the aberration function of the objective lens (essentially the same as in CTEM), $k_{max} = \alpha/\lambda$ is a maximal spatial frequency transferred by the objective aperture

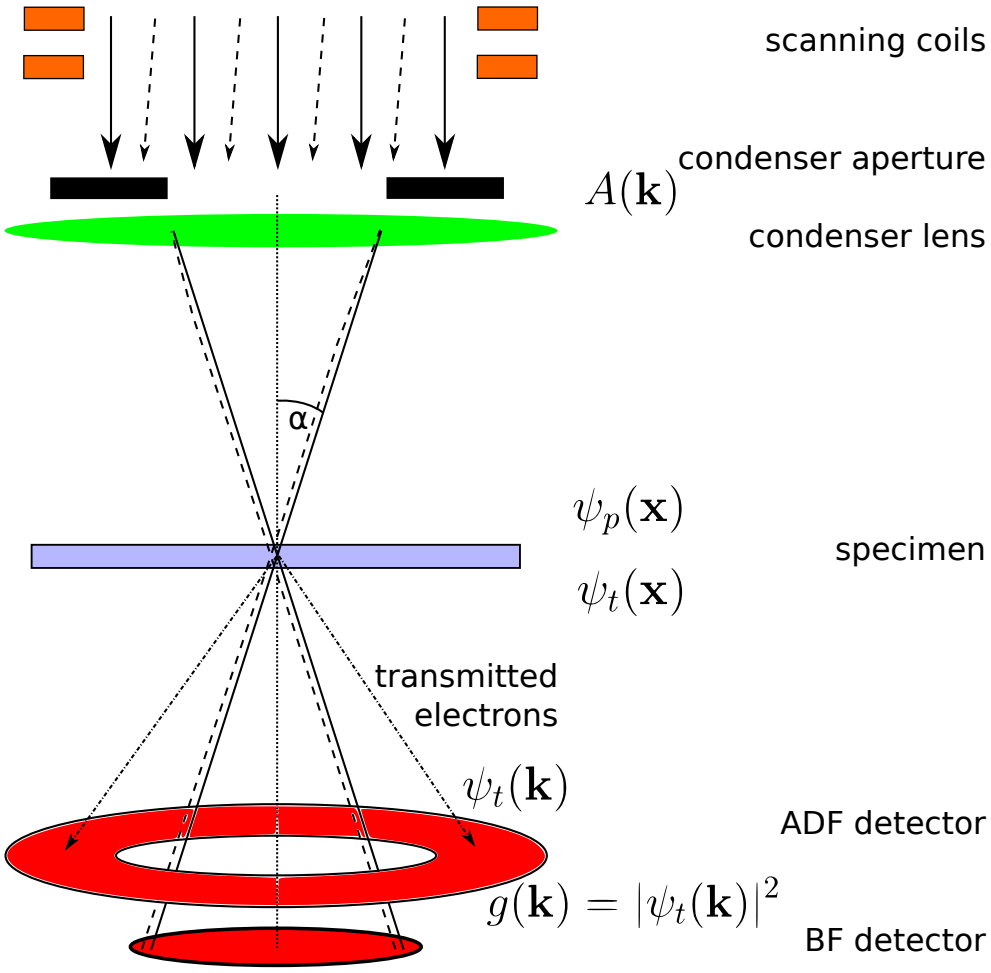

Fig. 2.7 *Schematic of wave optical description of STEM linear imaging approximation. A condenser aperture is used to select a circular probe* ($A(\mathbf{k})$) *which is focused by a condenser lens into fine probe* $\psi_p(\mathbf{x})$*, which interacts with the sample. A transmitted electron function* $\psi_t(\mathbf{x})$ *is detected in the detector plane as* $g(\mathbf{k})$ ($g(\mathbf{k}) = |\psi_t(\mathbf{k})|^2$)

(α is the probe convergence semi-angle) and A_p is a constant yielding:

$$\int |\psi_p(\mathbf{x})|^2 \, d^2\mathbf{x} = 1. \tag{2.10}$$

If there are no aberrations present in the imaging system ($\chi(\mathbf{k}) = 0$), $\psi_p(k)$ will essentially become an inverse Fourier transform of an image of the aperture in frequency space (FT of top hat disk):

$$\psi_0(\mathbf{x}) = A_p \int_0^{k_{max}} exp[-2\pi\imath\mathbf{k}\cdot\mathbf{x}]d^2\,\mathbf{k} = FT^{-1}[A(\mathbf{k})] = A(\mathbf{x}), \tag{2.11}$$

where $A(\mathbf{k})$ is the top hat disk function for which $A(\mathbf{k})|_{k<k_{max}} = 1$ and $A(\mathbf{k})|_{k>k_{max}} = 0$. $\psi_0(\mathbf{x})$ will be an ideal Airy disk function for frequency k_{max}. Assuming the thin specimen approximation, the electron beam transmission through the specimen is provided by the same multiplication with the specimen function $t(\mathbf{x})$ as for CTEM transmission:

$$\psi_t(\mathbf{x}) = \psi_p(\mathbf{x})t(\mathbf{x}). \tag{2.12}$$

A simple notation assuming the position of the beam around $\mathbf{x} = 0$ is used here. However, in the next chapter simulations of STEM signals will be provided by alternating the position of the beam over the theoretical specimen function.

The wave function of the electron beam in the diffraction plane (the detector plane in STEM) is a forward Fourier transform of $\psi_t(\mathbf{x})$:

$$\psi_t(\mathbf{k}) = FT[\psi_t(\mathbf{x})] = FT[\psi_p(\mathbf{x})t(\mathbf{x})]. \tag{2.13}$$

As the detectors in STEM are in the far field plane, various detector geometries can be used to select sources of signals of interest in the frequency domain. Projection lenses can be used to magnify the diffraction plane in STEM. Fig. 2.7 shows the two basic approaches used in STEM detection: that is BF and ADF detectors which acquire transmitted (direct beam) and scattered diffracted electrons respectively. Generally, the distribution of the intensity of the diffraction pattern in the detector plane can be described as:

$$g(\mathbf{k}) = |\psi_t(\mathbf{k})|^2 = |FT[\psi_p(\mathbf{x})t(\mathbf{x})]|^2, \tag{2.14}$$

which, for an objective lens with no aberrations gives:

$$g(\mathbf{k}) = |A(\mathbf{k}) \otimes t(\mathbf{k})|^2, \tag{2.15}$$

where $t(\mathbf{k})$ is the Fourier transform of a specimen function $t(\mathbf{x})$. The signal the detector acquires in STEM can be described by an integral over the detector geometry. The detector function then becomes:

$$g_{detector} = \int_{\substack{detector \\ geometry}} |FT[\psi_p(\mathbf{x})t(\mathbf{x})]|^2 d\mathbf{k}, \tag{2.16}$$

where it is assumed that the detector is ideal, i.e. it does not have its own transfer function.

With advances in technology, there is now also an option to image the profile of $g(\mathbf{k})$ with a pixelated detector, such as the CCD camera or direct electron detector and analyse STEM signal after the experiment [12–15]. Such imaging gives opportunities to analyse many forms of signals, which are normally summed by ADF, BF or DPC detectors. This will be the main topic of this thesis, and will be applied predominantly to magnetic imaging in STEM.

2.2.3 Aberrations

Electron lenses are subject to inherent aberrations, which influence the quality of their imaging function. Aberrations affect the different spatial frequencies imaged by the lens. The most significant aberration in electron lenses is spherical aberration [4]. Rotationally symmetric electron lenses focus electrons further from the optical axis more strongly than

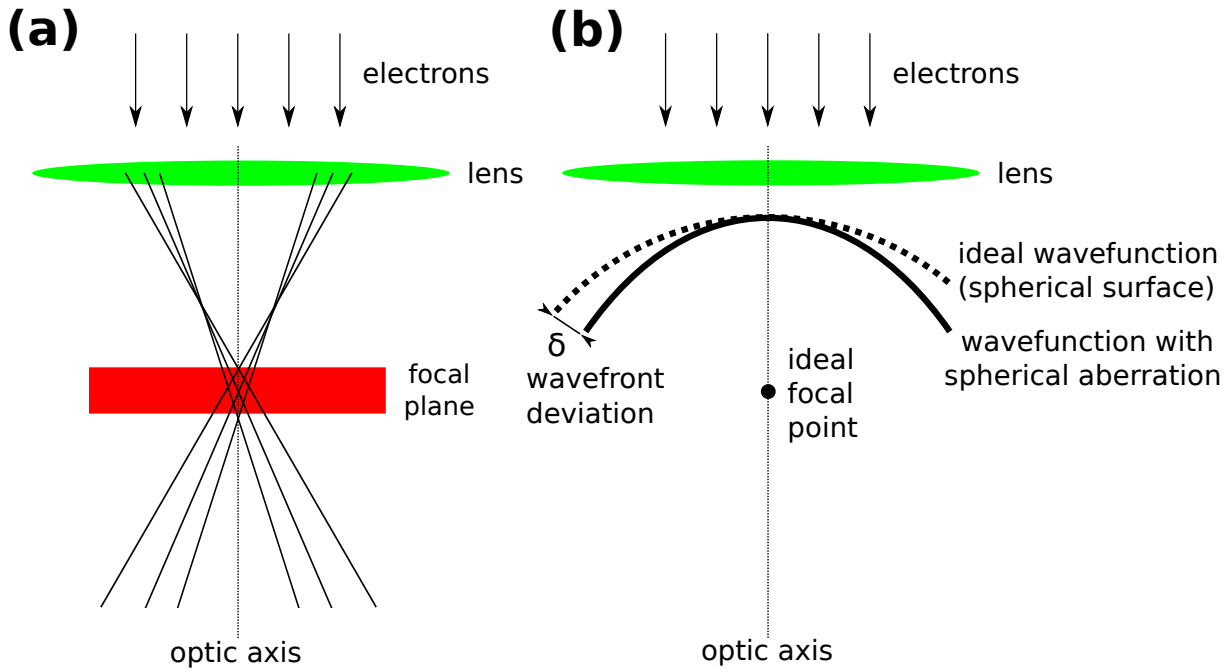

Fig. 2.8 *Schematic of spherical aberration. (a) positive spherical aberration effect on focal plane, (b) the wave-front of the electron beam deviates by δ from the ideal spherical profile*

required, therefore all such lenses have positive spherical aberration. This is schematically shown in Fig. 2.8, where the parameter δ defines the deviation of the wavefront from the ideal spherical surface. δ can be expanded to a function of even powers of a scattering angle α, due to the rotational symmetry of the objective lens. If it is assumed that the net phase error, χ, for most microscopes is produced by spherical aberration and defocus, then the phase error can be described as [4, 11, 16]:

$$\chi(\alpha) = \frac{2\pi}{\lambda}\,\delta = \frac{2\pi}{\lambda}\left(\frac{1}{4}\,C_s\,\alpha^4 - \frac{1}{2}\Delta f\,\alpha^2\right), \tag{2.17}$$

which can be converted into spatial frequency phase error by the relation $\alpha = \lambda\,k$:

$$\chi(k) = \frac{2\pi}{\lambda}\left(\frac{1}{4}\,C_s\,\lambda^4\,k^4 - \frac{1}{2}\Delta f\,\lambda^2\,k^2\right) = \pi\,\lambda\,k^2(0.5\,C_s\,\lambda^2\,k^2 - \Delta f). \tag{2.18}$$

This is an important relation as the spherical aberration C_s is a constant for the given lens and microscope's voltage, however, the defocus Δf can be changed with different excitation of the objective lens. A special defocus value known as the Scherzer defocus [6]:

$$\Delta f_{Scher} = -1.2\,(C_S\,\lambda)^{\frac{1}{2}}, \tag{2.19}$$

can be used to achieve optimal resolution by shifting the effect of the spherical aberration towards higher spatial frequencies. In this description, the influence of higher spherical aberrations and other non-symmetrical aberrations including coma and astigmatism are assumed to be zero.

Aberrations in CTEM imaging

Aberrations are important in CTEM imaging. An example will be given for the weak phase approximation, where the phase of the transmitted electrons is only weakly shifted by the specimen's function[2] (the small angle approximation can be used $e^{\imath x} \sim 1 + \imath x$). The transmitted wave function will then be [11]:

$$\psi_t(\mathbf{x}) \approx t(\mathbf{x}) \approx exp[\imath\sigma_e\nu_z(\mathbf{x})] \approx 1 + \imath\sigma_e\nu_z(\mathbf{x}) + ..., \tag{2.20}$$

where $\nu_z(\mathbf{x})$ is the projected atomic potential of the specimen and σ_e is an electron interaction constant. This formula can be explained due to a change of the wavelength of the electron in the crystal due to its electrostatic potential [16].

The detector image function can be then approximated by [11]:

$$g(\mathbf{x}) \approx 1 + 2\sigma_e\nu_z(\mathbf{x}) \otimes h_0(\mathbf{x}). \tag{2.21}$$

[2] If there is a magnetic or a long scale electric field present within the sample, these are regarded strong phase objects and small angle approximation cannot be used [17].

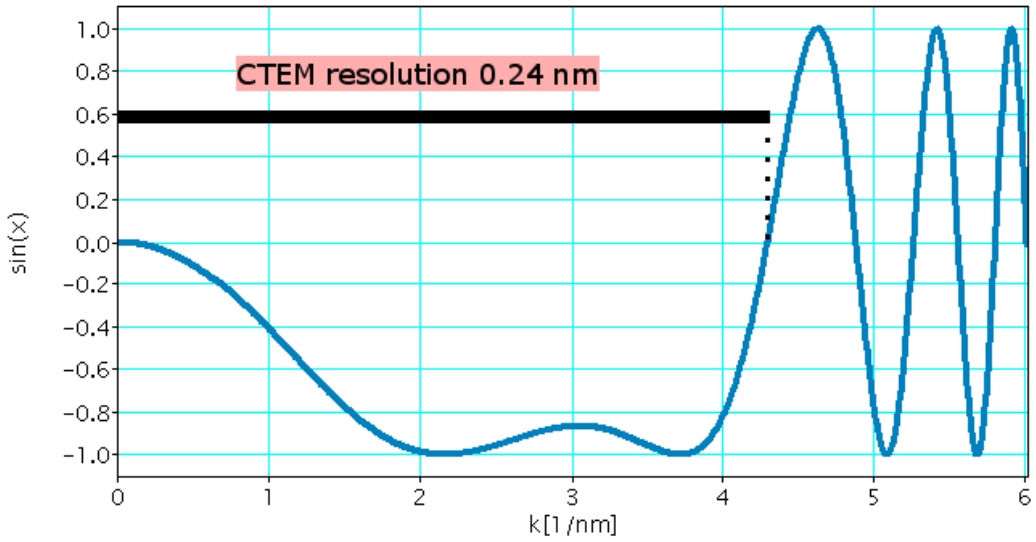

Fig. 2.9 *Contrast transfer function calculated for:* $C_s = 1.0\,mm$, $\Delta f = -57.8\,nm$ *(Scherzer defocus) for* $200\,kV$ *electrons. Calculated by [19]*

The Fourier transform of $g(\mathbf{x})$ gives an easier way to express the effect of aberrations:

$$g(\mathbf{k}) = FT[g(\mathbf{x})] = \delta(\mathbf{k}) + 2\sigma_e \nu_z(\mathbf{k}) \otimes h_0(\mathbf{k}), \tag{2.22}$$

where:

$$h_0(\mathbf{k}) = FT[h_0(\mathbf{x})] = sin[\chi(\mathbf{k})], \tag{2.23}$$

this means that the transfer function will be oscillatory in spatial frequency space. Therefore some frequencies that are in the image are larger than the first crossover of the CTF (see Fig. 2.9) will be transferred as positive ($h_0(\mathbf{k}) > 0$) and some as negative ($h_0(\mathbf{k}) < 0$). Consequently the contrast in the image will depend on the aberration function. However, the CTF for small spatial frequencies will be approximately flat for a significant region, see CTF for Scherzer defocus in Fig. 2.9. The interpretable resolution of the CTEM imaging is defined by the first crossover of $sin[\chi(\mathbf{k})]$.

The influence of the detector was assumed to be ideal, however, it can be included in the description as a convolution of the image function and the detector point spread function $h_{det}(\mathbf{x})$ [18]:

$$g'(\mathbf{x}) = |\psi_t(\mathbf{x}) \otimes h_0(\mathbf{x})|^2 \otimes h_{det}(\mathbf{x}), \tag{2.24}$$

which will be the final image described in weak phase approximation of multiplicative sample imaging.

Aberrations in STEM imaging

The situation in STEM is different. If only the imaging of incoherently scattered electrons is considered (HAADF imaging), the contrast transfer function will not oscillate with higher spatial frequencies but slowly decrease [4]. This is due to the nature of the contrast formation: Rutheford's scattering from close to a single atom [4]. Incoherent scattering for HAADF signals results in a contrast transfer function $H_{HAADF}(\mathbf{k})$ which is equal to the Fourier transform of the intensity of the probe function [20].

The intensity of the probe wave function (Eq. 2.9) can be calculated as:

$$h_{HAADF}(\mathbf{x}) = |\psi_p(\mathbf{x})|^2 = A_p \left| \int_0^{k_{max}} exp[-\imath\chi(\mathbf{k}) - 2\pi\imath\mathbf{k}\cdot\mathbf{x}] d^2\,\mathbf{k} \right|^2 . \tag{2.25}$$

and the HAADF contrast transfer function, $H_{HAADF}(\mathbf{x})$, as:

$$H_{HAADF}(\mathbf{k}) = FT[h_{HAADF}(\mathbf{x})]. \tag{2.26}$$

An example of a HAADF contrast transfer function is shown in Fig. 2.10. It was calculated assuming no aberrations and shows that the effective cut-off spatial frequency in HAADF STEM is double the maximum spatial frequency of the aperture [9].

STEM imaging is also influenced by the size of the electron source, which affects the size of the focused probe. This can be included in the computation of the point spread function by an additional convolution with the point spread function of the source $h_{source}(\mathbf{k})$ [21]. This is, however, not a significant issue in an aberration corrected cold FEG STEM,

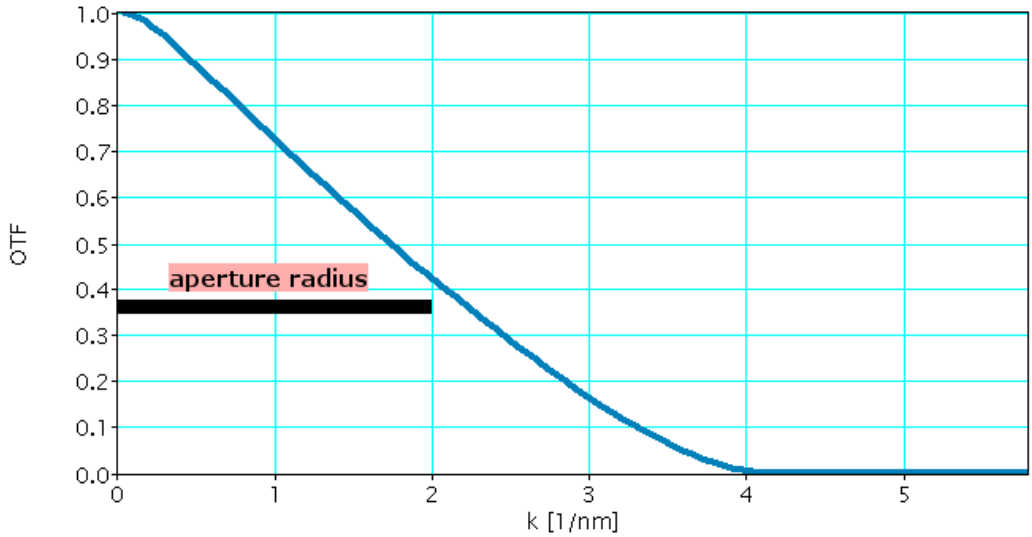

Fig. 2.10 *Optical transfer function for HAADF STEM with no aberrations, aperture size was* $\alpha = 5\,mrad$ $(k_\alpha = 2\,nm^{-1})$ *for* $200\,kV$ *illumination. The profile was calculated according to Eqs 2.25 and 2.26. It shows an effective cut-off frequency for HAADF STEM as* $2k_\alpha$

for which the demagnification of the probe in the pre-specimen optics achieves close to diffraction limited imaging.

In BF-STEM the situation is similar to the BF-TEM and the transfer function will again be oscillatory, due to the reciprocity principle [9, 20, 22].

2.3 Magnetic imaging in TEM

Imaging of magnetic materials is a crucial part of modern scientific efforts due to the importance of magnetic materials to technology and basic science. As the physical dimensions of electronic components get smaller [23], methods of analysis have to provide the best quality and resolution. Electron microscopy, with the right instrumentation, can offer a high spatial resolution of magnetic imaging. Specialised imaging modes of TEM can also provide quantitative analysis of thin samples.

2.3.1 Field free TEM

Every specimen imaged by the standard TEM sits in the large magnetic field ($> 1\,T$) of the objective lens, directed along the optical axis. Such a field is strong enough to fully saturate the vast majority of magnetic materials, therefore magnetic imaging is not generally possible in this mode. Switching the objective lens off provides close to a field free environment for the specimen, noting that the remanent field of the lens, $\sim$ 150–300 Oe is still present in the sample area [24, 25]. This can be corrected by specialised hardware, which can apply an opposite current through the objective lens [26]. The imaging role of the objective lens has to be replaced by a less powerful lens (objective mini lens) which is situated further away from the specimen. The spherical aberration of such a lens has a much larger impact, and the resolution of this mode is limited. Aberration correction has recently pushed the resolution of the field free STEM down to $\sim 1\,nm$ [25]. Additional adjustments have to be made to the room accommodating such an instrument, where even weak electromagnetic fields can have an influence on the imaging of the TEM. At the University of Glasgow, special measures were taken due to the dc currents from the subway line passing around $300\,m$ from the laboratory. It generates an oscillating magnetic field of about 2–3 mOe [27], which can influence the electron beam in the column. This is more problematic in field free mode, because the objective lens field does not shield the specimen and magnetic imaging is considered noisier [28].

2.3.2 Lorentz microscopy

Lorentz microscopy is an umbrella term for several methods of magnetic imaging in transmission electron microscopy. When electrons are transmitted through the specimen, they interact with its magnetic induction. In a classical description, electrons transmitted through the magnetic specimen experience a Lorentz force:

$$\mathbf{F} = -e(\mathbf{v} \times \mathbf{B}), \tag{2.27}$$

where e is the magnitude of the electronic charge, $\mathbf{v}$ is the velocity of the electron and $\mathbf{B}$ is the magnetic induction of the specimen. As the vector product is zero for parallel vectors, only magnetic induction with a component perpendicular to the electron beam trajectory will result in a Lorentz force. Consequently, the trajectory of the electron beam will be changed. The deflection angle, β_L, of an electron passing through the specimen of thickness t can be derived from the Lorentz force and Newton's second law as [17]:

$$\beta_L = \frac{e\,\lambda}{h}\, B_S\, t, \tag{2.28}$$

where λ is the wavelength of an electron, h is Planck's constant and B_S is the saturation magnetic induction of the specimen. A schematic is shown in Fig. 2.11. The calculated deflection in $10\,nm$ thick permalloy ($Ni_{0.8}Fe_{0.2}$) for $200\,kV$ electrons is $6.4\,\mu rad$ this is three orders of magnitude less than standard Bragg diffraction ($\sim 10\,mrad$).

Alternatively, the effect of the magnetic induction can be described as a phase shift in quantum mechanics. The phase shift of a charged particle will be due to the Aharonov-Bohm effect [29]. The phase difference, $\Delta\phi$, of two electrons travelling from the same origin to the same end by different trajectories (a schematic is shown in Fig. 2.12) will be [29]:

$$\Delta\phi = 2\pi\,\frac{e}{h}\,\oint \mathbf{A} \cdot d\mathbf{l}, \tag{2.29}$$

where $\oint \mathbf{A} \cdot \mathbf{dl}$ is a path integral along electron trajectories in which $\mathbf{A}$ is a magnetic vector potential. Interestingly, electrons may acquire a phase difference even when their paths do not cross any area with magnetic induction directly, as shown in Fig. 2.12, which was experimentally confirmed by electron holography [30].

If the Stokes theorem from vector calculus is used:

$$\oint \mathbf{F} \cdot d\mathbf{l} = \int (\nabla \times \mathbf{F}) \cdot d\mathbf{S}, \tag{2.30}$$

together with the magnetic potential equation in vector calculus notation:

$$\mathbf{B} = \nabla \times \mathbf{A}, \tag{2.31}$$

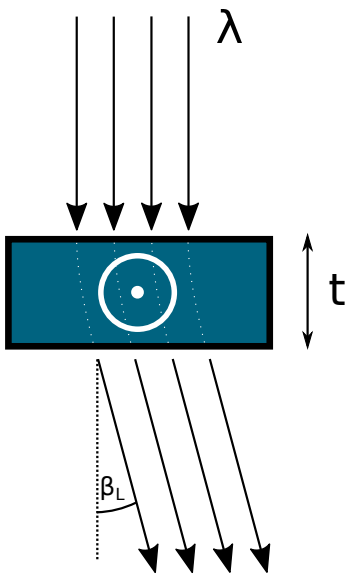

Fig. 2.11 *Schematic of a deflection of electrons due to the transmission through the material with an in-plane magnetic field of thickness t. λ is the wavelength of electrons and β_L is the deflection angle.*

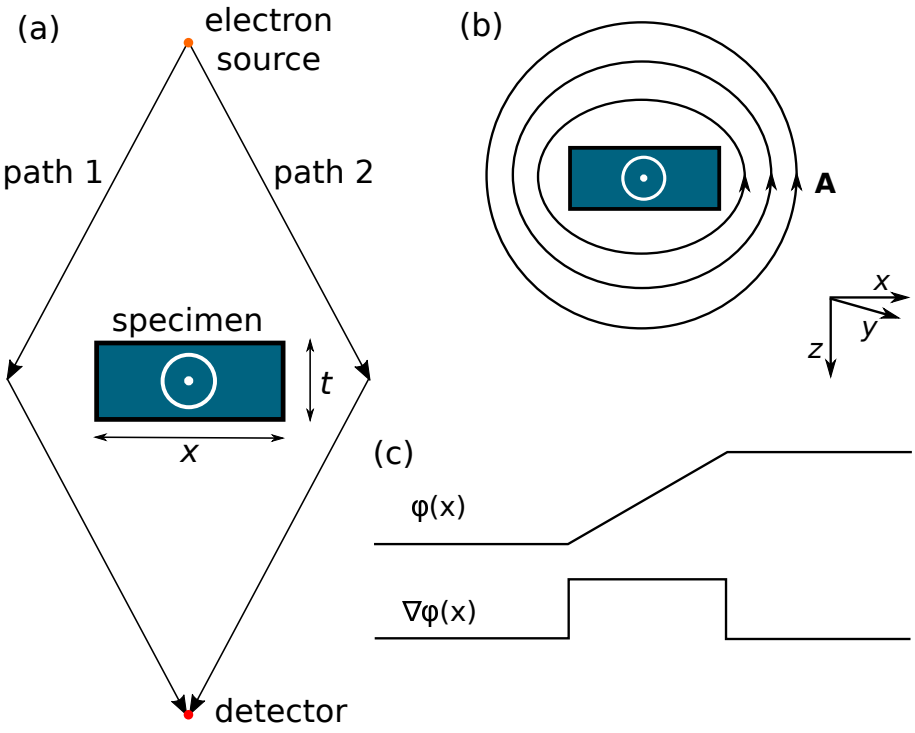

Fig. 2.12 *Schematic of Aharonov-Bohm effect applied to two electrons travelling from source to the detector by different trajectories. The enclosed magnetic induction relates to the phase difference that the two electrons acquire. (a) a schematic of the paths, (b) a schematic of magnetic vector potential around a sample in x direction, (c) a profile of the phase (ϕ) and its gradient ($\nabla\phi$) associated with the specimen function due to the integrated magnetic induction of the sample.*

an equation rather similar to 2.28 can be derived:

$$\Delta\phi = 2\pi \frac{e}{h} \oint \mathbf{A} \cdot d\mathbf{l} = 2\pi \frac{e}{h} \int \mathbf{B} \cdot d\mathbf{S}, \tag{2.32}$$

where the integral $\int \mathbf{B} \cdot d\mathbf{S}$ is a magnetic flux passing through an area between the two electron trajectories. If the magnetic flux is only constrained to the specimen and if the same assumptions are made as in the classical description - homogeneous $|\mathbf{B}| = B_S$ and constant thickness of the specimen t, the phase difference is simply:

$$\Delta\phi = 2\pi \frac{e}{h} B_S \, t \, x, \tag{2.33}$$

where $B_S \, t \, x$ is the magnetic flux through the specimen, as shown in Fig. 2.12.

Finally, if a gradient along the x direction is taken of Eq. 2.33, we see that the gradient of the phase difference is proportional to the Lorentz deflection angle in Eq. 2.28 [31]:

$$\frac{\partial}{\partial x}(\Delta\phi) = 2\pi \frac{e}{h} B_S \, t = 2\pi \frac{\beta_L}{\lambda}, \tag{2.34}$$

which shows the equivalency of the two descriptions. This quantum mechanical description will be required for image calculation and simulations, for which classical description is not satisfactory because it only explains deflections of electrons as particles. The quantum mechanical description considers the electron beam to be a wave object, which can be easily used in wave-optical calculation presented in the CTEM/STEM image formation section.

To be able to image deflections of the beam or equivalently, changes of the phase of the electrons, special modes of TEM are required along with a field free setup. In following sections, the main modes of Lorentz imaging will be introduced with a special focus on DPC in the following chapter as the main topic of this thesis. Every method images phase of the specimen, ϕ, by different means, (ϕ – holography, $\nabla\phi$ – DPC or $\nabla^2\phi$ – Fresnel, TIE), however physical limits restrict each of them in a different way.

2.3.3 Fresnel imaging

Fresnel imaging is widely used in CTEM. It can be easily used to visualise the magnetic structure of the specimen [17, 32–35]. Its main advantage is its simplicity, where along with a field free environment, it only requires the imaging lens to be defocused. As previously discussed, aberrations are partially a source of contrast in CTEM. The deflection angle, β_L, is rather small in magnetic specimens, therefore the imaging lens does not introduce enough aberrations to be able to visualise Fresnel contrast (phase contrast) in a focused image, and an additional strong aberration (defocus) needs to be added to the imaging.

A schematic of Fresnel image formation is shown in Fig. 2.13. The Fresnel method is based on the imaging of the Laplacian (second gradient) of the phase if the defocus is small

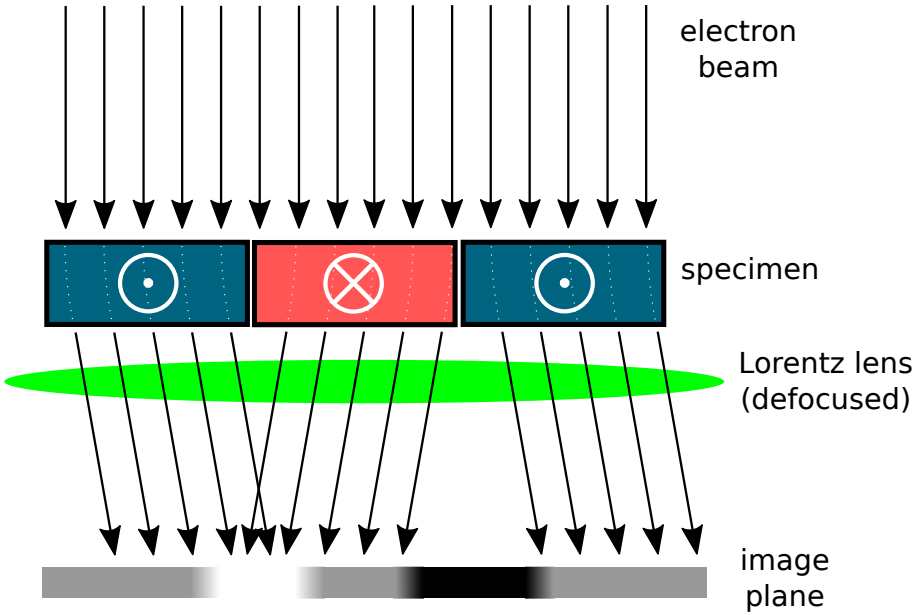

Fig. 2.13 *Schematic of the formation of Fresnel contrast in defocused CTEM, deflected beam combine into white or dark contrast at domain walls*

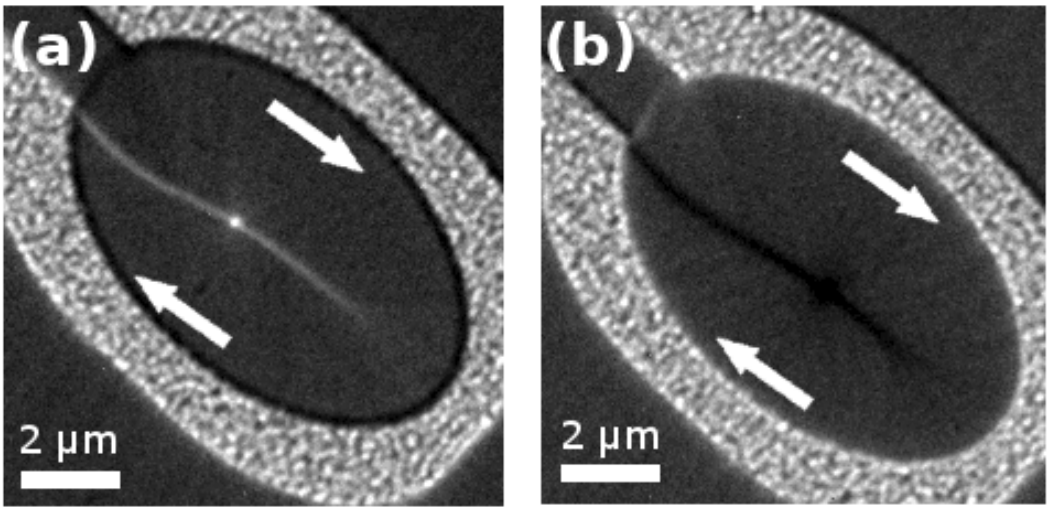

Fig. 2.14 *(a) overfocused and (b) underfocused Fresnel images of focus ion beam patterned ellipsoid in* 20 *nm thick Permalloy. The white line (a) and black line (b) separate two magnetic domains. White and black dot contrasts are due to the magnetic vortex and arrows indicate the direction of the integrated magnetic induction*

(the Laplacian is an approximation otherwise). If the magnetic structure of the specimen is saturated, there is no magnetic signal imaged in this mode; only the domain walls or other varying magnetic structures (e.g. vortices, skyrmions) produce a gradient of **B** and can be imaged in Fresnel mode.

An example of magnetic contrast observed in Fresnel images is shown in Fig. 2.14(a) and (b). Deflected electrons from different magnetic domains produce bright or dark contrast at the domain walls separating them. The apparent contrast of the domain wall can be changed by changing the sign of the defocus. Fresnel imaging is also very advantageous in dynamic process imaging, as it requires lower acquisition times compared to other methods. As the standard Fresnel method requires strong defocus, the imaging of magnetic structures is not directly quantitative, although, quantitative information can be extracted by the application of the field and other experimental techniques (i.e. by observing changes in the image - vortex repulsion, magnetic structure saturation, domain wall movement).

The transport-of-intensity equation (TIE) quantitative method is based on Fresnel imaging [36, 37]. In this method the information about the phase can be extracted by analysis of a slightly under and over focused Fresnel images, where the Laplacian of the phase is considered linear [36].

2.3.4 Foucault imaging

Foucault imaging, another CTEM method, is based on an idea that electrons passing through different magnetic domains will have different crossover positions in the diffraction pattern due to their different deflection angles. The central spot of the diffraction pattern will be split into multiple spots, whose spacing depends on the strength of the electron deflection due to the in-plane magnetic induction of the specimen. Under coherent conditions (e.g. using a cold FEG electron gun) it is capable of producing quantitative information, however it is very limited in the type of specimen that can be imaged and in practice it is a rather demanding technique due to the need of mechanical adjustments of an aperture and shifts of the beam/diffraction pattern [33, 38, 39].

A simple example of an experimental imaging can be given for a specimen containing two domains separated by a thin domain wall. An electron beam passing through such a specimen will be deflected differently for different domains and the central beam will become effectively split into two spots in diffraction plane. An objective aperture can be used to select one of the split spots corresponding only to the one type of the domain, as shown in schematic in Fig. 2.15. By allowing image formation only from one spot, the resulting image will have information only from the domains which were not masked by the aperture. An example is shown in Fig. 2.16. Diffraction patterns, displayed on the left top of the images (a) and (b), show which parts of the split central diffraction spots were allowed to form the contrast. The method is, however, very dependant on the ability

to chose the right position of the Lorentz aperture, which can be a difficult task. Other methods, electron holography and differential phase contrast offer much more versatile experimental acquisition.

2.3.5 Electron Holography

Electron holography was invented by Dennis Gabor in 1948 [41]. Its full potential was not achieved until the invention of the cold FE gun, a highly coherent source of electrons. There are many different experimental adaptations of holography in CTEM (twenty distinct variants were described in [42]). Nowadays, the most common technique is off-axis holography, a schematic of which is shown in Fig. 2.17. Off-axis means that the specimen has to be shifted from the centre of the optical axis and/or allow part of the beam to be transmitted through empty space. After the transmission through the specimen area, the beam is split by a biprism and interference fringes are detected in the image plane. A biprism works by applying a constant (but oppositely signed) potential to the reference and transmitted wave to create an interference pattern at the detector. Such a pattern is, however, not straightforward to analyse. The spacing of fringes will change according to electromagnetic fields present in the specimen. The resulting holograms carry information about the phase and intensity, and they have to be carefully analysed in the Fourier domain [43]. An example of the reconstructed phase of a magnetic particle is shown in Fig. 2.18. The main advantage of the method is that signals are quantitative and the method is applied in a focused imaging system. A problematic factor is the reconstruction and the combination of the magnetic and electrostatic potentials in the phase which are imaged indistinguishably (however, this is also a problem other phase imaging methods).

2.3.6 Differential Phase Contrast

Differential Phase Contrast is a STEM method which is based on the imaging of a gradient of the phase of the specimen [45, 46]. As mentioned before, the phase of electrons transmitted through the magnetic specimen is altered by the Aharonov Bohm effect. The equation

$$\frac{\partial}{\partial x}(\Delta\phi) = 2\pi \frac{e}{h} B_S \, t = 2\pi \frac{\beta_L}{\lambda}, \qquad \text{(2.34 revisited)}$$

shows that the gradient of the phase change is equivalent to the deflection of the electron beam, assuming constant magnetic induction within the specimen for a particular beam path. In DPC, the deflection of the beam is measured for each point of the scan (schematic is shown in Fig. 2.19). A segmented detector is used to measure the beam deflection angle, β_L, from the intensity in each quadrant. As the deflection angle is linearly dependent on the integrated magnetic induction, DPC provides direct quantitative imaging of the magnetic induction of the specimen. A detailed explanation will be given in the following chapter

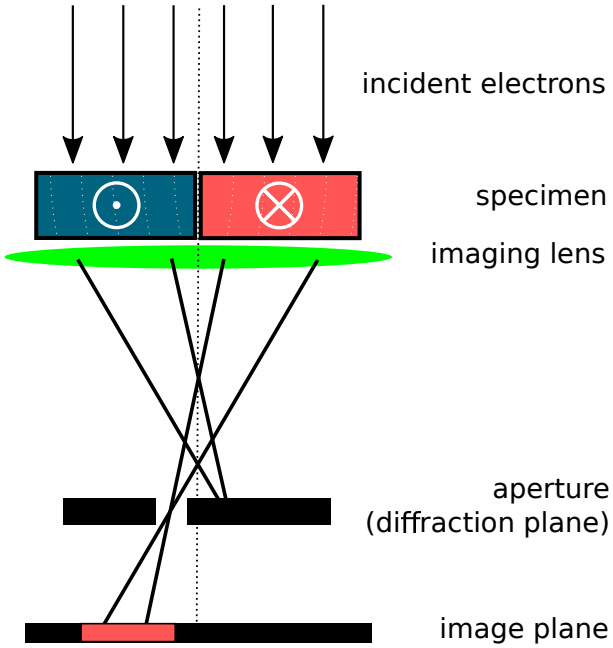

Fig. 2.15 *Schematic of formation of Foucault contrast. An aperture is used in the diffraction plane to select only the information from one of the domains of the specimen to form the image*

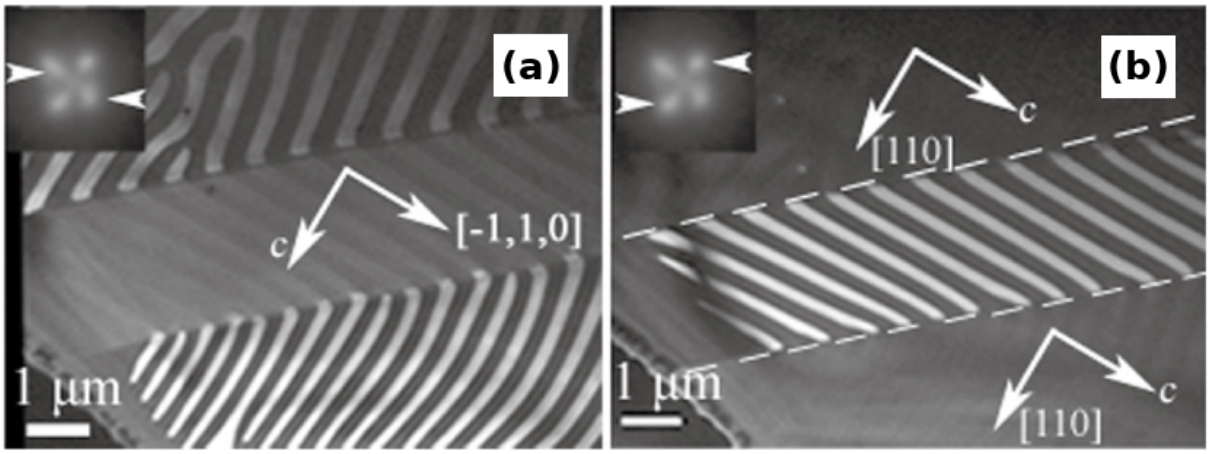

Fig. 2.16 *An example of the two orthogonal Foucault images. Selective signal of the split central spot is pointed at by arrows in diffraction pattern in the top left of images (the sample imaged is $La_{69}Ca_{31}MnO_3$ and signal from the opposite split spots was combined post the experiment) image was taken from a webpage describing the paper [40]*

in Sec. 3.2. Scanning over the specimen and detecting beam deflections results in two orthogonal maps of in-plane magnetic induction. An example of a DPC measurement is shown in Fig. 2.20. The images show clear contrast for two uniformly magnetised domains separated by a domain wall in 20 nm thick PyPt. It can be seen that although magnetic contrast is clear, there is a large amount of additional contrast due to diffraction from the crystallites of the specimen. The size of the crystallite grains in this material are of the same order of magnitude as the focused STEM probe ($\sim 5\,nm$). The effect of Bragg scattering from differently oriented grains of polycrystalline materials is an additional signal contribution. This is one of the main difficulties in DPC imaging of many thin film polycrystalline materials. Not only the intensity in the central spot varies due to the grain orientation (a schematic is shown in Fig. 2.21(a)), but inhomogeneous beam intensity variations also can be seen within the disk (see Fig. 2.21(b). This can result in an effective additional recorded deflection on the segmented detector, because the method assumes constant intensity within the disk (detailed description is given in Sec. 3.2).

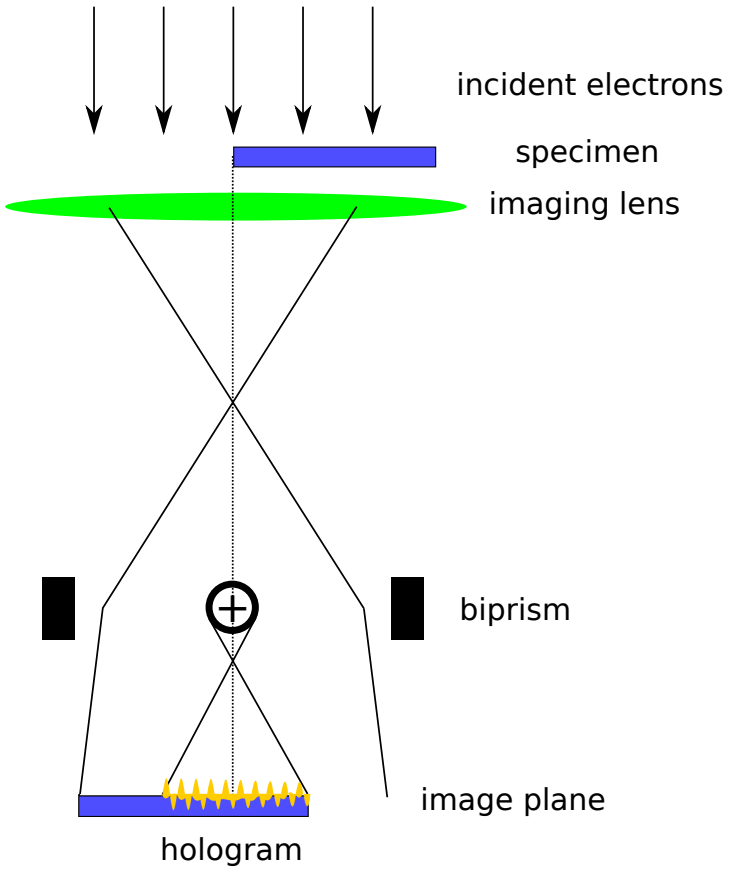

Fig. 2.17 *Schematic of contrast formation in off-axis holography, image needs to be reconstructed from the hologram acquired by CCD camera*

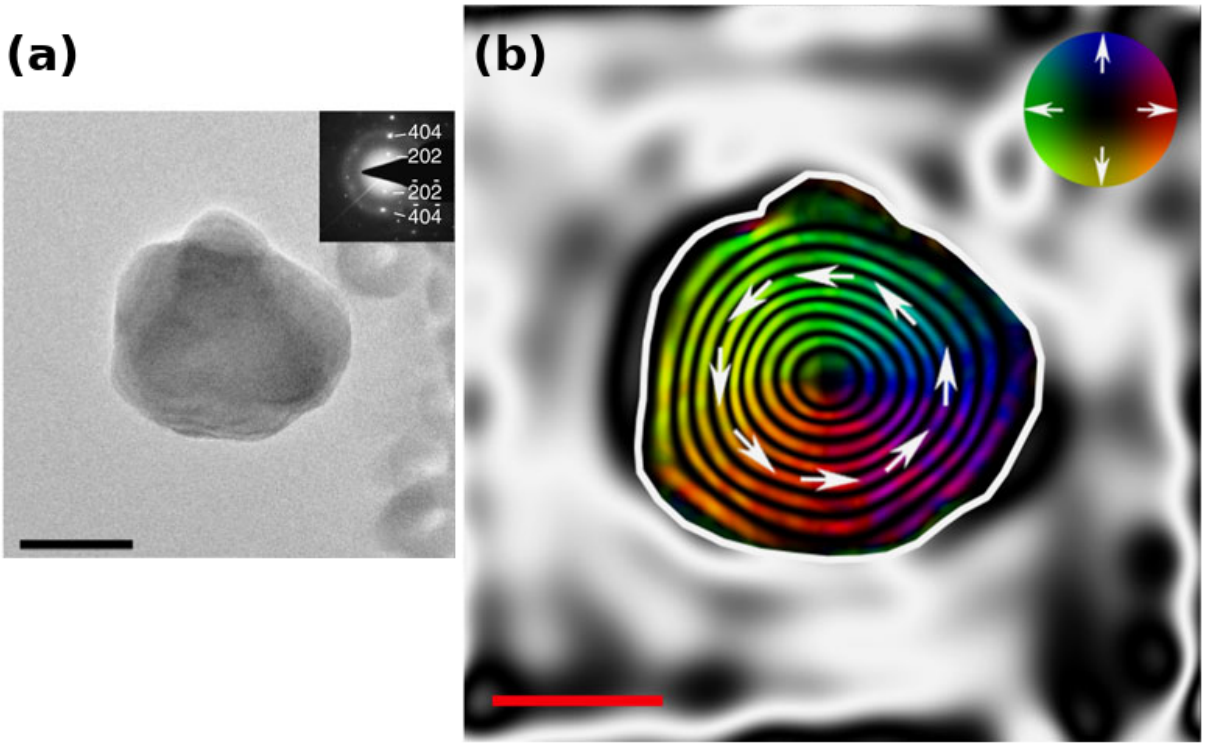

Fig. 2.18 *An example of holographic imaging (off-axis holography) of Fe_3O_4 magnetic particle, (a) the bright field image with the associated diffraction image pattern inset, (b) the reconstructed phase of a magnetic particle showing magnetic vortex structure, scale bars represent* 100 *nm and colour shows the orientation of magnetic induction. Courtesy of Dr Trevor P. Almeida. Images were obtained under Creative Commons 3.0 licence from [44]*

2.3.7 Limits of quantitative Lorentz microscopy and motivation for this thesis

Quantitative methods of Lorentz microscopy are limited by the fact that any diffraction contrast arising from non-magnetic sources in phase imaging are not easily separable. Such a problem is very apparent in the imaging of polycrystalline materials, as shown in Fig. 2.20. Neither electron holography nor DPC can simply overcome this effect.

Electrostatic effects due to sample structure can be filtered in both techniques by imaging the specimen from one side, flipping it over and imaging it from the other side. However, this is not very practical and careful matching of the two images limits the resolution assuming that the magnetic state does not change between the two acquisitions. Alternatively, a magnetic specimen can be imaged in two reversed magnetic configurations, from which electric phase can be deduced [47–49].

Advances in the filtering of high spatial information were made in the case of DPC, where four quadrant detection was enhanced by splitting the detector further into an annular quadrant geometry [50] however, this can only help to a certain extent. A detailed

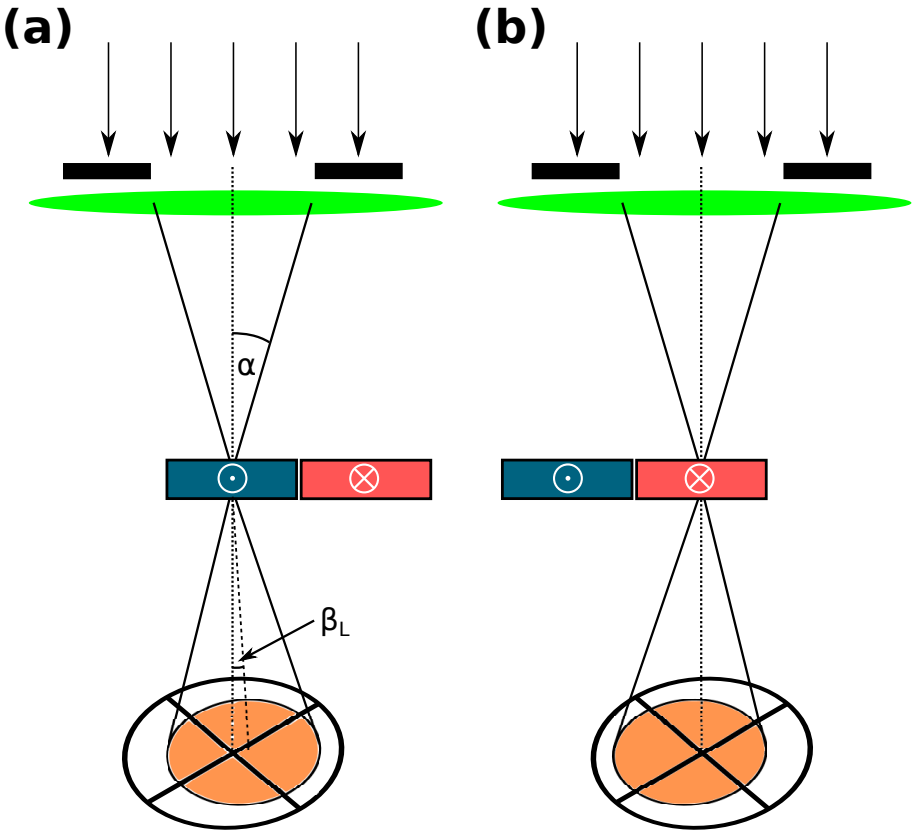

Fig. 2.19 *Schematic of DPC STEM measurement showing a focused electron beam deflected by in-plane magnetic induction of a specimen in two differently oriented magnetic domains (a) and (b). The detection is provided by segmented detector*

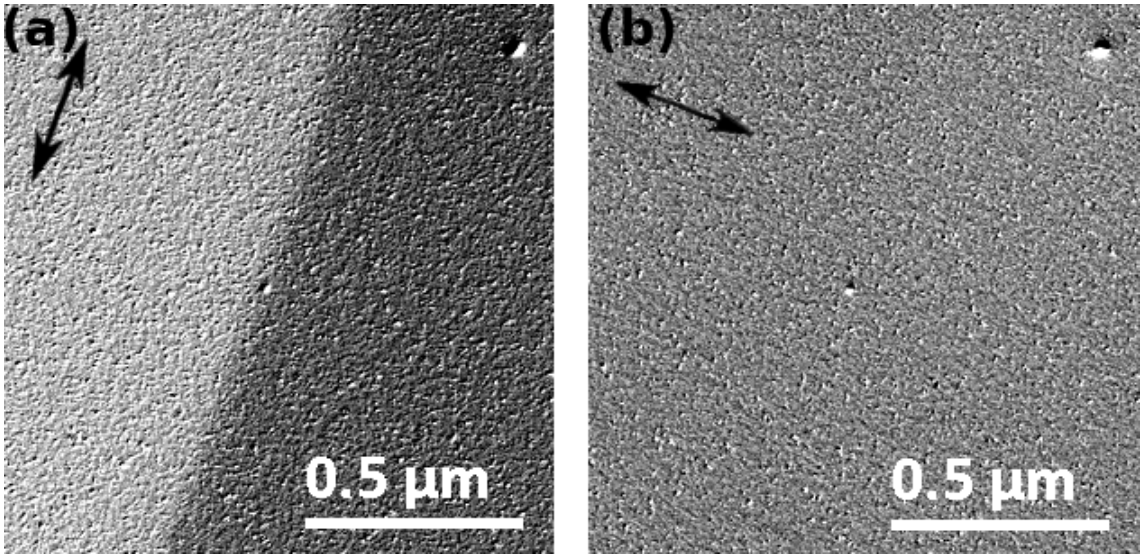

Fig. 2.20 *STEM DPC images of a magnetic domain wall in* 20 *nm thick* $Py_{95}Pt_5$ *specimen by a four quadrant detector. The integrated magnetic induction direction is shown by double headed arrows. Image was taken with convergent angle* $\alpha = 1\,mrad$*. Diffraction contrast from crystallites is partially masking the magnetic information.*

description of DPC imaging will be given in the following chapter. This thesis will present a method which can filter DPC imaging and allow the separation of magnetic and additional diffraction contrast. This is possible by acquisition of the full image of the central beam in STEM for each probe position, on which mathematical algorithms will be applied.

2.4 Simulation of phase contrast images of magnetic samples

A powerful algorithm for calculation of Lorentz microscopy images from micromagnetic simulations was suggested by M. Mansuripur [51] and implemented in Digital Micrograph® scripting by Mr Gordon White and Dr Stephen McVitie [52]. The algorithm is based on a calculation of the phase change of the electron beam, as it passes through a sample. If there is no specimen tilt, only m_x and m_y images are required. It used magnetisation configuration, which can be created by *MuMax*^{3} simulation (described in Sec. 1.5) or by a model describing a simple domain wall profile. The vector potential is then calculated and used to create a projection of 2D plane view of a phase change map of the sample. It

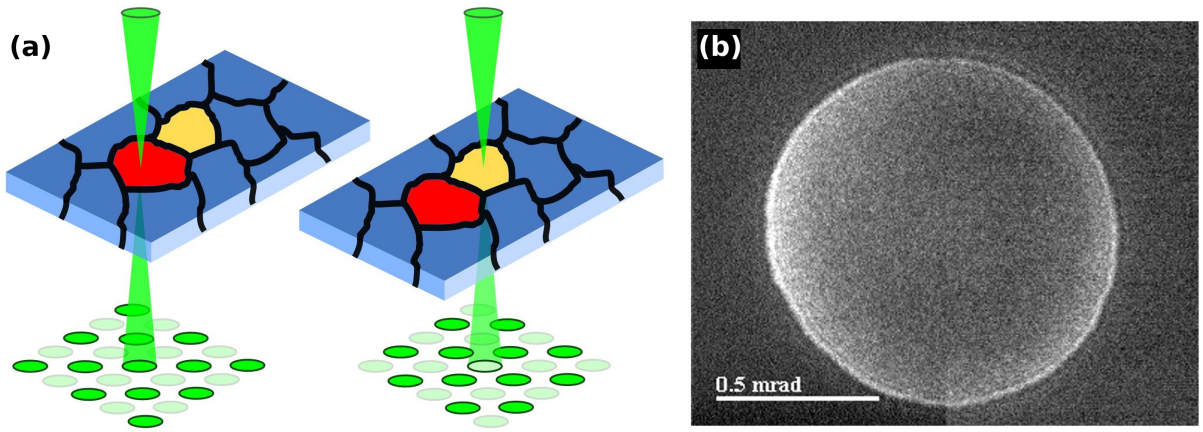

Fig. 2.21 *(a) Bragg scattering condition change between differently oriented grains, (b) an example of central diffraction disk imaged with CCD camera at a grain boundary*

combines m_x, m_y and m_z magnetisation images into a projected phase in the direction of the electron beam.

An example can be given for a Néel domain wall (its configuration was described in Sec. 1.4.1) in 20 nm thick permalloy sample, which has saturation magnetisation about 1 T. It will be assumed that the domain wall has magnetisation profile described by:

$$m_x = \sqrt{1 - m_y^2}, \tag{2.35}$$

$$m_y = tanh\left(\frac{x}{A}\right), \tag{2.36}$$

$$m_z = 0. \tag{2.37}$$

where A is the domain wall width parameter.

Symmetry is required in the source images. To avoid phase wrapping [51], a pair of domain walls were generated and magnetisation profiles m_x, m_y and m_z are shown in Figs 2.22(a), (b) and (c) respectively. This profile assumes an infinite pair of domain walls with $A = 50\,nm$ width parameter (in Eq. 2.36).

The result of the phase calculation is shown in Fig. 2.23(a). Because of the divergent magnetisation in the x direction, there is no variation in the y direction of the image (a) [35]. Differential phase contrast images can be simply calculated by taking a 2D gradient of a phase image (by Eq. 2.34). As is expected, there is no signal present in the B_x component of integrated magnetic induction in Fig. 2.23(b). The image (c) shows the B_y component of integrated magnetic induction, which is a quantitative measurement of the profile of the domain wall.

In the following chapter, phase images similar to Fig. 2.23(a) will be used to simulate STEM scanning in DPC. A contrast transfer in DPC will be studied for situations where the gradient of the phase varies on the length-scales of the focused electron probe.

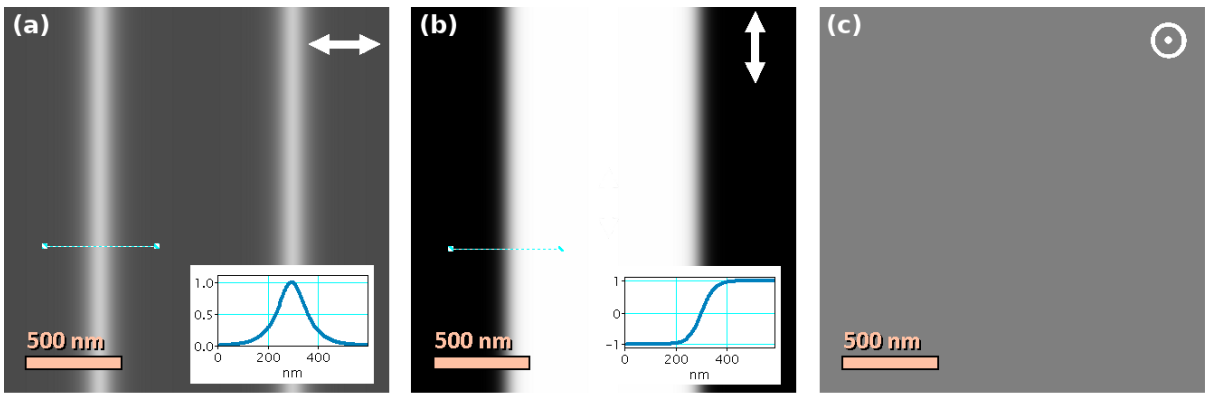

Fig. 2.22 *m_x, m_y and m_z components of Néel domain wall magnetisation with $A = 50\,nm$ width parameter, generated from a magnetisation configuration described by Eqs. 2.35, 2.36 and 2.37*

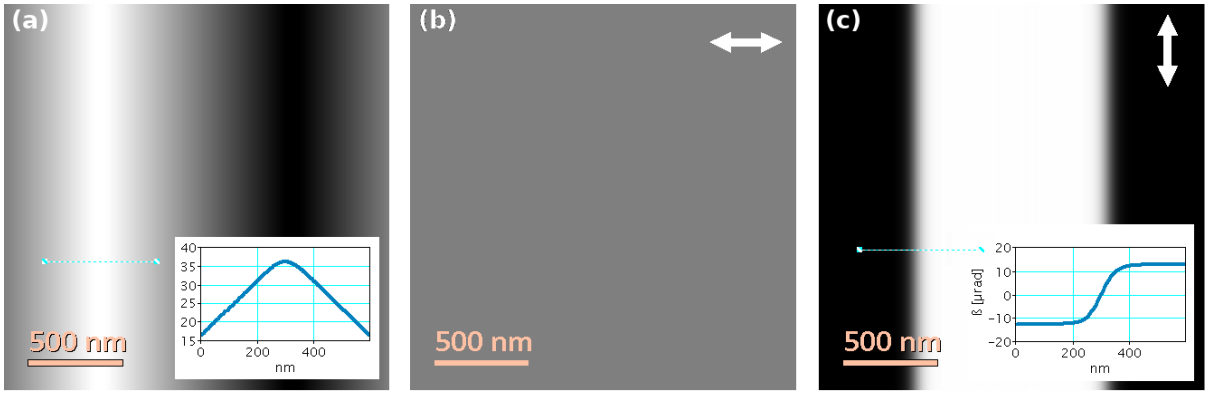

Fig. 2.23 *(a) calculated phase from magnetisation configuration in Eqs. 2.35, 2.36 and 2.37 and Fig. 2.22, (b) and (c) two orthogonal components of integrated magnetic induction generated as a gradient of image (a)*

The theory of Lorentz microscopy and simulations of sample magnetisation will be used in the following chapter to test detection methods for differential phase contrast, which will be also thoughtfully examined. It will be shown that advancing the detection method to pixelated detector can greatly improve contrast transfer in imaging of magnetic materials in DPC [14].

References

[1] A. Lipson, S. G. Lipson, and H. Lipson, *Optical physics*. Cambridge University Press, 2010.

[2] N. Dellby, G. Corbin, Z. Dellby, T. Lovejoy, Z. Szilagyi, M. Chisholm, and O. Krivanek, "Tuning high order geometric aberrations in quadrupole-octupole correctors," *Microscopy and Microanalysis*, vol. 20, no. S3, pp. 928–929, 2014.

[3] O. Krivanek, T. Lovejoy, and N. Dellby, "Aberration-corrected STEM for atomic-resolution imaging and analysis," *Journal of Microscopy*, vol. 259, no. 3, pp. 165–172, 2015.

[4] S. J. Pennycook and P. D. Nellist, *Scanning transmission electron microscopy: imaging and analysis*. Springer Science & Business Media, 2011.

[5] N. J. Zaluzec, "The influence of Cs/Cc correction in analytical imaging and spectroscopy in scanning and transmission electron microscopy," *Ultramicroscopy*, vol. 151, pp. 240–249, 2015.

[6] D. B. Williams and C. B. Carter, *Transmission Electron Microscopy*. Springer Science+Business Media, 2009.

[7] R. Egerton, P. Li, and M. Malac, "Radiation damage in the TEM and SEM," *Micron*, vol. 35, no. 6, pp. 399–409, 2004.

[8] B. R. Group, "Nanotechnology: A Brief Overview," March 2016. http://barrett-group.mcgill.ca/tutorials/nanotechnology/nano02.htm.

[9] P. Nellist and S. Pennycook, "The Principles and Interpretations of Annular Dark-Field Z-Contrast Imaging," *Advances in Imaging and Electron Physics*, vol. 113, pp. 148–204, 2000.

[10] J. Cowley, "Scanning transmission electron microscopy of thin specimens," *Ultramicroscopy*, vol. 2, pp. 3–16, 1977.

[11] E. J. Kirkland, *Advanced computing in electron microscopy*. Springer Science & Business Media, 2010.

[12] T. J. Pennycook, A. R. Lupini, H. Yang, M. F. Murfitt, L. Jones, and P. D. Nellist, "Efficient phase contrast imaging in STEM using a pixelated detector. Part 1: Experimental demonstration at atomic resolution," *Ultramicroscopy*, 2014.

[13] H. Yang, T. J. Pennycook, and P. D. Nellist, "Efficient phase contrast imaging in STEM using a pixelated detector. Part II: Optimisation of imaging conditions," *Ultramicroscopy*, vol. 151, pp. 232–239, 2015.

[14] M. Krajnak, D. McGrouther, D. Maneuski, V. O'Shea, and S. McVitie, "Pixelated detectors and improved efficiency for magnetic imaging in STEM differential phase contrast," *Ultramicroscopy*, vol. 165, pp. 42–50, 2016.

[15] M. W. Tate, P. Purohit, D. Chamberlain, K. X. Nguyen, R. Hovden, C. S. Chang, P. Deb, E. Turgut, J. T. Heron, D. G. Schlom, *et al.*, "High Dynamic Range Pixel Array Detector for Scanning Transmission Electron Microscopy," *Microscopy and Microanalysis*, vol. 22, no. 01, pp. 237–249, 2016.

References

[16] D. B. Williams and C. B. Carter, "The transmission electron microscope," in *Transmission electron microscopy*, pp. 3–17, Springer, 1996.

[17] J. Chapman, "The investigation of magnetic domain structures in thin foils by electron microscopy," *Journal of Physics D: Applied Physics*, vol. 17, p. 623, 1984.

[18] R. R. Meyer and A. I. Kirkland, "Characterisation of the signal and noise transfer of CCD cameras for electron detection," *Microscopy Research and Technique*, vol. 49, no. 3, pp. 269–280, 2000.

[19] D. Mitchell, "Conrast Transfer Function," accessed September 2016. Dave Mitchells DigitalMicrograph Scripting Website, http://www.dmscripting.com/contrast_transfer_function.html.

[20] S. Pennycook, A. Lupini, M. Varela, A. Borisevich, Y. Peng, M. Oxley, K. Van Benthem, and M. Chisholm, "Scanning transmission electron microscopy for nanostructure characterization," in *Scanning Microscopy for Nanotechnology*, pp. 152–191, Springer, 2006.

[21] R. Erni, M. D. Rossell, C. Kisielowski, and U. Dahmen, "Atomic-resolution imaging with a sub-50-pm electron probe," *Phys. Rev. Lett.*, vol. 102, no. 9, p. 096101, 2009.

[22] H. Rose and C. Kisielowski, "On the Reciprocity of TEM and STEM," *Microscopy and Microanalysis*, vol. 11, no. S02, pp. 2114–2115, 2005.

[23] R. R. Schaller, "Moore's law: past, present and future," *Spectrum, IEEE*, vol. 34, no. 6, pp. 52–59, 1997.

[24] J. Lau, M. Schofield, and Y. Zhu, "A straightforward specimen holder modification for remnant magnetic-field measurement in TEM," *Ultramicroscopy*, vol. 107, no. 4, pp. 396–400, 2007.

[25] S. McVitie, D. McGrouther, S. McFadzean, D. MacLaren, K. O'Shea, and M. Benitez, "Aberration corrected Lorentz scanning transmission electron microscopy," *Ultramicroscopy*, vol. 152, pp. 57–62, 2015.

[26] A. Kohn and A. Habibi, "Adapting a JEM-2100F for Magnetic Imaging by Lorentz TEM," *JEOLnews*, vol. 47, pp. 17–22, 2012.

[27] S. McFadzean, 2016. Technical measurements, The University of Glasgow.

[28] S. McFadzean, 2016. Private conversation.

[29] Y. Aharonov and D. Bohm, "Significance of electromagnetic potentials in the quantum theory," *Physical Review*, vol. 115, no. 3, p. 485, 1959.

[30] A. Tonomura, T. Matsuda, R. Suzuki, A. Fukuhara, N. Osakabe, H. Umezaki, J. Endo, K. Shinagawa, Y. Sugita, and H. Fujiwara, "Observation of Aharonov-Bohm effect by electron holography," *Phys. Rev. Lett.*, vol. 48, no. 21, p. 1443, 1982.

[31] J. Chapman, P. Batson, E. Waddell, and R. Ferrier, "The direct determination of magnetic domain wall profiles by Differential Phase Contrast electron microscopy," *Ultramicroscopy*, vol. 3, no. 0, pp. 203–214, 1978. http://www.sciencedirect.com/science/article/pii/S0304399178800278.

[32] J. Chapman, E. Waddell, P. Batson, and R. Ferrier, "The Fresnel mode of Lorentz microscopy using a scanning transmission electron microscope," *Ultramicroscopy*, vol. 4, no. 3, pp. 283–292, 1979.

[33] S. McVitie, J. Chapman, L. Zhou, L. Heyderman, and W. Nicholson, "In-situ magnetising experiments using coherent magnetic imaging in TEM," *Journal of magnetism and magnetic materials*, vol. 148, no. 1, pp. 232–236, 1995.

[34] C. Phatak, M. Tanase, A. Petford-Long, and M. De Graef, "Determination of magnetic vortex polarity from a single Lorentz Fresnel image," *Ultramicroscopy*, vol. 109, no. 3, pp. 264–267, 2009.

[35] M. J. Benitez, A. Hrabec, A. P. Mihai, T. A. Moore, G. Burnell, D. McGrouther, C. H. Marrows, and S. McVitie, "Magnetic microscopy and topological stability of homochiral Neel domain walls in a Pt/Co/AlOx trilayer," *Natre Communicatins*, vol. 6, DEC 2015.

[36] M. Beleggia, M. Schofield, V. Volkov, and Y. Zhu, "On the transport of intensity technique for phase retrieval," *Ultramicroscopy*, vol. 102, no. 1, pp. 37–49, 2004.

[37] S. McVitie and M. Cushley, "Quantitative Fresnel Lorentz microscopy and the transport of intensity equation," *Ultramicroscopy*, vol. 106, no. 4, pp. 423–431, 2006.

[38] A. Daykin and A. Petford-Long, "Quantitative mapping of the magnetic induction distribution using Foucault images formed in a transmission electron microscope," *Ultramicroscopy*, vol. 58, no. 3, pp. 365–380, 1995.

[39] S. McVitie, 2016. Private conversation.

[40] X. Yu, R.-W. Li, T. Asaka, K. Ishizuka, K. Kimoto, and Y. Matsui, "Possible origins of the magnetoresistance gain in colossal magnetoresistive oxide La 0.69 Ca 0.31 MnO 3: Structure fluctuation and pinning effect on magnetic domain walls," *Applied Physics Letters*, vol. 95, no. 9, pp. 092504–3, 2009.

[41] D. Gabor *et al.*, "A new microscopic principle," *Nature*, vol. 161, no. 4098, pp. 777–778, 1948.

[42] J. Cowley, "Twenty forms of electron holography," *Ultramicroscopy*, vol. 41, no. 4, pp. 335–348, 1992.

[43] A. Tonomura, "Applications of electron holography," *Rev. Mod. Phys.*, vol. 59, pp. 639–669, Jul 1987.

[44] T. P. Almeida, T. Kasama, A. R. Muxworthy, W. Williams, L. Nagy, T. W. Hansen, P. D. Brown, and R. E. Dunin-Borkowski, "Visualized effect of oxidation on magnetic recording fidelity in pseudo-single-domain magnetite particles," *Nature communications*, vol. 5, 2014.

[45] N. Dekkers and H. De Lang, "Differential Phase Contrast in a STEM," *Optik*, vol. 41, no. 4, pp. 452–456, 1974.

[46] J. N. Chapman, "The investigation of magnetic domain structures in thin foils by electron microscopy," *Journal of Physics D: Applied Physics*, vol. 17, no. 4, p. 623, 1984.

[47] R. J. Harrison, R. E. Dunin-Borkowski, and A. Putnis, "Direct imaging of nanoscale magnetic interactions in minerals," *Proceedings of the National Academy of Sciences*, vol. 99, no. 26, pp. 16556–16561, 2002.

[48] J. C. Loudon, N. D. Mathur, and P. A. Midgley, "Charge-ordered ferromagnetic phase in La0. 5Ca0. 5MnO3," *Nature*, vol. 420, no. 6917, pp. 797–800, 2002.

[49] F. A. M. Ramírez, *Holography: Different Fields of Application*. InTech, 2011.

[50] J. Chapman, I. McFadyen, and S. McVitie, "Modified differential phase contrast Lorentz microscopy for improved imaging of magnetic structures," *Magnetics, IEEE Transactions on*, vol. 26, pp. 1506–1511, sep 1990.

[51] M. Mansuripur, "Computation of electron diffraction patterns in Lorentz electron microscopy of thin magnetic films," *Journal of Applied Physics*, vol. 69, pp. 2455–2464, feb 1991.

[52] S. McVitie and G. White, "Imaging Amperian currents by Lorentz microscopy," *Journal of Physics D: Applied Physics*, vol. 37, no. 2, p. 280, 2003.

CHAPTER 3

Differential Phase Contrast and its Simulations

Introduction

In this chapter, DPC STEM imaging of magnetic materials will be explained. Its capabilities and limits will be shown with a possible approach towards practical enhancement. This will be demonstrated by central disk diffraction pattern simulation of imaging idealised magnetic specimens. The imaging characteristics of different detector geometries and algorithms will be extensively studied by simulation of scanning DPC datasets.

3.1 Brief history of DPC and motivation for this chapter

The idea that differential phase contrast can be generated in a scanning transmission electron microscope was first introduced by Dekkers and Lang in Phillips laboratories in Eindhoven. They proposed a split detector as a method to capture the DPC signal [1]. This idea was consequently applied in a study of magnetic thin films by John Chapman at the University of Glasgow [2] and was further developed to a quadrant detector system [3]. The latter for allowed simultaneous mapping of two orthogonal components of integrated magnetic induction. In the early 1990s, the detector geometry was split further into eight annular quadrants, which helped with the separation of high (structural) and low (magnetic) spatial frequency information in the image [4].

Recently, aberration correction allows a spatial resolution little below $1\,nm$ in field free STEM imaging [5, 6]. The Jeol ARM 200cF (MagTEM) at the University of Glasgow (a photograph is in Fig. 3.1) is equipped with additional, specialised hardware developed in a collaboration with Jeol (Lorentz lens), Deben UK Ltd. (annular DPC detector) and Andrew Armit Designs (amplifier), which provides superior field free DPC imaging [7].

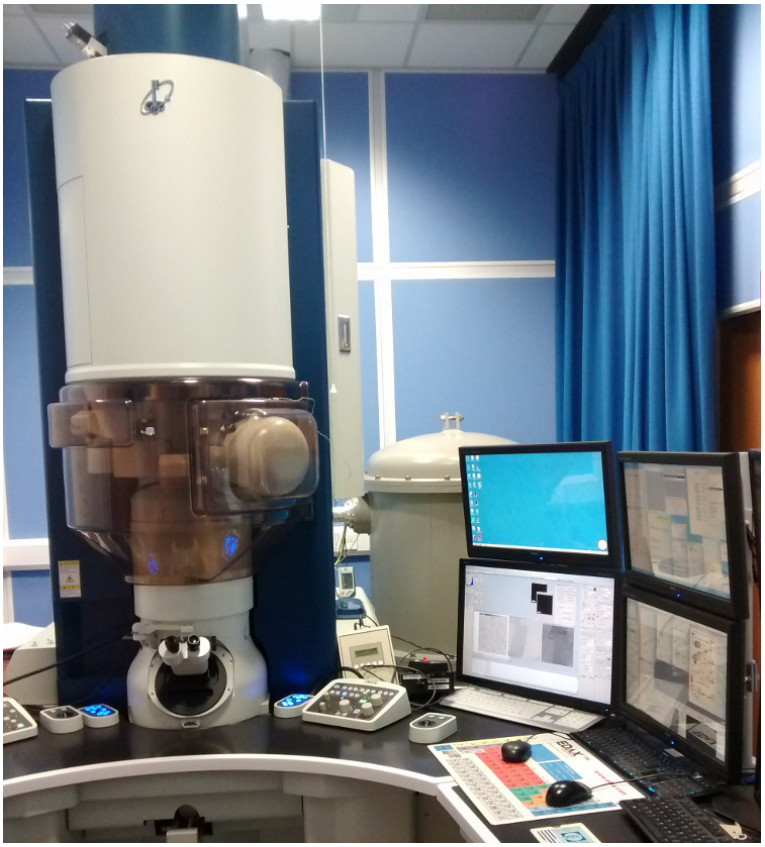

Fig. 3.1 *Jeol ARM 200cF TEM/STEM microscope (MagTEM) in operation at The University of Glasgow. The microscope is equipped with spacial hardware allowing world leading DPC STEM magnetic imaging*

The aberration corrector is provided by CEOS GmbH. The settings of the corrector were enhanced to participate in formation of the focused electron probe [5]. However, the spatial resolution is not the only factor in the quality of the DPC imaging. As discussed in the previous chapter, diffraction contrast can have a large influence on the resulting images (see Sec. 2.3.6). DPC images of thin, polycrystalline samples can contain strong diffraction contrast due to the comparable size of the focused probe and crystallites. This can be overcome with the usage of a smaller probe forming aperture, which makes the size of the beam larger and averages diffraction contrast over larger area of the sample (over a few crystallites). This is not only an issue in the case of the imaging of polycrystalline samples because effects related to crystal bending can also produce additional contrast, even for the imaging of single crystal samples.

In this chapter, the theory and practice of DPC will be explained. STEM DPC signals will be simulated for each point of a scan over an idealised magnetic specimen. It will be assumed that the specimen can be represented by a multiplicative transmission function. The resulting pixelated images for each probe position will be used to test various detector geometries and detection algorithms, which allows analysis of the expected results and will

also provide a better understanding of the limits of DPC imaging. The findings will form a the basis for the following chapter, which will explain experimental pixelated detection in DPC. It will be shown that pixelated detection is a vital step in the improvement of the DPC imaging of magnetic materials.

3.2 Theory of Differential Phase Contrast

In the previous chapter, the basic equivalence of the classical and quantum mechanical description of Lorentz microscopy was discussed. It was shown in Sec. 2.3.2 that in differential phase contrast, the deflection of the beam (β_L) due to in-plane magnetic induction in the saturated sample is equivalent to the 2D gradient of the phase assigned to the sample ($\nabla\phi$). This was shown for two electrons travelling from the same source to the same end point by different trajectories with magnetic flux present between them. The corresponding schematic is in Fig. 2.12 and explanation is in Secs 2.3.2 and 2.3.6. The phase difference the two electrons acquire, due to the Aharonov Bohm effect, can be generalised for the whole specimen. If Eq. 2.32 is used, the phase change of transmitted electrons $\phi(\mathbf{r})$ will be:

$$\phi(\mathbf{r}) = -2\pi \frac{e}{h} \int \mathbf{B}(\mathbf{r}) \cdot d\mathbf{S}, \tag{3.1}$$

where e is the magnitude of the electronic charge and h is Planck's constant.

An analytical explanation of DPC magnetic imaging was given by Chapman in Ref. [2]. It was shown that STEM BF acquisition with a split detector can be used to measure the gradient of the phase of the sample in the direction perpendicular to the split of the detector. This is done simply by difference of the two signals.

The accuracy of the imaging was discussed for a magnetic domain wall oriented in the direction of the split of the detector. If the profile of the wall is described by $B_y = B_S\, tanh(x/A)$, where B_S is the saturation induction and A is the domain wall width parameter, an accurate profile of the wall can be imaged in DPC if the coherent size of the probe, x_P, satisfies the following condition:

$$x_P < \sqrt{\frac{A\,\lambda}{10\pi\beta_{Lmax}}}. \tag{3.2}$$

where β_{Lmax} is the maximum deflection angle and λ is the wavelength of an electron in the TEM. Such a condition was more problematic to satisfy before the introduction of the aberration correction. An example can be given for the current system at the University of Glasgow: a probe semi-angle of $436\,\mu rad$ corresponds to the beam size of $x_P \sim 6\,nm$. If a sample, which causes a beam deflection of $\beta_{Lmax} = 10\,\mu rad$ at most is imaged, only

domain walls with a width larger than $A > 4.5\,nm$ will be imaged accurately. A semi-angle of $\alpha = 2150\,\mu rad$ allows observation of $A > 0.9\,nm$ wide walls, which should be sufficient for most of magnetic materials. However, this limit was introduced as possibly overly restrictive due to the analysis of the Fourier components of phase in [2].

If a gradient is applied in the x direction to Eq. 3.1 and imaging condition 3.2 is satisfied, the gradient of the phase can still be approximated by the classical, local deflection angle β_L [2] (a component in the x direction):

$$\beta_L(x) = \frac{e\,\lambda}{h} \int B_y(x, y, z)\, dz, \tag{3.3}$$

where only the y component of magnetic induction vector $B_y(x, y, z)$ will contribute to the deflection of the electron in the x direction (due to the Lorentz force cross-product). $B_y(x, y, z)$ can vary in the z direction, therefore the magnetic induction measurement is integrated over the path of transmitted electrons, which are here assumed to travel in the z direction.

However, Eq. 3.3 does not allow advanced calculations (structural/diffraction related) and will be valid only if the condition 3.2 is satisfied, as this theory assumes an ideal specimen without any diffraction contrast. Later in this chapter it will be shown that some of the DPC imaging characteristics of the experimental data can be simulated by the introduction of crystallite like variations into amplitude $S(\mathbf{x})$ and phase $\phi(\mathbf{x})$ of the specimen transmission function $t(\mathbf{x})$. Such a simulation will be used to test various detection algorithms.

3.3 Experimental realisation of DPC

3.3.1 4 quadrant detector

Chapman et al. discussed the theory and experimental realisation of DPC in [2] for the bi-split detector, however, it is much more convenient to split the detector further to four quadrants, as was done in [3]. The advantage is that in such geometry the two (orthogonal) components of the integrated magnetic induction can be imaged at the same time. A schematic of the detector is shown in Fig. 3.2(a). The four quadrants (A, B, C, D) detect a signal created within each of them by the electron beam. As the electron beam is scanned over the specimen, different values of the local integrated phase gradient deflect the beam to different positions on the detector. This is schematically show in Fig. 3.3.

The difference signals from the opposite quadrants, $(A - C)$ and $(B - D)$, will show two orthogonal maps of the integrated magnetic induction [2]. The magnitude of the deflection

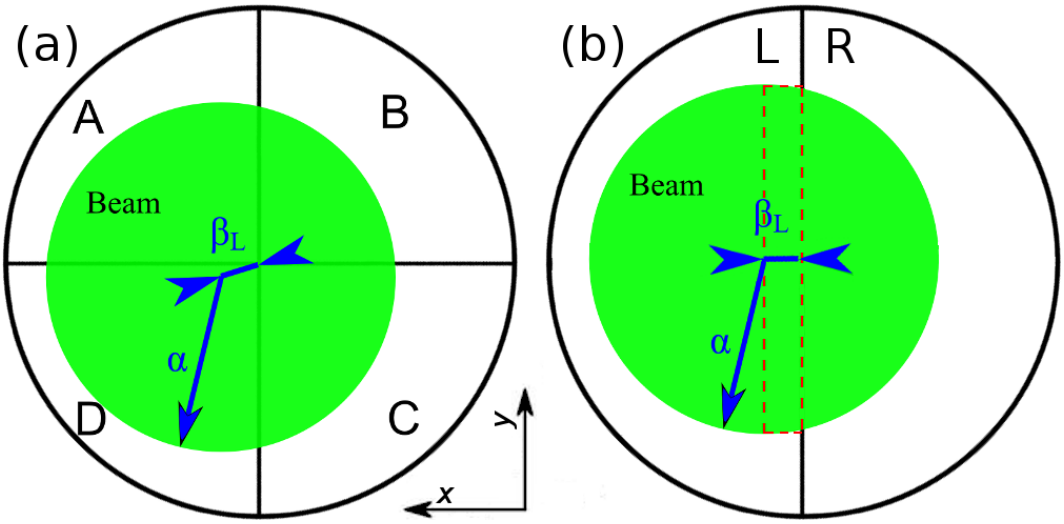

Fig. 3.2 *(a) schematic of a quadrant detector, (b) bi-split detector illustrating deflection signal linearity limit - highlighted area of the graph needs to be an approximately rectangle for linear imaging*

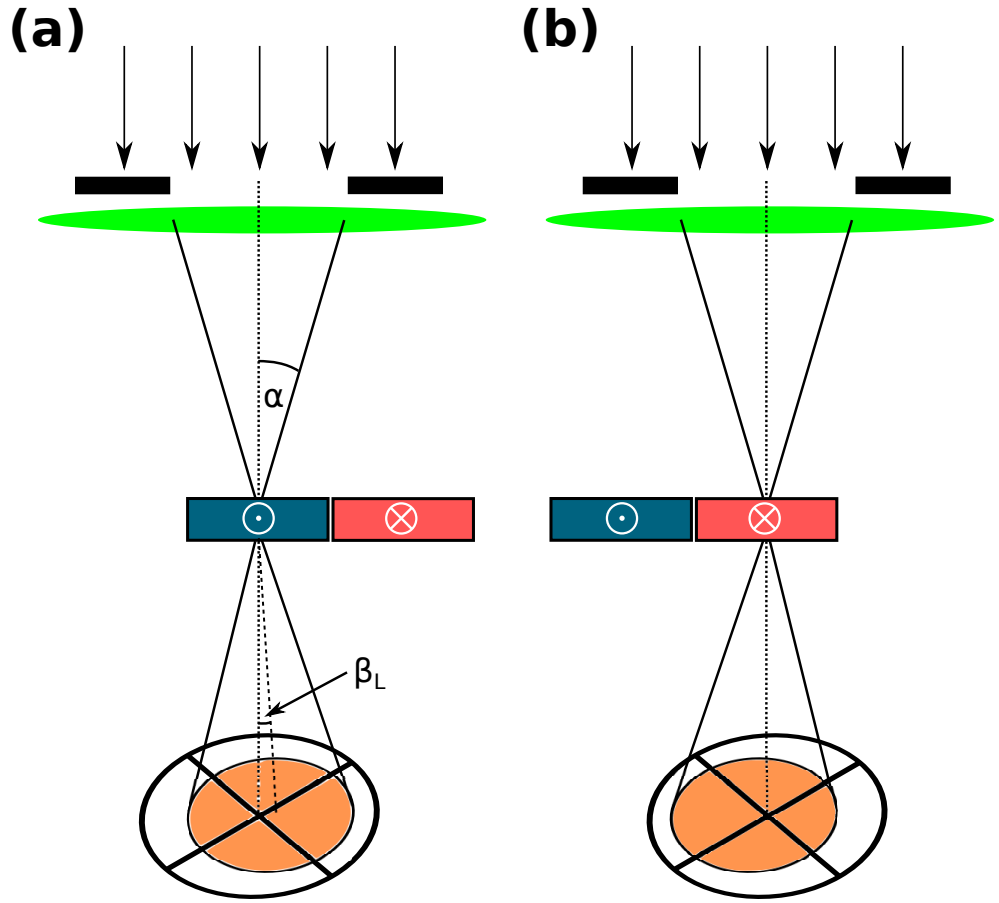

Fig. 3.3 *Schematic of DPC STEM imaging by a quadrant detector due to different in-plane orientation of magnetic induction. The deflection of the beam is calculated from intensity in each of the quadrants of the detector*

should not be larger than one tenth of the beam convergence semi-angle: $\beta_L/\alpha < 1/10$ [2]. The reason is illustrated in the schematic of the simplified bi-split detector in Fig. 3.2(b). If the ratio is larger ($\beta_L/\alpha > 1/10$), the red (highlighted) section cannot be approximated as a rectangle and the DPC signal will not be linear anymore.

The difference signal has to be calibrated to achieve quantitative measurements. The calibration will be demonstrated on the bi-split detector, which shown in Fig. 3.2(b). We assume the signal on the segment is linear to the area which the beam intercepted. The signal in left side of the detector will be:

$$L = \pi\alpha^2/2 + 2\alpha\beta_L, \tag{3.4}$$

and in the right side of the detector:

$$R = \pi\alpha^2/2 - 2\alpha\beta_L. \tag{3.5}$$

The difference signals from the two halves of the detector will be:

$$L - R = 4\alpha\beta_L. \tag{3.6}$$

We can now use $L + R = \pi\alpha^2$ to derive the quantitative deflection angle perpendicular to the split of the detector:

$$\beta_L = \frac{\pi\,\alpha}{4}\frac{L-R}{L+R}, \tag{3.7}$$

where α, the convergence semi-angle, is set by the aperture and optical properties of the microscope. Similarly, for a quadrant detector, the two orthogonal components of the deflection angle can be derived as:

$$\begin{aligned}\beta_L(x) &= \frac{\alpha\,\pi}{4}\frac{(A+D)-(B+C)}{A+B+C+D},\\ \beta_L(y) &= \frac{\alpha\,\pi}{4}\frac{(A+B)-(C+D)}{A+B+C+D},\end{aligned} \tag{3.8}$$

where $\beta_L(x)$ and $\beta_L(y)$ have the same axis orientation as shown in Fig. 3.2(a). Deflection angles can be converted into the integrated magnetic induction by Eq. 3.3:

$$\int B_{y,x}\,dz = \frac{h}{e\,\lambda}\,\beta_L(x,y). \tag{3.9}$$

Alternatively, the opposite quadrants can be used in the calculation, where the axes of orthogonal directions will be rotated by 45° and correction by a factor of $\sqrt{2}$ is needed.

Resulting deflection angles for opposite quadrants will be:

$$\beta_L(A-C) = \frac{\alpha\sqrt{2}\pi}{4}\frac{A-C}{A+B+C+D}, \qquad \beta_L(D-B) = \frac{\alpha\sqrt{2}\pi}{4}\frac{D-B}{A+B+C+D}. \tag{3.10}$$

For most cases the detector readout should be zero if there is no in-plane magnetic induction present in the sample. Post specimen projector coils of the microscope can be used to shift the beam to the desired position.

Eqs 3.7, 3.8 and 3.10 include a normalisation by the sum of the signal, therefore, if the intensity of the otherwise top hat profile of the beam is changing during the scan, the deflection signal will be correct. However, phase changes at crystallite boundaries or imperfections can create an uneven profile of the electron beam. In previous calculations of deflection angles, it was always assumed the profile of the beam is a top hat function, therefore such an effect will create unwanted contributions to the detected signals. An example of this is in Fig. 3.4, which is a DPC image of a domain wall in a 20 *nm* thick

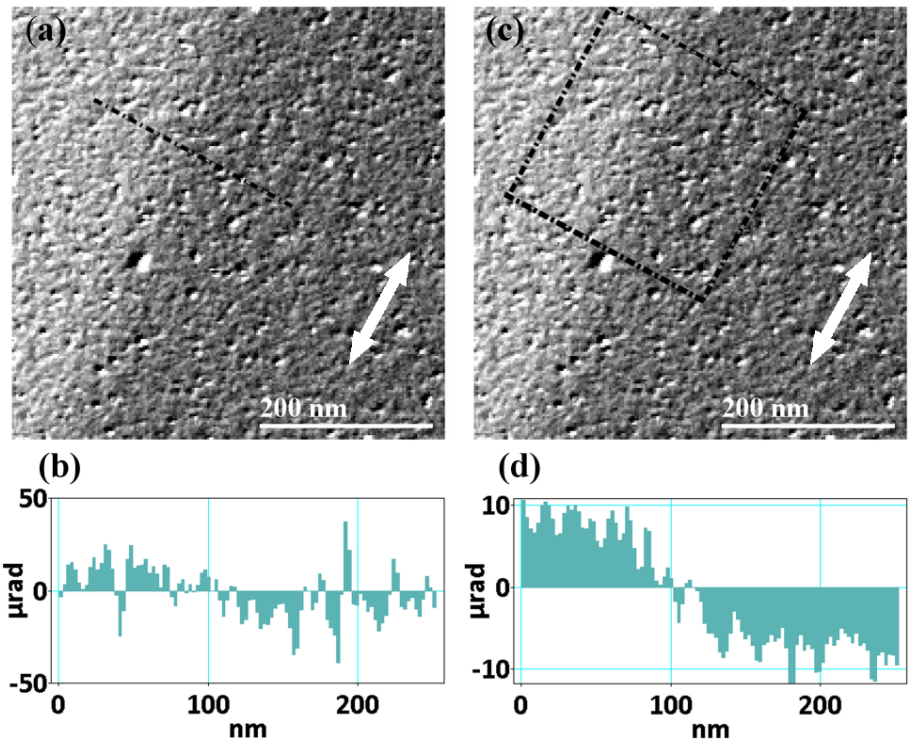

Fig. 3.4 *Measurement of wall profile by 4 quadrant detector in* 20 *nm thick PyPt specimen, (a) and (b) are DPC image with its single line profile showing low contrast of domain wall structure in the presence of diffraction contrast from crystallites, (c) and (d) shows that the averaging of 80 lines provides clearer contrast, albeit noise is still present. Direction of integrated magnetic induction is specified by the double headed arrow*

polycrystalline $Py_{95}Pt_5$ sample. The magnetic structure is visible to the human eye due to contrast averaging, however if a single line trace of the domain wall profile is plotted (Fig. 3.4(b)), the magnetic contrast is swamped by the diffraction contrast due to crystallites. The image can be averaged over many lines (Fig. 3.4(c) with its profile shown in (d)), which gives a better representation of the domain wall profile. However, in such an analysis resolution in one dimension of the image is lost. This is acceptable for the imaging of straight domain walls such as the one in Fig. 3.4, but if a 2D localised structure (e.g. vortex, skyrmion) is imaged, the possibility of averaging is limited. Furthermore, examples of diffraction disks are shown in Fig. 3.5, which were imaged by a CCD camera in the same sample. The disk (a) has a relatively flat profile and will produce an accurate readout. However, the second disk profile in (b) will produce an offset of $35\,\mu rad$ in this particular example, which is more than the expected deflection from the $20\,nm$ thick polycrystalline $Py_{95}Pt_5$ ($12.1\,\mu rad$). The position of the ideal readout (geometric centre) and the effective readout (intensity centre) is highlighted. In this analysis it was assumed that the profile of the electron beam only changes due to the diffraction effects from grain boundaries and imperfections in the polycrystalline sample.

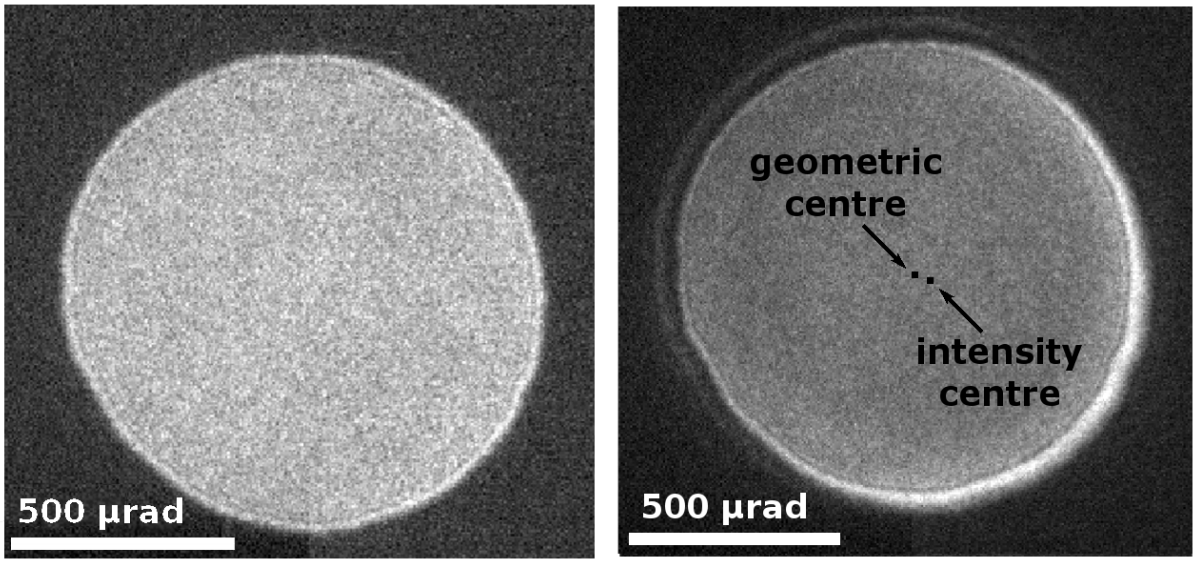

Fig. 3.5 *Examples of beam profiles imaged by CCD camera in* $20\,nm$ *thick PyPt specimen, variation between the images is due to different scattering when beam hits imperfect parts of the specimen - grain boundaries, multiple grains and others*

3.3.2 Annular 8 quadrant detector

Chapman et al. realised in 1990 that splitting the detector further into annular quadrants (8 segments) can improve the information transfer for magnetic imaging [4] and especially for the imaging of polycrystalline specimens. If it is assumed that the beam is again a top hat function and it covers the inner quadrant of the detector (schematic is shown in Fig. 3.6), signals from segments *A, B, C, D* cancel in the deflection calculation, because they are equal for a top hat disk profile. Using Eq. 3.10, the deflection angles for annular quadrant detector (opposite quadrants) can be calculated by:

$$\beta_L(E-G) = \frac{\alpha\sqrt{2}\pi}{4}\frac{E-G}{A+B+...+H},$$
$$\beta_L(H-F) = \frac{\alpha\sqrt{2}\pi}{4}\frac{H-F}{A+B+...+H}. \tag{3.11}$$

A simple geometrical argument can be given for diffraction contrast suppression by using an annular detector. In a four quadrant detector the unwanted variations can be considered as $\xi_4 \sim (\text{noise})^2$. This is due the subtractions $A-C$ and $D-B$ in Eq. 3.10 which involve the whole disk signal. However, in an annular detector the signal used is effectively restricted to arches of the whole disk signal - see Eq. 3.11 (signals in *E, F, G, H*). This reduces the diffraction signal contribution to $\xi_8 \sim$ (noise). Therefore overall magnetic

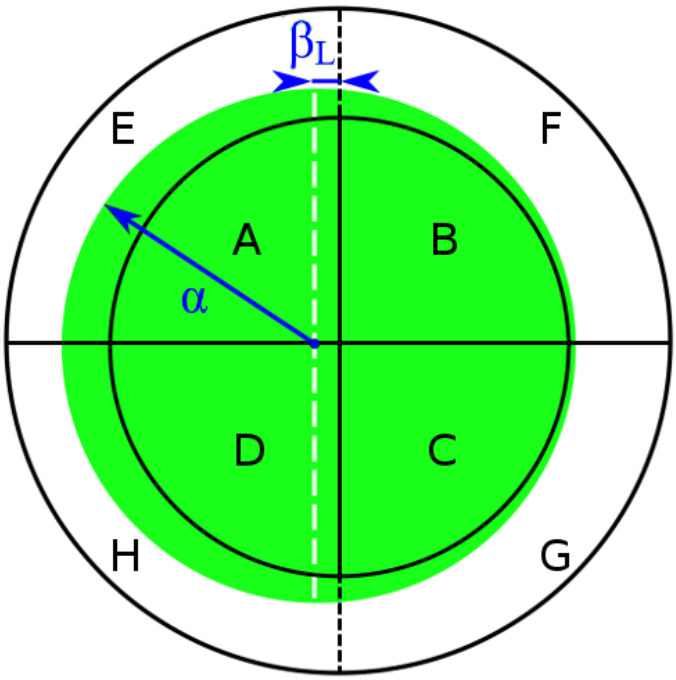

Fig. 3.6 *Schematic of annular detector, where the electron beam (green area) covers inner quadrants (A, B, C, D) completely*

information transfer will be enhanced for annular detector and it will be maximised for the beam being just outside the inner quadrants. This, however, does not solve problems if the magnitude of the signal in the disk varies, this will be later solved by using a pixelated detector and computer vision algorithms.

An additional explanation can be given by the introduction of the phase contrast transfer calculation, based on varying sinusoidal phase [4]. In this description, the electron beam passing through such a phase variation will be split into three diffraction disks, which can overlap depending on the frequency of the sinusoidal phase variation (as is shown in Fig. 3.7(a)). Magnetic phase often varies on much larger spatial frequencies (e.g. 2π phase change every $350\,nm$ in $10\,nm$ thick permalloy in the direction transverse to the magnetisation). This will only lead to the small shift of the disk, because the ratio of spatial frequency associated with such a phase gradient, $(350\,nm)^{-1}$, and frequency associated with the electron beam, $(1-6\,nm)^{-1}$ (in MagTEM), is very low [8]. The schematic of this is in Fig. 3.7(b).

Nevertheless, by restricting the analysis to the very edge of the central diffraction disk only the largest and the lowest spatial frequencies are present in the image, where the lowest are due to integrated magnetic induction and the highest mostly due to diffraction effects.

An example of the annular quadrant imaging can be found in Fig. 3.8. The signal from the four domain state in a $30\,nm$ thick square of permalloy (a) and (b), defined lithographically, was successfully revealed by the annular detector geometry with better quality than in the four quadrant detector imaging in Fig. 3.4. However, if the higher magnification detail of the magnetic vortex core in the centre of the square is required,

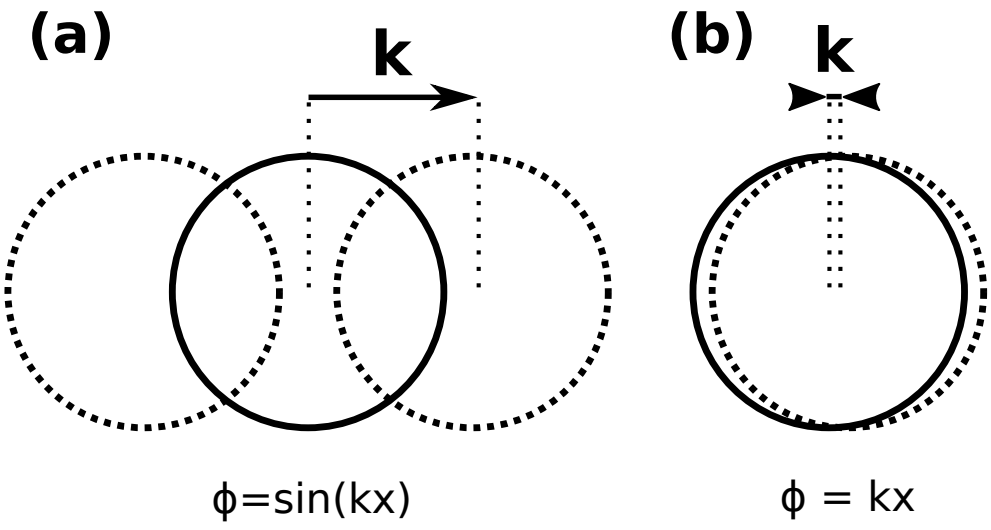

Fig. 3.7 *(a) three beam overlaping condition from sinusoidal phase variation, (b) single spatial frequency shift of the disk*

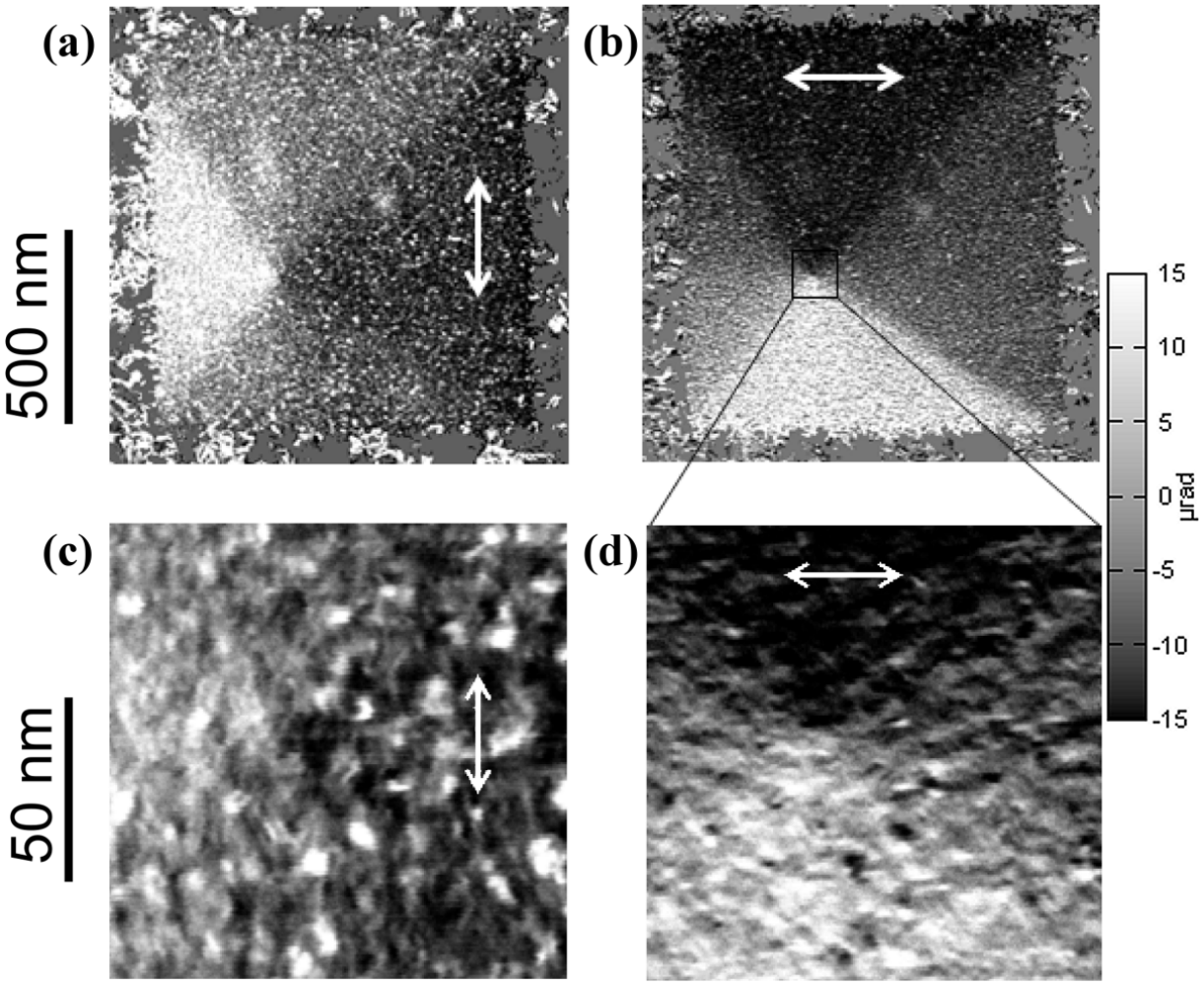

Fig. 3.8 *Imaging of square in polycrystalline Py by an annular DPC detector in* 30 *nm thick specimen, (a) and (b) two orthogonal components of the integrated magnetic induction in low magnification, (c) and (d) are high magnification images showing additional diffraction contrast (image provided by the courtesy of Dr Damien McGrouther)*

images (c) and (d), the signals are still dominated by the additional crystallite contrast and measurement of the size of the vortex core can be difficult to achieve.

3.4 Scanning Simulations of DPC

In this section, an advanced type of DPC simulation will be introduced. The model is based on STEM linear imaging as was explained in the previous chapter (Sec. 2.2.2). In such an approach, STEM diffraction patterns can be computed by convolving the aperture

function (STEM probe) with the transmission function of the specimen. This is basically a simulation of Fourier optics based imaging of a sample with assigned amplitude and phase with a probe limited by a cut-off frequency. The following assumptions will be in place until the end of this chapter: it will be assumed that the phase transfer is linear (and can so be computed by a convolution), that the magnetic phase is a constant over the thickness of the sample and that there are no aberrations in the optical system of the microscope, $\chi(\mathbf{k}) = 0$. This approach simulates the profile and shift of the central disk related to the gradient of the phase and amplitude of the sample. It is used to calculate changes in the disk image due to scanning over a theoretical model of a sample represented by its complex transmission function $t(\mathbf{x})$, introduced in the previous chapter.

It was also shown (assuming no aberrations) that the diffraction pattern (central disk in this case) in STEM imaged by the detector can be described by:

$$g(\mathbf{k}) = \left| A(\mathbf{k}) * FT[S(\mathbf{x})e^{\imath\,\phi(\mathbf{x})}] \right|^2, \tag{3.12}$$

where $A(\mathbf{k})$ is the aperture function, a complex function with an imaginary part equal to zero (due to $\chi(\mathbf{k}) = 0$ assumption); $*$ is the convolution operator; FT is the inverse Fourier transform; and $S(\mathbf{x})$ and $\phi(\mathbf{x})$ are the amplitude and the phase of the specimen's transmission function $t(\mathbf{x})$. $A(\mathbf{k})$, $S(\mathbf{x})$ and $\phi(\mathbf{x})$ can be represented by real 2D images (matrices) and the expected central disk pattern $g(\mathbf{k})$ can be calculated by the use of Fast Fourier Transforms.

It is also important to note that in this chapter only non-atomic simulations will be provided. This is due to the convergence semi-angles involved in field free imaging, in which the cut-off spatial frequency does not allow standard imaging with an atomic resolution.

The simplest type of magnetic specimen can be represented by the specimen transmission function with the amplitude part equal to one $S(\mathbf{x}) = 1$ and phase $\phi(\mathbf{x})$ representing the configuration of in-plane integrated magnetic induction. Extension of the amplitude part, $S(\mathbf{x}) \neq 1$, can be used to introduce amplitude contrast related effects.

The result of an interaction of the beam with the strongly varying non-linear phase gradient is not accessible in the classical theory. Images in Fig. 3.9 illustrate expected beam profiles from the simulation of an ideal magnetic specimen ($S(\mathbf{x}) = 1$) for: (a) no magnetic phase present, (b) constant phase gradient (scan within a magnetic domain) and (c) scan over the middle of a magnetic domain wall. The phase in Figs 3.9(b) and (c) was chosen for a $100\,nm$ thick permalloy sample with $A = 30\,nm$ domain wall width parameter to provide strong influence of the non-linear phase gradient. The wavelength of the electrons was $\lambda = 2.51\,pm$. Images in Figs 3.9(d), (e) and (f) show the profile of the phase for simulation images in Figs 3.9(a), (b) and (c) respectively. The resulting pattern in Fig. 3.9(c) shows distorted disk due to the varying phase gradient on the scale of the size of the electron probe.

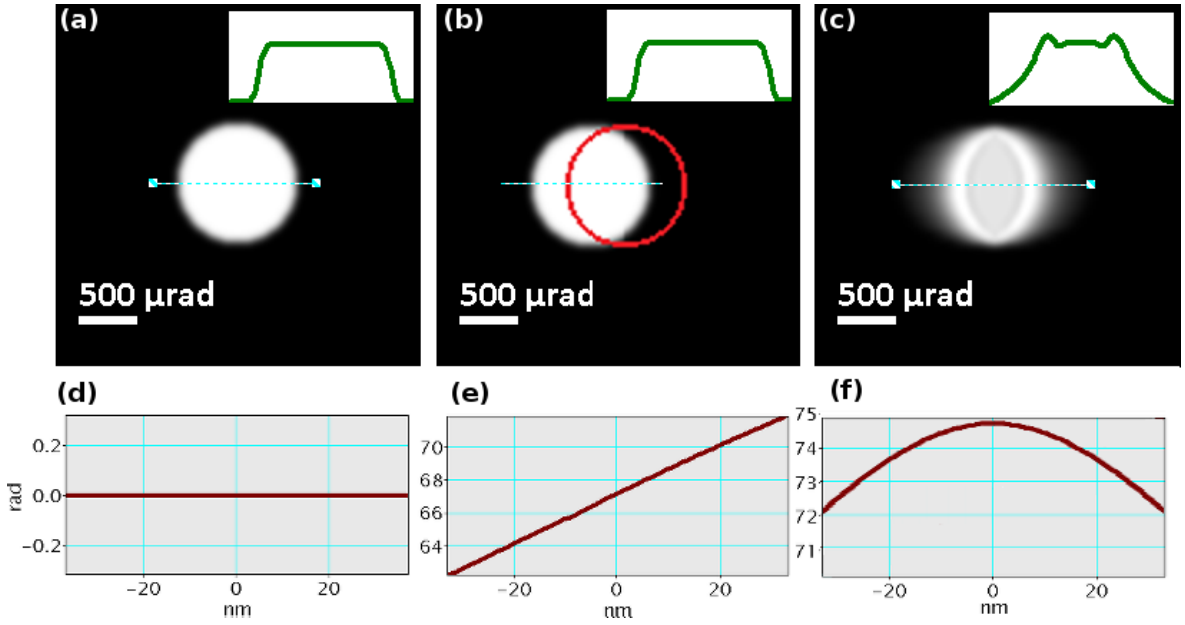

Fig. 3.9 *STEM central disk simulation of various phase gradients present in ideal specimen* ($S(\mathbf{x}) = 1$)*, (a) beam passing non magnetic parts of a specimen* ($\nabla\phi = 0$)*, (b) beam passing through a magnetic domain; red circle shows the central position of the beam* ($\nabla\phi = const$)*, (c) the beam passing through a middle of the domain wall* ($\nabla\phi \neq const$)*. To enhance the effect of the different types of phase, simulated sample was* 100 *nm thick permalloy with a domain wall width parameter* $A = 30\,nm$ *and the convergence semi-angle* $\alpha = 436\,\mu rad$*, for* 200 kV *electron illumination. Inset images in (a), (b) and (c) show a line profile of the beam. Images are 256x256 and aperture radius was 32 px. Aperture was smoothed for reasons discussed in the following section*

3.4.1 Scanning algorithm

The scanning algorithm introduced in this work aims to reproduce STEM DPC imaging. The procedure is based on mathematical manipulation of images represented by matrices. The size of the aperture image, $A(\mathbf{x})$, has to be smaller than the specimen image, $t(\mathbf{x})$, to allow for scanning of the sample. To allow simple mathematical computation the algorithm selects a subset of $t(\mathbf{x})$ the same size as $A(\mathbf{x})$ for each scan point. The scanning will be provided by sequential shift of the subset of the $t(\mathbf{x})$. This will be indicated by probe position $\mathbf{x}_P$. The algorithm is described in the following list.

1. An inverse FFT is applied to the aperture function image:
   $FFT^{-1}[A(\mathbf{k})] = A(\mathbf{x})$

2. A region of interest of the same size as $A(\mathbf{x})$ is selected from the amplitude and phase images of the transmission function $S(\mathbf{x}, \mathbf{x_P})$ and $\phi(\mathbf{x}, \mathbf{x_P})$. A complex transmission function is created by their multiplication $t(\mathbf{x}, \mathbf{x_P})$, which is centred around point $\mathbf{x_P}$, which is the position of the beam in the simulation

3. $A(\mathbf{x})$ is multiplied by $t(\mathbf{x}, \mathbf{x_P})$ which gives the transmitted wave function $\psi_t(\mathbf{x}, \mathbf{x_P})$ (for the multiplicative sample)

4. An FFT is applied to $\psi_t(\mathbf{x}, \mathbf{x_P})$ and the detector function (diffraction pattern) is generated by calculation of the intensity of the result $g(\mathbf{k}, \mathbf{x_P}) = |IFFT[\psi_t(\mathbf{x}, \mathbf{x_P})]|^2$

5. Scanning is generated by the calculation of $g(\mathbf{k}, \mathbf{x_P})$ for different beam positions and repeating steps 2, 3 and 4. Final dataset $G(\mathbf{k}, \mathbf{x_P})$ will be four dimensional, which means that each probe position in real x-space (two dimensional scan) will have a two dimensional reciprocal k-space image assigned.

Aperture function

A very important parameter of the DPC simulation is the image of the aperture function $A(\mathbf{k})$. A instinctive choice is a top hat function as this selects which spatial frequencies will form the image (as in the real microscope). An example is shown in Fig. 3.10. The aperture function has to be calibrated so the probe $A(\mathbf{x}) = FT^{-1}[A(\mathbf{k})]$ will match the calibration of the specimen function $t(\mathbf{x})$. The radius of the aperture function can be calculated from the following variables:

- R is the radius of an aperture in pixels
- N is the size of the aperture function image in pixels
- Δk is the calibration of a pixel in reciprocal k-space
- Δx is a calibration of a pixel in real x-space
- α is the convergence semi-angle of the beam
- λ is the wavelength of the illuminating electrons

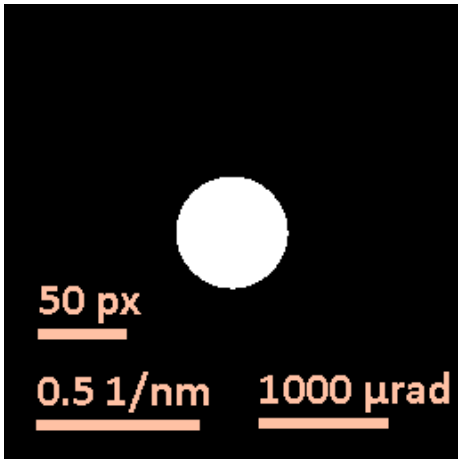

Fig. 3.10 *Example of* $256x256\,px$ *aperture top hat function with different calibrations shown,* $R = 32\,px$, $k_\alpha = (5.8\,nm)^{-1}$ $(\alpha = 436\,\mu rad)$

Δk and Δx are related through [9]:

$$\Delta k = \frac{1}{N\,\Delta x}.$$

The maximum spatial frequency of the beam (aperture) can be calculated from the convergence semi-angle and wavelength of the electrons:

$$k_\alpha = \frac{\alpha}{\lambda} = R\,\Delta k,$$

therefore the radius of the aperture can be calculated as:

$$R = \frac{\alpha}{\lambda} N\,\Delta x. \tag{3.13}$$

An example of the aperture top hat function is shown in Fig. 3.10, parameters are shown as a calibration. Size of the aperture can be defined either in a convergence semi-angle α or maximum spatial frequency k_α, where again $k_\alpha = \alpha/\lambda$. The aperture function will be later modified due to problems associated with the abrupt edge of the top hat function.

Unlike the traditional HAADF-STEM, where the highly scattered incoherent information is of the most interest (detector angles $\sim$ 30–200 $mrad$) [10–12], DPC imaging requires great precision in very low scattering information ($\lesssim 10\,\mu rad$). For this reason the simulation is required to be very precise in the reciprocal frequency **k**-space and also the real **x**-space. To avoid issues in both Fourier domains, two different measures will be introduced.

Firstly, the aperture is smoothed, which helps with ringing noise when images with large contrast gradients are used in FFT filtering [13]. The smoothing of the top hat function is provided by convolution with the 2D symmetric normalised Gaussian function:

$$G_\sigma = \frac{1}{\sigma\sqrt{2\pi}} \exp\left(\frac{|\mathbf{r}|^2}{2\sigma^2}\right). \tag{3.14}$$

where σ is the standard deviation of the Gaussian function and $|\mathbf{r}|$ is the distance from the centre of the image. An example of a Gaussian with $\sigma = 4\,px$ (G_4) is shown in Fig. 3.11. Secondly, the radius of the aperture in the image window is kept below $R < N/4$, due to the precision issues related to the contrast transfer of low spatial information. The probe is in the form of an Airy disk, which contains most of the information in a small radius around its centre (example with G_2 smoothing is shown in Fig. 3.12). If the radius of the aperture is too large, the central maximum and the first minimum ring of the probe will be averaged together and the results of the simulation will be inaccurate. Such an effect has been researched further in astronomy [14, 15], where it is suggested that the diameter of the first zero of an Airy function should be at least three pixels.

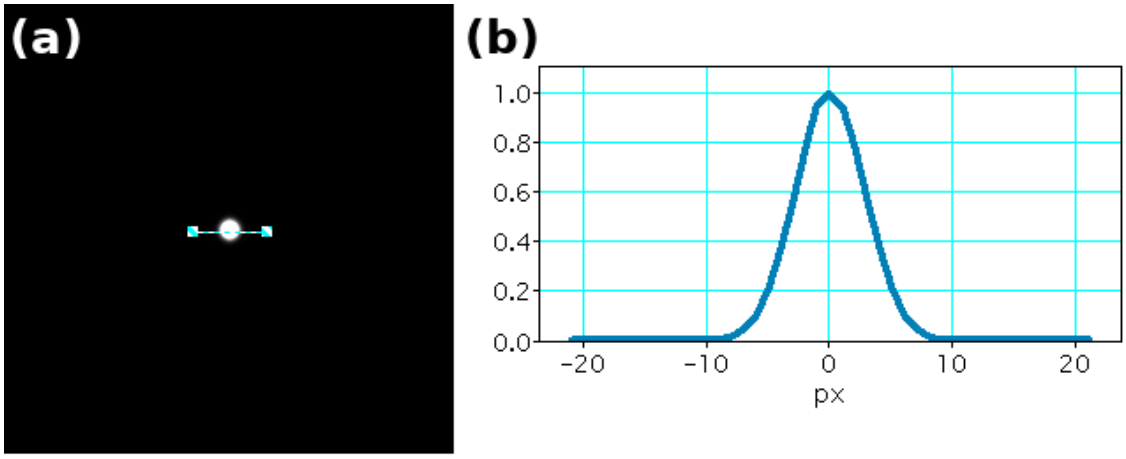

Fig. 3.11 *(a) example of a normalised 2D symmetric Gaussian function G_4 with $\sigma = 4\,px$, image is $256x256$ px, (b) is its maximum line profile*

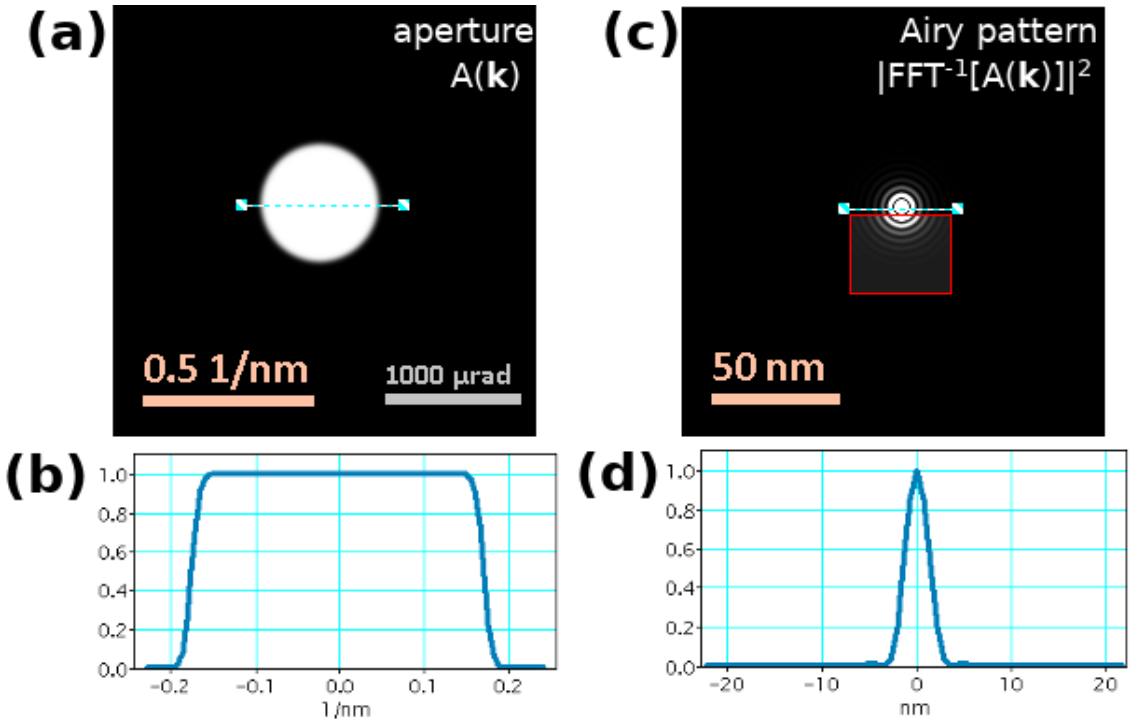

Fig. 3.12 *Example of the computation of the probe function, (a) aperture $A(\mathbf{k})$ with maximum spatial frequency $k_\alpha = (5.8\,nm)^{-1}$ with its profile in (b), (c) intensity of the probe $|FT^{-1}[A(\mathbf{k})]|^2$ with its profile in (d). The aperture was smoothed due to ringing noise in FFT. The contrast was highlighted in the red box in (c) to show the small variations of the intensity in the Airy pattern*

In the field free mode of the Jeol ARM 200cF at 200 kV electron acceleration, the 20 μm aperture corresponds to $\alpha = 860\,\mu rad$ convergent angle ($k_\alpha = (2.9\,nm)^{-1}$). If the pixel spacing of the specimen function is $\Delta x = 1\,nm$ and window size is $N = 256\,px$, the radius of the beam equals $R = 180\,px$, which is not possible to fit the computing window. The 50 μm aperture with $\alpha = 2150\,\mu rad$ ($k_\alpha = (1.1\,nm)^{-1}$) will, for the same parameters, give $R = 36\,px$, which is more suitable.

The signal to noise consideration of the DPC pixelated detection favours a larger ratio of the beam and the window size (R/N), therefore a larger aperture will function better if detector efficiency is to be tested. This is due to a larger number of pixels corresponding to the edge of the disk in the simulation, which will give better averaged result. For this reason the size of the beam was kept $R = 32\,px$ for all the processing introduced in this chapter (within a 256x256 px window), and other parameters - such as the Δx pixel spacing were changed accordingly to fit the simulation parameter setup.

Specimen function

The specimen function representing the magnetic phase of the sample can be calculated from the magnetisation configuration [16], which was described in Sec. 2.4. A 2D gradient of a generated phase function can be used to calculate DPC images, however, it does not take into account the non-negligible size of the focused probe in STEM experiments. Therefore, any abrupt variations in the phase or the amplitude of the sample (comparable to the size of the focused probe) will result in imprecise calculation. By using the scanning algorithm introduced in Sec. 3.4.1, a more versatile approach to image calculation is possible. Effects of noise, intensity changes and even grain boundary contrast can be added to the amplitude and phase of the complex specimen transmission function.

The magnetic phase ϕ_m of the sample will be generated from its magnetisation model by the algorithm introduced in Sec. 2.4. It will be again a 180° Néel wall with profile:

$$\begin{aligned} m_x &= \sqrt{1 - m_y^2}, \\ m_y &= \tanh\left(\frac{x}{A}\right), \\ m_z &= 0. \end{aligned} \tag{3.15}$$

where A is again the domain wall width parameter (Fig. 2.22 shows an example of this magnetisation profile) and $m_{x,y,z} = M_{x,y,z}/M_s$. A subset of magnetic phase ϕ_m corresponding to this magnetisation configuration, with its profile indicating a nonlinear phase in the centre of the wall, is shown in Fig. 3.13. Note that the parameters used to generate this configuration were: the width parameter was $A = 10\,nm$ and pixelsize $1\,nm$. The highlighted box is the same size as the aperture function. Scanning is provided by moving the box (region of interest) along the highlighted direction and convoluting with

the aperture function at each position. The highlighted box is 256x256 *px*, which is the same size as the aperture image used in simulations throughout this chapter.

An ideal measurement of integrated magnetic induction without tilting of the sample, with magnetisation configuration described by Eq. 3.15 will be described by [17]:

$$\begin{aligned} B_x &= 0 \\ B_y &= B_S \tanh\left(\frac{x}{A}\right), \end{aligned} \tag{3.16}$$

and its B_y component is plotted for $A = 10\,nm$ and normalised B_S in Fig. 3.14. The figure also contains examples of disk patterns, where the influence of a non-linear phase gradient is visible for edges of disks for -7, 0 and $7\,nm$ distances from the centre of the

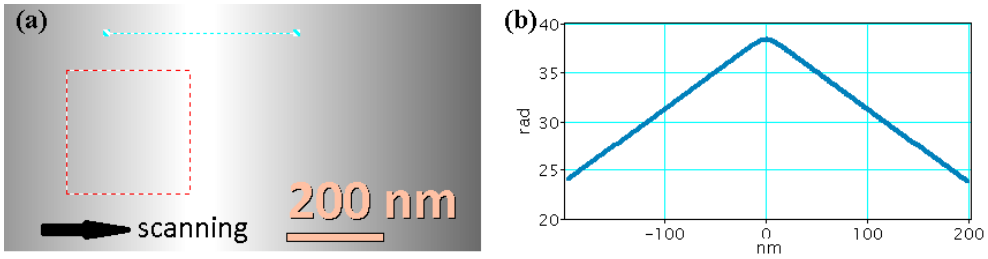

Fig. 3.13 *(a) ϕ_m the magnetic phase of the sample with domain wall ($A = 10\,nm$), pixelsize $1\,nm$ and the size of the selected window 256x256 px (red box), (b) the line profile (blue line in (a)) showing non-linear profile in the centre of the domain wall*

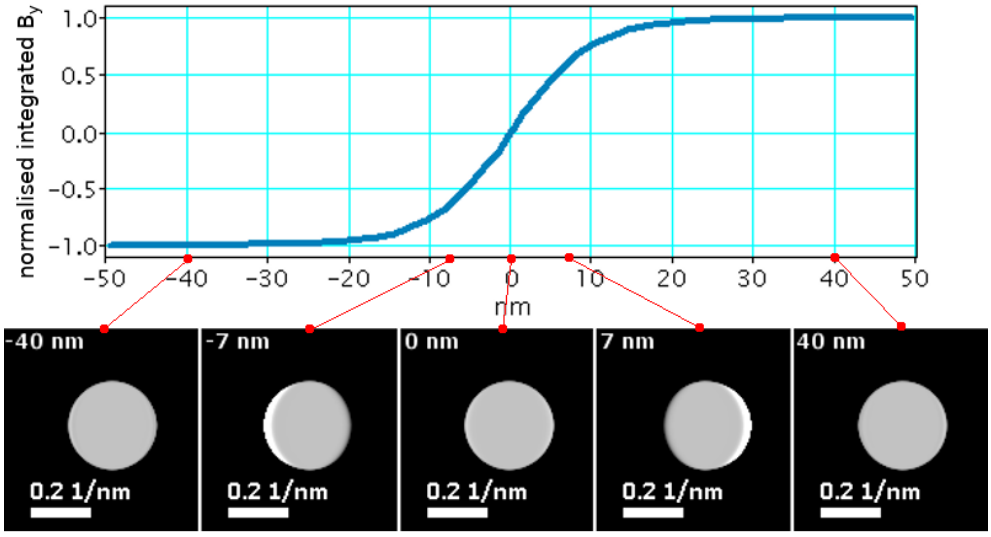

Fig. 3.14 *Theoretical normalised integrated magnetic induction profile with a set of images showing the $g(\boldsymbol{k})$ disk images resulting from a scan over a $A = 10\,nm$ wide magnetic domain wall in $t = 20\,nm$ thick permalloy with highlighted position in the domain wall profile ($k_\alpha = (5.8\,nm)^{-1}$). The contrast is enhanced to see the fine changes of intensity due to the nonlinear phase gradient of the domain wall*

domain wall. The contrast of disk images was enhanced to show the intensity variations at their edges. B_x is equal to zero due to divergent character of the magnetisation for this component [18], which cancels the contrast in Lorentz microscopy.

The resulting simulated disk patterns will be analysed for disk shifts using algorithms which will be introduced in the following section. The images generated for these disk patterns will then be compared to calculations of the theoretical profile, which assumed an infinitely small probe size.

3.4.2 Detection of the beam deflection

Segmented DPC

Standard DPC detection described in Sec. 3.3.1 is provided by the segmented detector. The simulation algorithm described in Sec. 3.4.1 creates a fully pixelated diffraction image of the central disk, which can be split into four quadrants (A, B, C, D) and DPC signals can be generated similarly to the real detector. This results in two orthogonal components of the integrated magnetic induction which can be calculated by Eqs 3.8 and 3.9. If we assume a pure phase specimen ($S(\mathbf{x}) = const$), the magnetic phase $\phi(\mathbf{x})$ is solely responsible for the contrast. If $\phi(\mathbf{x})$ varies on the order of size of the focused probe, the STEM disk can contain a relatively high spatial information resulting from the non-linear gradient of the phase.

Centre of mass and threshold

The availability of the fully pixelated diffraction image $g(\mathbf{k})$ is advantageous, because new types of detectors can be designed theoretically and their efficiency can be tested. This does not only involve standard types of detectors as the quadrant or the annular quadrant detector, but even more complicated algorithmic detectors involving computer vision can be used, this is essential to the main topic of this thesis: pixelated detectors in DPC STEM.

As a first step in the advancement of detection methods, the centre of mass (COM) algorithm can be used to find the position of the circular beam in $g(\mathbf{k})$:

$$\mathbf{COM}[g(\mathbf{k})] = \frac{\sum I(\mathbf{k}) \cdot \mathbf{k}}{\sum I(\mathbf{k})}, \tag{3.17}$$

where $I(\mathbf{k})$ is the intensity of a pixel at position $\mathbf{k} = (k_x, k_y)$. The advantage of COM detection is that there is no maximum deflection limit (as described in Sec. 3.3.1) and the centre of the detector can be defined after the experiment. Additionally, a threshold can be applied before the COM algorithm. This suppresses variations of intensity of the central disk in $g(\mathbf{k})$, not an issue with simulated data. This proves important for the analysis of experimental pixelated datasets from polycrystalline materials, which will be

shown in the following chapter. This is because it allows for the filtering of non-magnetic, diffraction related contrast and results in surpassing of the performance of the annular quadrant detector.

where it surpasses the performance of the annular quadrant detection. It allows the filtering of non-magnetic diffraction related contrast, and the analysis of such will be shown in the following chapter.

Cross-correlation and edge filtering

Cross-correlation is widely used in image template matching across the sciences [19–22]. It can be used to find the position of a pattern within the image and is applied here to measure the deflection of the central electron disk, $A(\mathbf{k})$. In usual practise, smoothing and edge filtering is used prior to cross-correlation to avoid false detection and to achieve a higher signal to noise ratio [22–24]. Cross-correlation can be used in electron microscopy to align EFTEM images with subpixel precision [22].

To use cross-correlation in disk deflection analysis, the following approach was taken:

1. The real part of the aperture function $Re\{A(\mathbf{k})\}$ is edge filtered to create $\nabla A(\mathbf{k})$ (shown in Figs 3.15(a) and (b))

2. disk image $g(\mathbf{k})$ is edge filtered by the Sobel filter to create $\nabla g(\mathbf{k})$ (shown in Fig. 3.15(c))

3. two edge filtered images are cross-correlated to create correlation pattern (shown in Fig. 3.15(d))

4. the position of the maximum in the correlation pattern represents the shift between the two images (note the shift of the peak to the left in Fig. 3.15(d))

This algorithm can be used for each point of the scan, which will generate DPC like map of the shifts of the central diffraction disk. It is essential to use smoothing before the edge generation, as any small signal variations can become large in an edge filtered (gradient) image and cross-correlation may not be precise [25]. The cross-correlation can only find the beam deflection as an integer value, but if a second order parabola is used to fit pixels surrounding the maximum of the correlation pattern, subpixel precision deflections can be achieved [22, 26]. The cross-correlation edge registration process will be further discussed in the following chapter, where experimental pixelated datasets will be analysed (subpixel registration is described in Sec. 4.2.2).

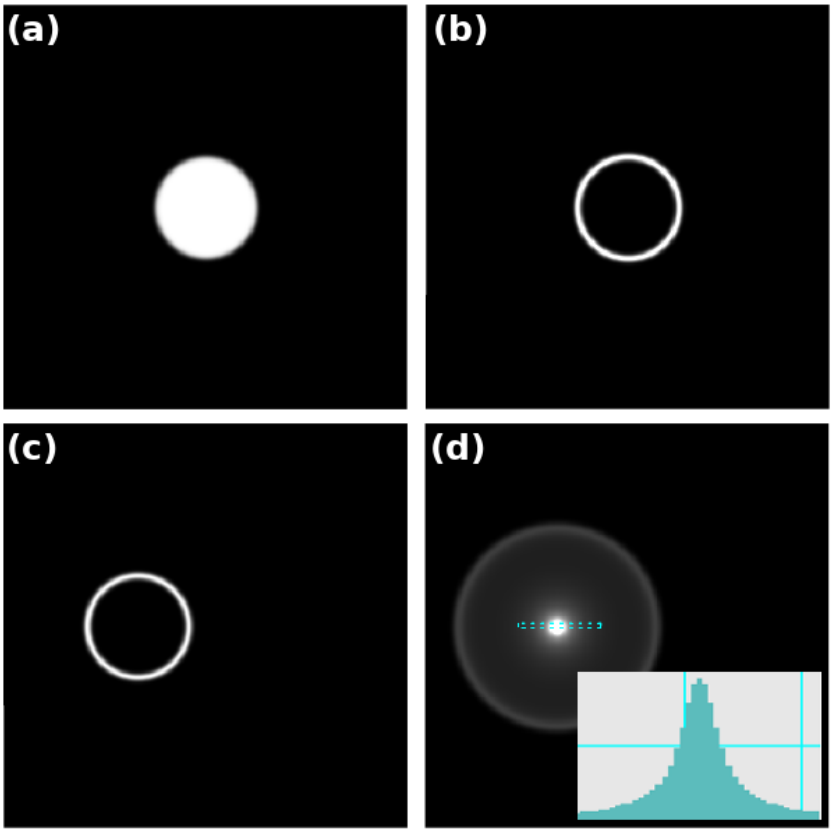

Fig. 3.15 *An example of ideal cross-correlation processing, (a) the real part of the aperture function* $Re\{A(\mathbf{k})\}$*, (b)* $\nabla A(\mathbf{k})$ *edge generated by Sobel algorithm from (a), (c) manually shifted edge, (d) cross-correlation pattern with maximum at the pixel corresponding to the shift direction and magnitude. A line profile of the maximum is shown in subset image*

3.5 STEM DPC simulation results and analysis

In this section, results of DPC simulations will be shown for various types of virtual detectors and compared to the theoretical integrated magnetic induction profiles. The integrated magnetic induction contrast transfer will be tested on a theoretical 180° Néel magnetic domain wall with magnetic induction described by [17]:

$$B_y = B_S \tanh\left(\frac{x}{A}\right), \tag{3.18}$$

which was discussed in Sec. 3.4.1.

The domain wall width parameter A will be altered to find the limits of different types of detector algorithms. Simulations will be studied in the parameter space based on the imaging characteristics of the field free mode of the Jeol ARM 200cF at The University of Glasgow.

3.5.1 Pure phase simulation result

The simulation of STEM DPC will be first studied for a specimen with a transmission function only containing magnetic phase ϕ_m variation ($S(\mathbf{x}) = constant$).

Fig. 3.16 shows a graphical comparison of normalised integrated magnetic induction measurements of the magnetic domain wall ($A = 10\,nm$) by different virtual detectors in $t = 20\,nm$ thick permalloy. The maximum spatial frequency in the probe was $k_\alpha = (5.8\,nm)^{-1}$, which corresponds to a $10\,\mu m$ aperture (convergence semi-angle $\alpha = 436\,\mu rad$) in field free mode of the Jeol ARM 200cF microscope. The requirement of the maximal ratio of the deflection to the convergence semi-angle from Sec. 3.3.1 was satisfied ($\beta_L/\alpha < 0.03$). The graph in Fig. 3.16 compares theoretical hyperbolic tangent profile of B_y with segmented DPC detection (DPC), centre of mass calculation (COM) and cross-correlation disk registration (CrossCorr). The graph also illustrates an important limit of DPC measurements. It shows that an electron beam with $k_\alpha = (5.8\,nm)^{-1}$ produces a small systematic error in the case of a narrow domain wall ($A = 10\,nm$) for most of the detection

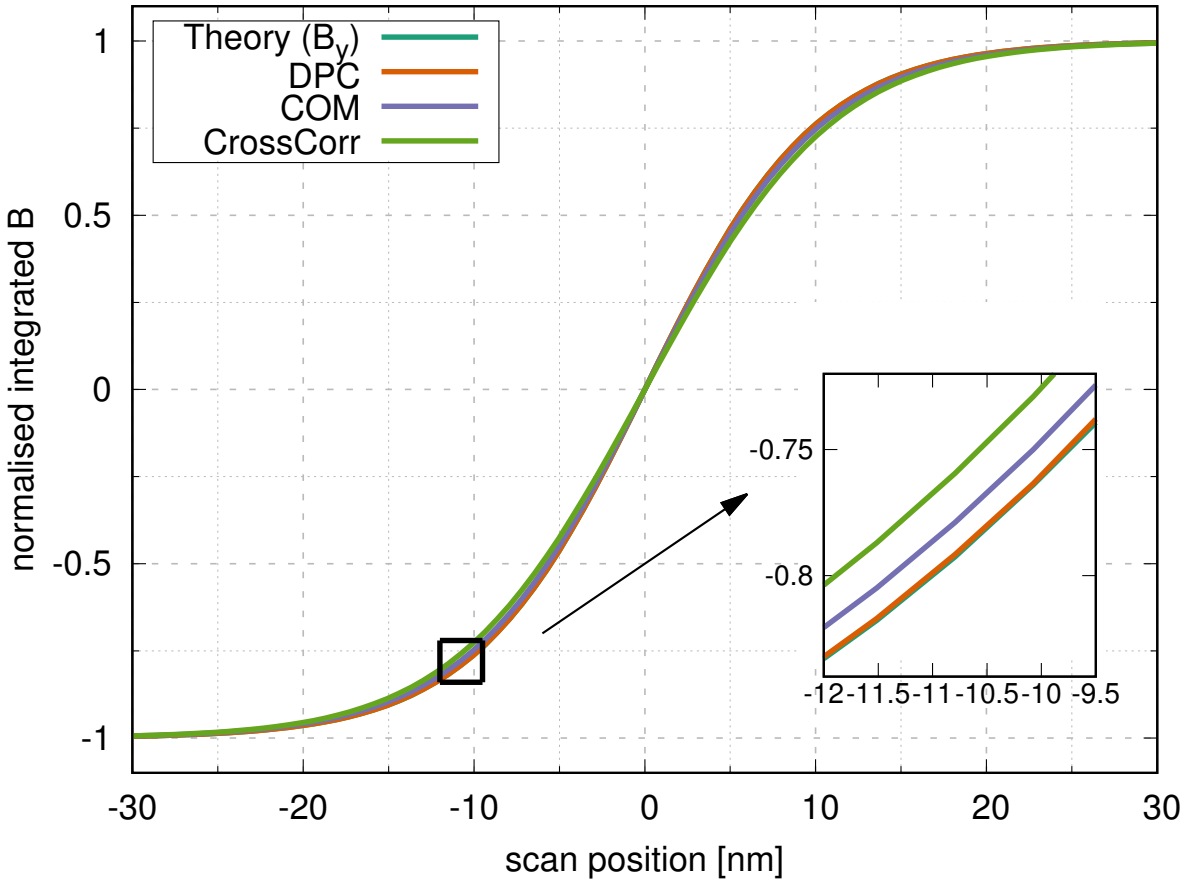

Fig. 3.16 *Virtual detector measurement of integrated magnetic induction in STEM DPC simulations; the specimen transmission function was a pure phase function* $t(\mathbf{x}) = e^{\imath\phi_m(\mathbf{x})}$, *maximum probe spatial frequency was* $k_\alpha = (5.8\,nm)^{-1}$ *and domain wall width was* $A = 10\,nm$

algorithms, except segmented DPC which completely matches the theoretical profile. The reason for this is the nonlinear phase gradient associated with the domain wall.

Discussion

An example of how a nonlinear phase gradient changes the profile of the disk when imaging close to the centre of the domain wall is shown in Fig. 3.17. (a) shows the disk image with its line trace in (b). Additional signals due to the non-linear phase gradient appear at the edge of the disk and are pointed to by arrows in Fig. 3.17(b). These intensity changes transfer differently into deflection measurements for three tested algorithms.

Segmented DPC provides the best position read-out (see Fig. 3.16). The reason is that the additional signal is summed without any change to the sum in the left or the right part of the detector (for the given combination of the domain wall width parameter and the size of the probe). Using the COM algorithm, this signal is weighted and can create a small offset. The precision of the cross-correlation is mostly affected by changes in the edge of the disk.

Comparison between least square fits of the hyperbolic tangent to the measured profiles in Fig. 3.16 is shown in the Table 3.1. The offset of the measured width parameter,A_m, depends on the maximum frequency of the beam and the width of the wall, A, itself. The width parameter of the wall, $A = 10\,nm$, is rather narrow and slight differences are expected when the size of the probe, $k_\alpha = (5.8\,nm)^{-1}$, is close to this value.

This type of simulation can be used as a guide for experiments and/or as a check for whether the imaging is in or close to the linear regime. In the pure phase simulation, centre of mass and cross-correlation algorithms do not produce a better result than the

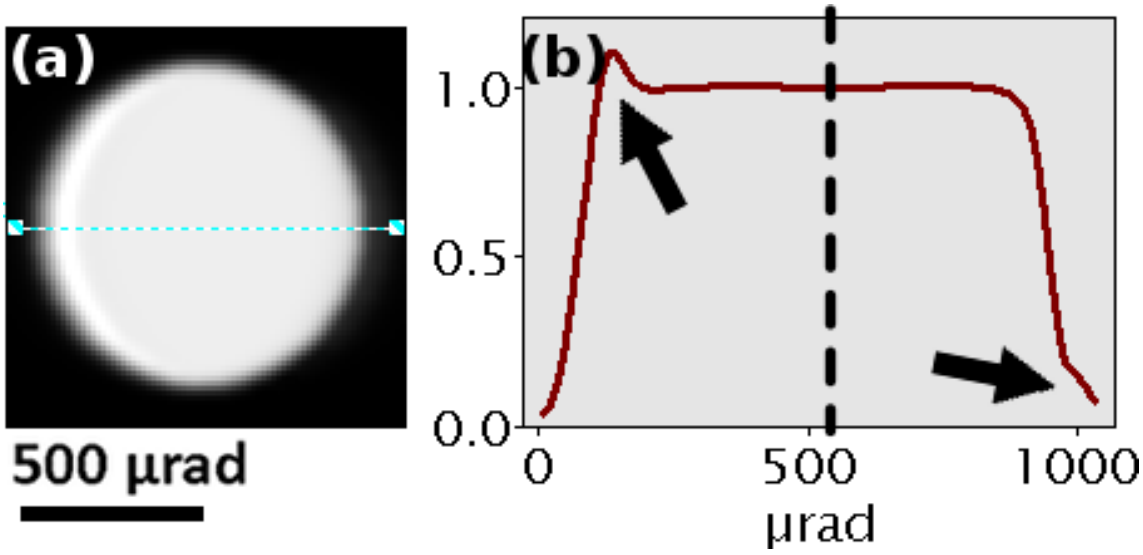

Fig. 3.17 *(a), (b) image of single simulated detector function $g(\mathbf{k})$ close to domain wall centre with its profile ($A = 10\,nm$, $k_\alpha = (5.8\,nm)^{-1}$ probe angle*

method	A_m $[nm]$
Theory (B_y)	10.0135(3)
DPC	10.0240(4)
COM	10.3589(9)
CrossCorr	10.90(1)

Table 3.1 *Comparison of least square fits of hyperbolic tangent wall width parameter* $\left(\tanh\left(\frac{x}{A_m}\right)\right)$ *to measured profiles in Fig. 3.16, wall was simulated with* $A = 10\,nm$ *parameter*

segmented DPC detection. Their true potential will be revealed when additional variations are added to the specimen transmission function and most importantly in the analysis of experimental pixelated datasets.

3.5.2 Amplitude step specimen function

The response of virtual detectors can be also studied for a step in the amplitude of the specimen function. Instead of a $S(\mathbf{x}) = 1$ function, we use:

$$S(\mathbf{x}) = 1 + h(\mathbf{x}) * G_\sigma, \tag{3.19}$$

where $h(\mathbf{x})$ is Heaviside step function, $*$ is the convolution operator and G_σ is the symmetric Gaussian defined in Eq. 3.14. The step function will be smoothed for the same reason as an aperture function in Sec. 3.4.1, that is that a pure step with infinite gradient would create ringing artefacts in the spatial domain. The phase will be kept zero ($\phi(\mathbf{x}) = 0\,rad$).

The response of a scan over such function should be zero in differential phase contrast, however it is not true for all detection methods as is visible in Fig. 3.18. The figure shows a simulation of an integrated magnetic induction measurement with a $k_\alpha = (1.1\,nm)^{-1}$ beam scanning over a step function smoothed by a Gaussian with $\sigma = 0.25\,nm$ ($G_{0.25}$). It shows that the segmented detector (DPC) responds to the amplitude step function and shows apparent beam deflection. Its profile looks similar to negative gradient of a Gaussian, whereas centre of mass (COM) and cross-correlation (CrossCorr) methods show almost flat profile and follow the phase $\phi = 0\,rad$. Examples of resulting disk profiles will be shown in the following section for a 2D scan. Fig. 3.18 shows that segmented detector can create an apparent deflection of the beam only due to a change of the intensity of the transmitted beam.

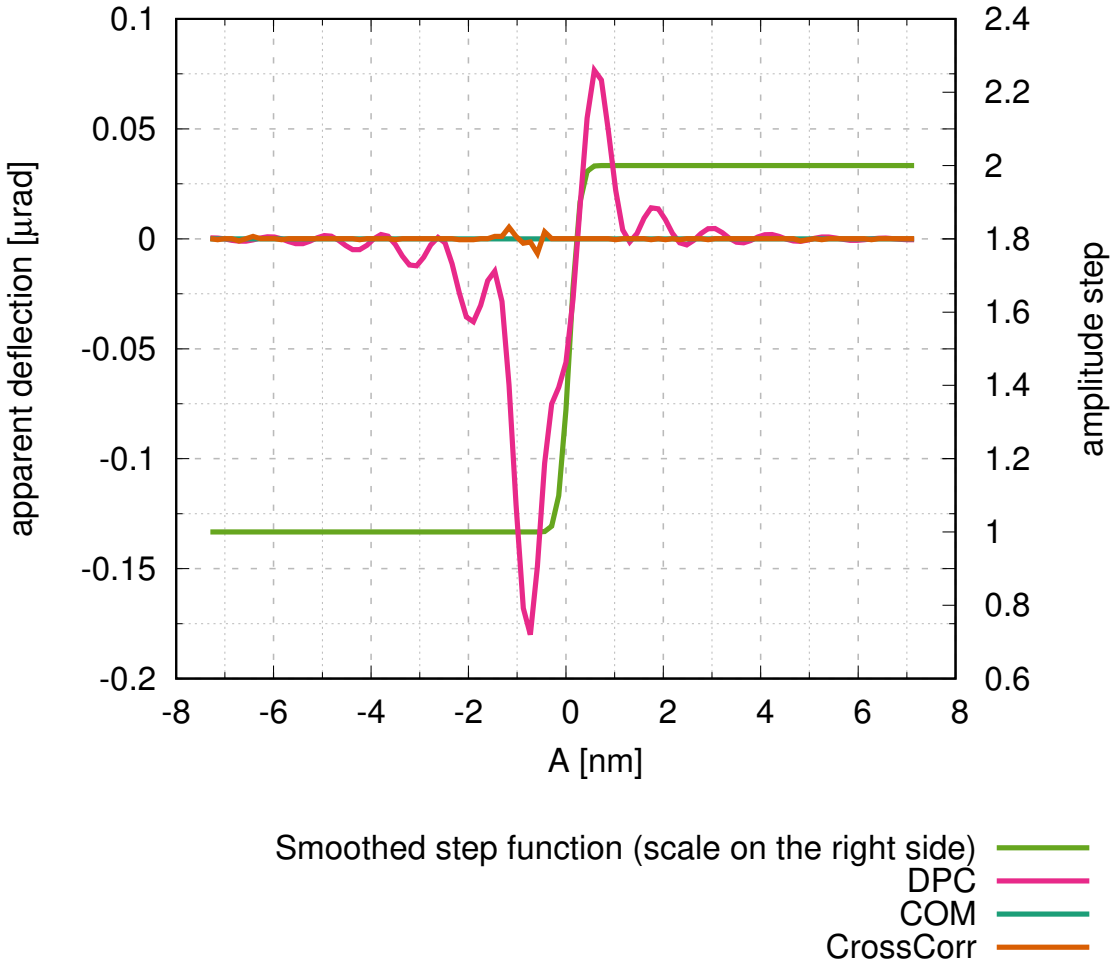

Fig. 3.18 *Measured deflection by virtual detectors due to an amplitude step function in* $S(\mathbf{x})$*. The phase of the sample was zero. The amplitude function was a smoothed step from 1 to 2, however here it is scaled to show its spatial spread. The maximum frequency in the beam was* $k_\alpha = (1.1\,nm)^{-1}$

3.6 Polycrystalline sample simulation

Additional signal due to crystallites can swamp magnetic contrast in DPC to the point that precise imaging of localised structures, like vortices or skyrmions, can be compromised. In the previous sections, effect of phase and amplitude changes were studied in line scans. In this section, 2D scans will be used to study the response of the segmented detector (DPC), centre of mass (COM) and cross-correlation (CrossCorr) disk registration method. We will try to reproduce some aspects of experimental imaging. It will be shown how virtual detectors deal with additional signals in the phase and amplitude of the transmission function of the specimen. Simulations in this section will be again based on phase generated from magnetisation configuration of a Néel domain wall with width parameter $A = 10\,nm$, see Eqs 3.15 and 3.16. Modelled amplitude and phase changes due to crystallites will

be added to the specimen transmission function. These will be modelled as an artificial specimen, generated from white noise and Fourier filtered to match characteristics of the experimental image of a real specimen. This approach was chosen because of an easier control of the data and spatial frequencies present in them especially the presence of shot noise, which can influence the phase of the specimen.

3.6.1 Amplitude effects

A bright field STEM image of a 20 nm thick $Py_{95}Pt_5$ sample in Fig. 3.19(a) illustrates changes in the intensity of the transmitted beam due to the different Bragg diffraction conditions from randomly orientated crystallites in the sample (a schematic is shown in Fig. 3.19(b)).

White noise can be filtered in the Fourier domain to match the characteristics of polycrystalline sample. Digital Micrograph® was again used for this purpose. An example of such a filtering is given in Fig. 3.20. The image of white noise in Fig. 3.20(a) was Fourier transformed and circular mask with Gaussian decay was applied (the result of which is shown in Fig. 3.20(b)). The frequency of the mask was chosen to slowly decay from frequencies of $(4\text{–}6\,nm)^{-1}$ (the size of crystallites in permalloy) to $(1.1\,nm)^{-1}$, which was the cut-off frequency. This was chosen to match the highest frequency in the beam for $50\mu m$ aperture in free field mode of MagTEM - $k_\alpha = (1.1\,nm)^{-1}$. The pixel spacing of the amplitude and phase images was $\Delta = 0.15\,nm$.

The filtered white noise image contains a similar number of white and black clusters, therefore the image was filtered further by subtracting its average, taking the absolute value and inverting the image. This operation created darker crystallites, which are generally more apparent in BF image in 3.19, and also created sharper grain boundaries. In summary,

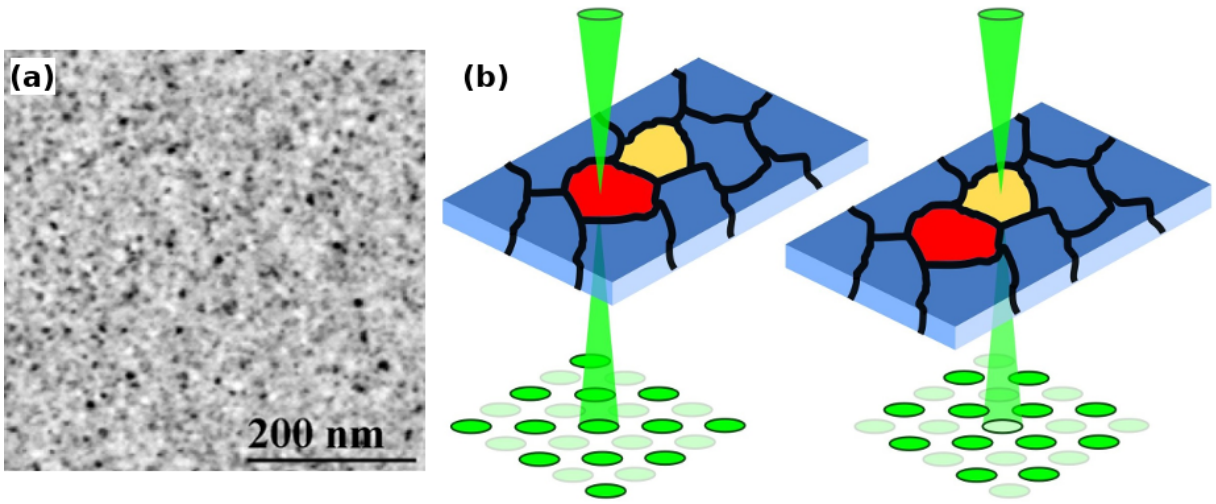

Fig. 3.19 *(a) bright field STEM image of* 20 *nm thick* $Py_{95}Pt_5$ *sample, (b) schematic of Bragg diffraction in differently oriented crystallites*

the resulting image in Fig. 3.20(c) was created by formula:

$$(c) = const - abs\left[FFT^{-1}(b) - average(FFT^{-1}(b))\right]. \tag{3.20}$$

The standard deviation and mean of the image in Fig. 3.20(c) were matched to the BF image in Fig. 3.19(a). The model is completely artificial, however, it is not used here to match the sample completely and compare to the experiment, but to explore what effects can be included in the simulation and how they resemble experimental images of differential phase contrast.

Fig 3.21 shows source images for the simulation. (a) is an image of an aperture with $k_\alpha = (1.1\,nm)^{-1}$; (b) is an amplitude image, $S(\mathbf{x})$, (subset of Fig. 3.20(c)) and (c) is an image of a phase, ϕ_m, of the centre of the domain wall with width parameter $A = 10\,nm$.

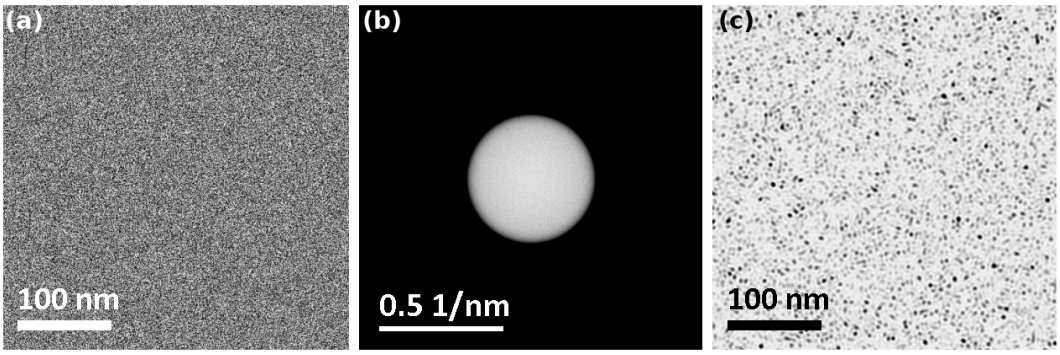

Fig. 3.20 *(a) image of a white noise, (b) circular decaying mask filtered FFT of (a), the frequencies were used to match the size of crystallites in PyPt sample (c) artificial polycrystalline sample created from Fourier filtered white noise in (b). The mathematical formula used to create this image is in Eq. 3.20*

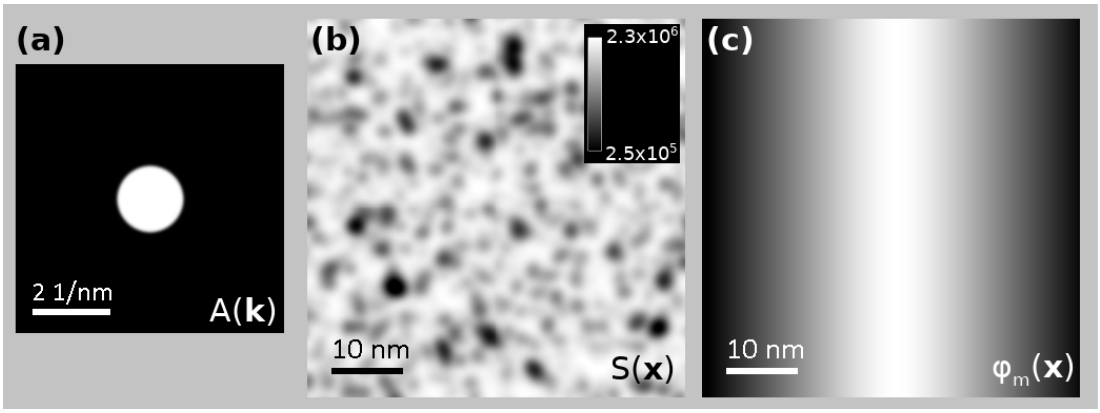

Fig. 3.21 *Source images for polycrystalline sample magnetic imaging simulation, (a) image of the aperture function $A(\mathbf{k})$, (b) image of the amplitude $S(\mathbf{x})$, subset of Fig. 3.20, (c) image of the magnetic phase $\phi_m(\mathbf{x})$ corresponding to subset of 10 nm wide 180° Néel domain wall created from Eqs 3.15 and 3.16. (b) and (c) are 360x360 pixels, however a larger area was used to allow scanning (the size of the probe image has to fit subset of $S(\mathbf{x})$ and $\phi_m(\mathbf{x})$)*

These images are now used to simulate a 4D dataset using the convolution algorithm introduced in the previous section (Sec. 3.4.1) and analysed by the beam deflection detection algorithms (DPC, COM, CrossCorr), which were introduced in Sec. 3.4.2.

The result of disc deflection algorithm analysis of a scan based on the aperture and specimen function in Fig. 3.21 is shown in Fig. 3.22. Only the y components of the integrated magnetic induction are shown, as x components will be zero for magnetisation deflection (only containing noise components) due to the divergent character of Néel walls in

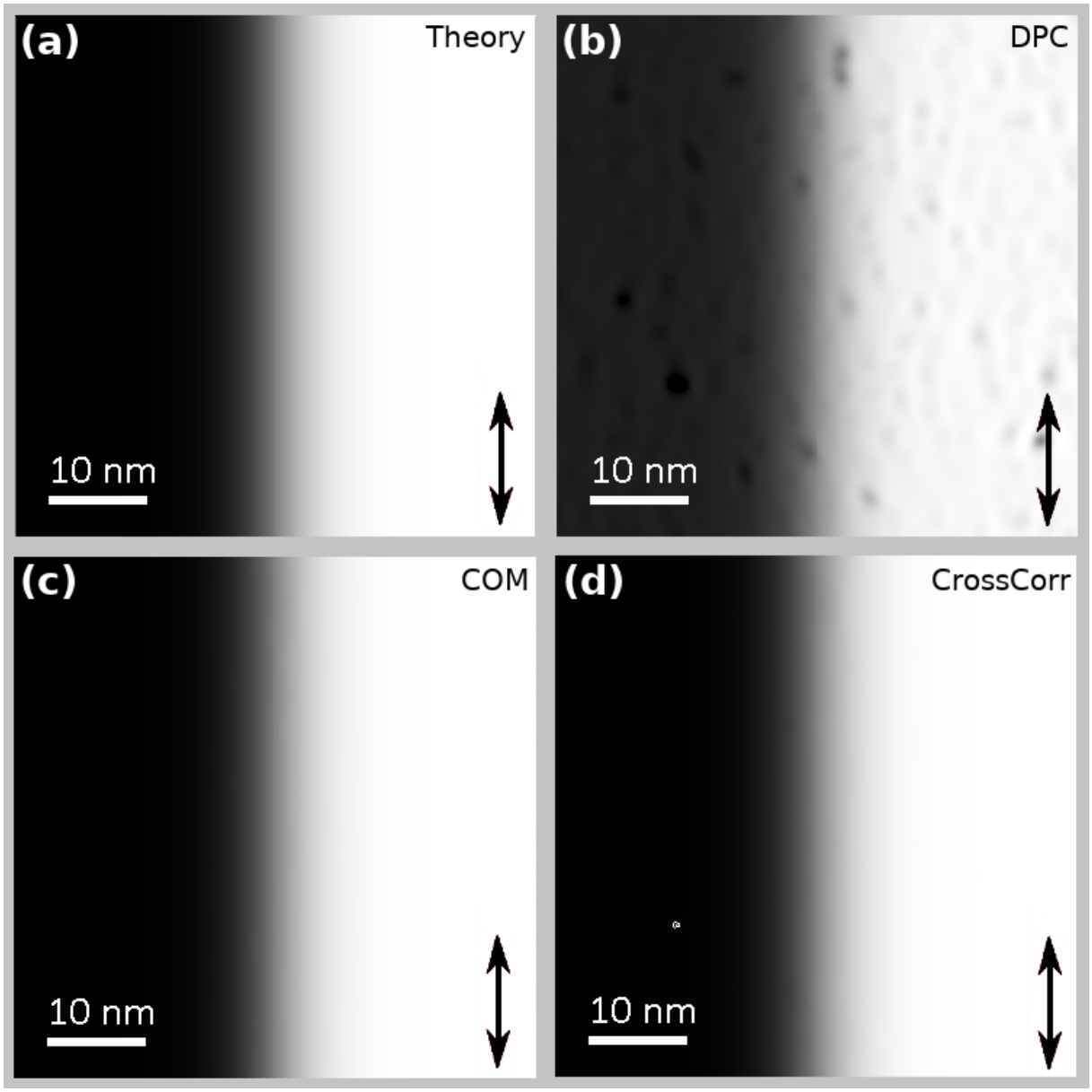

Fig. 3.22 *Polycrystalline sample magnetic imaging simulation result images, (a) theoretical B_y profile of the integrated magnetic induction, measured B_y profile by (b) segmented detector, (c) centre of mass detector, (d) cross-correlation detector. Arrows show the direction of integrated magnetic induction. The scale of (b) was adjusted to show the signal variation, the signal levels are the same in all the images*

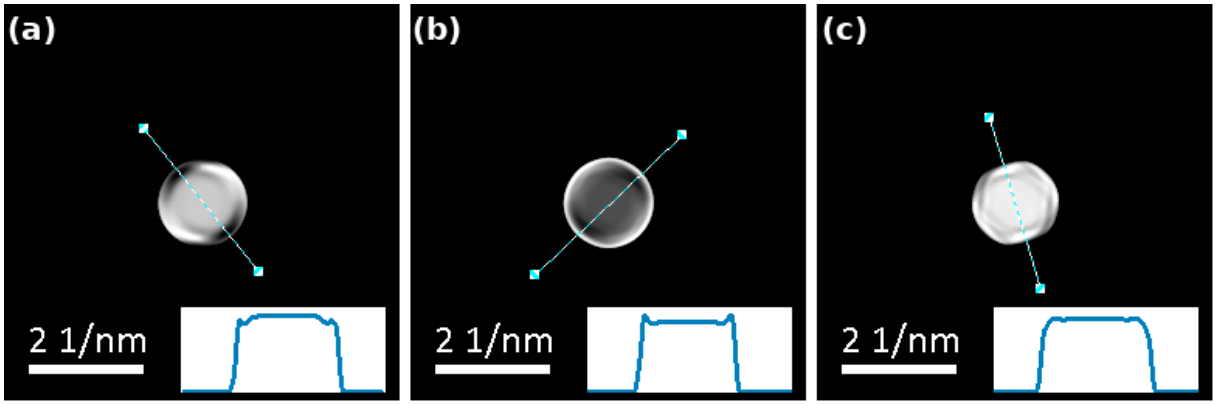

Fig. 3.23 *Examples of the diffraction patterns from simulation in Figs 3.21 and 3.22, contrast variation was enhanced for visibility, line profiles are plotted in insets to compare the variation to the normalised signal level (this was required due to changes in the amplitude of the transmission function)*

this direction (details were shown in Sec. 2.4). Image in Fig. 3.22(a) shows the theoretical result of an integrated magnetic induction measurement, where the size of the beam is considered infinitesimally small. Image (b) is the segmented detector result, for which it was already shown that it responds to changes in the amplitude function of the specimen. Image (c) is the result of the centre of mass algorithm, which is expected to show a clear profile of a domain wall without any additional noise due to changes of amplitude of the specimen. Similarly, the cross-correlation result in image (d) shows again a clear profile. The simulation was calculated using a script in Digital Micrograph. The 4D dataset of 360x360 probe positions, which were 256x256 pixels each, took about 5 hours to complete.

The accurate result of COM detection in Fig. 3.22(c) shows that variations in the amplitude of the specimens transmission function create a central diffraction disk with a centre of symmetry (the COM algorithm is weighted). This is illustrated in Fig. 3.23 for three $g(\mathbf{k})$ disk images. This also explains non ideal read out of the segmented detector (DPC) in Fig. 3.22, where summing the signal in segments does not respond ideally to such variations. For the cross-correlation algorithm, only the position of the edge contributes to the detected deflection and changes in the amplitude of $t(\mathbf{x})$ do not contribute (as is expected).

3.6.2 Amplitude and phase effects

In this section we will try to simulate the result of an additional fine phase variation in an attempt to simulate the effect of crystallite boundaries. The source images for the simulation will be created for aperture size $k_\alpha = (5.8\,nm)^{-1}$ (see Fig. 3.24(a)). The pixel spacing of the amplitude and phase images was $\Delta x = 0.72\,nm$. The variations in spatial frequency were kept the same as in previous analysis of pure amplitude variations.

The source images, $A(\mathbf{k})$, $S(\mathbf{x})$ and $\phi_{m+c}(\mathbf{x})$, are shown in Fig. 3.24(a), (b) and (c) respectively. In image (b), the amplitude of the transmission function, $S(\mathbf{x})$, was again created using the same process as for Fig. 3.20. Image (c) shows the phase of the transmission function, ϕ_{m+c}. It was created as a combination of the magnetic phase, ϕ_m, and the phase related to crystallite boundaries, ϕ_c. ϕ_m is based on a Néel domain wall with width parameter $A = 40\,nm$. ϕ_c was created by Sobel filtering of Fig. 3.24(b) which was then scaled to create small, grain boundary like variations in the phase. Their sum $\phi_{m+c} = \phi_m + \phi_c$ is shown in Fig. 3.24(c), where the top half of the image was Sobel filtered to show small scale variations of ϕ_{m+c}. The line profile of the phase, ϕ_{m+c}, with the profile of the grain related phase, ϕ_c, is shown in Fig. 3.25.

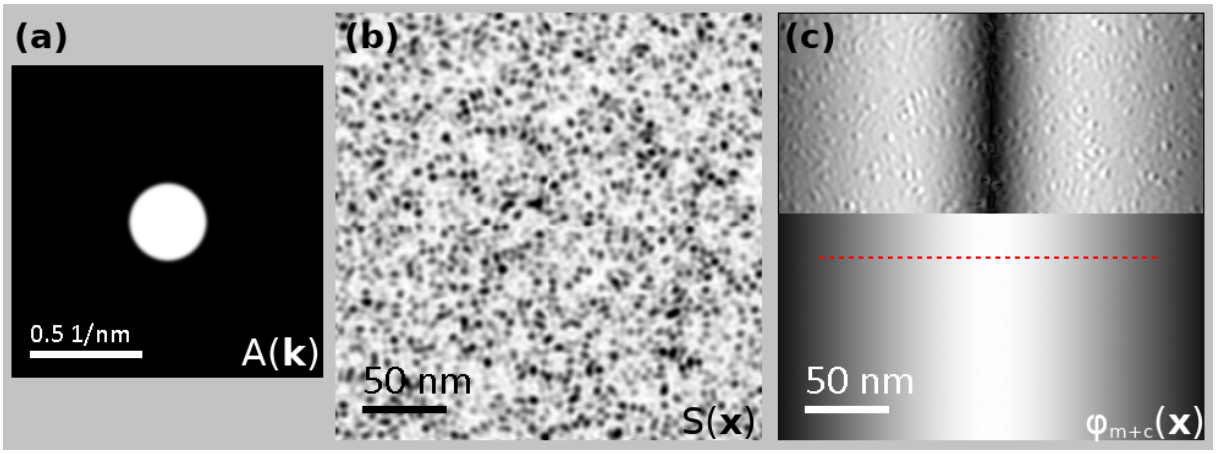

Fig. 3.24 *Source images for polycrystalline sample magnetic imaging simulation with fine phase variation due to crystallite boundaries, (a) image of the aperture function $A(\mathbf{k})$, (b) image of the amplitude $S(\mathbf{x})$ created from white noise by the same approach as in Fig. 3.20, (c) image of the magnetic and crystallite boundary phase $\phi_{m+c}(\mathbf{x})$ corresponding to 40 nm wide 180° Néel domain wall created from Eqs 3.15 and 3.16 and Sobel filtered and scaled image (b) .(b) and (c) are 360x360 pixels, however a larger area was used to allow scanning (the size of the probe image has to fit subset of $S(\mathbf{x})$ and $\phi_m(\mathbf{x})$)*

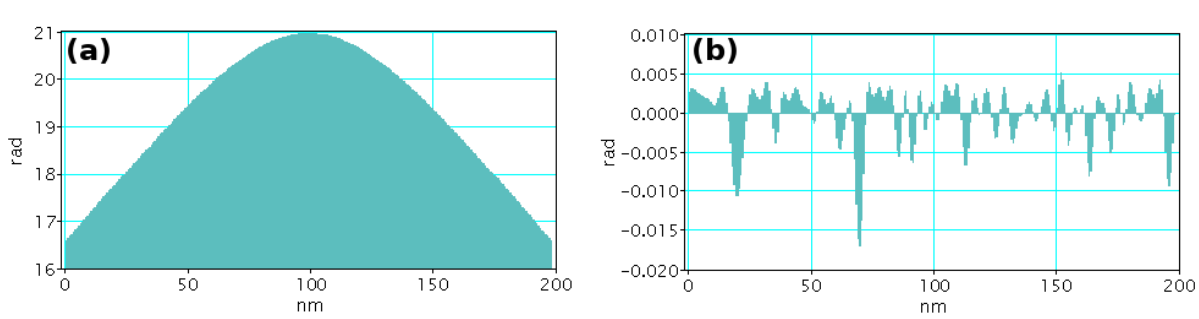

Fig. 3.25 *Comparison line profiles of (a) ϕ_{m+c} and (b) ϕ_c from a line shown in red in Fig. 3.24(c)*

Resulting images showing the y component of the integrated magnetic induction are shown in Fig. 3.26. To show the variation of higher frequency signals, there is a rectangular inset in each image which shows the signal on an equal scale for each of the detection methods. The theoretical gradient of the phase (a) contains higher frequency signals which were added to represent crystallite boundary contrast. The segmented DPC result in image (b), includes the signal due to the variation of the amplitude and phase of the transmission

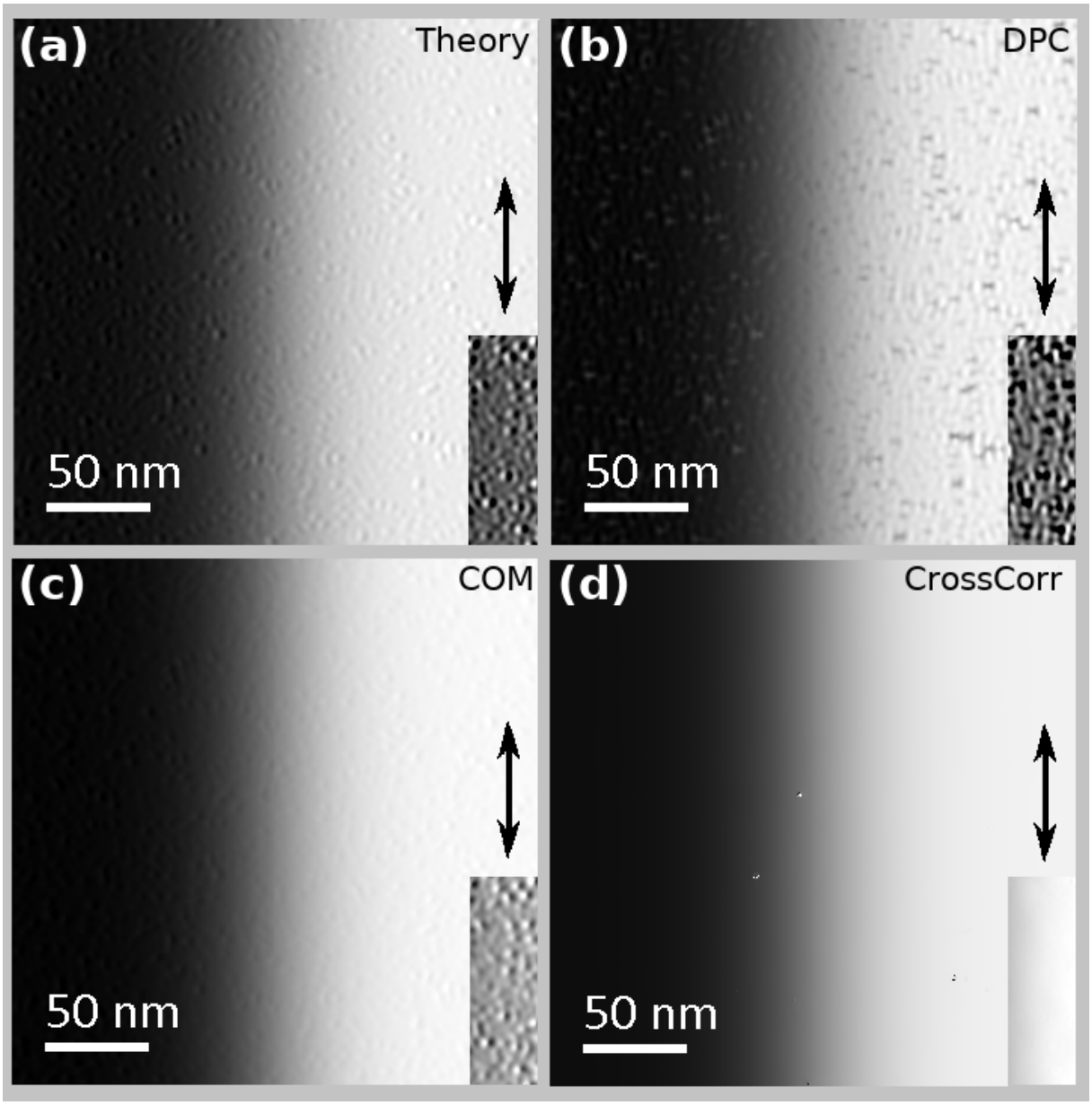

Fig. 3.26 *Polycrystalline sample magnetic imaging simulation result images with fine phase variation due to crystallite boundaries, (a) theoretical B_y profile of the integrated magnetic induction, measured B_y profile by (b) segmented detector, (c) centre of mass detector, (d) cross-correlation detector. Small rectangles show the contrast variations on an equal scale for all images. Arrows show the direction of integrated magnetic induction*

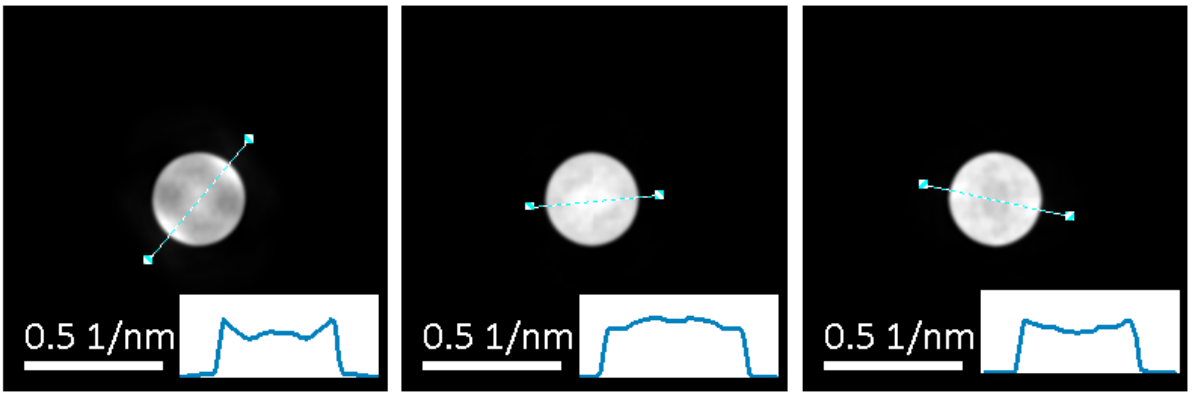

Fig. 3.27 *Example of three disk images g(k) from the simulation in Figs 3.24 and 3.26. Contrast variation was enhanced for visibility, line profiles are plotted to compare the variation to the normalised signal level (this was required due to changes in the amplitude of the transmission function)*

function. The centre of mass result in image (c), shows a similar gradient of the phase as the theoretical profile in (a). Image (d), resulting from the edge cross-correlation method, shows a clear profile representing low spatial frequency information - gradient of the magnetic phase. The high spatial frequency information is filtered. This can be further argued by comparison of the spatial frequencies of the two signals. ϕ_m will be around $k_m = (175\,nm)^{-1}$, given the deflection angle is $12.7\,\mu rad$ for a $20\,nm$ thick permalloy sample. In contrast, the frequency due to the grain boundaries is much higher and it is expected be close to the size of the crystallites 4–6 nm, this difference suggests great potential for this method. Fig. 3.26(d) shows that cross-correlation can be used to filter high spatial frequencies in differential phase contrast, which will be crucial in analysis of the experimental pixelated STEM DPC in the following chapter.

The variations in $g(\mathbf{k})$ shown in Fig. 3.27 look symmetric, however, the effects which we are trying to replicate may be rather small on these scales. This is because the size of the beam, $k_\alpha = (5.8\,nm)^{-1}$, can average some high frequency information, which would be imaged with a finer probe.

3.7 Discussion and conclusions

In this chapter, the theoretical background of differential phase contrast was presented. It was discussed how the current imaging system, based on a segmented detector, operates and what its advantages and limits are. Differential phase contrast was studied using simulations, where a sample model (based on a transmission function) was used to create 4D datasets (two spatial and two reciprocal dimensions). New detection methods were

tested on simulated datasets, which will be the base of study of experimental pixelated DPC datasets in the following chapter. Limits of contrast transfer were discussed for different detection methods. It was shown that in an ideal sample with no amplitude contrast, segmented detection measures DPC precisely. The methods of centre of mass and cross-correlation of edge filtered disks were tested and it was shown that they give a very small offset when imaging structures close to the size of the probe.

It was also shown that segmented algorithm does not respond ideally when the amplitude of the transmission function of the specimen changes - which is a common occurrence in experimental imaging of polycrystalline specimens. Two possible sources of grain contrast in polycrystalline sample imaging were shown in the simulations: amplitude changes (on length-scales of the size of the probe) due to diffraction and phase changes, which are used to represent grain boundaries. The first can be argued from a simple argument of different Bragg conditions due to a random orientation of crystallites. The second effect is not fully understood, however, it was discussed as a possibility and measured for some types of grain boundaries in electron holography [27, 28].

In this chapter, the aim of the simulations was not to try to completely replicate STEM DPC imaging, but to show that imaging the full diffraction pattern (the central disk) can be advantageous in differential phase contrast and that various algorithms can offer a better response to sample related issues than standard segmented imaging. In particular, cross-correlation was shown to be very useful in the separation of high (structural and possibly electrostatic phase) and low frequencies (magnetic phase) in the images for both phase and amplitude of the specimen transmission function. This will be successfully implemented in the experimental analysis in the following chapter.

References

[1] N. Dekkers and H. De Lang, "Differential Phase Contrast in a STEM," *Optik*, vol. 41, no. 4, pp. 452–456, 1974.

[2] J. Chapman, P. Batson, E. Waddell, and R. Ferrier, "The direct determination of magnetic domain wall profiles by Differential Phase Contrast electron microscopy," *Ultramicroscopy*, vol. 3, no. 0, pp. 203–214, 1978. http://www.sciencedirect.com/science/article/pii/S0304399178800278.

[3] J. Chapman, "The investigation of magnetic domain structures in thin foils by electron microscopy," *Journal of Physics D: Applied Physics*, vol. 17, p. 623, 1984.

[4] J. Chapman, I. McFadyen, and S. McVitie, "Modified differential phase contrast Lorentz microscopy for improved imaging of magnetic structures," *Magnetics, IEEE Transactions on*, vol. 26, pp. 1506–1511, sep 1990.

[5] S. McVitie, D. McGrouther, S. McFadzean, D. MacLaren, K. O'Shea, and M. Benitez, "Aberration corrected Lorentz scanning transmission electron microscopy," *Ultramicroscopy*, vol. 152, pp. 57–62, 2015.

[6] B. Freitag, M. Bischoff, H. Mueller, P. Hartel, and H. von Harrach, "Sub-nanometer Resolution in Field-free Imaging using a Titan 80-300 with Lorentz lens and Image Cs-Corrector at 300kV Acceleration Voltage," *Microscopy and Microanalysis*, vol. 15, no. S2, pp. 184–185, 2009.

[7] D. McGrouther, M. J. Benitez Romero, S. McFadzean, and S. McVitie, "Development of aberration corrected differential phase contrast (DPC) STEM," *JEOL News*, vol. 49, 2014.

[8] M. Krajnak, D. McGrouther, D. Maneuski, V. O'Shea, and S. McVitie, "Pixelated detectors and improved efficiency for magnetic imaging in STEM differential phase contrast," *Ultramicroscopy*, vol. 165, pp. 42–50, 2016.

[9] E. W. Weisstein, "Discrete fourier transform," *From MathWorld – A Wolfram Web Resource*, 2002. http://mathworld.wolfram.com/DiscreteFourierTransform.html accessed May 2016.

[10] T. Yamazaki, M. Kawasaki, K. Watanabe, I. Hashimoto, and M. Shiojiri, "Effect of small crystal tilt on atomic-resolution high-angle annular dark field STEM imaging," *Ultramicroscopy*, vol. 92, no. 3, pp. 181–189, 2002.

[11] S. Pennycook and D. Jesson, "High-resolution incoherent imaging of crystals," *Phys. Rev. Lett.*, vol. 64, no. 8, p. 938, 1990.

[12] X. Peirong, E. J. Kirkland, J. Silcox, and R. Keyse, "High-resolution imaging of silicon (111) using a 100 keV STEM," *Ultramicroscopy*, vol. 32, no. 2, pp. 93–102, 1990.

[13] R. Archibald and A. Gelb, "A method to reduce the Gibbs ringing artifact in MRI scans while keeping tissue boundary integrity," *Medical Imaging, IEEE Transactions on*, vol. 21, no. 4, pp. 305–319, 2002.

[14] M. Gai and R. Cancelliere, "An efficient point spread function construction method," *Monthly Notices of the Royal Astronomical Society*, vol. 377, no. 3, pp. 1337–1342, 2007.

References

[15] Martin Shepherd, "Correct Sampling of Diffraction Limited Images," 2012, accessed Jan 2016. http://www.ccatobservatory.org/docs/ccat-technical-memos/DiffractionLimitedSampling_11-12-12.pdf.

[16] M. Mansuripur, "Computation of electron diffraction patterns in Lorentz electron microscopy of thin magnetic films," *Journal of Applied Physics*, vol. 69, pp. 2455–2464, feb 1991.

[17] S. McVitie and J. Chapman, "Measurement of domain wall widths in Permalloy using Differential Phase Contrast imaging in STEM," *Journal of Magnetism and Magnetic Materials*, vol. 83, no. 1, pp. 97–98, 1990.

[18] M. J. Benitez, A. Hrabec, A. P. Mihai, T. A. Moore, G. Burnell, D. McGrouther, C. H. Marrows, and S. McVitie, "Magnetic microscopy and topological stability of homochiral Neel domain walls in a Pt/Co/AlOx trilayer," *Natre Communicatins*, vol. 6, DEC 2015.

[19] Y. Lee, T. Hara, H. Fujita, S. Itoh, and T. Ishigaki, "Automated detection of pulmonary nodules in helical CT images based on an improved template-matching technique," *Medical Imaging, IEEE Transactions on*, vol. 20, no. 7, pp. 595–604, 2001.

[20] J. Lewis, "Fast normalized cross-correlation," in *Vision interface*, vol. 10, pp. 120–123, 1995.

[21] T. A. Scambos, M. J. Dutkiewicz, J. C. Wilson, and R. A. Bindschadler, "Application of image cross-correlation to the measurement of glacier velocity using satellite image data," *Remote Sensing of Environment*, vol. 42, no. 3, pp. 177–186, 1992.

[22] B. Schaffer, W. Grogger, and G. Kothleitner, "Automated spatial drift correction for EFTEM image series," *Ultramicroscopy*, vol. 102, no. 1, pp. 27–36, 2004.

[23] P. Chacón and W. Wriggers, "Multi-resolution contour-based fitting of macromolecular structures," *Journal of molecular biology*, vol. 317, no. 3, pp. 375–384, 2002.

[24] S.-M. Lai, X. Li, and W. Biscof, "On techniques for detecting circumscribed masses in mammograms," *Medical Imaging, IEEE Transactions on*, vol. 8, no. 4, pp. 377–386, 1989.

[25] L. G. Brown, "A survey of image registration techniques," *ACM computing surveys (CSUR)*, vol. 24, no. 4, pp. 325–376, 1992.

[26] V. Hou, "Cross Correlate plugin." http://donation.tugraz.at/dm/source_codes/144, accessed February 2015.

[27] V. Ravikumar, R. Rodrigues, and V. P. Dravid, "Direct imaging of spatially varying potential and charge across internal interfaces in solids," *Physical review letters*, vol. 75, no. 22, p. 4063, 1995.

[28] V. Ravikumar, R. P. Rodrigues, and V. P. Dravid, "Space-Charge Distribution across Internal Interfaces in Electroceramics Using Electron Holography: I, Pristine Grain Boundaries," *Journal of the American Ceramic Society*, vol. 80, no. 5, pp. 1117–1130, 1997.

CHAPTER 4

Pixelated Detectors for Differential Phase Contrast

Introduction

In this chapter, we will study experimental pixelated detection in differential phase contrast. The principle will be first demonstrated on a dataset acquired by a CCD camera. However, due to the limits of CCD technology, a direct electron detector (Medipix3) will be later utilised for this work. Electron beam position registration methods introduced in the previous chapter will be used in the analysis of the deflection of the central disk in STEM imaging. Methods of segmented detection, centre of mass, thresholded centre of mass and edge cross-correlation will be used and compared. A measurement of magnetic domain wall width will be provided and compared to that for segmented DPC. It will be shown that this approach provides clean magnetic DPC imaging in the presence of polycrystals in STEM microscopy.

4.1 New approach to STEM detection

Traditionally, STEM detection is provided by solid state detectors integrating different scattering signals in reciprocal space, which leads to the loss of potentially useful information. The recording of a full image of the scattered signal for each beam position should allow for the analysis of multiple types of signals after the experiment. This can be already provided by CCD cameras, however such an approach is very impractical mainly due to their acquisition speed. Datasets need to be acquired with sufficient speed to avoid problems with sample drift and the general stability of the environment. Recently, pixelated

direct electron detectors have allowed for more practical acquisition of 4D datasets in STEM. Such a dataset contains 2D pixelated image of diffraction pattern for each point of a 2D scan - therefore two spatial and two reciprocal dimensions. These datasets can be very large in size but the depth of the information provided can allow for advanced types of analysis that are not accessible in standard STEM detection [1–5].

There are a number of direct pixelated detectors available at the moment, which are able to provide sufficient acquisition speeds. Generally, the ideal STEM pixelated camera would provide sufficient acquisition speed, dynamic range and number of pixels. The K2 camera from Gatan Inc. [6] provides sufficient speeds, however its cost is restrictive. It was designed as a fast TEM camera, therefore its resolution (16/14 Mpix) can produce very large datasets. This means the detector and readout hardware have to be optimised for huge data throughput. Other companies and research groups are working on fast smaller sized cameras, which should be much more practical in STEM microscopy [7–9]. The Medipix2 detector was tested at The University of Glasgow [10] as a promising practical and affordable detector for STEM microscopy. The Medipix detector family is developed by a CERN consortium, which also includes members of Particle Physics Experimental group in the School of Physics and Astronomy at The University of Glasgow. The newest available Medipix detector (at the moment of writing), Medipix3 [5, 11, 12], was used to capture STEM DPC signals for magnetic materials in this chapter. However, first introductory work on a CCD camera is presented to prove the versatility and principle of pixelated detection in STEM DPC.

A CCD camera was already used as a DPC detector in [13], however in that paper only an equivalent quadrant detector approach was studied. In this work it will be shown how imaging of the central diffraction disk in STEM using a pixelated camera can be analysed by advanced algorithms and pixelated DPC realised with great potential for nanomagnetic imaging.

4.2 CCD camera data acquisition

In this section, a $20\,nm$ thick permalloy sample doped with 5% platinum will be studied. This material was sputtered on the top of a Si_3N_4 support TEM membrane at The University of Leeds by Dr Aleš Hrabec. Permalloy is a soft ferromagnet, which has a very large permeability, low coercivity and small magnetic anisotropy. This material supports formation of domain walls (at this thickness the walls are Néel type [14]) and also vortices and other structures in confined geometries.

Fig. 4.1 shows an image of a 180° Néel domain wall acquired by segmented DPC in $20\,nm$ thick $PyPt$, which was already shown in previous chapters. The beam convergence

semi-angle was $\alpha = 537\,\mu rad$, which corresponds to a maximum spatial frequency of $k_\alpha = (5\,nm)^{-1}$. The pixel spacing was $2.5\,nm$ and the camera length was $300\,cm$. The same field of view was imaged by a CCD camera (Fig. 4.2), however pixel spacing was doubled to $5\,nm$, because of the restricted size of the 4D dataset. For the same sampling conditions, the field of view would be too small for the wall width analysis (the magnetic domain wall would cover most of the image).

The dataset in Fig. 4.2 was acquired by a Gatan Orius CCD camera with 11MPix resolution (4008x2672 pixels) and spectrum imaging plugin in Gatan Digital Micrograph® , which also allows scanning diffraction experiments. The camera is capable of reading out 14 frames per second, which is a rather limiting factor in the STEM imaging. The speed of acquisition and the size of the generated dataset practically limited the number of probe positions to 100x100. Dwell time per probe position was $50\,ms$, which led to $12\,min$ overall acquisition time. By imaging of the whole central disk for all probe positions, the bright field image can simply be generated as a sum of each frame. The reconstructed bright field image is shown in Fig. 4.2(a), with an example of two disk images in (b) and (c). The CCD camera acquired dataset was binned 4x to shrink its size. The disk was $\sim 235\,pix$ in radius after binning. Dimensions of resulting probe images were 650x490 pixels and the dataset was $4\,GB$.

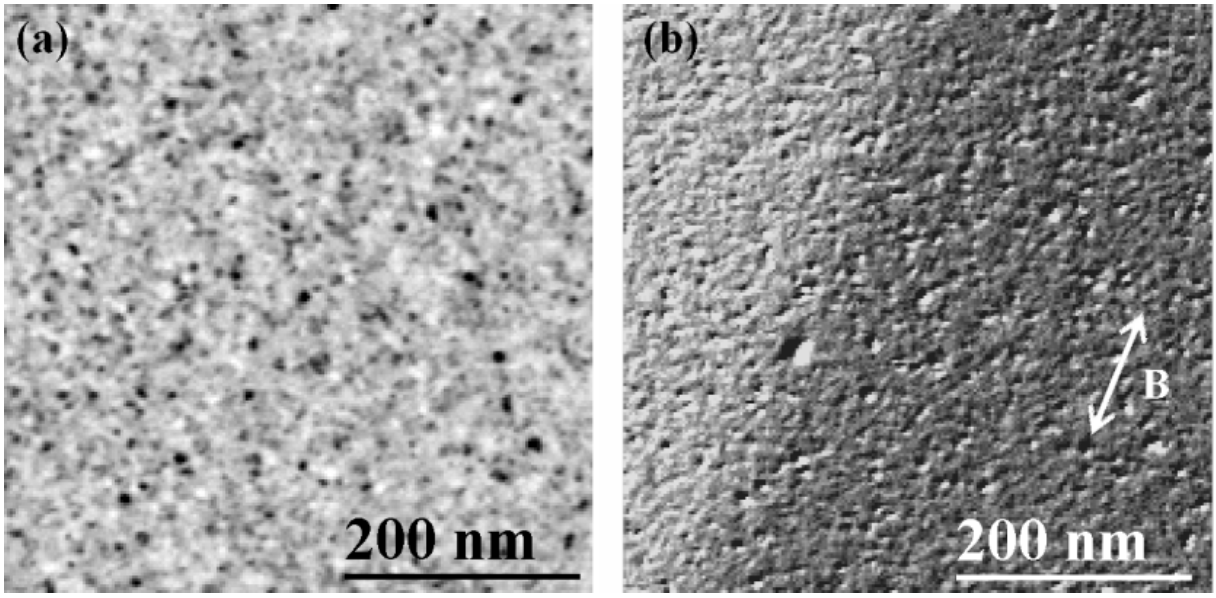

Fig. 4.1 *Results of standard segmented DPC imaging of* $20\,nm$ *thick PyPt: (a) bright field image generating by a sum of all quadrant signal, (b) integrated magnetic induction (with an arrow for directionality)*

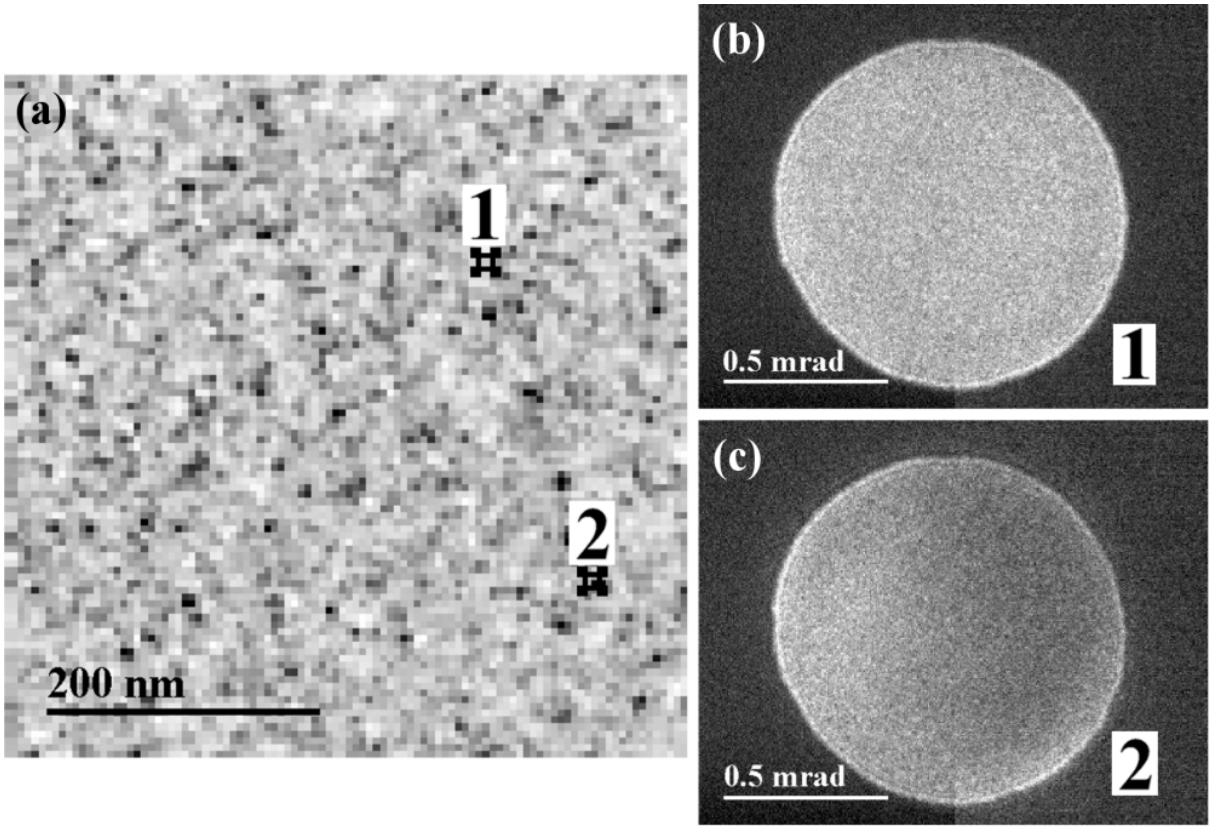

Fig. 4.2 *(a) reconstruction of bright field image from 100x100 images of central beam disk with two examples of disk in (b) and (c)*

4.2.1 CCD camera data analysis

Recording the full diffraction pattern for each probe position is advantageous for segmented detection because additional filtering and novel types of analysis can be applied to the data, as was shown for simulated datasets in the previous chapter. It will be shown how the experimental data can be analysed by the algorithms introduced in Sec. 3.4.2, that was: centre of mass, thresholded centre of mass and cross-correlation edge registration. This will be compared to a dataset acquired by the current segmented DPC system under the same imaging conditions.

It will be assumed that the signal variation within the diffraction disk is not due to changes of the in plane magnetic induction, this assumption is satisfied by simulations introduced in the previous chapter. The scripting language of Gatan Digital Micrograph® was used for all CCD camera data analysis.

Centre of mass analysis

One of the simplest methods to find the position of the circular disk in a pixelated image, $g(\mathbf{k})$, is the centre of mass algorithm introduced in Eq. 3.17.

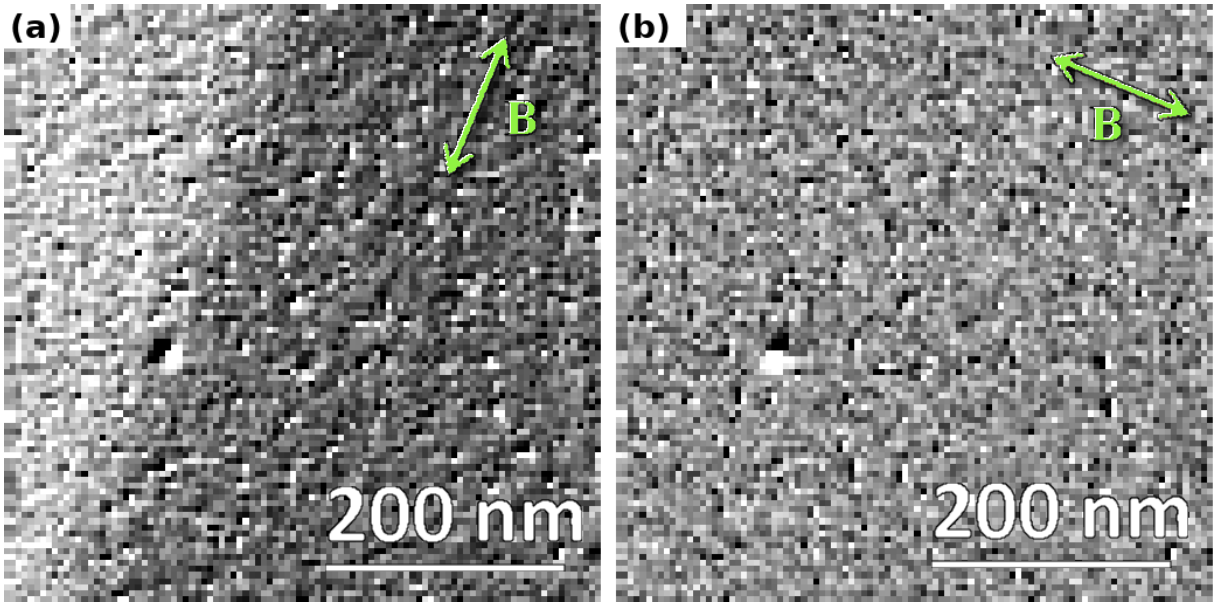

Fig. 4.3 *2 orthogonal components of integrated magnetic induction generated by centre of mass disk deflection analysis for each probe position, (a) is signal parallel to the magnetic domain wall, (b) is perpendicular*

This algorithm has an advantage over standard detection in that the deflection angle of the beam, β_L, and beam convergence semi-angle, α, do not need to fulfil the condition, $\beta_L < \alpha/10$, due to small angle approximation which was applied to the arc of the diffraction disk as explained in Sec. 3.3.1. However, a problematic factor is that if the beam profile is not homogeneous (due to diffraction contrast from crystallites), the centre of mass algorithm will give inaccurate position of the beam, similar to the quadrant detector in such a situation. This is shown in Fig. 4.3, which is clearly hampered by diffraction contrast and there is no noticeable improvement in comparison to segmented detection, illustrated in Fig. 4.1(b).

This algorithm was suggested as a detection method for atomic electric fields in [15], where no or a very tiny shift of the diffraction disk is expected. However, in our case the algorithm needs to be able to suppress high spatial frequencies. The simulation in Sec. 3.5 shows, that the centre of mass algorithm does not filter diffraction like high spatial frequency contrast in DPC STEM, therefore, it is an expected outcome.

Thresholded centre of mass analysis

The threshold can be applied before the application of the centre of mass algorithm, which will in an ideal case create a top hat function and provide enhanced beam deflection analysis. Any signal variations within the disk can be suppressed, as an equal value is given to all pixels above the threshold. The threshold function should adapt the level of the signal in the central disk due to its the variation, which is apparent from the bright

field image in Fig. 4.2(a). The level of threshold can be set as the FWHM of the diffraction disk, which can be estimated from the bright field signal. This approach will work if the intensity profile is close to a top hat function as in Fig. 4.4, but for a very inhomogeneous profile, like image (b), this will not create a top hat function. An example can also be given for whole disk images, where the result of the right threshold conditions is shown in Figs 4.5(b) and (d). However, if the threshold fails to create a top hat function like in Figs 4.5(c) and (e), the measurement of the disk deflection will be inaccurate. This failure is due to the strong crystallite contrast in the thin film.

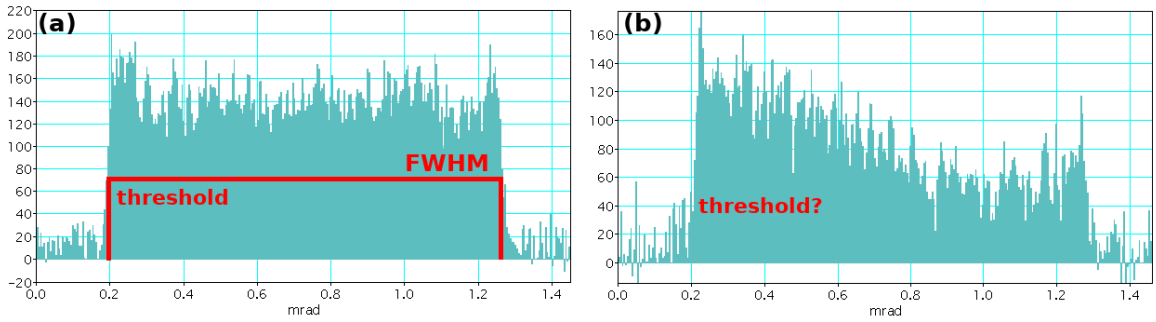

Fig. 4.4 *Threshold in COM algorithm, (a) noisy top hat like profile with an accurate result, (b) inhomogeneous profile with problematic threshold calculation*

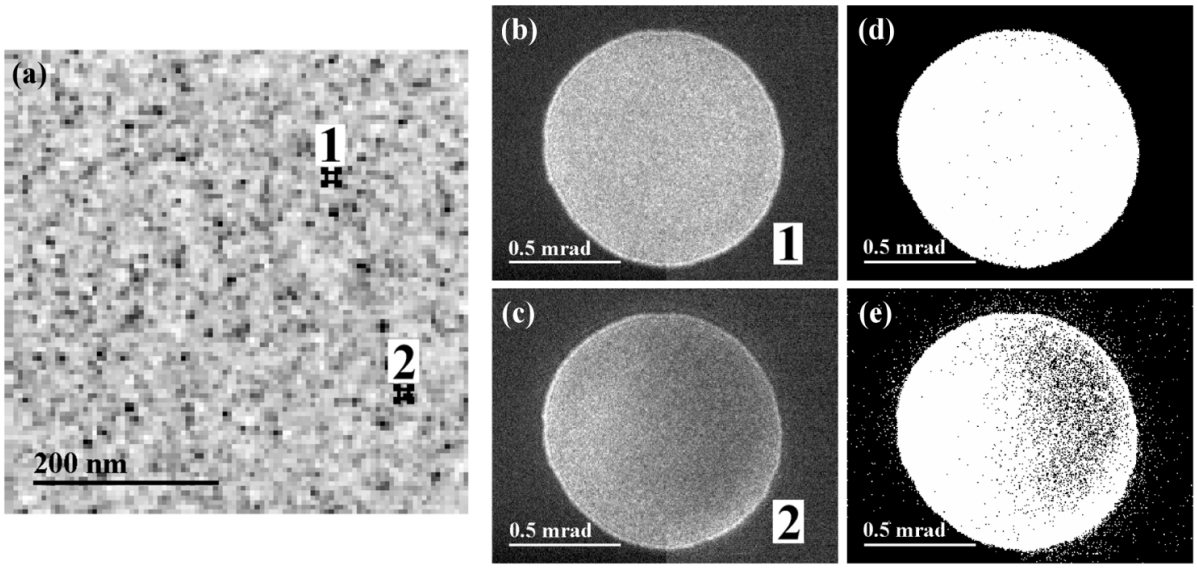

Fig. 4.5 *Example of threshold processing on 2 disks already shown in Fig. 4.2, (a) reconstructed bright field image, (b) and (c) example of two disks corresponding to highlighted probe positions, (d) and (e) example of successful threshold and failed threshold processing due to a strong crystallite scattering*

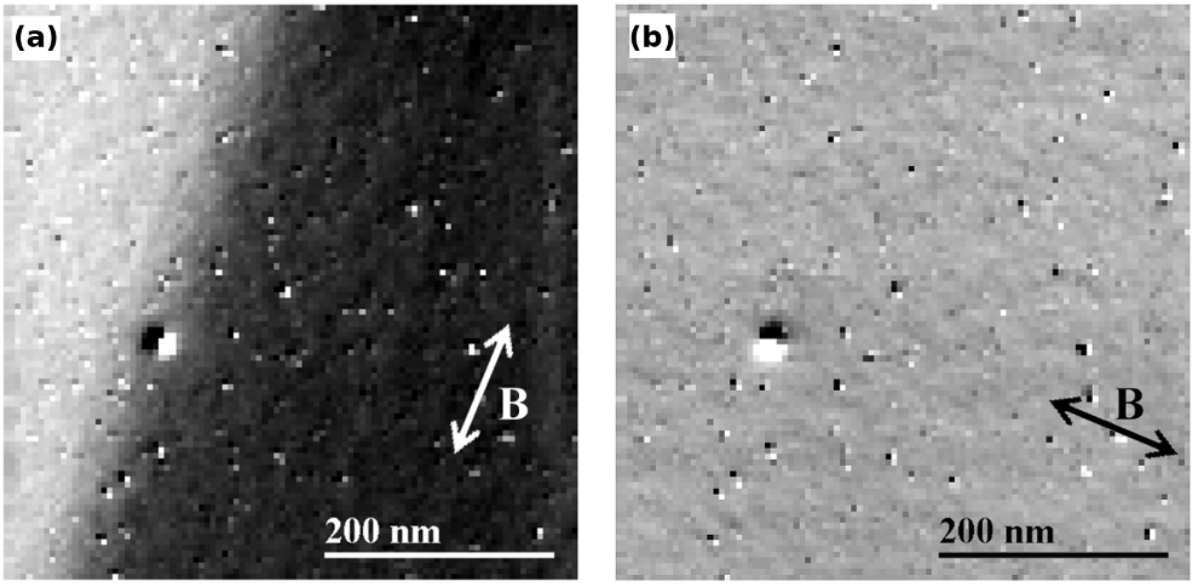

Fig. 4.6 *Result of thresholded centre of the mass algorithm, (a) and (b) two orthogonal images of integrated magnetic induction, with the field direction shown by double headed arrows. Note areas where the algorithm failed due to the strong crystallite contrast. Images were corrected for scanning errors by a method shown in Sec. 4.2.4*

The result of thresholded centre of mass registration is shown in Figs 4.6(a) and (b). The points for which the algorithm failed are clearly visible. However, a thresholded centre of the mass approach provides a considerable improvement in the filtering of high frequency signal variations from crystallites and the variation of the integrated magnetic induction within the domain wall can be seen as shading in the image in Fig. 4.6(a). A rotation matrix was applied to the resulting images to align the integrated induction components parallel (a) and perpendicular (b) to the magnetic domain wall.

There are other types of threshold, however if the signal within the disk is strongly inhomogeneous, the algorithm will be still inaccurate. However, there is a better approach which can realise beam deflection analysis more accurately and which will be introduced in the following section.

4.2.2 Cross-correlation disk edge deflection analysis

A computer vision algorithm, cross-correlation of edge filtered images, will be discussed in this section. The algorithm was successfully introduced in the previous chapter (Sec. 3.4.2), where it was used to separate high and low spatial frequencies in simulations of DPC. It was shown to be reliable for deflection detection and a potential candidate for an ideal algorithm to be used with experimental pixelated DPC, where sensitivity to the smallest deflection of the beam in **k**-space is crucial.

Fig. 4.7 shows an example of a CCD camera image of the central diffraction disk showing inhomogeneous intensity within the disk in 20 nm thick $PyPt$. In this image we see that the edge of the beam is rather sharp and does not vary as much as the signal within the disk. This suggests that the edge of the beam could be used with a better precision to find the position of the disk than using the signal from the disk as a whole (assuming the edge shape has not changed). Focusing only on the position of the edge of the beam will enable, as discussed in the case of an annular DPC detection in [16] and in Sec. 3.3.2, separation of low and high spatial frequencies. However, in the case of the cross-correlation analysis, it will be shown that it is possible to almost completely separate the two by the cross-correlation algorithm.

The cross-correlation algorithm can be used in a similar manner as for the registration of simulation images in the previous chapter, albeit with one change - the image of the aperture needs to be acquired in free space to get the best edge profile. Alternatively, an idealised beam image can be generated from the dataset itself, an example of which is

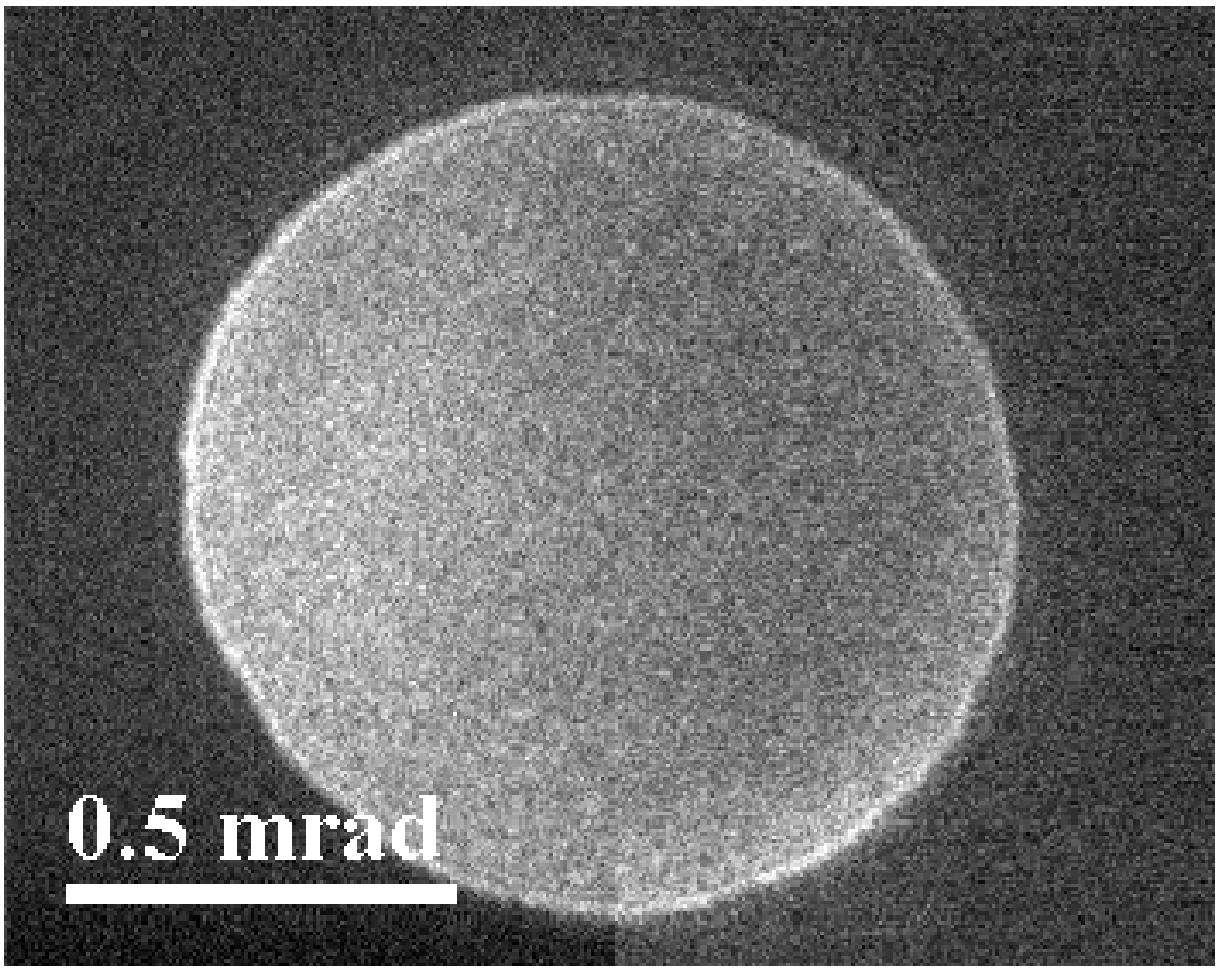

Fig. 4.7 *Example of the central diffraction disk with inhomogeneous intensity from* 20 *nm thick PyPt. Note the level of noise from the CCD camera. The edge of the beam is consistent and can be extracted by edge detection algorithms.*

shown in Fig. 4.8. The disk should be extracted from an area of the sample which is either a single domain or non-magnetic. This should minimise any distortions in the extracted edge. By extracting a generally flat disk image (a), and an application of a threshold, a top hat disk profile can be created (b). If there are any irregularities in the top hat profile of the beam, e.g. white or black noise pixels, they can be filtered in *ImageJ* processing software by *Remove Outliers* function (c). Idealised edge generation can be also performed on an upsampled image which achieves a more precise profile (will be used for the analysis of Medipix3 dataset later in the chapter). The top hat function is smoothed to match the spread of the edge of the aperture/beam to produce a more accurate result (d). This will provide a higher correlation value because an idealised edge will compare like with like, and minimise the chance of false deflection detection if the profile of the beam changes slightly. The edge of the disk is at last generated by a Sobel algorithm, which now does not contain additional signal variations (e).

As a next step, the idealised edge is cross-correlated to all the edge filtered images of the central diffraction disk in the dataset. Cross-correlation is achieved by standard normalised phase-correlation algorithm [17], which is implemented in Digital Micrograph® software.

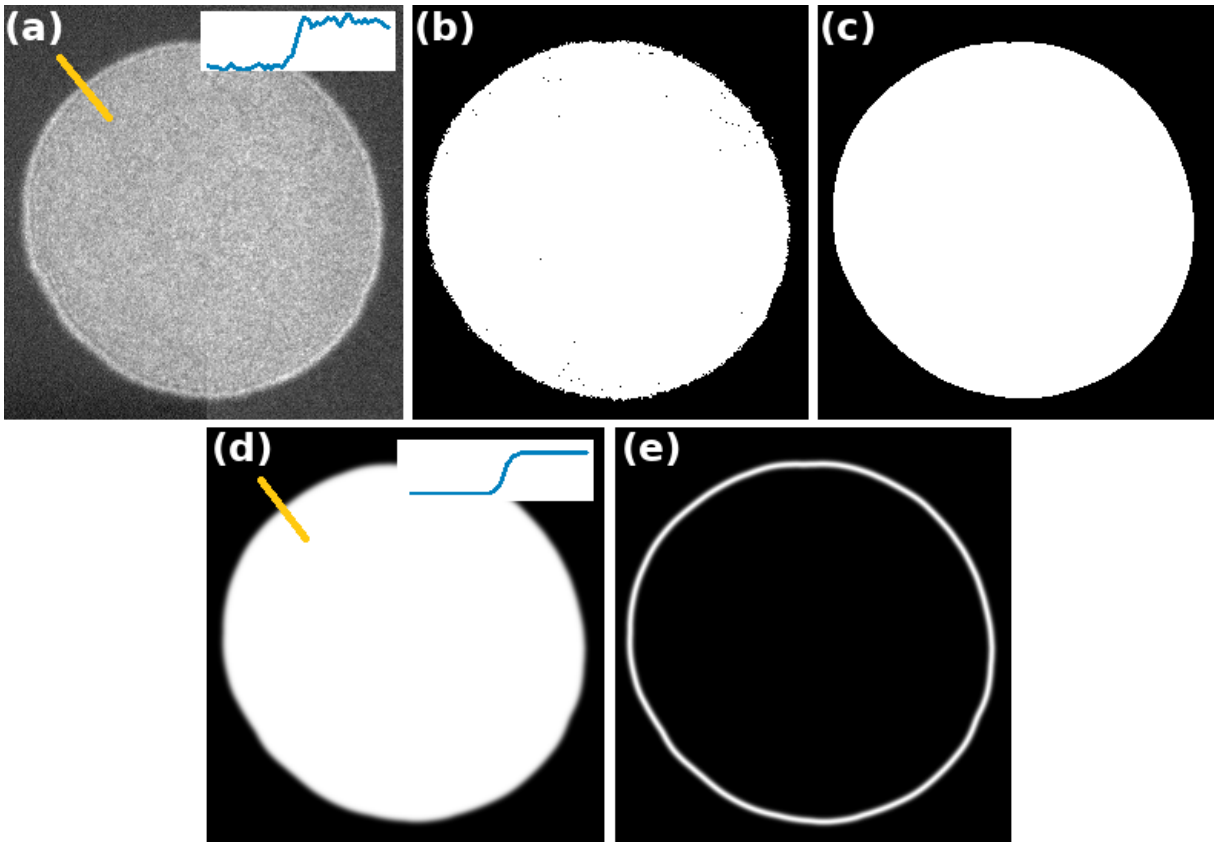

Fig. 4.8 *Schematic of idealised edge creation, (a) diffraction disk with relatively constant profile, (b) result of threshold, (c) noise removal, (d) smoothing to match original beam edge dispersion, (e) edge generated by Sobel algorithm*

For 100x100 probe positions 10000 cross-correlations and edge generations need to be computed. An example of the processing is shown in Fig. 4.9, where (a) is an example diffraction disk image, (b) is the image smoothed by a Gaussian, G_σ, function, (c) is after subsequent application of a Sobel filter, (d) is an idealised edge from Fig. 4.8 and finally (e) is the correlation pattern with the profile showing the maximum. The position of the maximum represents the shift between the two cross-correlated edge images. The edge image does not need to be centred because the cross-correlation deflection measurement is always relative to the position of the idealised disk.

This type of processing was used in TEM by B. Schaffer in [18] where it provided sample drift correction for energy filtered EFTEM images. The problematic factor in that work was the precision of the Sobel algorithm, which could return an improper result of the cross-correlation. In that paper the precision was enhanced by a statistical approach where each of the EFTEM images was correlated to all the others. This is easy if the number of images is low. In the case of pixelated STEM DPC, this is not the case (the number of involved images is larger than 10000). It is also worth noting that we are correlating essentially the same image, whereas the contrast in the datasets in [18] varied more substantially.

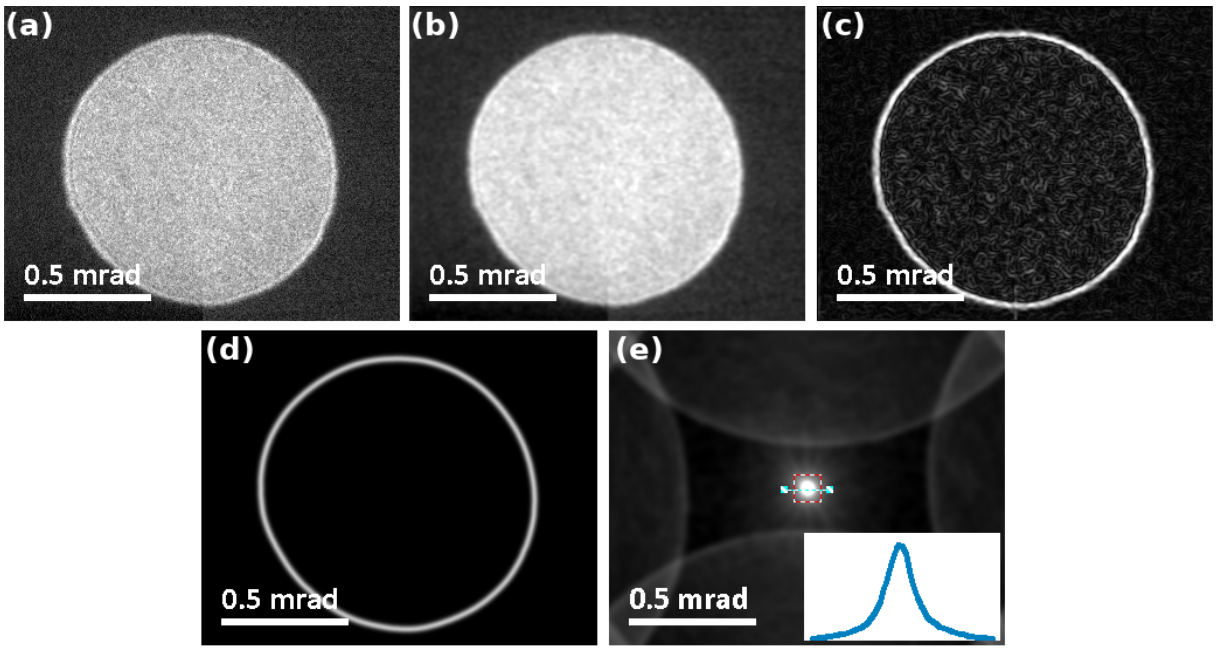

Fig. 4.9 *Example of cross-correlation edge processing for a single probe position, (a) CCD image of central diffraction disk, (b) result of smoothing of (a) by G_σ with $\sigma = 3px$, (c) Sobel algorithm applied to (b), (d) idealised edge, (e) correlation pattern of (c) and (d) with a profile of the maximum*

Smoothing of the image is essential before cross-correlation and edge generation, as it suppresses high spatial frequencies which can cause inaccurate registration in such data [19–21]. Image A can be smoothed by convoluting with G_σ, symmetric 2D Gaussian:

$$A_{smoothed} = A * G_\sigma, \tag{4.1}$$

where $*$ denotes convolution:

$$A * B = FFT^{-1}[FFT(A)FFT(B)],$$

and G_σ is a 2D symmetric Gaussian function:

$$G_\sigma = \frac{1}{\sigma\sqrt{2\pi}} \exp\left(\frac{\mathbf{x}^2}{2\sigma^2}\right). \tag{4.2}$$

In this analysis, smoothing and Sobel algorithms will be used. However, greater precision can be achieved by combining the two algorithms together, which will be demonstrated in the analysis of a Medipix3 direct electron detector dataset in Sec. 4.4. The choice of σ is not crucial, however if exceedingly large value is used then BF variations will be enhanced in DPC images. Similarly, σ chosen too small can produce inaccurate disk registration due to shot noise in pixelated images.

A problematic factor is that cross-correlation only gives precision down to an integer pixel value but shifts of the probe can be less than a pixel depending on the strength of in-plane magnetic induction; the sample thickness; the convergence semi-angle of the probe; the camera length of the projector system (which defines the size of the disk); and the electron energy. Subpixel precision can be achieved by quadratic interpolation of the pixel values surrounding the maximum of the correlation pattern [18, 22–25]. The following equations were used to calculate subpixel position for which Fig. 4.10 shows the position of particular variables in the image:

$$\delta_x = \frac{a_x - b_x}{2\,(a_x + b_x - 2\,Max)}, \tag{4.3}$$

$$\delta_y = \frac{a_y - b_y}{2\,(a_y + b_y - 2\,Max)}, \tag{4.4}$$

which are based on a three point interpolation of a parabola and are a standard approach to peak location in relatively smooth cross-correlation pattern images [25, 26].

There is an alternative approach to subpixel image registration suggested in [18]. Images can be up-sampled before processing, however this is computationally demanding. If only first decimal place accuracy of the registration was considered, it would be necessary to process a 100x larger dataset with an additional cost associated with processing larger

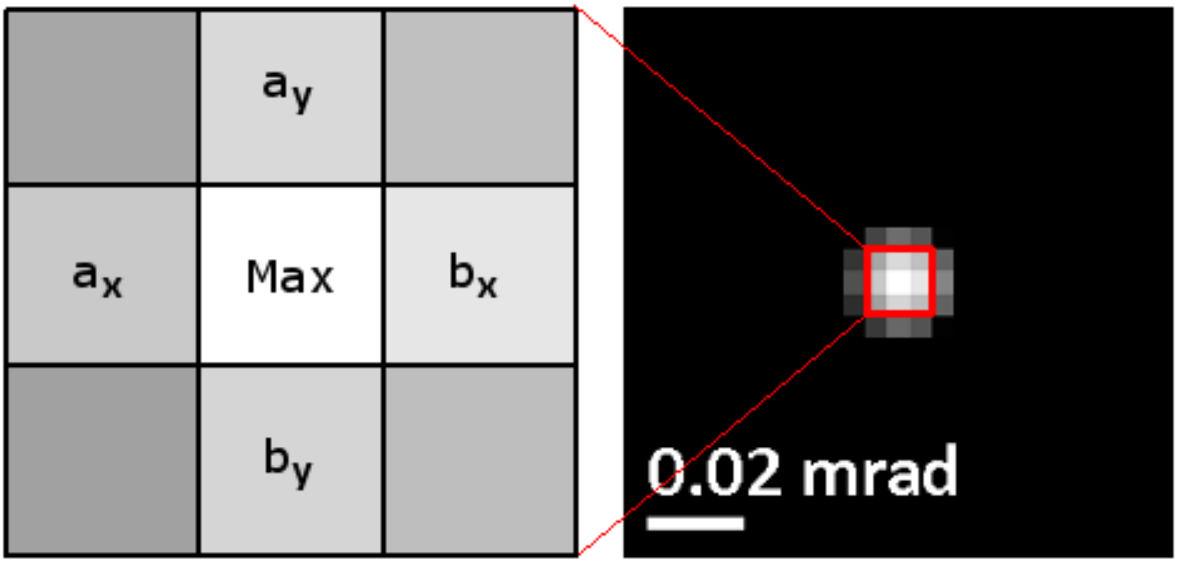

Fig. 4.10 *Schematic of pixel position used for subpixel maximum position calculation in Eqs 4.3 and 4.4. Image (b) is a subset of Fig. 4.9(e), highlighted by the red box. Intensity was scaled to show intensity variation of the surrounding pixels of the maximum*

images (FFT/cross-correlation). In [18] this was required to achieve better resolution in EFTEM images that were more varying than shifts of edge patterns in DPC STEM.

The resulting integrated magnetic induction images created by the cross-correlation method can be seen in Fig. 4.11. The edge was generated by smoothing with a Gaussian with $\sigma = 1$ (G_1) and standard Sobel 3x3 kernels. These images are almost without any crystalline contrast. The variation of the registered deflection within a single domain has standard deviation of $0.1\,px$, which will be thoroughly discussed in Sec. 4.2.5. This result shows that cross-correlation edge registration can separate high spatial frequency signals (grain contrast) from low spatial frequency contrast (magnetic induction/phase gradient) in pixelated DPC STEM. Images were corrected for the descan by method shown in Sec. 4.2.4.

4.2.3 Bivariate analysis of 2D vector field

The enhanced integrated magnetic induction images can be analysed in a novel way, due to low levels of non-magnetic signal. A bivariate histogram for two orthogonal components of the integrated magnetic induction will show the distribution of an integrated magnetic induction vector. It is also a scatter plot of all the positions where the beam was detected in the scan. Hence, it can be also used in scan correction analysis (which is shown in the following section), however, here we will demonstrate the concept on already corrected images. If imaging of a two domain state with a single domain wall between them is considered, we expect the beam to form a pattern of two spots with a line between them,

similar to a low angle diffraction experiment[1]. An example is generated from Fig. 4.11 and shown in Fig. 4.12(a). The analysis also demonstrates the option to colour code the image, so the magnetic vector distribution can be correlated to real space image, which is shown in Figs 4.12(b) and (c). Bivariate histograms can show beam deflections, β_L, which are equivalent to the beam positions on the detector or the integrated magnetic induction distribution (a 90° clockwise rotation of the deflection due to the Lorentz force).

[1]this will be not different from a contrast formed by stripe domains, an example of stripe contrast domain can be found in [27]

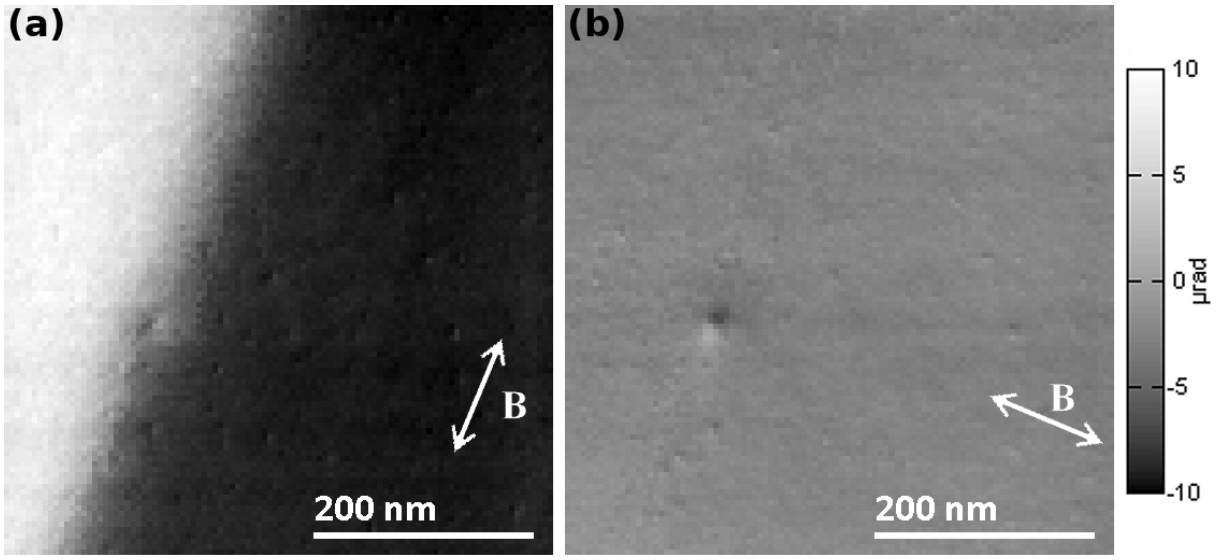

Fig. 4.11 *Result of cross-correlation edge shift algorithm, (a) and (b) two orthogonal images of integrated magnetic induction, with the field direction shown by double headed arrows. Note substantial quality of the analysis, where only a very few spots show additional contrast. Images were corrected for scanning errors by a method shown in Sec. 4.2.4*

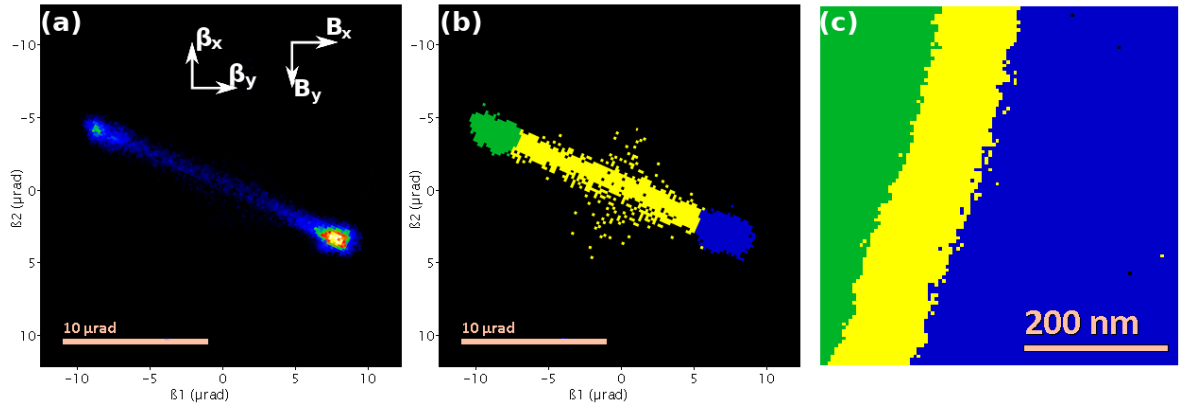

Fig. 4.12 *(a) bivariate analysis of image in Fig. 4.11, (b) the same image colour coded, (c) colour coded spatial distribution of magnetic induction from bivariate analysis in (b)*

4.2.4 Scanning correction

An important limit is the precision of the scanning of the STEM microscope. In an ideal microscope, the STEM disk would not change its position in the detector plane during the scan. However, in a real system, the stability of the electron beam depends on the quality of the electron-optical system of the microscope and its alignment. If the scanning is not ideal, it can appear as if there is an additional deflection in DPC STEM. One of the ways to minimise this is to use post specimen lenses to achieve a static beam while scanning at low magnification.Another option is to make a measurement of empty space without the sample in the rod. This allows for correction of any additional scanning effects and will be very important in Chap. 6, where uncorrected scanning effects are very strong and limit the experiment. Small scanning issues can be also corrected by fitting a linear ramp to a supposedly flat signal from a nonmagnetic area of the sample or a single magnetic domain (assuming no change in thickness), for which the deflection of the beam is constant.

The integrated magnetic induction images in Fig. 4.11 were corrected for microscope scanning issues. The results are shown in Fig. 4.13, where the two images of the integrated

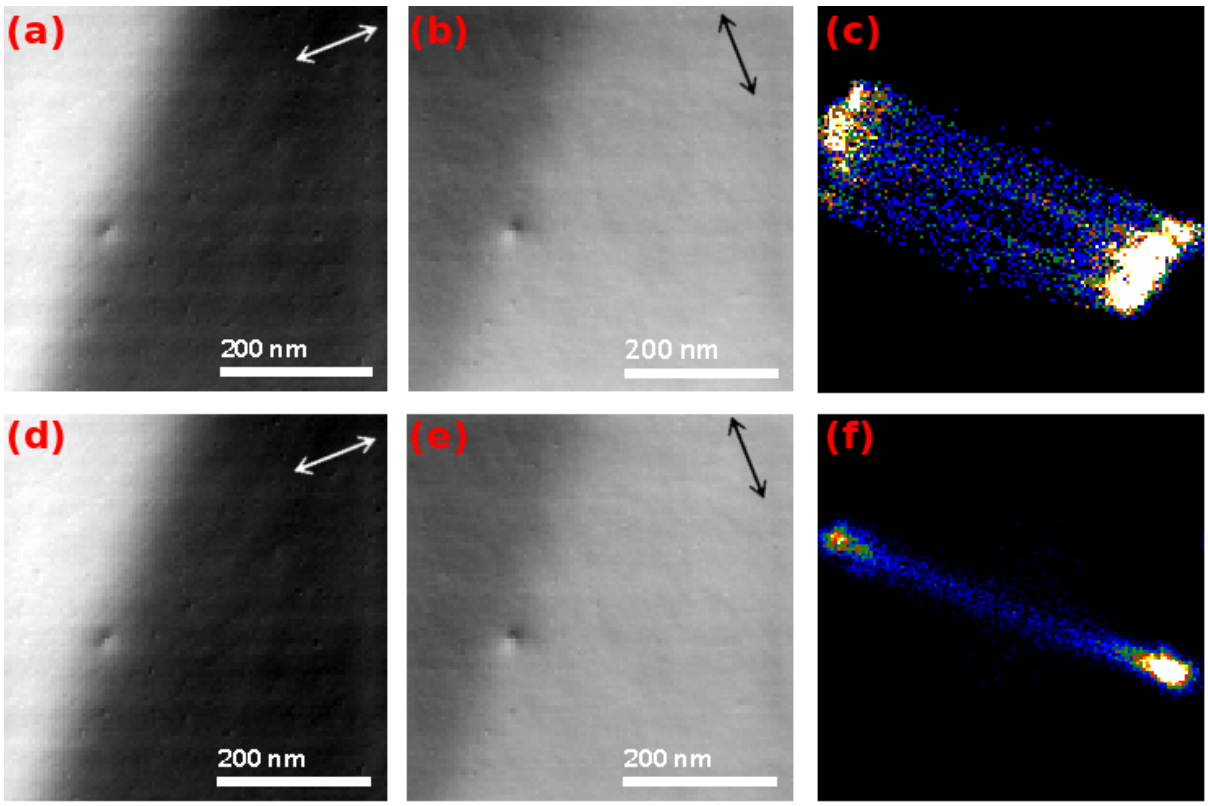

Fig. 4.13 *Bivariate histogram analysis and descan correction, (a) and (b) images which are a result of CrossCorr algorithm, (c) scatter plot created from (a) and (b), (d) and (e) descan corrected images, (f) scatter plot showing no descan issues*

magnetic induction, (a) and (b), are shown without any component rotation[2]. Image (c) is the bivariate histogram (introduced in the previous section) created from (a) and (b). This shows the vector scatter configuration of the domain wall image and it was already introduced in [28]. It also shows the position of the beam on the detector, which can be used for a discussion of accuracy of the measurements. A plane fitting DM script (provided by Dr Donald MacLaren) was used here to remove a scanning plane from images in Figs 4.13(a) and (b), the result of which is shown in Figs 4.13(d) and (e). If scatter plots before and after the correction are compared, i.e. Figs 4.13(c) and (f) respectively, the effect of the correction is clear and image (f) now contains two spots corresponding to the signal from magnetic domains and a line connecting them due to the variation of the field within the magnetic domain wall.

4.2.5 CCD camera result analysis and discussion

In this section we will compare magnetic imaging generated by 3 different DPC methods: segmented DPC, thresholded centre of mass and cross-correlation registration[3]. These results, together with their line profiles are shown in Fig. 4.14. Centre of mass without threshold was dismissed for the comparison, as it did not provide any improvement to the imaging of polycrystalline magnetic materials for this sample (it is an equivalent of

[2] the orientation of the two components of integrated magnetic induction can be changed by using a standard rotational matrix

[3] thresholded centre of mass and cross-correlation registration were corrected for scanning issues, the level of noise in segmented detection does not allow the corrections, a direct comparison of bivariate histogram showing the level of noise in both methods is shown in Fig. 4.15

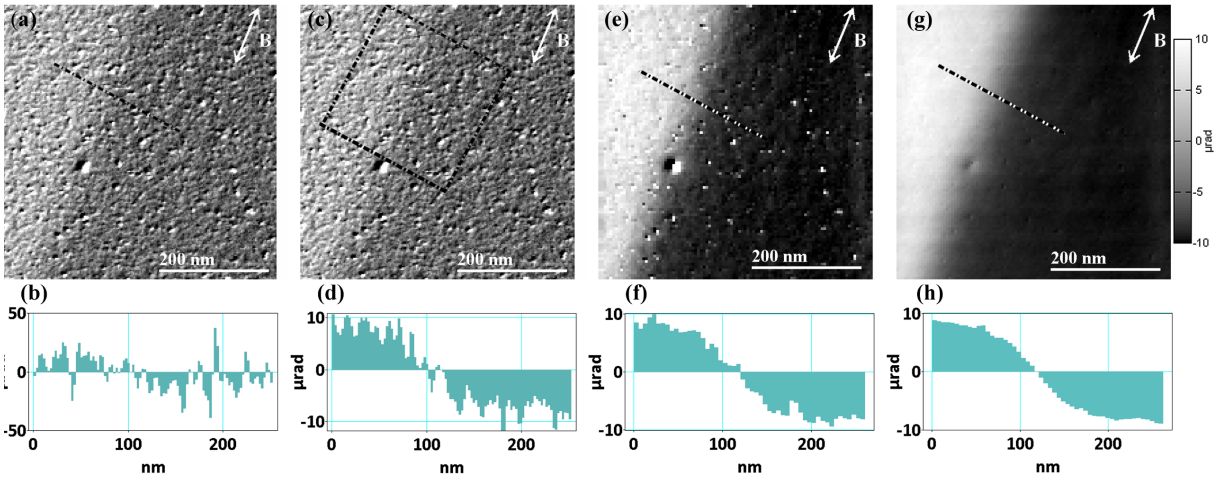

Fig. 4.14 *Comparison of digitally corrected magnetic induction of* 180° *domain wall. (a),(b) standard DPC image and its profile, (c),(d) same image with* 80 *line average profile, (e),(f) Centre of mass result with its profile, (g),(h) Cross-correlation result with its profile. Quantification of the grey scale of the images is shown in the right of image (g).*

segmented DPC). It can be safely assumed this will be the case for all polycrystalline samples with grains sized similarly to the size of the focused probe.

Fig. 4.14(a) shows a rather noisy image acquired using the segmented DPC detector In this image magnetic contrast is visible, although if a single line profile is plotted, as is in (b), the profile is almost obscured by the crystallite profile variations. This image can be averaged over a larger area, shown in Figs 4.14(c) and (d), but this compromised the spatial resolution in one direction (so it is only suitable for 1D object). The profile in (d) is improved, but it still contains noise due to crystallite contrast.

The thresholded centre of mass result in Fig. 4.14(e) shows a large reduction in non-magnetic signal variations, however some areas of the sample were still affected by diffraction contrast. A single line profile in (f) shows substantial improvement and outperforms even the averaged segmented DPC line profile in (d).

Finally, a cross-correlation result using edge filtered disks is shown in Fig. 4.14(g). This type of processing achieves almost full separation of the magnetic and non-magnetic diffraction contrast. A single line profile in (h) contains very little noise and proves that pixelated DPC can be used for quantitative imaging of magnetic materials in STEM, where even pixel to pixel precision can be achieved. This is crucial for the imaging of localised magnetic structures like skyrmions or vortices, where the detailed local distribution of the integrated magnetic induction is of great interest.

The profiles in Figs 4.14(d), (f) and (h) can be least squares fitted to the hyperbolic tangent function ($\tanh\left(\frac{x}{A}\right)$), and the width parameter of the wall, A, can be measured. Table 4.1 shows a comparison between the three given methods.

Wall width parameter	$A\,[nm]$
DPC	44 ± 5
Thresholded centre of mass	46 ± 4
Cross-correlation	48 ± 1

Table 4.1 *Comparison of measured domain wall width parameter A (from 1D hyperbolic tangent function) generated using least square fitting. The measurements were made from the profiles in Figs 4.14(d) for the averaged DPC, (f) for the centre of mass method and (h) for the edge filtered cross-correlation*

As was shown before, not only integrated magnetic induction images are useful, but also useful is bivariate histogram analysis of the magnetic field vector configuration. It can offer a novel approach for the correlation of experiment and theory, which was hard to achieve in segmented DPC imaging. Fig. 4.15 shows two bivariate histograms corresponding to Figs 4.14(a) segmented detection and (g), cross-correlation analysis. It is clear that the level of noise in the segmented detection prevents any meaningful field scatter analysis, however, for the cross-correlation we can see two spots corresponding to two domains and a line between them due to the domain wall. The line is oriented horizontally because the components of

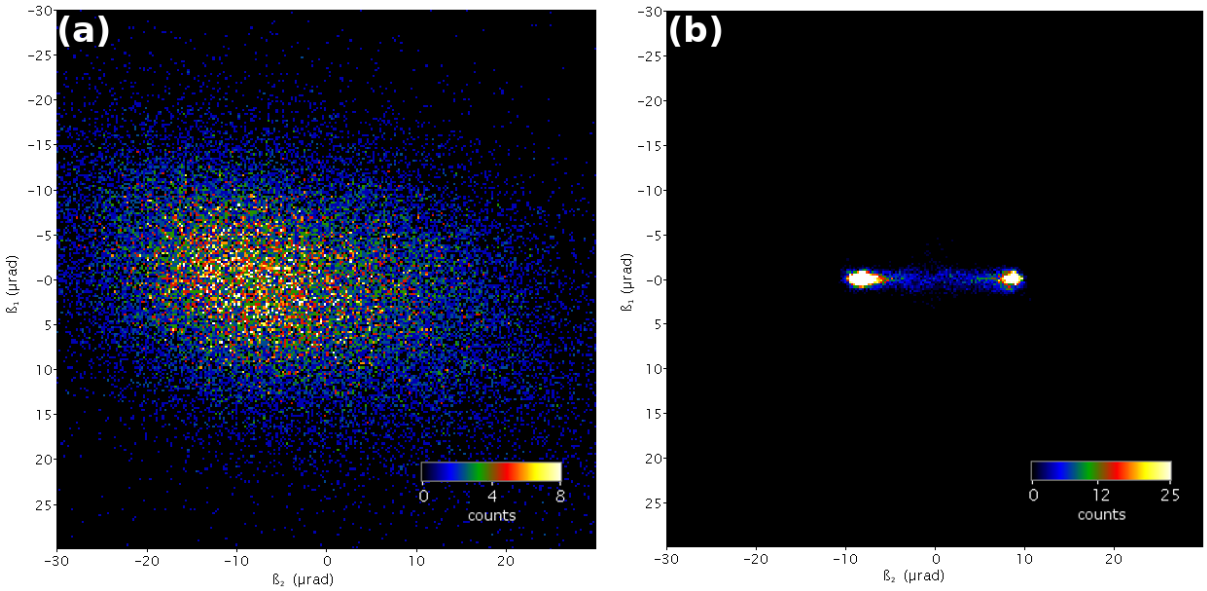

Fig. 4.15 *Comparison of bivariate histograms (field scatter plots) from (a) segmented DPC, (b) pixelated DPC (cross-correlation edge filtering). Both scatter plots show deflection of the beam based on the orientation of the domain wall*

the images were aligned with the direction of the domain wall. The correction of scanning may be almost impossible from image 4.15(a) compared to corrections shown in Fig. 4.13(c) and (f).

Here we will give a quantification of the noise improvement for pixelated detection in DPC. The statistical spread of the spots in Fig. 4.15 can be used to analyse level of noise in such imaging. The source of the noise could be from: scanning issues, the detection algorithm, variations of the magnetic induction of the sample and also residual diffraction contrast from non-magnetic sources.

In Figs 4.16(a),(b), (c) and (d), an area is highlighted within a single magnetic domain, which was used for noise considerations. The standard deviation of the signals and 2D symmetric Gaussian fit to the bivariate histograms for both segmented and pixelated DPC (cross-correlation method) are compared in Table 4.2.

	STDEV [μrad]	Gaussian fit (σ) [μrad]
Segmented DPC	9.6	8.3
Cross-correlation	0.50	0.44

Table 4.2 *Comparison of standard deviation of Figs 4.16(e), (f), (g) and (h) and Gaussian fit of bivariate histograms in Figs 4.16(i) and (j) of segmented DPC and edge cross-correlation analysis. Segmented DPC result is a magnitude of standard deviations generated from two orthogonal components*

Both methods of noise analysis show about a $\sim$ 20x better value for the pixelated cross-correlation analysis. This analysis should be considered only as an approximation

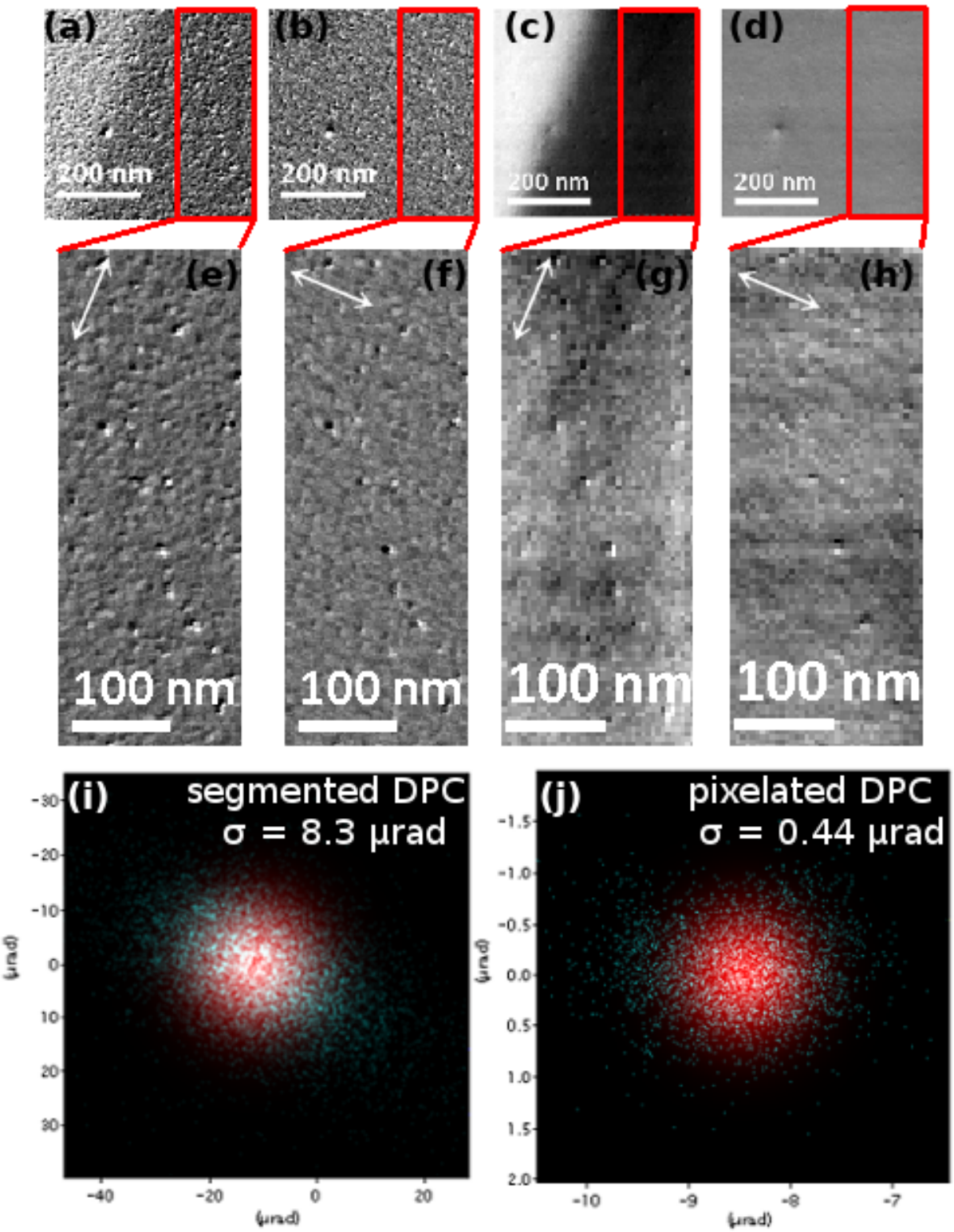

Fig. 4.16 *Signal to noise comparison of segmented DPC and pixelated cross-correlation DPC, (a), (b) segmented DPC images with box outlined for noise analysis in a single domain, (c) and (d) the same for pixelated (cross-correlation) DPC, (e), (f), (g), and (h) signals extracted from boxes in (a), (b), (c), (d) respectively. (i) and (j) are colour combination of Gaussian fitting (red blob) and bivariate histogram analysis (blue speckles). σ parameters of least square fits are shown. Note beam scanning issues (horizontal lines) and beam induced contamination visible in the pixelated DPC image (g) and (h)*

as bivariate histograms show clear differences between the fitting and the data spots in histograms in Figs 4.16(i) and (j). Segmented DPC was not scan corrected because the noise was too strong to determine this reliably. Pixelated DPC still shows some residual scanning issues, which could be due to non-linear beam instability or environmental factors.

Additional analysis of the scanning and algorithm precision will be shown in the following section for empty space DPC imaging. Data acquisition will be provided by a novel detector - Medipix3 which enabled practical acquisition of 256x256 images in two minutes. Medipix3, a direct electron detector, has much better imaging capabilities and is more suited to pixelated DPC due to its speed [29].

4.3 Medipix3 data acquisition

As mentioned before, the CCD camera is a very limited detector in the case of STEM imaging. Here we will present a dataset (and its analysis) acquired from a direct radiation detector - Medipix3 [5] which can offer sustained frame-rates up to 500 fps (at the moment of writing) and noiseless signal readout compared to CCD technology [29]. The most important difference for pixelated STEM is that, where a CCD camera usually has only 1–4 read-out pixels (to which the signals have to be shifted), the Medipix3 detector is designed with a counter for each pixel of the detector. The detector has 256x256 pixels, each of them $55\,\mu m$ sized. Highly energetic TEM electrons ($200\,kV$) hit the detector plate (Si) and generate X-ray photons, which are then detected. Details of the architecture of the detector can be found in [11, 12].

The Medipix3 detector was purchased with a Merlin read out system, provided by Oxford instruments Ltd. This system is capable of transferring data at $80\,\mathrm{MB}/s$ into the memory of the computer. This limits the frame-rate to roughly 500 fps for imaging with a 12-bit counter. This is likely to be improved towards 3000 fps in the future [30], which is the limit of the Medipix3 detector itself. However such a frame rate requires enough electrons to be hitting the detector, this may prove to be a limiting factor in the imaging of thicker or highly scattering samples (e.g. containing materials with high atomic numbers).

The Medipix3 detector has been fitted onto a JEOL ARM microscope in a fixed configuration in a port above the viewing screen, as shown in the photograph in Fig. 4.17. The disadvantage of this setup is that there is no other detector above the Medipix3 port - therefore changes of alignment, samples, tilts or general manipulation of wave-optical system of the microscope make it difficult to produce well aligned datasets.

The Gatan Digiscan system was used to drive the acquisition by TTL signal triggering, which is supported by the Merlin readout system. TTL pulses are transferred over a coaxial cable. Development is still in progress and in the near future we expect to have

the detector integrated into Gatan DM such that we will be able to run it completely by scripting/plugin from within DM. However, in this work we will focus on the usage of the Medipix3 detector for scientific measurements and not the technical aspect of the work.

The Medipix3 and Merlin acquisition system allowed practical acquisition of 256x256 probe positions in 125 s for a 1 ms dwell time and a 1 ms readout time. If the bit depth of the detector is set to 12-*bit* the size of the dataset will be 8 GB. Images are acquired in 12-*bit* depth, however due to the Merlin system they are stored as 16-*bit* into a binary file. In a comparison, the 100x100 dataset which was shown in the CCD section of this chapter, can be acquired with the Medipix3 within 20 seconds at 500 fps (it took 12 min by the CCD camera). This comparison clearly demonstrates the advantage of Medipix3 over standard CCD in STEM.

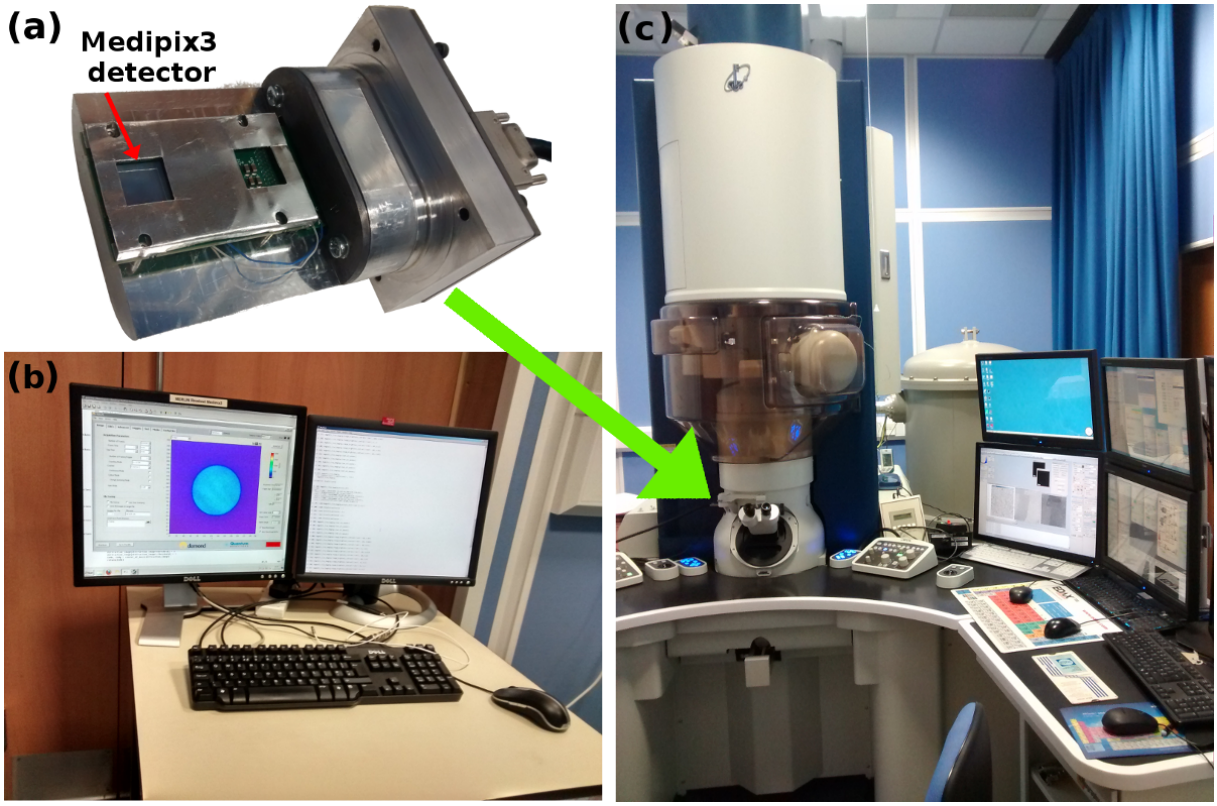

Fig. 4.17 *Photograph of Medipix3 detector (a) in the prototype setup at the moment of writing, (b) is a photograph of Merlin read out computer showing acquisition of centrad diffraction disk, (c) Jeol ARM 200cF at The University of Glasgow with green arrow pointing the port of the microscope where the detector is fitted. An active area of the detector is pointed to by a red arrow*

4.4 Medipix3 data processing

The data processing for the Medipix3 was altered to achieve higher sensitivity to beam shifts (better resolution in **k**-space). If we also want to achieve high real space resolution a large aperture needs to be used and therefore the relative shift of the beam will be smaller. In this case the shift of the beam can easily fall bellow 1 pixel on the detector. An example can be given for 2150 μrad convergence semi-angle ($k_\alpha = (1.1\,nm)^{-1}$). If such a beam covers 200 pixels of the detector, the shift for 10 nm permalloy (6.4 μrad) will be only $\sim 0.3\,pix$. This puts great pressure on the precision of the detection. Therefore a different approach will be taken to generate the edge of the beam more precisely. The Sobel algorithm will be changed to a more generalised version, of which Sobel is only an approximation. To achieve the sufficient resolution in the spatial and reciprocal space, the Sobel kernel size will be effectively expanded to the size of the image [18]. Convolution of such a pattern will be provided by Fourier transforms. Smaller Sobel kernels are only an approximation of the gradient of a Gaussian function [31–33]. Gradients of a Gaussian are perfect, rotationally symmetric, edge generating kernels. Based on previous arguments, the edge detection in image A will be computed by:

$$\nabla A_\sigma = \sqrt{[A * \partial_x G_\sigma]^2 + [A * \partial_y G_\sigma]^2} \tag{4.5}$$

where $*$ is the convolution operator, G_σ is the 2D Gaussian defined in Eq. 4.2, which define the strength of smoothing and also the width of the edge detection and $\partial_{x,y}$ are partial derivatives in the two orthogonal directions in the image. The expense of this approach is the computational time for two convolutions, which is tackled by using GPU processing software developed for this purpose. For the processing ArrayFire [34], library based on C++, was used to create a fast CUDA based analysis program. Parallel computation allows reduction of the running time of the analysis to 3 minutes, which is close to the acquisition time. This suggests it can be possible to use such analysis in 'live' or 'pseudolive' imaging, however, this was not pursued further in this thesis. If the same dataset is analysed by CPU based processing in Digital Micrograph® , it takes about 10 minutes. The frequency space precision for the GPU method is also better, because each image of the probe position is by default zero-padded to 512x512 pix - which effectively up-samples the image in the frequency domain.

The cross-correlation part of the edge detection algorithm was computed by normalised phase correlation with Fast Fourier Transforms [24]:

$$A \otimes B = FFT^{-1}\left(\frac{FFT[A]FFT[B]^*}{|FFT[A]FFT[B]^*|}\right), \tag{4.6}$$

where A and B are two images, $\otimes$ denotes the cross-correlation operation and * indicates the complex conjugate. Interestingly, the calculation of the denominator can be neglected because it only linearly scales the cross correlation pattern but does not change the position of its maximum.

Fig. 4.18 shows the result of analysis with subpixel precision in $20\,nm$ thick PyPt. It was reconstructed from 256x256 probe positions with a probe convergence semi-angle $\alpha = 2150\,\mu rad$, which correspondents to a spatial frequency of $(1.1\,nm)^{-1}$. The pixel size is $5.6\,nm$, therefore imaging is under-sampled. However, it still produces a significant result as the variations in magnetic contrast are on the order of the exchange length, which is $\sim 5\,nm$ for permalloy. Images 4.18(a) and (b) are two orthogonal components of the integrated magnetic induction. (c) is the magnitude of (a) and (b) highlighting the position of the vortex core and domain walls. (d) is a colour combination showing the direction of the induction and its magnitude. (e) is a vector stream plot, which enhances visual perception of the orientation of integrated magnetic induction of the sample. Finally, (f) is a Fresnel image of the structure showing the geometry of the detailed pixelated DPC images. The maximum deflection measured in this dataset was $1.1\,px$.

Fig. 4.19 shows bivariate histogram analysis, which demonstrates subpixel precision of the cross-correlation algorithm. If the bivariate histogram (d) is plotted from orthogonal integrated induction images (a) and (b), the magnetic configuration of the sample can be shown in the scatter plot. The axes of this plot are marked with deflection angles and pixels, showing that subpixel precision in indeed possible. This graph does not contain any spatial information, however, it can be colour coded (e) and the position of each of colour can be shown with respect to its position in the spatial image (f). Here we see that localised contrast peaks correspond to magnetic domains, and the lines connecting them corresponded to domain walls as expected. Such analysis will be shown to be important in correlation of the theory and experiment, which will be important in Chaps 5 and 6, where detailed internal structure of magnetic skyrmions and imaging of electric fields will be shown.

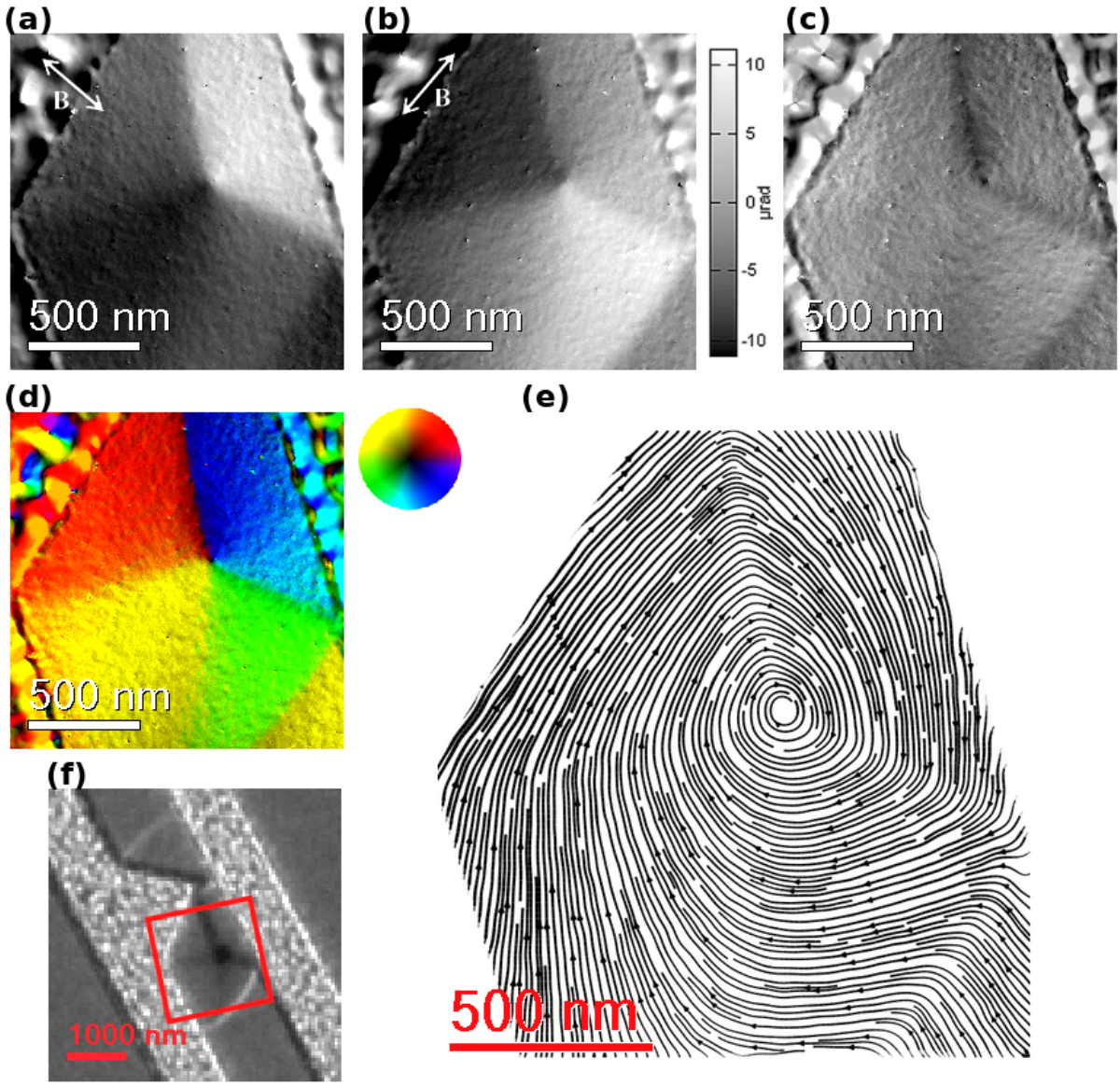

Fig. 4.18 *Medipix3 imaging of patterned* 20*nm thick PyPt in which a magnetic vortex was formed. The geometry, wire with a notch, is defined by FIB patterning. (a), (b) two orthogonal components of integrated magnetic induction, orientation is shown by doubleheaded arrows, (c) image of a magnitude balanced around vortex - shows divergence of strong domain walls and out of plane signal from the vortex core, (d) a colour image showing the orientation and magnitude of the field, (e) Fresnel image of the same structure showing outer geometry of the wire created by FIB sputtering, (f) vector stream image highlighting the orientation of the integrated magnetic induction (the lines do not form loops in such a image and therefore their spacing in not quantitative)*

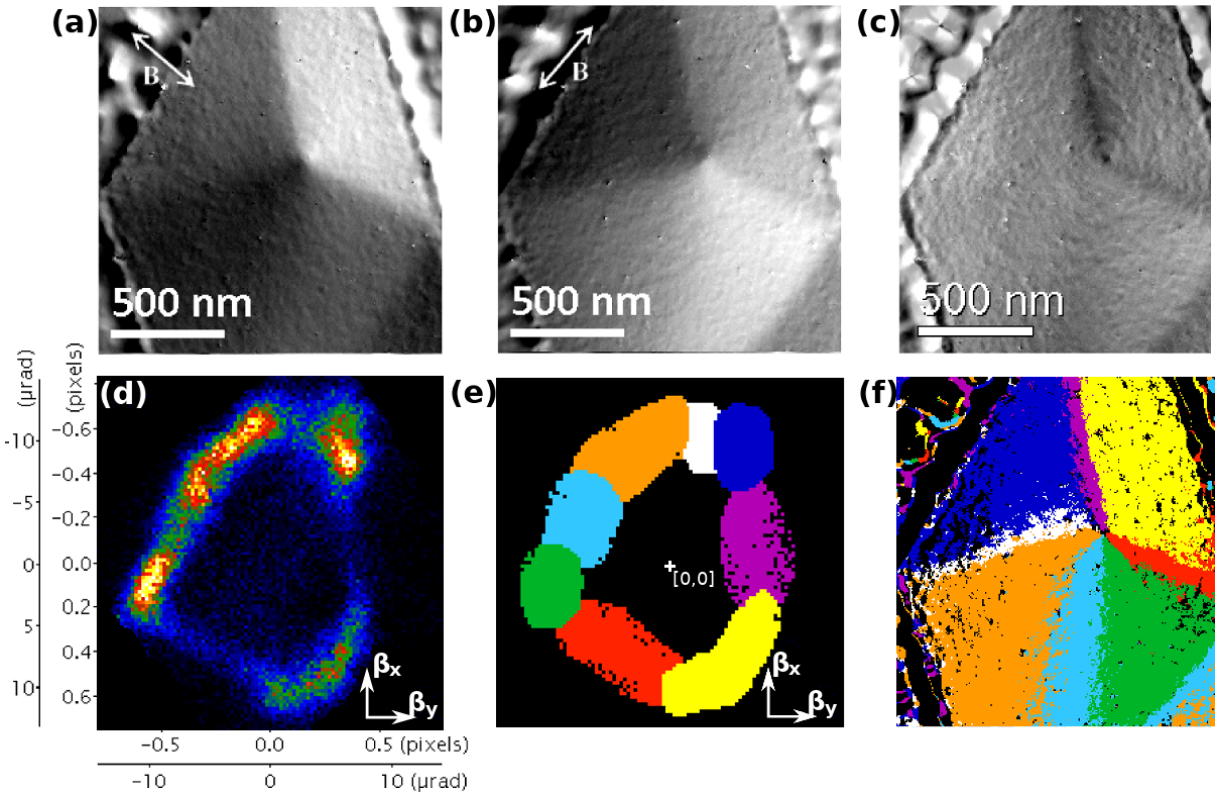

Fig. 4.19 *Demonstration of the subpixel resolution achieved by Medipix3 detector, (a), (b) two orthogonal components of integrated magnetic induction, (c) magnitude of (a) and (b), (d) bivariate histogram showing the subpixel resolution, (e) colour marked histogram to show the relation to the real space image in (f)*

4.5 Empty space scan analysis and algorithm uncertainty

The limits of the cross-correlation algorithm can be tested by the analysis of a scan in free space. This can contain residual scanning issues which were not corrected by the alignment of the microscope - such as noise due to the environment changes in electric and magnetic field and errors due to the processing. An extensive study of scanning systems was done in [35]. Residual scanning should be clearly visible as it has a linear ramp/plane character, while environmental noise can appear as sharper transitions. However, the processing itself should produce a symmetric point spread function as the edge of the beam used for the processing was generated by symmetric edge generating kernels.

Fig. 4.20 shows the analysis of a 256x256 scan of empty space at 600kx magnification with a convergence semi-angle $\alpha = 2150\,\mu rad$ ($k_\alpha = (1.1\,nm)^{-1}$). Images (a) and (b) are orthogonal beam deflection maps plotted with the same contrast levels, showing a larger ramp character in y direction, in (b).

Bivariate analysis of scanning in empty space is shown in Fig. 4.21. (a) shows a bivariate histogram created from the components of beam deflection shown in Figs 4.20(a) and

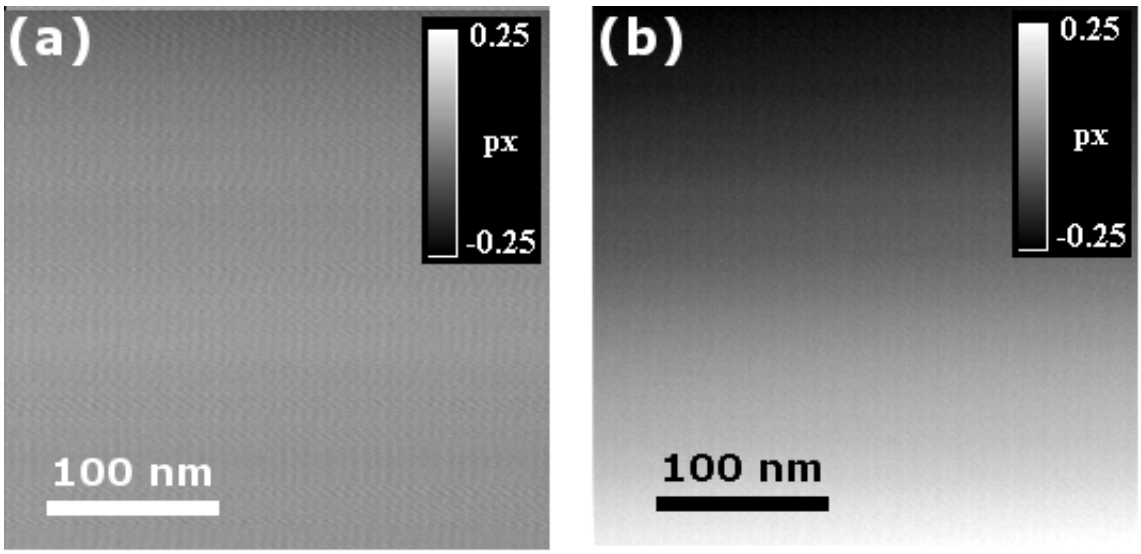

Fig. 4.20 *Imaging of an empty space - scanning and algorithm precision test, (a) x component of disk shift in empty space, (b) y component of disk shift in empty space*

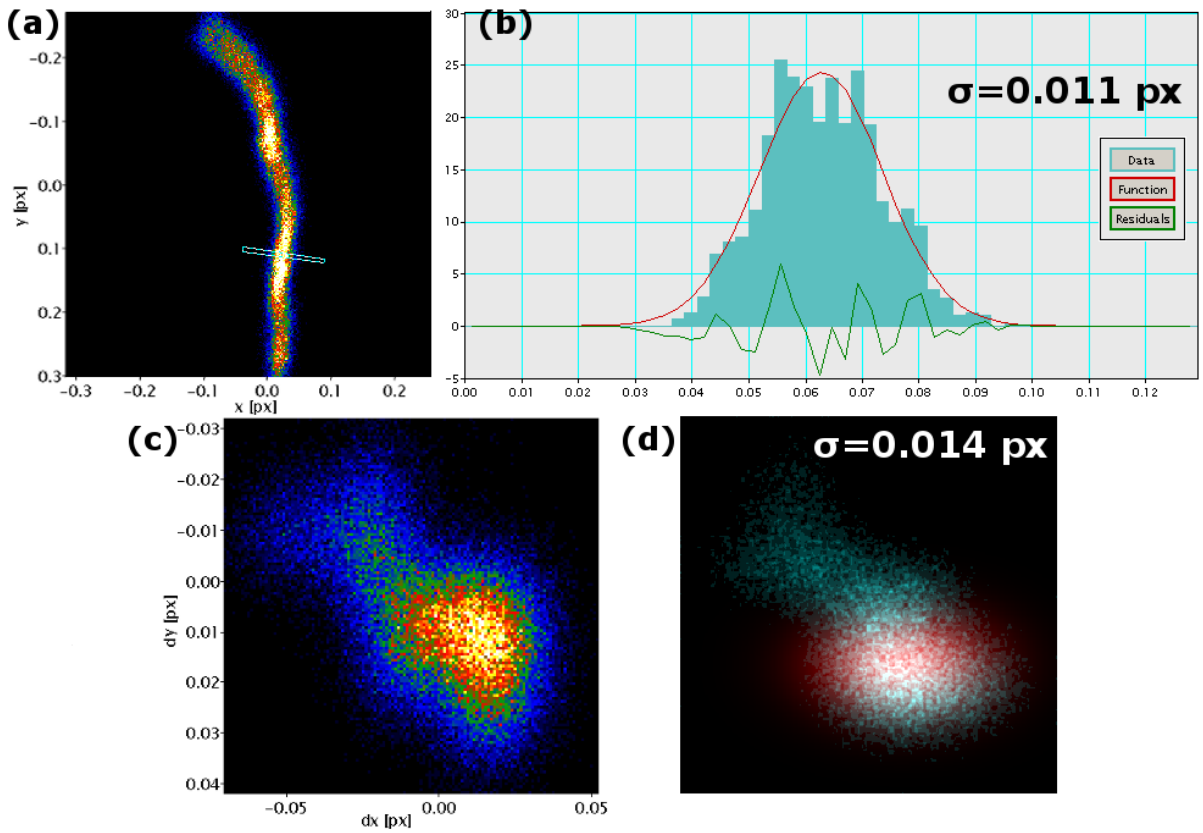

Fig. 4.21 *Imaging of an empty space - scanning and algorithm precision test, (a) bivariate histogram from 4.20(a) and (b) width of the detected line - test of the precision of the algorithm, (c) scan corrected bivariate histogram - higher order noise in scanning system/environment, (d) Gaussian fit of (c)*

(b). It is clearly visible that residual beam scanning contains not only a linear (plane) signal but also a non-linear signal. If the spread of the line is least square fitted with the Gaussian function, this will give maximum uncertainty in the precision of the algorithm (see image in Fig. 4.21(b)). In this case the least square fit gives $\sigma = 0.011\,px$. If the linear contribution to the scanning issues is taken away (see image (c)), the bivariate histogram can be fitted with a symmetric Gaussian, and sigma of the same order of magnitude as in (b) can be produced ($\sigma = 0.014\,px$ by least squares fitting). These values can help estimate the minimal beam deflection which can be measured by pixelated DPC. If $\alpha = 2150\,\mu rad$ convergence angle ($k_\alpha = (1.1\,nm)^{-1}$) is used and the beam covers a diameter of $200\,px$ on the detector, a single pixel will correspond to $21.5\,\mu rad$ and the deflection resolution will be approaching $\Delta_\sigma = 0.32\,\mu rad$ which corresponds to the deflection angle from a single in-plane magnetised domain in a $0.5\,nm$ thick permalloy. However, this is the case assuming ideal beam transmission without any distortions due to the structure of the sample. If a convergence angle of $\alpha = 436\,\mu rad$ is used, the same calculation gives potential sensitivity to $0.1\,nm$ thickness of permalloy, which is on the scale of a mono-layer.

4.6 Conclusions

Diffraction contrast from polycrystalline films has long been a problem for STEM DPC imaging of magnetic thin films. In this chapter we have shown how the combination of a pixelated detector and software processing of the bright field disk images results in a huge improvement in the efficiency with which the magnetic phase information can be imaged. This was first demonstrated with a standard CCD camera by implementing beam edge analysis and a cross-correlation algorithm. The CCD camera is not practical due to a prohibitive speed of acquisition and charge spreading, therefore the direct electron detector Medipix3 was utilised to achieve sustainable frame-rates of 500 *fps*. The sensitivity to very small Lorentz deflections has been clearly shown ($\gtrsim 0.5\mu rad$ for an empty space scan in Fig. 4.21), which is very important for imaging extremely thin and perpendicularly magnetised films. Sub-pixel resolution was demonstrated with sensitivities better than $< 0.1\,px$. It was shown that the resolution in **k**-space (disk deflection measurement) is as important as the real **x**-space resolution that is possible with aberration corrected systems. It was also shown that the enhanced imaging can also be used for bivariate vector scatter analysis, which can be helpful in correlation of theory and experiment and also for the analysis of noise in a scanning system of the STEM.

References

[1] C. Ophus, P. Ercius, M. Sarahan, C. Czarnik, and J. Ciston, "Recording and Using 4D-STEM Datasets in Materials Science," *Microscopy and Microanalysis*, vol. 20, no. S3, pp. 62–63, 2014.

[2] T. J. Pennycook, A. R. Lupini, H. Yang, M. F. Murfitt, L. Jones, and P. D. Nellist, "Efficient phase contrast imaging in STEM using a pixelated detector. Part 1: Experimental demonstration at atomic resolution," *Ultramicroscopy*, 2014.

[3] H. Yang, T. J. Pennycook, and P. D. Nellist, "Efficient phase contrast imaging in STEM using a pixelated detector. Part II: Optimisation of imaging conditions," *Ultramicroscopy*, vol. 151, pp. 232–239, 2015.

[4] C. Gammer, V. B. Ozdol, C. H. Liebscher, and A. M. Minor, "Diffraction contrast imaging using virtual apertures," *Ultramicroscopy*, vol. 155, pp. 1–10, 2015.

[5] M. Krajnak, D. McGrouther, D. Maneuski, V. O'Shea, and S. McVitie, "Pixelated detectors and improved efficiency for magnetic imaging in STEM differential phase contrast," *Ultramicroscopy*, vol. 165, pp. 42–50, 2016.

[6] Gatan Inc, "K2 Direct Detection Cameras," http://www.gatan.com /products/tem-imaging-spectroscopy/k2-direct-detection-cameras accessed 2016.

[7] PNdetector, "The pnCCD (S)TEM Camera," http://pndetector.de/ wp-content/uploads/2016/03/Flyer_TEM.pdf accessed 2016.

[8] M. W. Tate, P. Purohit, D. Chamberlain, K. X. Nguyen, R. Hovden, C. S. Chang, P. Deb, E. Turgut, J. T. Heron, D. G. Schlom, *et al.*, "High Dynamic Range Pixel Array Detector for Scanning Transmission Electron Microscopy," *Microscopy and Microanalysis*, vol. 22, no. 01, pp. 237–249, 2016.

[9] Quantum Detectors, The University of Glasgow, "Medipix 3RX / MERLIN STEM detector," http://quantumdetectors.com/stem/ accessed 2016.

[10] R. Beacham, A. Mac Raighne, D. Maneuski, V. O'Shea, S. McVitie, and D. McGrouther, "Medipix2/Timepix detector for time resolved transmission electron microscopy," *Journal of Instrumentation*, vol. 6, no. 12, p. C12052, 2011.

[11] R. Ballabriga, M. Campbell, E. Heijne, X. Llopart, and L. Tlustos, "The Medipix3 prototype, a pixel readout chip working in single photon counting mode with improved spectrometric performance," in *Nuclear Science Symposium Conference Record, 2006. IEEE*, vol. 6, pp. 3557–3561, IEEE, 2006.

[12] R. Ballabriga, M. Campbell, E. Heijne, X. Llopart, L. Tlustos, and W. Wong, "Medipix3: A 64k pixel detector readout chip working in single photon counting mode with improved spectrometric performance," *Nuclear Instruments and Methods in Physics Research Section A: Accelerators, Spectrometers, Detectors and Associated Equipment*, vol. 633, pp. S15–S18, 2011.

[13] A. Yasuhara, W. Inami, K. Yamazaki, A. Saitow, K. Okamoto, H. Endo, M. Kawazu, T. Suzuki, I. Ohnishi, and Y. Kondo, "Observation of Magnetic and Electric Field in STEM by using CCD camera," *Microscopy and Microanalysis*, vol. 15, no. S2, pp. 1058–1059, 2009.

References

[14] S. McVitie and J. Chapman, "Measurement of domain wall widths in Permalloy using Differential Phase Contrast imaging in STEM," *Journal of Magnetism and Magnetic Materials*, vol. 83, no. 1, pp. 97–98, 1990.

[15] K. Müller, F. F. Krause, A. Béché, M. Schowalter, V. Galioit, S. Löffler, J. Verbeeck, J. Zweck, P. Schattschneider, and A. Rosenauer, "Atomic electric fields revealed by a quantum mechanical approach to electron picodiffraction," *Nature communications*, vol. 5, 2014.

[16] J. Chapman, I. McFadyen, and S. McVitie, "Modified differential phase contrast Lorentz microscopy for improved imaging of magnetic structures," *Magnetics, IEEE Transactions on*, vol. 26, pp. 1506–1511, sep 1990.

[17] J. Lewis, "Fast normalized cross-correlation," in *Vision interface*, vol. 10, pp. 120–123, 1995.

[18] B. Schaffer, W. Grogger, and G. Kothleitner, "Automated spatial drift correction for EFTEM image series," *Ultramicroscopy*, vol. 102, no. 1, pp. 27–36, 2004.

[19] D.-M. Tsai, C.-T. Lin, and J.-F. Chen, "The evaluation of normalized cross correlations for defect detection," *Pattern Recognition Letters*, vol. 24, no. 15, pp. 2525–2535, 2003.

[20] L. Meng, G. Jin, and X. Yao, "Application of iteration and finite element smoothing technique for displacement and strain measurement of digital speckle correlation," *Optics and Lasers in Engineering*, vol. 45, no. 1, pp. 57–63, 2007.

[21] M. Hansen, P. Anandan, K. Dana, G. Van der Wal, and P. Burt, "Real-time scene stabilization and mosaic construction," in *Applications of Computer Vision, 1994., Proceedings of the Second IEEE Workshop on*, pp. 54–62, IEEE, 1994.

[22] V. Hou, "Cross Correlate plugin." http://donation.tugraz.at/dm/source_codes/144, accessed February 2015.

[23] M. Guizar-Sicairos, S. T. Thurman, and J. R. Fienup, "Efficient subpixel image registration algorithms," *Opt. Lett.*, vol. 33, pp. 156–158, Jan 2008.

[24] H. Foroosh, J. Zerubia, and M. Berthod, "Extension of phase correlation to subpixel registration," *Image Processing, IEEE Transactions on*, vol. 11, pp. 188–200, Mar 2002.

[25] Q. Tian and M. N. Huhns, "Algorithms for subpixel registration," *Computer Vision, Graphics, and Image Processing*, vol. 35, no. 2, pp. 220–233, 1986.

[26] V. Dvornychenko, "Bounds on (deterministic) correlation functions with application to registration," *IEEE Transactions on Pattern Analysis and Machine Intelligence*, no. 2, pp. 206–213, 1983.

[27] T. Koyama, Y. Togawa, K. Takenaka, and S. Mori, "Ferromagnetic microstructures in the ferromagnetic metallic phase of La0. 825Sr0. 175MnO3," *Journal of Applied Physics*, vol. 111, no. 7, p. 07B104, 2012.

[28] J. Chapman, R. Ploessl, and D. Donnet, "Differential phase contrast microscopy of magnetic materials," *Ultramicroscopy*, vol. 47, no. 4, pp. 331–338, 1992.

[29] J. Mir, R. Clough, R. MacInnes, C. Gough, R. Plackett, I. Shipsey, H. Sawada, I. MacLaren, R. Ballabriga, D. Maneuski, *et al.*, "Medipix3 Demonstration and understanding of near ideal detector performance for 60 & 80 keV electrons," *arXiv preprint arXiv:1608.07586*, 2016.

[30] D. Maneuski, 2016. Private conversation.

[31] R. Szeliski, *Computer vision: algorithms and applications*. Springer Science & Business Media, 2010.

[32] H. Farid and E. P. Simoncelli, "Optimally rotation-equivariant directional derivative kernels," in *International Conference on Computer Analysis of Images and Patterns*, pp. 207–214, Springer, 1997.

[33] W. T. Freeman and E. H. Adelson, "The design and use of steerable filters," *IEEE Transactions on Pattern analysis and machine intelligence*, vol. 13, no. 9, pp. 891–906, 1991.

[34] P. Yalamanchili, U. Arshad, Z. Mohammed, P. Garigipati, P. Entschev, B. Kloppenborg, J. Malcolm, and J. Melonakos, "ArrayFire - A high performance software library for parallel computing with an easy-to-use API," 2015.

[35] L. Jones and P. D. Nellist, "Identifying and correcting scan noise and drift in the scanning transmission electron microscope," *Microscopy and Microanalysis*, vol. 19, no. 04, pp. 1050–1060, 2013.

CHAPTER 5

Imaging of the internal structure of magnetic skyrmions in *FeGe* thin film

5.1 Introduction

In this chapter, pixelated detection in differential phase contrast will be used to image the fine structure of a magnetic skyrmion lattice in a thin sample of *FeGe*. The internal structure of the skyrmion will be shown at a nanometre resolution together with bivariate scatter analysis. The results will be compared with a simple 3Q model, which is a basic model that can be used to simulate a skyrmion lattice by the combination of three helical phases oriented in-plane at 120° to each other [1–3]. It will be shown that the 3Q model can be altered to match some aspects of the presented experiment.

5.2 Lorentz TEM of magnetic skyrmions in cubic helimagnets

In magnetic systems with broken inversion symmetry, a competition of the Dzyaloshinskii-Moriya exchange and the Heisenberg exchange can lead to a state where a helical configuration is present when a zero or a small external magnetic field is applied out of plane of a thin sample [4]. The details of the phase diagram of such a system were given in Sec. 1.4.2. In Figs 1.7(a) and (b), a schematic and a Lorentz microscopy image of the helical ordering were given. If an out of plane field is applied to such a sample at a temperature close to the Curie temperature, a skyrmion lattice can be created [5, 6]. This is again shown schematically, together with a Lorentz microscopy image, in Figs 1.7(c) and

(d). The structure of a skyrmion in a thin chiral magnet, a Bloch skyrmion, was shown in Fig. 1.8(a).

Chiral structures in magnetism are of considerable interest in science and technology because they could allow new generations of spintronic devices. Skyrmions show promising properties such as: topological protection, stability (under external applied field) [7]; movement by low spin polarised currents (compared to domain walls) [8]; and they do not pin as easily as domain walls [8].

Skyrmions were first observed by neutron scattering in reciprocal space in *MnSi* [1] and later, a real space image was obtained by Lorentz microscopy [9] in $Fe_{0.5}Co_{0.5}Si$. The highest spatial resolution images of skyrmions were to date observed by spin polarised scanning tunnelling microscopy in a single atomic layer of iron [10]. This technique offers atomic resolution, however only the surface states are accessible (i.e. the magnetism of atomically thin layers). This is problematic for helical magnets where skyrmions form in the centre of the thin film, and surfaces are more likely to have an uneven structure. High resolution TEM imaging of skyrmions was presented in [9, 11], however the precise structure of the skyrmion within a skyrmion lattice in helical magnets was not yet provided. In this chapter, we will focus on detailed imaging of the internal structure of the integrated magnetic induction of skyrmions within a skyrmion lattice in a thin sample of *FeGe*.

5.3 Sample information and data acquisition

In this chapter a thin *FeGe* sample will be investigated. A nanowedge TEM sample was prepared by collaborators at The University of Hiroshima by vapour growth and sample thinning techniques [12]. The sample was a B20 single crystal, which was oriented with the ⟨110⟩ normal for the imaging in TEM. An investigation with the mean free path technique in EELS [13] was used to reveal the thickness of the sample. This was found to be a 60 nm at the edge of the sample which scaled linearly to 150 nm within 3 μm into the sample

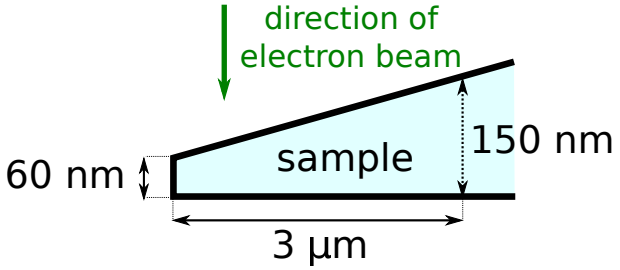

Fig. 5.1 *FeGe sample geometry measured by mean free path technique in EELS by Dr Sam McFadzean (not to scale)*

(see Fig. 5.1). This EELS investigation was carried out by Dr Sam McFadzean at The University of Glasgow.

As is visible from the phase diagram in Fig. 1.6, a skyrmion lattice can be created by an application of external field to a helical magnet within a given temperature range [11, 14]. In this TEM study, the skyrmion lattice was stabilised at $253\,K$ by applying a $798\,Oe$ out of plane magnetic field using the objective lens of the TEM. The skyrmion lattice was then imaged with pixelated differential phase contrast [15] using the Medipix3 pixelated direct electron detector in the Jeol ARM 200cF in Lorentz mode, as was described in Chap. 4. The imaging was carried out with the current (prototype) setup of pixelated detection, which allowed acquisition in a 'blind' setup. That is, only images of the central diffraction disks were shown by the detector software, this makes the data acquisition difficult (magnetic contrast of interest is not displayed during the scan). At first, the skyrmion lattice was located by defocusing (using Fresnel mode), after which beam was again focused and STEM acquisition was started. Great care is needed to set up the illumination optics of the microscope for this type of approach because any defocus and astigmatism are not easily visible during the scan [1]. In the future, the Medipix3 detector will be placed on a retractable plate, therefore the alignment process will be easier and more practical. It is also possible to place a dark field detector around the detector chip, which could be used for the same purpose. A photograph of the detector is shown in the previous chapter (Fig. 4.17).

In this chapter, the dataset was acquired with a beam convergence semi-angle $\alpha = 2150\,\mu rad$. This corresponds to a maximum spatial frequency of $k_\alpha = (1.1\,nm)^{-1}$ at $200\,keV$ electron energy. A pixel spacing of $0.92\,nm$ was used. The scan size was of 256×256 probe positions and the final 4D dataset was $8\,GB$ in size. The diffraction disk was $240\,px$ in diameter at $800\,cm$ camera length which gives an angle calibration of $17.9\,\mu rad$ per pixel.

5.4 Data analysis

The data processing procedures introduced in the previous chapter will be used in this analysis. One of the disk images from the dataset was used to create an idealised disk edge (Sec. 4.2.2), which was then cross-correlated to all edge filtered disk images. Because of the relatively large beam convergence semi-angle (the probe size was $k_\alpha = (1.1\,nm)^{-1}$), the relative deflection angles of the beam due to the in-plane magnetic induction were very

[1] A problematic factor was the saturation of the detector when no condenser aperture was inserted while setting up a STEM Ronchigram. This can be partially solved by changing the extraction voltage and therefore the number of electrons, but this is not the most practical approach

small. The core of the skyrmion is about $\sim 20\,nm$ (see analysis in Chap. 3) - this is much larger than the size of the beam, hence, it can be safely assumed the beam geometry is unchanged by the magnetic phase of the skyrmion. The analysis of the size of the core diameter was given in [12], where the dependence on an applied field was both simulated and experimentally observed with the segmented DPC setup.

Quadratic interpolation was again used to find the subpixel disk deflection using the maxima of the cross-correlation pattern for each probe position. A convolution with gradients of a symmetric Gaussian ($G_{0.5}$) of the same size as the image was performed to generate the edge images. The resulting images are shown in Fig. 5.2. Figs 5.2(a) and (b) show two orthogonal components of the integrated magnetic induction, where the double headed arrows show the orientation of magnetic induction sensitivity (the two components are calibrated as deflection angles). Fig. 5.2(c) is the magnitude of Figs 5.2(a) and (b) clearly showing the hexagonal symmetry of the skyrmion lattice. Fig. 5.2(d) is a colour combination of Figs 5.2(a) and (b) showing the direction (given in the colour wheel) and the magnitude of the in-plane integrated magnetic induction. The resulting images were corrected for small residual scan issues by fitting and removing a plane in reciprocal space, which was $0.15\,px$ in magnitude. The use of a free space scan image to correct for imperfect scan plane alignment was discussed in Sec. 4.5.

The analysis of an empty space scan for similar imaging conditions in Sec. 4.5 indicates that the precision of the scan is about ~ 0.02 pixel. The line profile shown in Fig. 5.2(b) is now least square fitted with:

$$\text{a } 6^{\text{th}} \text{ order polynomial:} \quad a_1 + a_2x + a_3x^2 + a_4x^3 + a_5x^4 + a_6x^5 + a_7x^6,$$

$$\text{and a sinusoid:} \qquad a + b\,sin\left(\tfrac{x-c}{d}\right).$$

The standard deviations of the residuals are equal to 0.020 px and 0.026 px respectively. The profile and least square fits are shown in Fig. 5.3. If polynomial fit is used to analyse the noise in imaging, the precision of the analysis can be estimated to about $\pm 0.5\,\mu rad$ deflection angle. If the two fits in Fig. 5.3 are compared, we can conclude that the sinusoid is less accurate then the sixth order polynomial. Results of the fitting are:

6^{th} order polynomial:

$$-2.1 \times 10^{-3} + 0.040x - 1.37 \times 10^{-3}x^2 + 0.10x^3 - 4.0x^4 - 0.10x^5 + 4.0x^6,$$

$$\text{sinusoid:} \qquad 3.5 \times 10^{-3} + 0.31\,sin\left(\tfrac{x+0.80}{12.4}\right),$$

where all parameters are in pixels normalised for nanometres. This result can be used to find the size of the skyrmion. In case of sixth order polynomial, the size of the periodic skyrmion is $73.9\,nm$. Periodicity of the best fit for the sinusoid gives the size $77.8\,nm$. This difference suggests that the profile of a skyrmion slightly deviates from a pure sinusoid function.

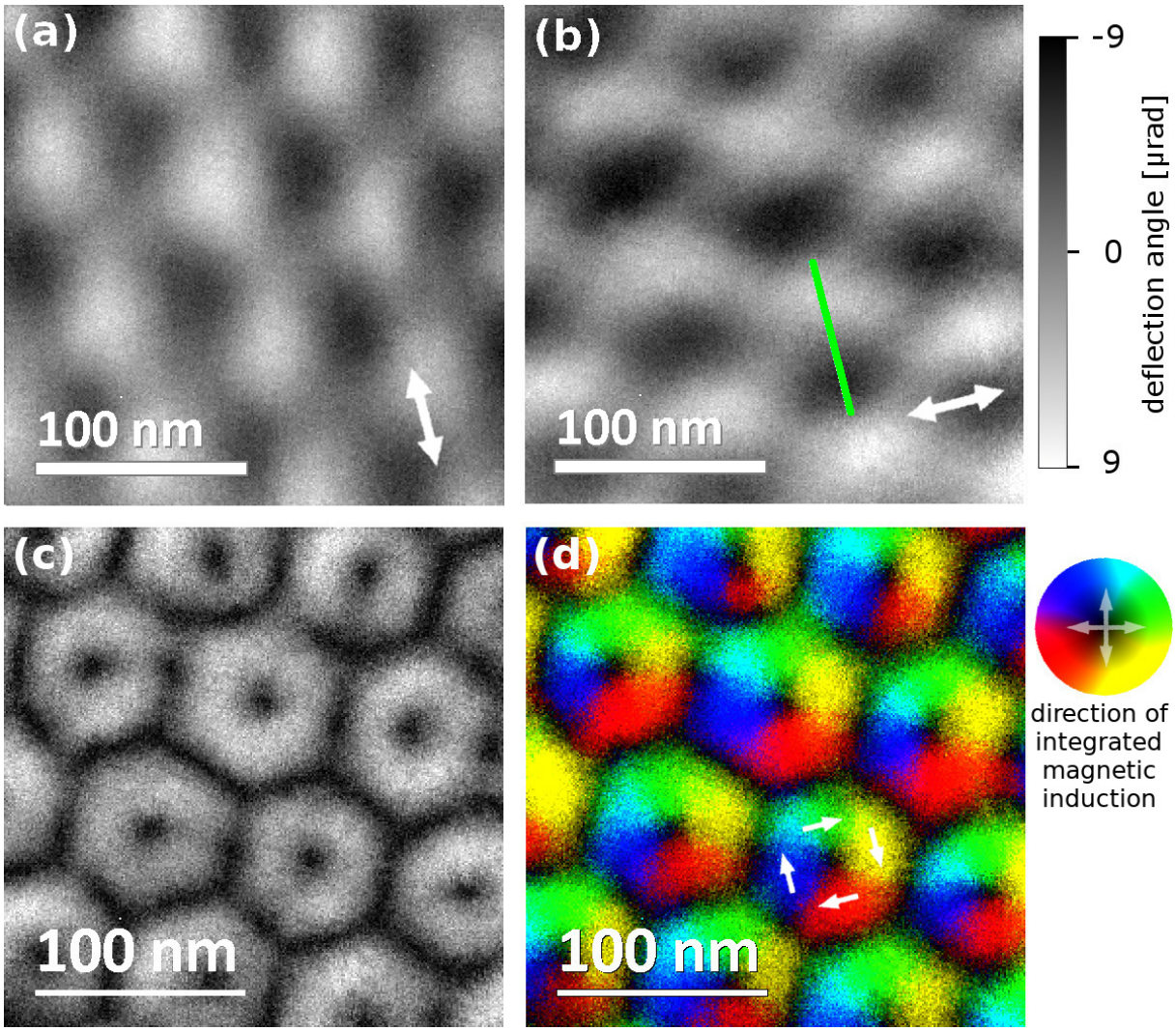

Fig. 5.2 *Pixelated DPC result of skyrmion lattice imaging in thin film FeGe helimagnet. The imaged area was* 60-80 *nm thick and sample was oriented with the* ⟨110⟩ *normal. The skyrmion lattice was aligned with the edge of the sample. (a), (b) are orthogonal components of integrated magnetic induction calibrated as a beam deflection; (c) magnitude of magnetic induction calculated from images (a) and (b); (d) is the colour combination of (a) and (b) showing the direction and magnitude of the in plane induction. The sample was imaged at* $253\,K$ *and a* $798\,Oe$ *out of plane field was applied to form the skyrmion lattice. The beam convergence semi-angle was* $\alpha = 2150\,\mu rad$*. The camera length was* $800\,cm$ *and the acquisition took* 2 *minutes. The green line in image (b) shows a profile which is plotted in Fig. 5.3 and used for a noise and profile analysis.*

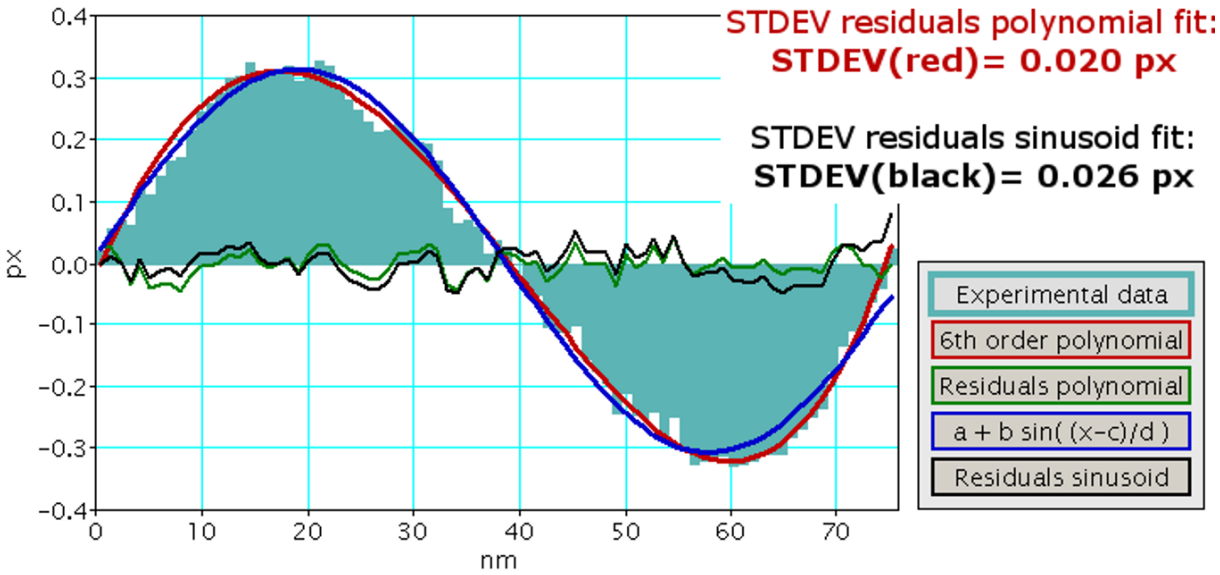

Fig. 5.3 *Analysis of the noise and the line profile shown in Fig. 5.2(b) by a green line, least square method fitted functions were a sixth order polynomial and a sinusoid. Standard deviation of residuals were equal to* 0.020 *px and* 0.026 *px respectively. Measured periodicities were* 73.9 *nm and* 77.8 *nm respectively*

The images in Fig. 5.2 show that pixelated DPC can achieve detection with a good signal to noise ratio (compared to the segmented DPC images of the same sample shown in [12]). Interestingly, there seems to be some natural variation in the size and profile of the skyrmions within the hexagonal lattice, which is clearly shown in the image of magnitude of in-plane integrated magnetic induction in Fig. 5.2(c). Moreover, this can be studied with the help of bivariate analysis - introduced in the previous chapter. Fig. 5.4(a) shows the four skyrmions used for the bivariate analysis. Figs 5.4(b), (c), (d) and (e) are bivariate histograms with their position shown in Fig. 5.4(a). The images show a variation in the integrated magnetic induction vector configuration of single skyrmions from a hexagonal skyrmion lattice. This variation was found to be a natural property of skyrmions in a skyrmion lattice.

To correlate the distribution of the integrated magnetic induction vectors to real space image, the bivariate histogram in Fig. 5.4(b) was chosen for a further analysis in Fig. 5.5. Fig. 5.5(a) shows the position of chosen skyrmion. The regions of interest in histogram in Fig. 5.5(b) are coloured in Fig. 5.5(c). This is matched in the real space coloured image in Fig. 5.5(d). The orange coloured ring in the bivariate histogram in Fig. 5.5(c) corresponds to the highest beam deflections, themselves arising from the maximal magnitude of the rotating in-plane integrated magnetic induction and show a distorted structure. The following sections of the chapter will study the structure of the histogram further.

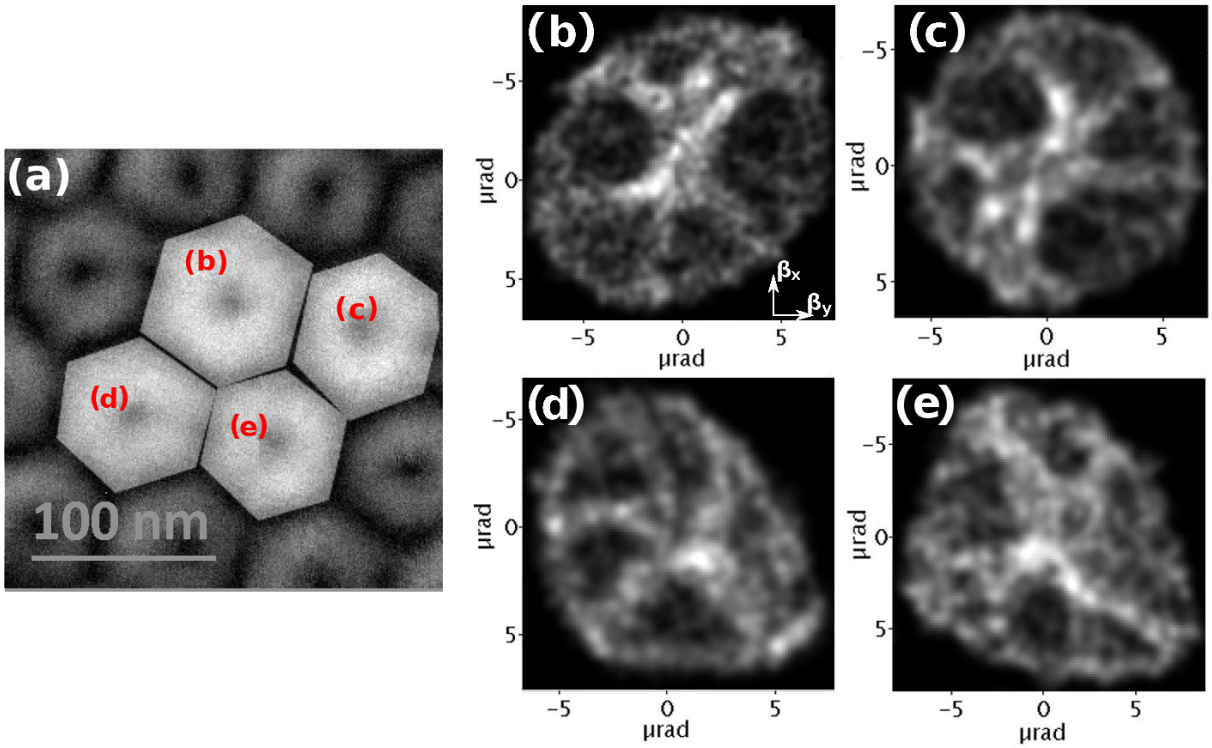

Fig. 5.4 *Bivariate analysis of single skyrmions from skyrmion lattice in FeGe, (a) magnitude image overlayed with the positions of analysed skyrmions, (b), (c), (d) and (e) bivariate analysis of single skyrmions - examples of natural variation of skyrmion field profiles*

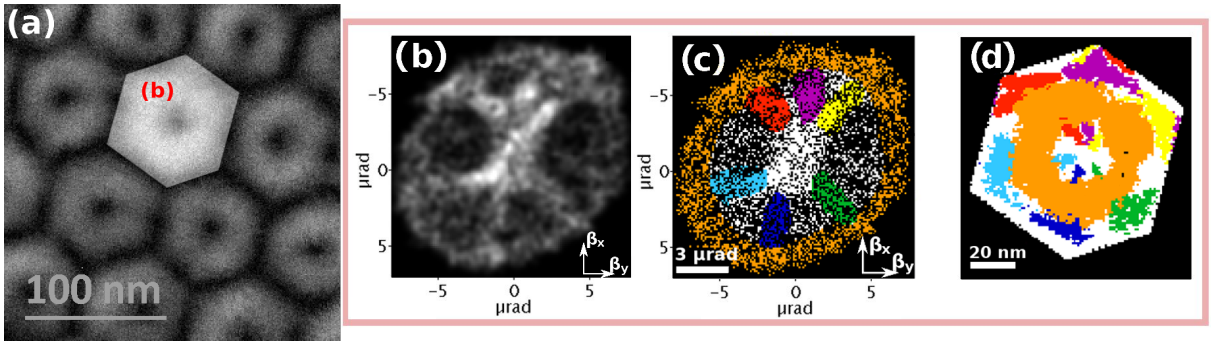

Fig. 5.5 *Bivariate analysis of single skyrmion from skyrmion lattice in FeGe, (a) magnitude image overlayed with the position of analysed skyrmion, (b), (c) and (d) are colour analysis of a skyrmion, structure from bivariate plot in image (b) was colour coded in image (c). Image (d) shows a real space diagram, where colours match the scatter in (c).*

5.5 Comparison of skyrmion field profile to the simulation of circular and hexagonal permalloy structures

The analysis of the profile of the skyrmion in the bivariate histogram in Fig. 5.5(b) shows a distorted structure which could be considered hexagonal (the level of noise prevents any clear conclusion). However, it shows that the profile of the induction of the skyrmion in the hexagonal lattice is not completely circularly symmetric. In fact, it can be shown that it has some resemblance to the domain structure in a hexagonal magnetic particle.

MuMax^3 micromagnetic simulation software [16] was used to simulate 20 nm thick permalloy samples with round and hexagonal boundaries. The calculation of the DPC imaging of a round particle is shown in Fig. 5.6. This shows a magnetic induction configuration circling around the centre, where a vortex core is present. The magnetisation simulation was provided by Mumax^3, with pixel size 1 nm. Diameter of the particle was 200 nm and the data cube was 256 x 256 x 1 nm^3. The thickness of the sample was 20 nm. The exchange stiffness was $E_x = 13 \times 10^{-12}\ J/m$ and the saturation magnetisation was $M_s = 860 \times 10^3\ A/m$. The Lorentz image calculation was provided by method described in Sec. 2.4. Figs 5.6(a) and (b) are the two orthogonal components of the integrated magnetic induction. Fig. 5.6(c) is a magnitude of (a) and (b) showing an out of plane component - a vortex core. The image in Fig. 5.6(d) is the bivariate histogram of (a) and (b) showing a circularly symmetric vector configuration of the integrated magnetic induction (with a spot in the centre of the histogram corresponding to the vortex core and non-magnetic area of the surrounding area). As expected, this shows a circularly symmetric profile.

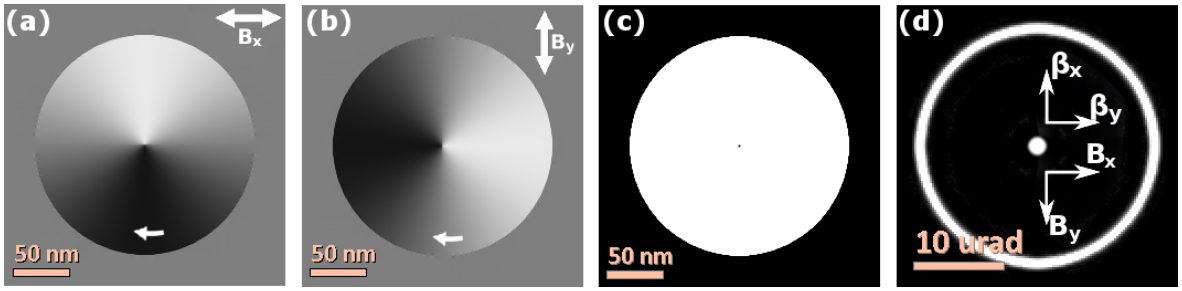

Fig. 5.6 *DPC imaging calculation of a round ferromagnetic particle, (a) and (b) are the two orthogonal components of the integrated magnetic induction, (c) is a magnitude of (a) and (b) showing an out of plane component - vortex core. Image (d) is the bivariate histogram of (a) and (b) showing a circularly symmetric vector configuration of integrated magnetic induction. The magnetisation simulation was provided by Mumax*^{3} *software, with pixel size* 1 nm. *Diameter of the particle was* 200 nm *and the data cube was* $256x256x1\ nm^3$. *The thickness of the sample was* 20 nm. *The exchange stiffness was* $E_x = 13 \times 10^{-12}\ J/m$ *and the saturation magnetisation was* $M_s = 860 \times 10^3\ A/m$.

We will now analyse a ferromagnetic, permalloy particle with a hexagonal boundary (magnetisation components were shown in Fig. 1.11), where the side of the hexagon was chosen as $200\,nm$. The size of a cell in the simulation was $1.6 \times 1.6 \times 20\,nm^3$, the exchange stiffness was $E_x = 13 \times 10^{-12}\,J/m$ and the saturation magnetisation was $M_s = 860 \times 10^3\,A/m$. The data cube was $320 \times 320 \times 1$ points. The surrounding grey area is non-magnetic. Fig. 1.11 shows the expected six domain state with a vortex in the middle. Figs 1.11(a), (b) and (c) contain m_x, m_y and m_z respectively. Fig. 1.11(c) shows the vortex in the centre with magnetisation pointing out of plane. Domains in the hexagonal particle (in Fig. 1.11) are separated by Néel domain walls, which exist due to the divergence of magnetisation (i.e. with associated magnetostatic energy) induced by the outer shape of the particle (discussed in Sec. 1.3.2). This magnetisation configuration was used to simulate DPC images (by the approach described in Sec. 2.4) in Figs 5.7(a) and (b), which show the two orthogonal components of the integrated magnetic induction. Fig. 5.7(c) is the magnitude of Figs 5.7(a) and (b) and shows the divergence of magnetisation at domain walls, where the reduction of the magnitude of the in plane induction is clear. Fig.

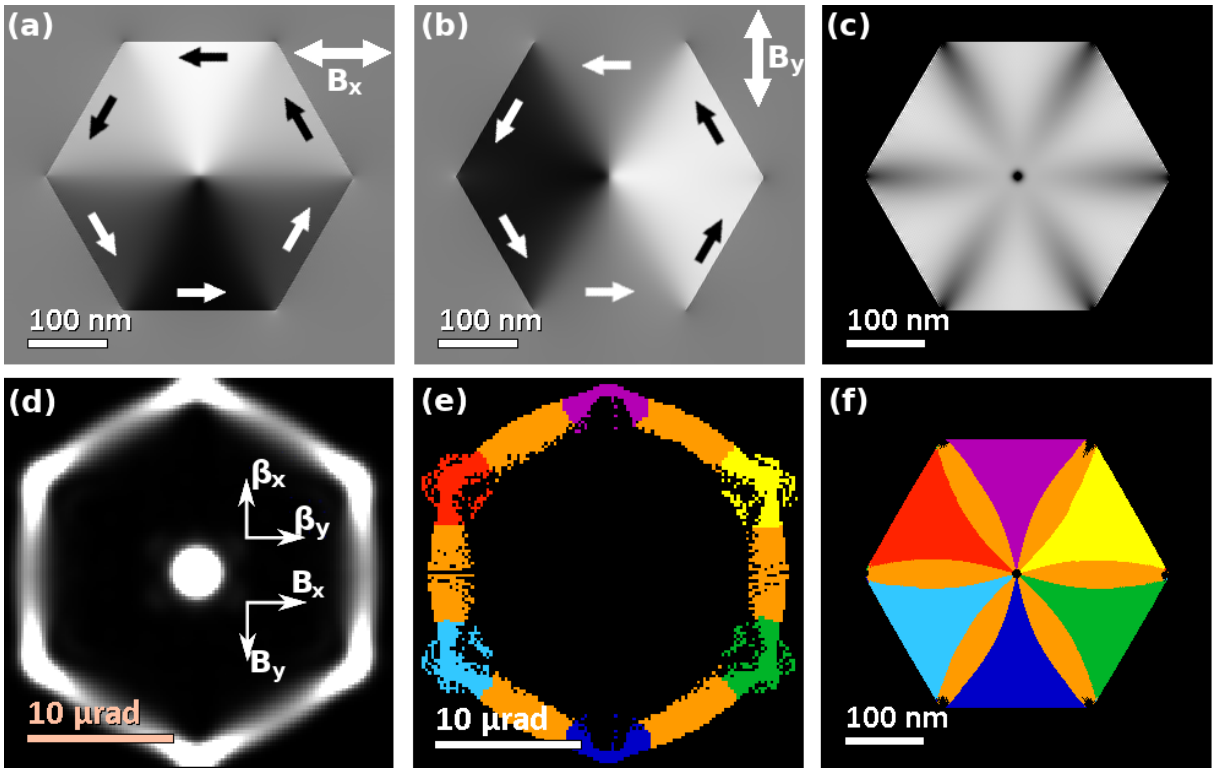

Fig. 5.7 *Bivariate analysis of a hexagonal permalloy particle with divergent domain walls, (a), (b) orthogonal components of integrated magnetic induction, (c) magnitude of the two components, (d) bivariate histogram, (e) coloured regions of interest within bivariate histogram with a matching coloured real space image in (f), the middle of the histogram was not coloured as it mostly contains stray field pixels from outside of the hexagon and only a tiny proportion of signal due to the vortex and the divergent walls (these are therefore black in (f))*

5.7(d) is the bivariate histogram, showing hexagonal configuration of magnetic induction of the sample. The histogram was colour coded in Fig. 5.7(e) which enables regions of interest to be localised in the colour coded spatial image in Fig. 5.7(f). The orange colour represents the domain walls and the remaining colours represent the six domains oriented 60° with respect to their neighbours. The integrated induction at walls is lowered due to the divergence of magnetisation, which creates the hexagonal outer shape of the bivariate histogram. The centre of the histogram corresponds to the area outside of the particle and the vortex core, where in-plane magnetic induction is low. This was not included in the colour analysis, as this is a small effect.

We can now compare the histograms of the round particle in Fig. 5.6(d) and of the hexagonal particle in Fig. 5.7(d). It is clearly visible that the presence of domain walls changes the vector configuration of the integrated magnetic induction, which is an important point when considering a skyrmion in a skyrmion lattice.

The histograms of the skyrmion and the hexagonal particle are compared in Fig. 5.8. The largest magnitude of integrated induction (the outer edges in bivariate histograms

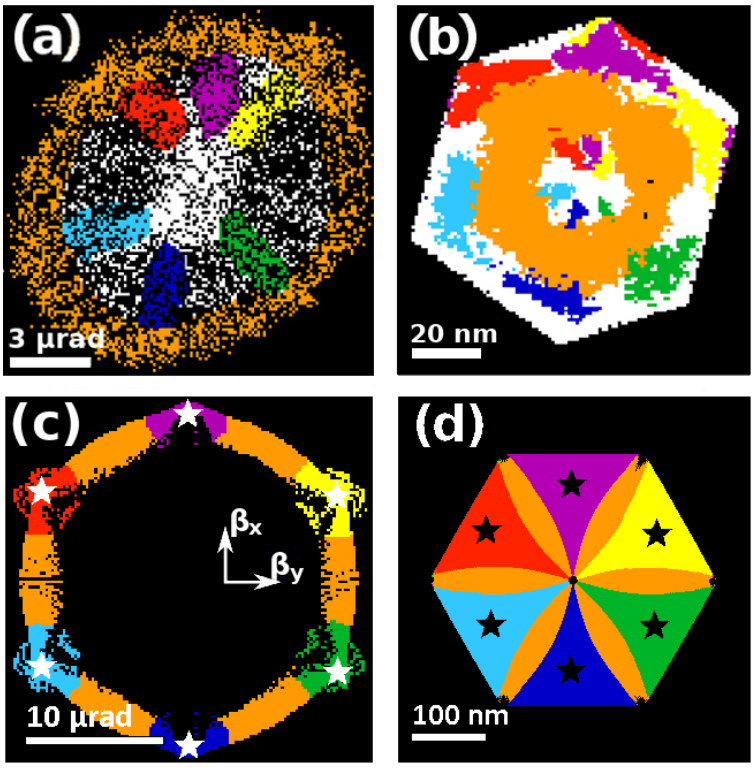

Fig. 5.8 *Comparison of the symmetries in a skyrmion and a hexagonal particle. Images (a) and (b) show bivariate histogram and related colour correlation with real space configuration from experimental pixelated DPC of a skyrmion, where images (c) and (d) show bivariate histogram and related colour correlation with real space configuration from simulated permalloy particle. The symmetry is similar, however the skyrmion configuration is* 30° *rotated compared to the hexagon simulation - this can be seen by noting the position of the 'star' marks and is schematically shown in Fig. 5.10.*

(a) and (c)) is hexagonal for the particle but has neither a clear hexagonal nor circular symmetry for the skyrmion. However, the orientations of the induction with respect to the edge/boundary are different, as shown in Fig. 5.8. Firstly, we look at a schematic of a skyrmion magnetisation configuration, where the position of magnetic induction vectors affected by divergence is highlighted in red colour in Fig. 5.9. In the experimental skyrmion image, the highest magnitude of skyrmion field corresponds to the three skyrmion boundary and lower magnitude to the two skyrmions boundary (schematically shown in Fig. 5.10(b)). However, if the orientation of the hexagon is examined, the highest magnitude is not located at the same positions for the skyrmion and hexagonal particle, but it is rotated by 30° with respect to each other. This is shown schematically in Fig. 5.10.

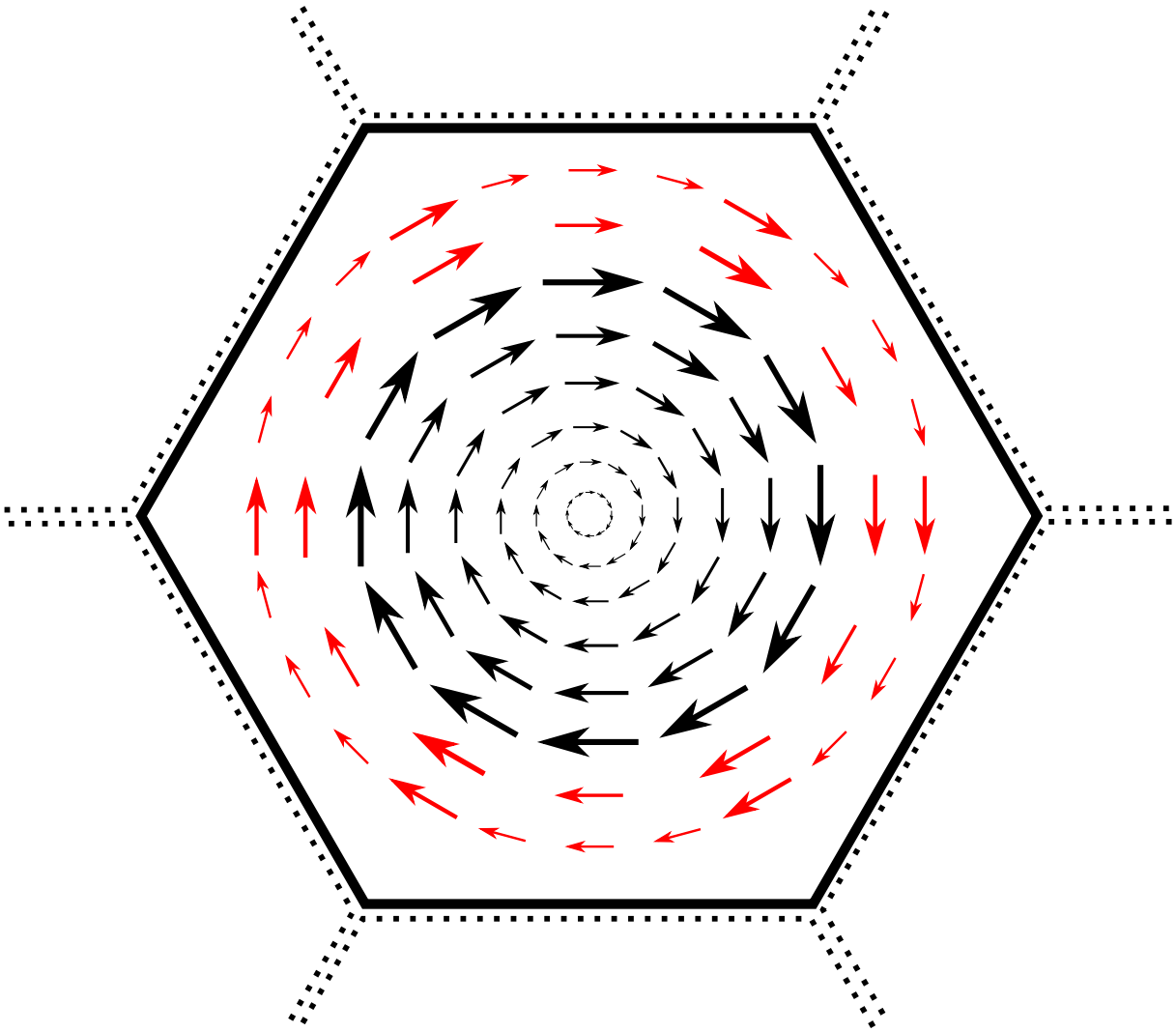

Fig. 5.9 *Schematic of the possible configuration of the integrated magnetic induction of a skyrmion in a skyrmion lattice. Red coloured vectors are affected by the divergence of the magnetisation.*

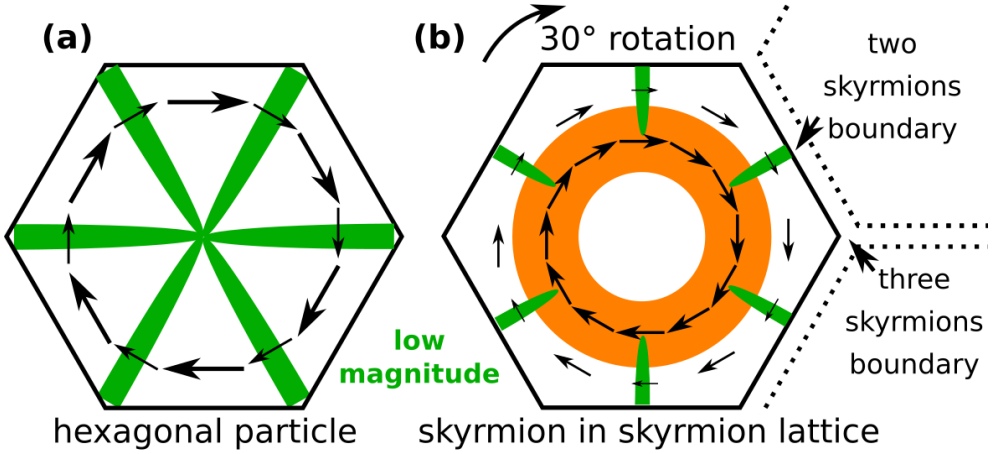

Fig. 5.10 *Schematics of high and low magnitude in-plane magnetic induction configuration within (a) a hexagonal isolated permalloy particle and (b) a skyrmion from a skyrmion lattice. The orange colour highlights a high magnitude of in-plane magnetic induction within the skyrmion. The green colour shows lowered in-plane magnetic induction, which is due to domain walls in the hexagonal particle and, a new result presented in this chapter for a skyrmion within a skyrmion lattice. The symmetry of the magnitude of the field is rotated by* 30° *between the two cases.*

The internal structure of high magnitude induction of a skyrmion was not observed in previous work in the imaging of helical magnets [17, 18]. It was stated that skyrmions have cylindrical symmetry [17]. The source of the circular and hexagonal symmetry remains an open question. There is a possibility that the contrast is affected by bend contours, however that effect should be minimised with the utilisation of $\sim 1\,nm$ resolution of DPC STEM imaging in this work. The other possibility is that it could arise due to surface states, where divergent twists in the spin configuration could cause the lowering of the in-plane magnitude of the integrated magnetic induction [19]. An interesting study would be to compare the measured bivariate scatters of the internal field of a skyrmion in a skyrmion lattice (Fig. 5.4) and that of a single skyrmion.

5.6 Comparison with 3Q skyrmion lattice model

5.6.1 3Q model

The 3Q model of a magnetic skyrmion lattice is based on the principle that three helical phases rotated 120° to each other can by used to create a skyrmion lattice, as shown in Fig. 5.11 [1–3, 20]. Each of the three helical phases can be represented by a pure sinusoidal variation of a single spatial frequency. This model fulfils the micromagnetic condition $||\mathbf{m}|| = 1$. The 3Q model of magnetisation in Fig. 5.11 was created using the

Digital Micrograph® scripting by Dr Damien McGrouther. Figs 5.11(a), (b) and (c) show the three helical waves which are combined into Figs 5.11(d) and (e) to create the two orthogonal components of the in plane magnetisation of the 3Q skyrmion lattice model. Fig. 5.11(f) is the out of plane component which was calculated from the magnitude of Figs 5.11(d) and (e). By the simulation of Lorentz DPC images, this model can be compared to experimental DPC images introduced in previous sections of this chapter. Fig. 5.12 shows the simulated in-plane magnetic induction of the 3Q skyrmion lattice. Figs 5.12(a) and (b) are the two components of integrated magnetic induction and (c)

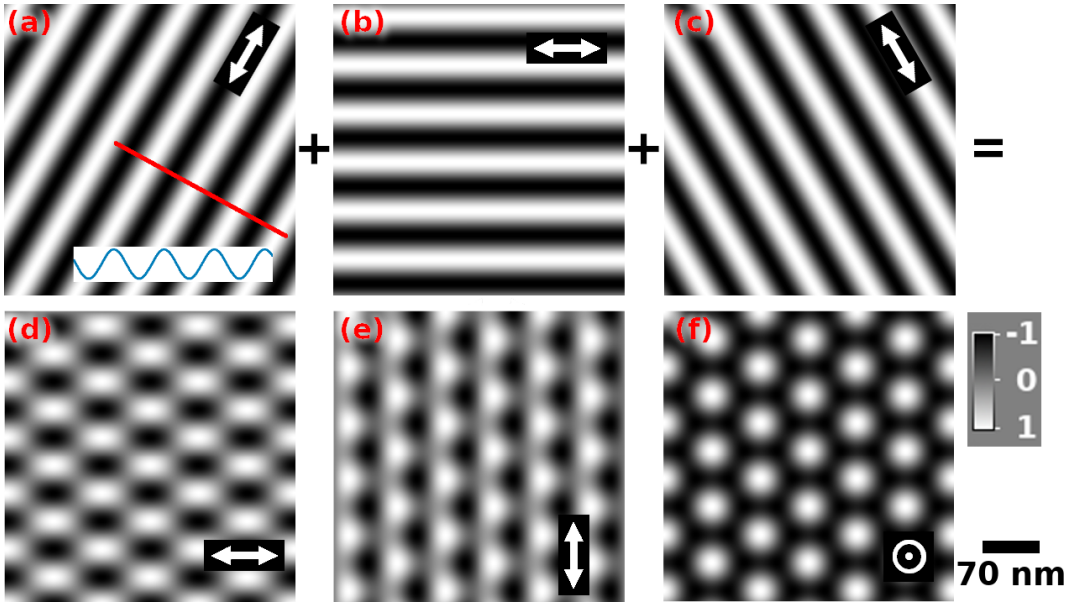

Fig. 5.11 *3Q model, (a), (b) and (c) show the three sinusoidal phases used to create the magnetisation profile of 3Q skyrmion, (c) and (d) show two orthogonal components of in-plane magnetisation of a 3Q skyrmion lattice, (e) shows the out of plane component created from the* $||\mathbf{m}|| = 1$ *condition*

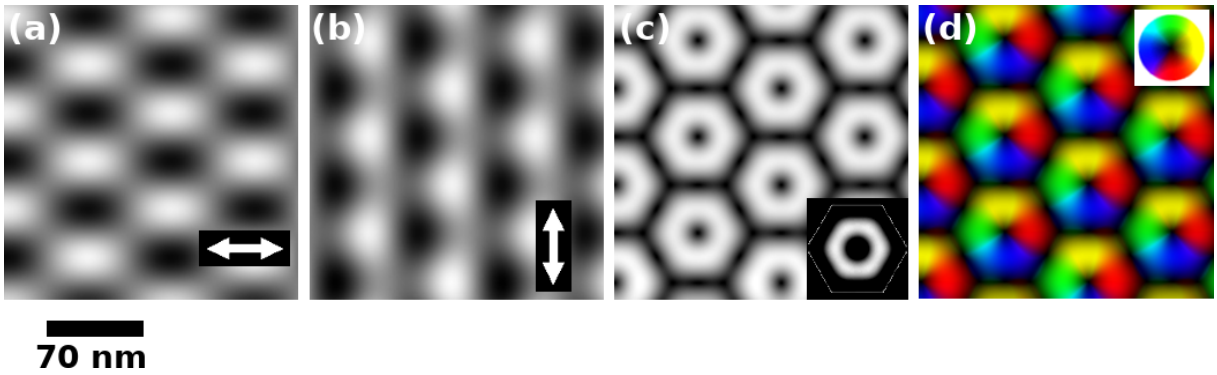

Fig. 5.12 *Simulation of Lorentz DPC images for 3Q skyrmion model, (a) and (b) are two components of integrated magnetic induction and (c) is their magnitude, (d) is the colour combination of in-plane components. The inset in (c) highlights constant high magnitude of in plane integrated induction for a single skyrmion, which will be important to compare with the modified 3Q model.*

is their magnitude. Fig. 5.12(d) shows colour combination of in-plane components. Fig. 5.13(a1) is the bivariate histogram of Figs 5.12(a) and (b). Interestingly, the maximum deflection in the bivariate histogram appears more circular than the experimental image in Fig. 5.13(b1). The hexagonal spikes within the bivariate histogram in Fig. 5.13(b1) are caused by low magnetic induction in-plane moments present between the skyrmions in the skyrmion lattice (due to the components of the 3Q contribution).

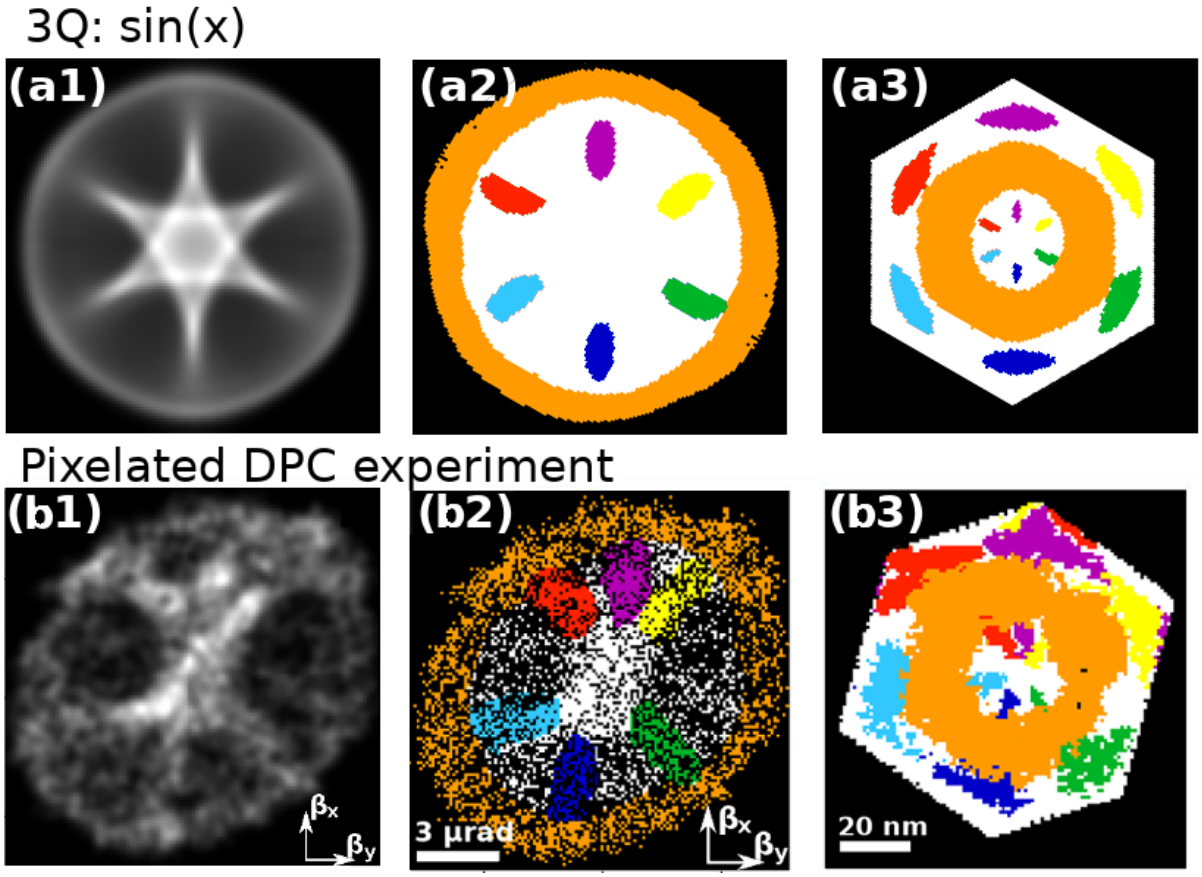

Fig. 5.13 *Bivariate comparison of Lorentz DPC images for 3Q skyrmion model and experimental images, (a1) is the bivariate histogram of 5.12(a) and (b) and shows a slight but insignificant hexagonal symmetry of the outer edge. Image (a1) was colour coded in (a2) and compared to a real space image in (a3). The same is used for experimental images in (b1), (b2) and (b3) respectively. It is important to note that the spikes from inside of the histogram (a1) do not touch the edge of the structure but they seem to for experimental image in (b1).*

5.6.2 3Q model with a third harmonic

A simple way to modify the 3Q model from the previous section to further compare some of the experimental result in Fig. 5.4(b) is to add a higher harmonic signal to the 3Q helical phases [3, 20]. From this modified model the magnetisation profile and DPC integrated magnetic induction images can be created. Fig. 5.14 shows an example of a modification of 3Q, which is a combination of the first and third harmonics (sinusoids):

$$sin(x) + 0.05\, sin(3x).$$

The magnitude of the third harmonic, (0.05), was chosen to show that a rather small change to a sinusoid profile can alter the 3Q which can be then compared with an experimental image. The modified profile of a single Q vector is shown as the blue, filled colour (in Fig. 5.14). Now, we use this altered sinusoidal profile as a base for the 3Q model of the skyrmion lattice as was already done in Fig. 5.11. The calculation of the integrated magnetic induction images is shown in Figs 5.15(a) and (b). Their magnitude and colour combination is shown in Figs 5.15(c) and (d) respectively. Such a modification results in a hexagonal shaped bivariate histogram shown in Fig. 5.16(a1). The histogram is colour coded in Fig. 5.16(a2) and compared to the real space image in Fig. 5.16(a3). The histogram and its colour analysis of experimental results are shown similarly in Figs 5.16(b1), (b2) and (b3). This analysis is empirical rather than model based (due to the breaking of $||\mathbf{m}|| = 1$). But it does show the possibility of an additional third harmonic signal as being a source of the hexagonal shaped symmetry of the integrated magnetic

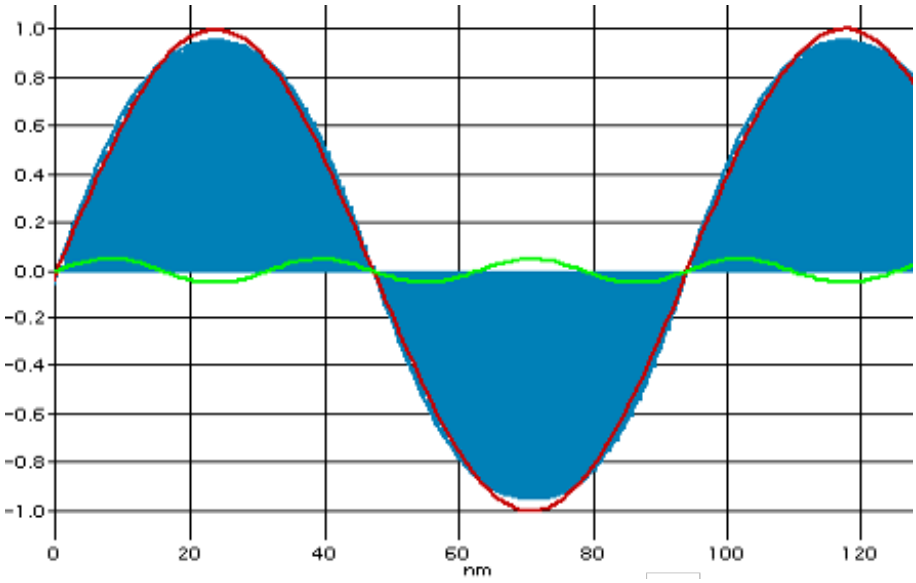

Fig. 5.14 *Modification of the 3Q harmonic (red) by an additional harmonic of three times the frequency and 0.05 times the amplitude (green). The resulting profile is shown as blue filled curve*

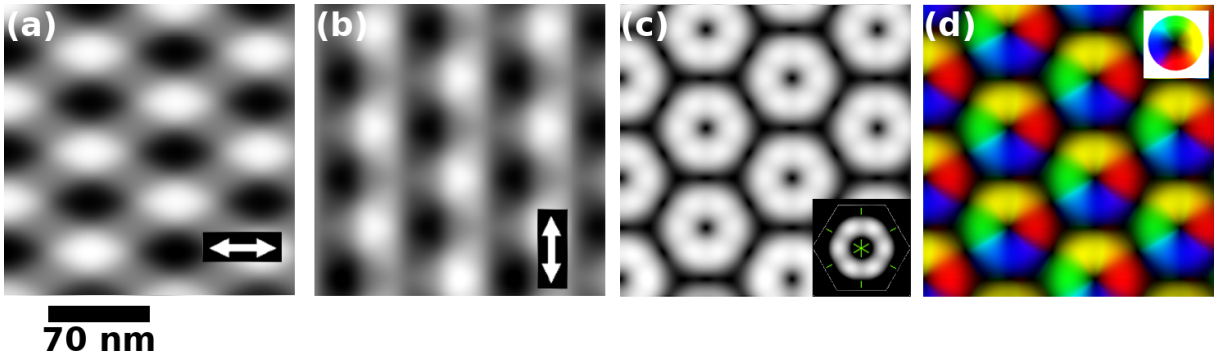

Fig. 5.15 *Simulation of Lorentz DPC images for 3Q skyrmion model with a third harmonic. Images (a) and (b) are the two components of the integrated magnetic induction and (c) is their magnitude, (d) is the colour combination of the in-plane components. The inset in (c) highlights the changes in high magnitude of in plane integrated induction for a single skyrmion.*

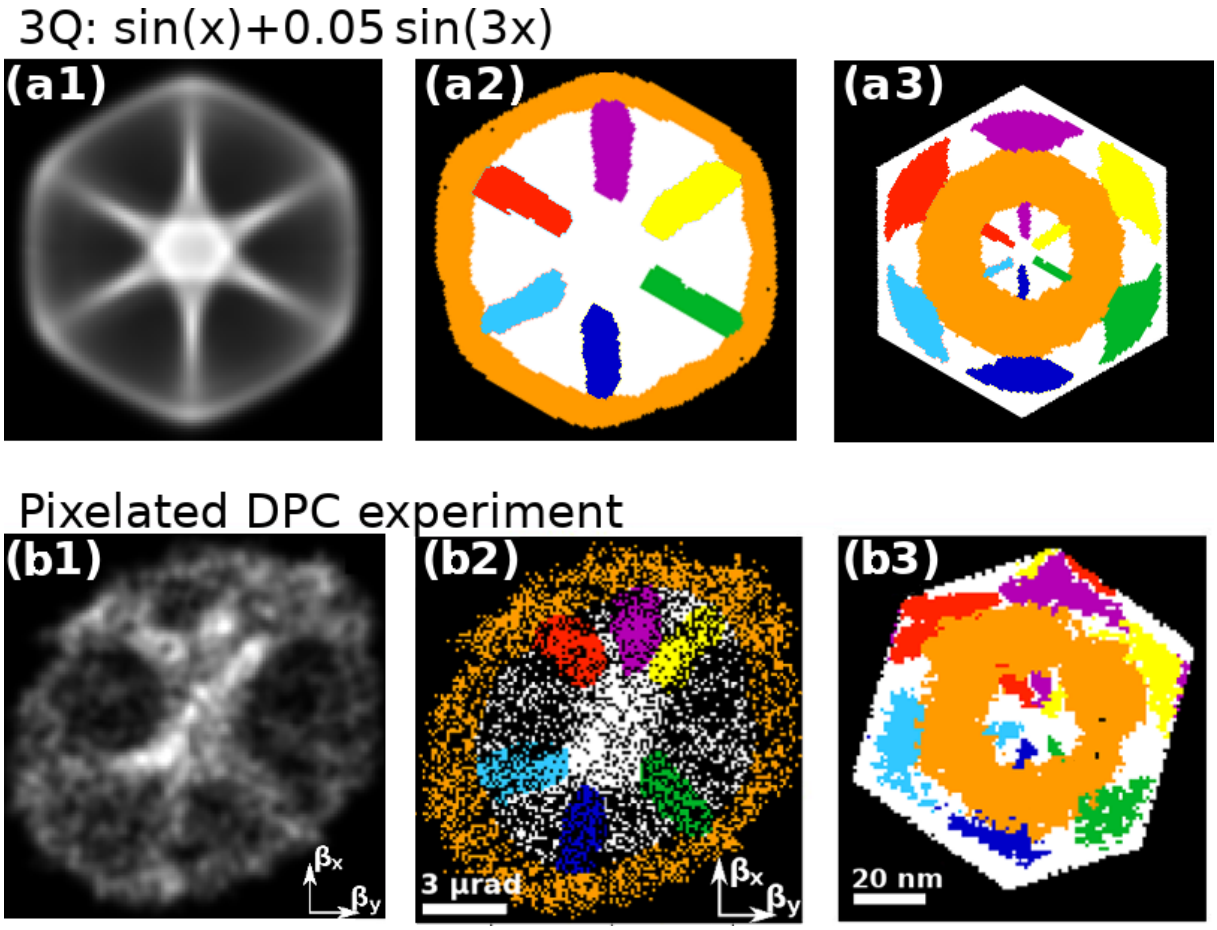

Fig. 5.16 *Bivariate comparison of Lorentz DPC images for 3Q skyrmion model with a third harmonic and experimental images, (a1) is the bivariate histogram of 5.15(a) and (b) and shows a clear hexagonal symmetry of the outer edge. Image (a1) was colour coded in (a2) and compared to a real space image in (a3). The same is used for experimental images in (b1), (b2) and (b3) respectively. The spikes from inside of the histogram (a1) now touch the edge of the structure.*

induction of a skyrmion lattice in a thin sample of *FeGe*. This hexagonal symmetry could be present in experimental observation in Fig. 5.16(b1), however more statistics are required to comment on this point further due to the level of noise in the image.

Finally, a comparison of the bivariate histograms obtained from the 3Q, modified 3Q and experimental pixelated detection is shown in Fig. 5.17. In this figure we can clearly see that adding additional harmonics to 3Q can empirically model hexagonal like variations in the maxima of integrated magnetic induction of a skyrmion in a skyrmion lattice. It should also be noted, that the spike signals from the skyrmion boundaries reach the edge of the histogram for 3Q with higher harmonics (if images in Figs 5.17(a1) and (b1) are compared). Domain wall like contrast (lower moment) can be also appointed to the spikes touching the edge of the structure in the bivariate histogram. If we compare the images in Figs 5.12(c) and 5.15(c), there is a clear lowering of the magnitude of integrated induction for the latter. This is shown in the insets where the lowering of the magnitude is present for a modified 3Q model, which incidentaly coincides with the 3Q axes. The point to be made here is that the skyrmion structure appears to be dominated by the 3Q configuration, however there is also evidence of some deviation from this purely sinusoidal structure. It is possible that the visible structure in the bivariate histograms is due to surface states, however this point needs further investigation.

5.7 Discussion and conclusions

State of art, high resolution, pixelated DPC analysis has shown for the first time in experiment that the profile of a skyrmion within a skyrmion lattice may be not completely circularly symmetric. Bivariate histograms of experimentaly acquired images of integrated magnetic induction show similarities with 3Q model and 3Q with an additional higher harmonic. However with the signal to noise present in the imaging, it remains a question which model is fitting the experiment better and this should be approached by further investigation.

If skyrmions contain aspects of the third harmonic in 3Q model, there is a posibility of a domain wall like contrast and an associated divergence of the magnetisation (with respect to the rotation around their centre).

It was shown that the hexagonal symmetry of integrated magnetic induction of a skyrmion is rotated by 30° compared to the symmetry of the integrated magnetic induction of a hexagonal ferromagnetic particle. This points to the possibility of an internal boundary in a hexagonal skyrmion lattice. An easy explanation for this effect could be the strong packing of skyrmions within such a lattice. It would be interesting to compare this result to the structure of a single skyrmion.

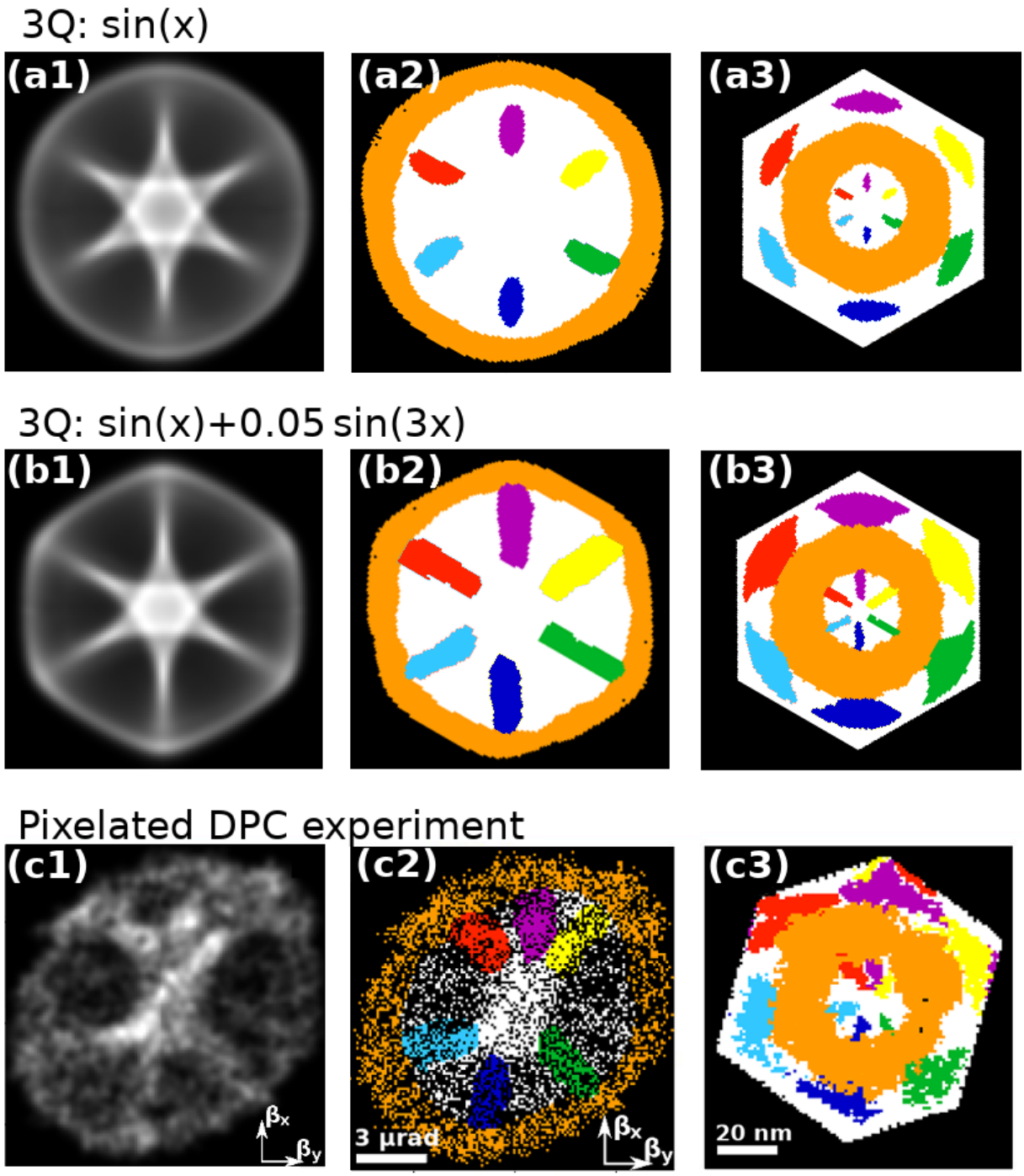

Fig. 5.17 *A comparison of the bivariate histograms of the (a) 3Q, (b) modified 3Q and (c) experimental pixelated detection. The images with index (1) are bivariate histograms, index (2) are coloured bivariate histograms and index (3) are coloured real space position of points in histograms (2)*

The pixelated DPC results were also analysed and compared to the 3Q model with the addition of a higher harmonic signal. The model showed characteristic features which correlate to the imaged structure of the skyrmion within the skyrmion lattice. This, however should be treated with some care due to breaking of the $||\mathbf{m}|| = 1$ micromagnetic condition. A more advanced model needs to be sought. One solution could be a multilayered Mumax^3 simulation, on which Lorentz microscopy prediction algorithms can be used (and which were shown in Sec. 2.4).

Another consideration is crystal bending, which could also influence the data. This is expected to be a very small effect as the size of the probe was rather narrow - with a corresponding spatial frequency of $(1.1\,nm)^{-1}$. This diminishes all strong bend contour effects. The size of bend contours in the studied material are visible in Figs 1.7(b) and (d), where they cover a significantly larger region than the spatial frequency used in this chapter (the skyrmions in that image are $\sim 70\,nm$).

References

[1] S. Mühlbauer, B. Binz, F. Jonietz, C. Pfleiderer, A. Rosch, A. Neubauer, R. Georgii, and P. Böni, "Skyrmion lattice in a chiral magnet," *Science*, vol. 323, no. 5916, pp. 915–919, 2009.

[2] T. Okubo, S. Chung, and H. Kawamura, "Multiple-q states and the skyrmion lattice of the triangular-lattice Heisenberg antiferromagnet under magnetic fields," *Physical review letters*, vol. 108, no. 1, p. 017206, 2012.

[3] A. Leonov and M. Mostovoy, "Multiply periodic states and isolated skyrmions in an anisotropic frustrated magnet," *Nature communications*, vol. 6, 2015.

[4] I. Dzyaloshinskii, "Theory of helicoidal structures in antiferromagnets. 1. Nonmetals," *Sov. Phys. JETP*, vol. 19, p. 960, 1964.

[5] A. Leonov, Y. Togawa, T. Monchesky, A. Bogdanov, J. Kishine, Y. Kousaka, M. Miyagawa, T. Koyama, J. Akimitsu, T. Koyama, *et al.*, "Chiral surface twists and skyrmion stability in nanolayers of cubic helimagnets," *arXiv preprint arXiv:1512.04179*, 2015.

[6] A. Bogdanov and A. Hubert, "Thermodynamically stable magnetic vortex states in magnetic crystals," *Journal of magnetism and magnetic materials*, vol. 138, no. 3, pp. 255–269, 1994.

[7] U. Rößler, A. Bogdanov, and C. Pfleiderer, "Spontaneous skyrmion ground states in magnetic metals," *Nature*, vol. 442, no. 7104, pp. 797–801, 2006.

[8] J. Sampaio, V. Cros, S. Rohart, A. Thiaville, and A. Fert, "Nucleation, stability and current-induced motion of isolated magnetic skyrmions in nanostructures," *Nature nanotechnology*, vol. 8, no. 11, pp. 839–844, 2013.

[9] X. Yu, Y. Onose, N. Kanazawa, J. Park, J. Han, Y. Matsui, N. Nagaosa, and Y. Tokura, "Real-space observation of a two-dimensional skyrmion crystal," *Nature*, vol. 465, no. 7300, pp. 901–904, 2010.

[10] S. Heinze, K. Von Bergmann, M. Menzel, J. Brede, A. Kubetzka, R. Wiesendanger, G. Bihlmayer, and S. Blügel, "Spontaneous atomic-scale magnetic skyrmion lattice in two dimensions," *Nature Physics*, vol. 7, no. 9, pp. 713–718, 2011.

[11] X. Yu, N. Kanazawa, Y. Onose, K. Kimoto, W. Zhang, S. Ishiwata, Y. Matsui, and Y. Tokura, "Near room-temperature formation of a skyrmion crystal in thin-films of the helimagnet FeGe," *Nature materials*, vol. 10, no. 2, pp. 106–109, 2011.

[12] D. McGrouther, R. J. Lamb, M. Krajnak, S. McFadzean, S. McVitie, R. L. Stamps, A. O. Leonov, A. N. Bogdanov, and Y. Togawa, "Internal structure of hexagonal skyrmion lattices in cubic helimagnets," *New Journal of Physics*, vol. 18, no. 9, p. 095004, 2016.

[13] R. Egerton and S. Cheng, "Measurement of local thickness by electron energy-loss spectroscopy," *Ultramicroscopy*, vol. 21, no. 3, pp. 231–244, 1987.

[14] S. Huang and C. Chien, "Extended skyrmion phase in epitaxial FeGe (111) thin films," *Phys. Rev. Lett.*, vol. 108, no. 26, p. 267201, 2012.

References

[15] M. Krajnak, D. McGrouther, D. Maneuski, V. O'Shea, and S. McVitie, "Pixelated detectors and improved efficiency for magnetic imaging in STEM differential phase contrast," *Ultramicroscopy*, vol. 165, pp. 42–50, 2016.

[16] A. Vansteenkiste, J. Leliaert, M. Dvornik, M. Helsen, F. Garcia-Sanchez, and B. Van Waeyenberge, "The design and verification of MuMax^3," *Aip Advances*, vol. 4, no. 10, p. 107133, 2014.

[17] H. S. Park, X. Yu, S. Aizawa, T. Tanigaki, T. Akashi, Y. Takahashi, T. Matsuda, N. Kanazawa, Y. Onose, D. Shindo, *et al.*, "Observation of the magnetic flux and three-dimensional structure of skyrmion lattices by electron holography," *Nature nanotechnology*, vol. 9, no. 5, pp. 337–342, 2014.

[18] A. Kovács, Z.-A. Li, K. Shibata, and R. E. Dunin-Borkowski, "Lorentz microscopy and off-axis electron holography of magnetic skyrmions in FeGe," *Resolution and Discovery*, vol. 1, no. 1, pp. 2–8, 2016.

[19] A. O. Leonov, Y. Togawa, T. L. Monchesky, A. N. Bogdanov, J. Kishine, Y. Kousaka, M. Miyagawa, T. Koyama, J. Akimitsu, T. Koyama, K. Harada, S. Mori, D. McGrouther, R. Lamb, M. Krajnak, S. McVitie, R. L. Stamps, and K. Inoue, "Chiral Surface Twists and Skyrmion Stability in Nanolayers of Cubic Helimagnets," *Phys. Rev. Lett.*, vol. 117, p. 087202, Aug 2016.

[20] T. Garel and S. Doniach, "Phase transitions with spontaneous modulation-the dipolar Ising ferromagnet," *Phys. Rev. B*, vol. 26, no. 1, p. 325, 1982.

CHAPTER 6

Comparison of electron holography and pixelated differential phase contrast

6.1 Introduction

In this chapter, electron holography and pixelated differential phase contrast will be compared in a simple experiment. A measurement of an electric field generated by two needles with an applied bias in free space will be shown. Electron holography and differential phase contrast will be performed under the same conditions in the same TEM and compared. Advantages and limits of both techniques will be also discussed. The experimental acquisition of the datasets and holography reconstruction was provided by Dr Vadim Migunov and Prof Rafal E. Dunin-Borkowski at The Ernst Ruska-Centre for Microscopy and Spectroscopy with Electrons and The Peter Grünberg Institute in Jülich, Germany.

The aim of this experiment is to show how these two complementary techniques can be used to acquire quantitative data. The challenges which arise in both techniques in such a simple experiment (within the same microscope) will be shown. This work should be of an interest to researchers working in field involvings the potentials around sharp tips (e.g. in field emission or atom probe studies) and to those working towards the mapping of long-range electric fields within materials.

A number of studies have reported measurements of electric fields in electron holography [1–4] and DPC [5–9]. In materials, there are number of mechanisms behind the electron phase shift, such as local structure changes at internal interfaces; the changes in the density at heterointerfaces; and polarisation effects. In some cases (i.e. imaging of polarised materials) DPC signals can arise only due to diffraction effects where no electric field is present [10]. Similar effects were shown in a simple simulation of magnetic DPC imaging

of a polycrystalline sample in Sec. 3.5. Therefore, great care is needed when interpreting DPC or holography data from materials in which long-range electric fields are expected.

6.2 Base of the experiment

Electric fields between two needles with a 100 nm gap will be imaged by two complementary techniques in the same microscope. The TEM used for this observation was a FEI Titan HOLO with 300 kV acceleration voltage. A schematic of the geometry of the experiment is shown in Fig. 6.1. A 20 V potential difference is applied between the needles, which is measured by off-axis electron holography and pixelated detection differential phase contrast. The phase change measured using electron holography and integrated electric field measured using DPC will be compared. However, both techniques can be influenced by intrinsic factors. These will be shown to be:

1. a non-complete electric field free reference beam for electron holography; and
2. a scanning system stability for pixelated differential phase contrast.

The complementarity of the two techniques is extremely important for reliable, artefact-free imaging of electric fields within materials on a nanometre scale.

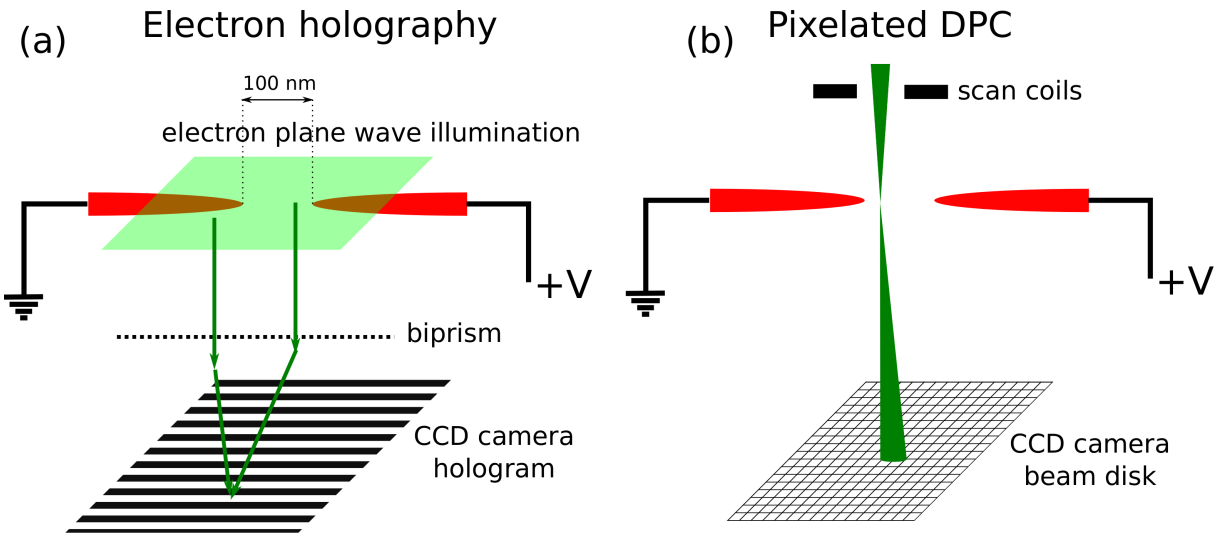

Fig. 6.1 *Schematic of the experimental layout for (a) electron holography and (b) pixelated DPC experiments in the same microscope. The two needles are separated by* 100 nm *and are biased (which creates an electrostatic field around them)*

6.3 Electric fields in differential phase contrast and electron holography

The physics of the experiment is very similar to the magnetic induction measurements described in the previous chapters. Here we will only focus on the transverse component of the electric field, which is perpendicular to the trajectory of the electrons in the TEM (a schematic is shown in Fig. 6.2). The main difference is that here the electrons are deflected due to the electric component of the Lorentz force, given by:

$$\mathbf{F} = \frac{d\mathbf{p}}{dt} = -e\mathbf{E}, \tag{6.1}$$

where $\mathbf{p}$ is the transverse component of the momentum of the electron and $\mathbf{E}$ is the strength of the electric field (perpendicular to the trajectory of the electron), which deflects the

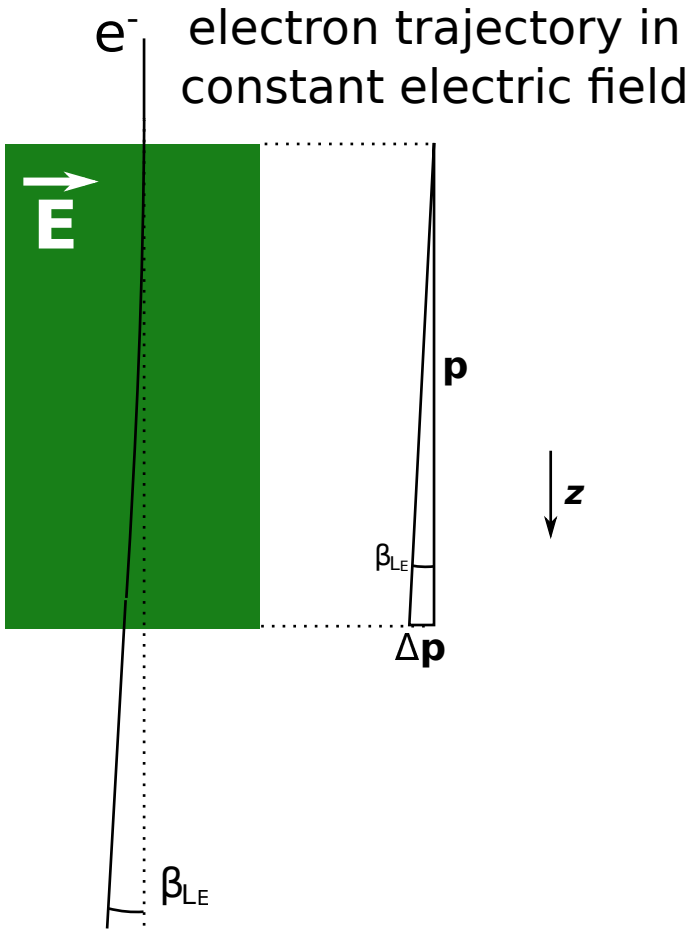

Fig. 6.2 *Schematic of the deflection of the electron in a constant electrostatic field. The small angle approximation can be used to find the transverse momentum* $\Delta\mathbf{p}$ *from the deflection angle* β_{L_E}*. The field is assumed constant withing the green rectangle and zero outside.*

electron beam in the TEM. Similar to the imaging of the magnetic induction described in the previous chapters, the total deflection angle of the electron will be linearly dependent on the path integral of the electric field along the trajectory of the electron. To prove this, we will integrate Eq. 6.1 along the z direction. Firstly, the left side of the equation (dp/dt) will be:

$$\int \frac{d\mathbf{p}}{dt} dz_{|_{dz=v_z\,dt}} = \int \frac{d\mathbf{p}}{dt}\, v_z\, dt = v_z \Delta\mathbf{p}, \tag{6.2}$$

where it was assumed that the speed of an electron in the z direction is constant, i.e. $v_z = const.$

Integrating the right side of the equation: $(-e\mathbf{E})$, gives:

$$-\, e \int \mathbf{E}\, dz, \tag{6.3}$$

which we can now combine into:

$$v_z \Delta\mathbf{p} = -e \int \mathbf{E}\, dz. \tag{6.4}$$

To relate the deflection angle and the transverse momentum, a small angle approximation can be used. The electron acquires only a very small transverse momentum (due to the electric field) compared to its relativistic momentum (due to the acceleration in TEM). This is shown in a schematic in Fig. 6.2. The De Broglie definition of a wavelength can be also used to get:

$$\beta_{L_E} = \frac{\Delta\mathbf{p}}{p} = \frac{\lambda\, \Delta\mathbf{p}}{h}, \tag{6.5}$$

therefore the electric Lorentz force deflection angle can be calculated as (by combination with Eq. 6.4):

$$\beta_{L_E} = -\frac{e\,\lambda}{h\,v_z} \int \mathbf{E}\, dz, \tag{6.6}$$

where h is the Planck's constant, λ and v_z are the relativistic wavelength and speed of the electron, and $\int \mathbf{E}\, dz$ is the integrated electric field. In this experiment, $300\,kV$ accelerated electrons are used. Their velocity is $v = 2.328 \times 10^8\, ms^{-1}$ and their wavelength $\lambda = 1.969\, pm$. The typical deflection angle will be tens of μrad, which will be calculated for a constant electric field inside a capacitor later in this chapter. The capacitor will have similar dimensions to this experiment. Based on Eq. 2.34, the Lorentz deflection angle is related to the gradient of the phase difference by:

$$\nabla\phi_E = \frac{2\pi}{\lambda}\, \beta_{L_E} = -\frac{2\pi}{h\,v_z} \int \mathbf{E}\, dz. \tag{6.7}$$

Here we will assume that the change in the electrons momentum is negligible in the z direction compared to the momentum of the $300\,kV$ TEM electrons in this experiment.

Off-axis electron holography measures the phase difference of two electron plane waves which passed though the sample area and though free space. To relate the two techniques, the 2D gradient of the phase (acquired by holography), needs to be computed. DPC and electron holography can be then related by Eq. 6.7.

A clear distinction should be made between slowly varying electric fields occurring as a result of the potential differences, and the quickly varying (atomic scale) electric fields around each atom. The resolution of STEM imaging is defined by the probe forming aperture and aberrations of the wave-optical system of the microscope. As mentioned before, the aperture works essentially as a bandpass filter therefore the two length scales - atomic scale fields and 'macroscopic' electric fields - can be imaged independantly choosing the right probe size.

To give an example of an expected beam deflection, we can assume a homogeneous field in a capacitor with the same dimensions as the spacing between the needles. The capacitor has the same bias as the needles (the schematic is shown in Fig. 6.3). The integrated electric field will have a value of $20\,V/100\,nm \times 100\,nm = 20\,V$. If a $300kV$

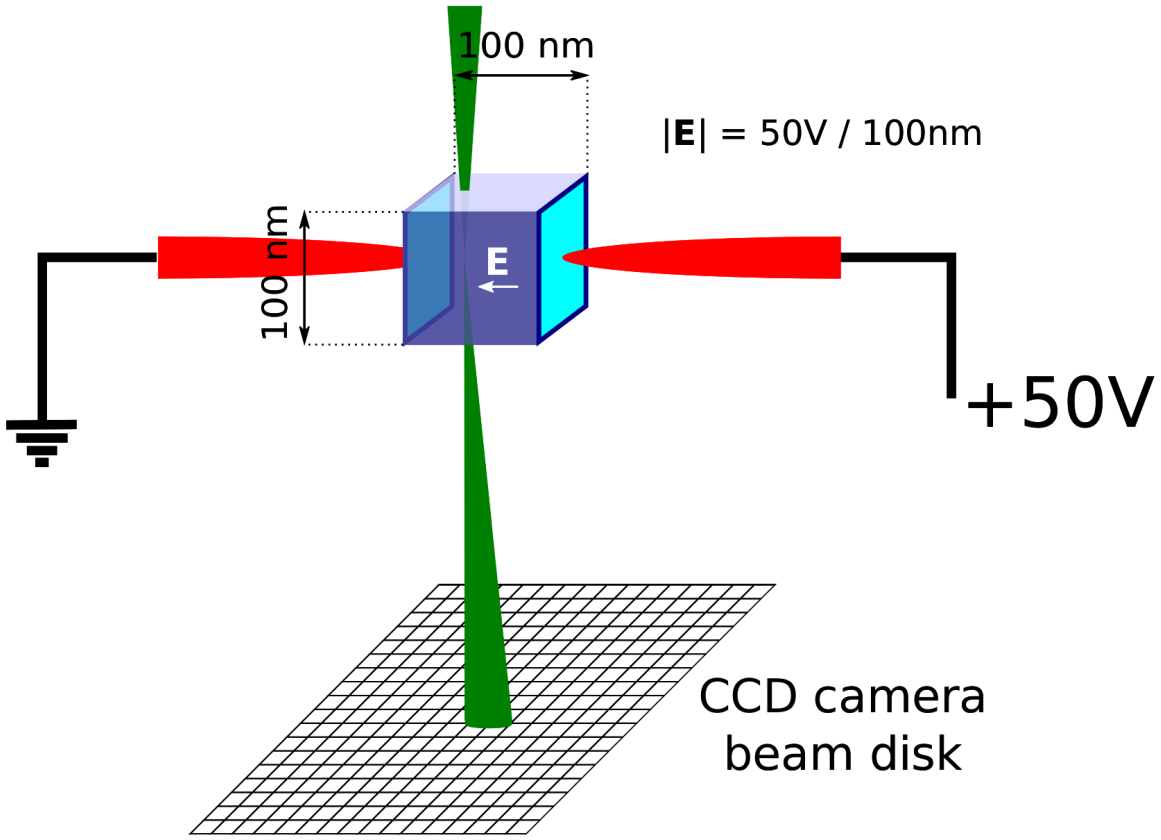

Fig. 6.3 *Schematic of an idealised structure of electric field between the plates of the capacitor with similar dimensions to the experimental setup*

electron is passing through such an idealised electric field, the expected deflection angle will be $\beta_{L_E} \sim 41\,\mu rad$. We can now compare this to the sensitivity of pixelated DPC shown in the previous chapters. Because the disk needs to fit the detector, a large enough camera length ($1.050\,m$) was chosen. The angular size of the pixel in the detector plane was $22.4\,\mu rad$. This is detectable on a CCD camera given that in a similar experiment precise detection of shifts larger than 0.1 pixel was possible [11].

This experiment is a simplified version of the measurement of electric fields within materials. The advantage is that by measuring the electric field in free space the electron beam does not interact with matter and therefore the detected electron disk will have no intensity variations (other than those due the electron source). Such situations have already been investigated in a number of studies [4, 12–14], especially those with applications in electron field emitters and atomic probe microscopy. However, here it gives the first direct comparison between pixelated DPC and electron holography in the same configuration for a simple experimental system inside the TEM.

6.4 Experimental parameters

The experiment was performed in a FEI Titan HOLO microscope at $300\,kV$ electron acceleration voltage. The electric field was created by applying a potential difference between two needles held in a Nanofactory scanning probe microscopy (SPM-TEM) holder. The microscope's objective lens was switched off. This was not required for the experiment. However, doing so enhanced the sensitivity of the measurement because of the larger ratio of STEM disk deflection to its radius. The geometry of the experiment is shown in Fig. 6.1.

In the experiment, two different distances between the tips of the needles were used ($50, 100\,nm$), however only the $100\,nm$ spacing allowed sufficient separation to image the field directly between the needles by pixelated DPC. Voltages from 1-50 V were applied, however only the $20\,V$ dataset from the $100\,nm$ separation is used for the remainder of this chapter. Smaller voltages lead to very small disk shifts, which were greatly affected by instabilities in the scanning system of the microscope. The $50\,V$ bias was not used because it requires phase unwrapping for electron holography.

For holography experiments, a Möllenstedt type electrostatic biprism [15] was used together with the inbuilt imaging aberration corrector in the microscope (which had no role in the experiment). Holograms were acquired using a 2K x 2K Gatan UltraScan 1000 CCD camera with the biprism voltage set to $135\,V$, which results in an interference fringe spacing of $2.5\,nm$ and sampling of about 14 pixels per fringe. The biprism was placed parallel to the needles axis so that the reference wave passed through a vacuum region adjacent to the field of view.

Pixelated DPC was performed in the same microscope (without moving the sample in any way) in STEM mode, using the smallest condenser aperture available. A large enough camera length was chosen ($1.050\,m$) allow for imaging of the whole disc on the CCD camera. The convergence semi-angle was $3.76\,mrad$, which measured 168 pixels on the detector. The pixel size in reciprocal space was, in this case, $22.4\,\mu rad/pixel$. Datasets were recorded using TIA software and were 20x20 probe position scans, which covered $1\,\mu m$ in real space. Therefore, the pixel separation was $50\,nm/pixel$

Holograms were reconstructed using a standard FFT method, where a sideband from the Fourier transform of the hologram was selected and centred, then an inverse FFT was applied. The resulting complex image was phase unwrapped [1]. These routines are standardised and used in electron holography. The image of the phase was directly provided by Dr Vadim Migunov. The electrostatic field of the needles extends well beyond their physical extent, and penetrates the reference wave region. Conseqently some effect of this perturbed reference wave [16] can be present in the holographic phase maps.

The profile of the beam does not change in free space, therefore the processing of pixelated DPC creates the same edge for each probe positions, as long as the beam does not hit either of the needles. The electric field does not vary significantly over the size of the focused probe ($k_\alpha = (0.52\,nm)^{-1}$). It is estimated that the error in determining the disc position is better than 0.1 pixels, which corresponds to $2.25\,\mu rad$ in this experiment (as discussed in Chap. 4).

The scanning of the beam is not ideal (due to the scanning and detector planes in STEM being not completely conjugate) and introduces disks shifts not due to the electric fields between the needles (detailed discussion of scanning issues was given in Sec. 4.5). The magnitude of these shifts was actually larger than the detected electric field (scanning instabilities get larger with low magnification in STEM [17]). To be more precise, the magnitude of the disk shifts in the scanning system was about 15 times larger than shifts due to the electric field. Therefore, it was necessary to subtract shifts measured at $0\,V$ bias for the voltage of interest. It was assumed that there was no residual field (charge) between the needles at $0\,V$, because the errors in the scan were too large to detected any residual field (at $0\,V$).

6.5 Results

Figure 6.4 shows the reconstructed phase map measured by holography, for a $20\,V$ bias applied between two needles that were $100\,nm$ apart. The highest phase gradient is located between the two tips. This is equivalent to the electric field being the strongest between the tips of needles, as expected. This image was reconstructed using established methods by Dr Vadim Migunov.

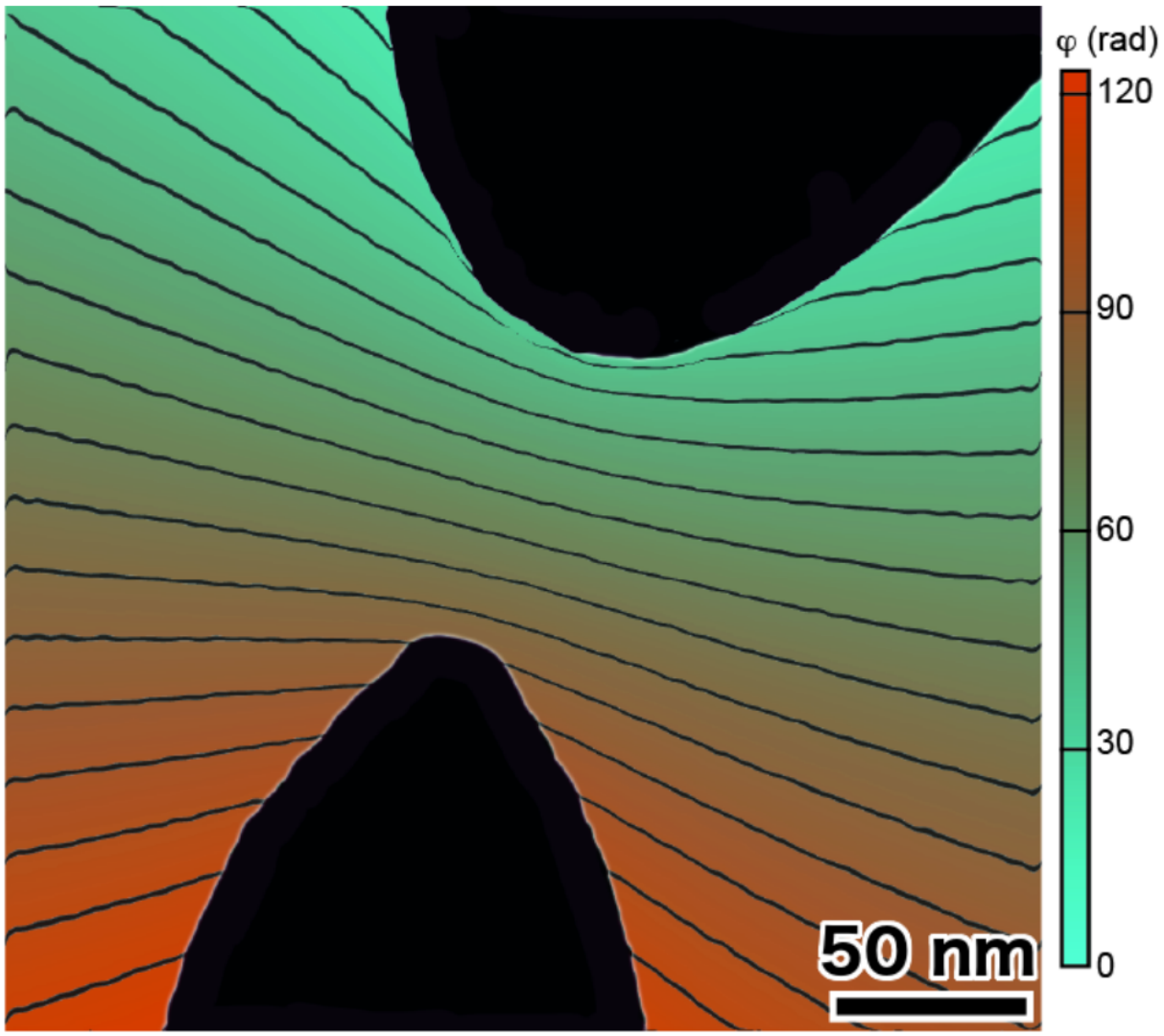

Fig. 6.4 *Reconstructed phase from electron holography between two needles* $100\,nm$ *apart for a* $20\,V$ *potential difference. The phase is shown as a colour map with a shadow image of the needles. Equiphase lines are separated by* 2.5π*. Image was reconstructed by Dr Vadim Migunov*

Fig. 6.5 shows two orthogonal components of the disk shifts for the $20\,V$ and $0\,V$ datasets as measured by DPC and determined by the cross-correlation algorithm. Figs (a) and (b) are for $20\,V$ and (c) and (d) are for $0\,V$ bias. If images (a) and (c) or (b) and (d) are compared, there is no visible difference in shift maps. To extract the disk shifts corresponding to a $20\,V$ bias, the differences of the x and y components need to be computed (shown in Figs (e) and (f)). The rotation of the detector is also an important parameter, and was found to be 10° clockwise in this case. This is the rotation of the diffraction plane relative to the orientation of scanning. The rotation means that after the calculation, the shifts will be rotated by 10° with respect to the resulting images. Corrected maps of the disk deflections which now correspond to the integrated electrostatic induction maps are shown in (g) and (h).

Fig. 6.5 shows that the main sources of error were irregularities in the scanning system of the microscope. The resulting images, Figs 6.5(g) and (h), contain scanning instability effects. The errors induced by cross-correlation registration algorithm are insignificant compared to this.

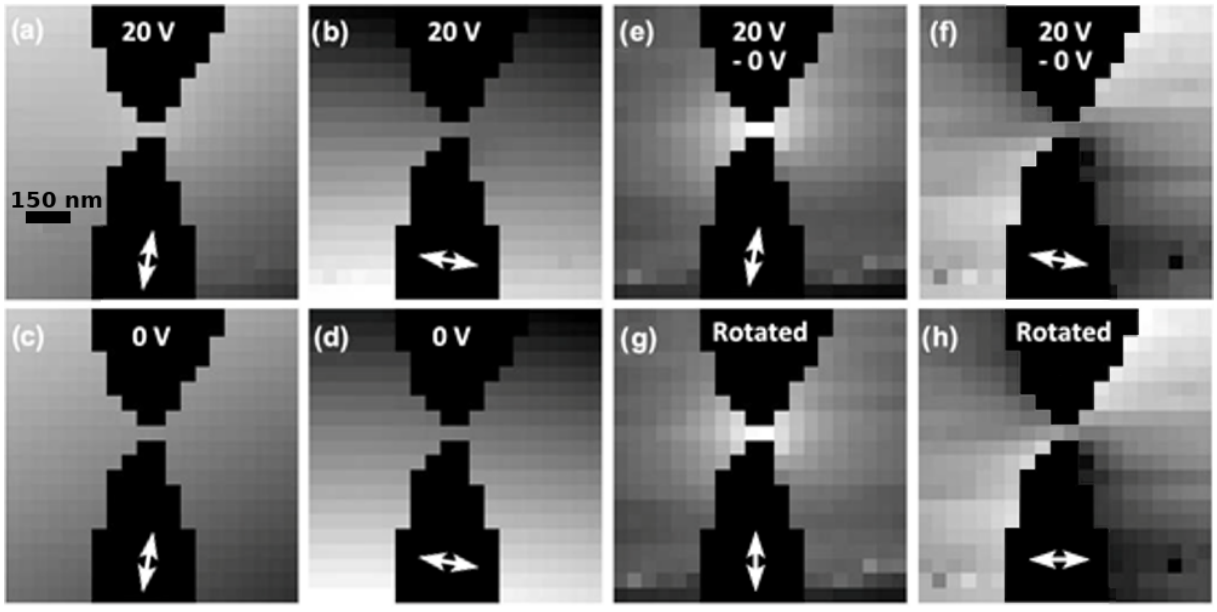

Fig. 6.5 *Orthogonal maps of disk shifts processed from pixelated DPC dataset with arrows showing the sensitivity to the shift, (a) and (b)* $20\,V$*, (c) and (d)* $0\,V$*, (e) and (f) corrected* $20\,V$*, (g) and (h) corrected* $20\,V$ *after compensation for detector to image rotation and correction for symmetry of the experiment described in the following figure together with appropriate scales*

The problematic factor in this analysis was the drift of the electron beam between the two DPC acquisitions. This has been estimated by bivariate histogram analysis in Fig. 6.6, where the symmetry of the experiment was used to find the reference position for the pixelated DPC experiment. Figs (a) and (b) were not corrected for rotation between the scanning direction and the CCD camera - this is clear from (c) which shows a small rotation and from the beam deflection map which is not symmetric as expected around zero deflection. Figs (d) and (e) were rotated and shifted according to the symmetry of the experiment (this is shown in Fig. 6.5).

To prove that the symmetry of the histogram is expected to be centred on the zero field point, the theoretical field profile for two point charges of the same magnitude and sign is shown in Fig. 6.7. Images (a), (b) and their histogram (c) show a similar configuration to the experiment - where two opposite point charges are masked and their field resembles the experiment. The important point to note from image (c) is that the zero field point is the centre of the symmetry in the bivariate pattern (the source of the bivariate vector pattern).

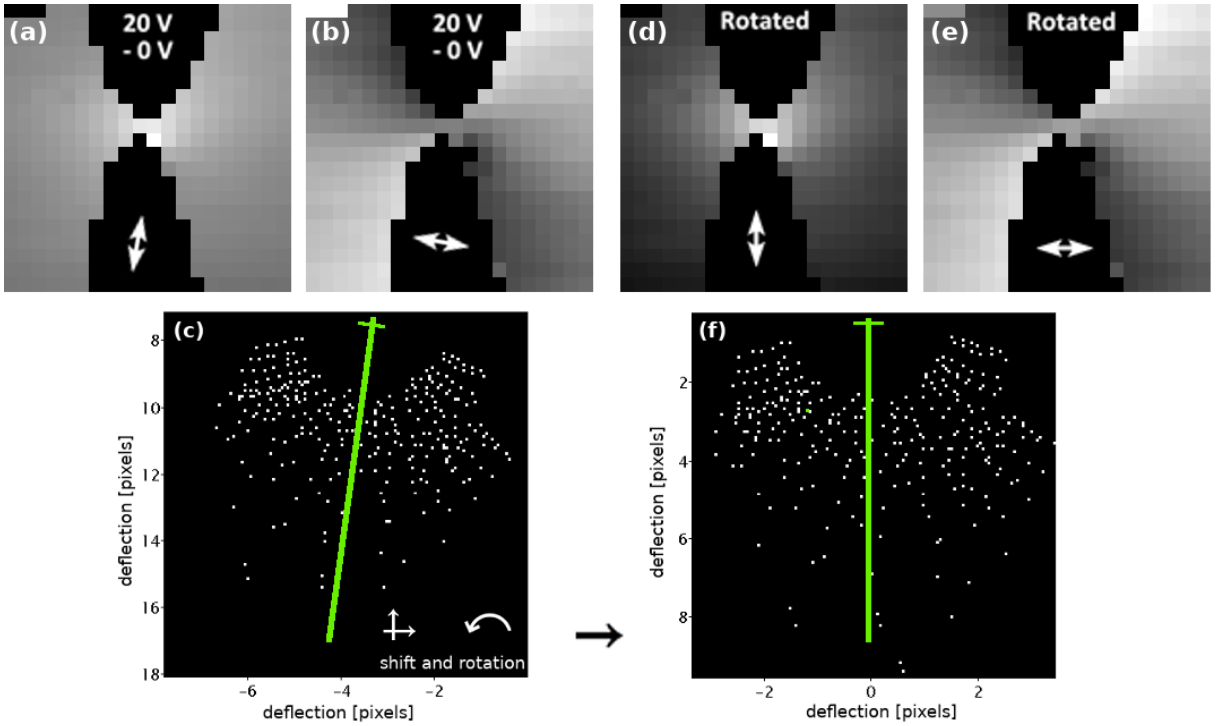

Fig. 6.6 *Bivariate analysis of the geometry of detected beam deflections, (a) and (b) orthogonal shift components for* $20\,V$ *bias applied to the needles, (c) is bivariate histogram of (a) and (b) showing the positions of the beam on the detector, (d) and (e) corrected orthogonal shift components for* $20\,V$ *bias applied to the needles, (f) is a bivariate histogram of corrected images (d) and (e) showing the positions of the beam on the detector*

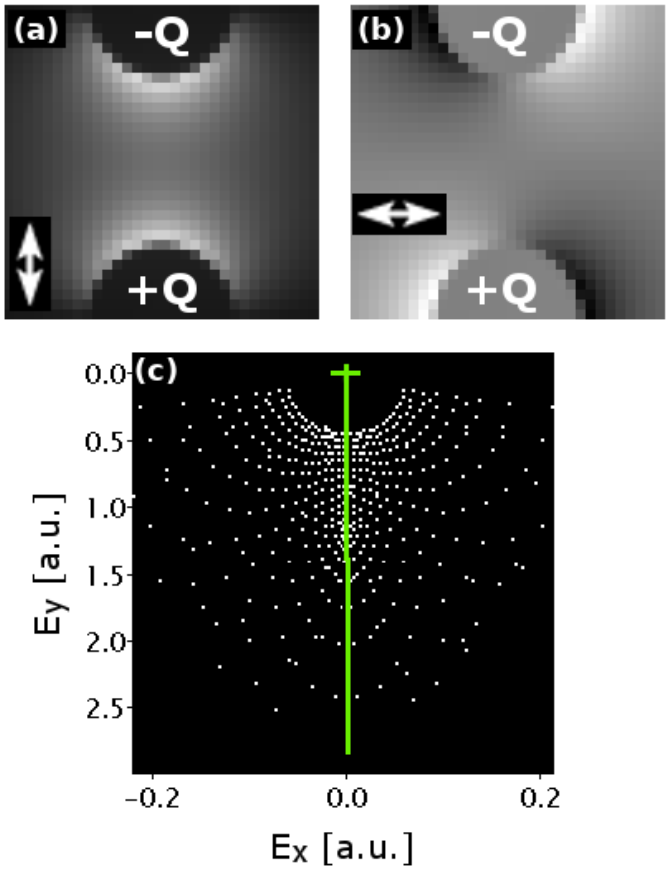

Fig. 6.7 *Bivariate analysis showing the geometry of the electric fields for simulated point charges, (a), (b) and (c) components of the theoretical electric field from two point charges with opposite sign with their bivariate histogram, showing the centre of the symmetry to be equal with zero field and effectively matching the experimental data in Fig. 6.6. The point charges were masked to resemble the tips of needles and to allow the symmetry analysis.*

Even if the $0\,V/m$ reference estimate in Fig. 6.6(f) is not precise, this will only result in a constant offset from the true field values. And even so, the field measurement in pixelated DPC is still quantitatively comparable with holographic mapping of integrated potentials.

Fig. 6.8 shows a schematic of the processing of the pixelated DPC data. Image in Fig. 6.8(a) is the magnitude of the deflection signal with five colour highlighting points of interest. From each position of interest the disk edge was extracted in Fig.6.8(b) and overlayed with each other in Fig. 6.8(c). As expected, the strongest shift was present in the gap between the needles (red edge/pixel) and the other four have shifts similar to each other due to lower field values in those regions. Any spot in which the beam hit the needle was masked out. The boxes in image in Fig. 6.8(c) show magnified details of the edges and their centroids, as these were small compared to the size of the electron disk.

To extract disk shifts with subpixel precision, the cross-correlation method introduced in previous chapters and in [11] was used. Each of the diffraction disks was smoothed and Sobel filtered to extract an edge pattern which was then cross-correlated with an idealised

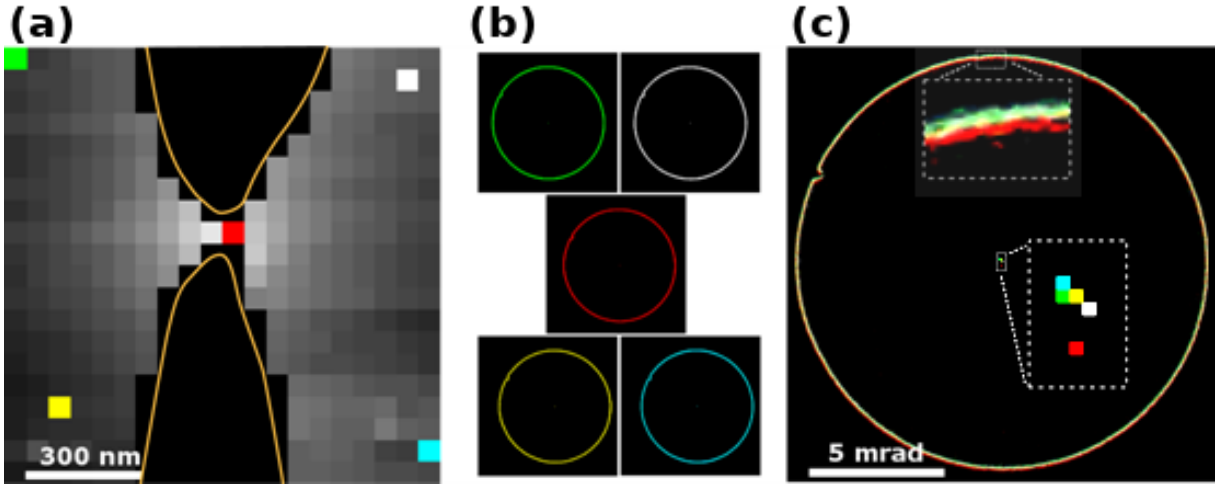

Fig. 6.8 *Mapping beam deflections by the Lorentz force, (a) the scanned area with 5 representative pixels highlighted in different colours (the approximate needle edges are indicated with the yellow lines), (b) the discs for each of these points, after the application of an edge-detection filter, (c) the image showing the overlaying all the discs and the shifts of the centroids in the box*

edge of the disk. The position of the maximum in the cross-correlation pattern corresponds to the disk shift. Subpixel precision was achieved by quadratic interpolation of the pixels surrounding the maximum in the correlation pattern. As the diffraction disks were assumed to have a constant profile during the scan, one disk was chosen, a threshold was applied to it (to filter the shot noise) to create the top hat function[1]. This was then smoothed to match the beam edge spread and Sobel algorithm was used to create an idealised beam profile. The beam intensity does not change in free space, therefore the processing creates the same beam edge function for all points of the scan, as long as the beam does not hit either of the needles. It is estimated that the error in determining the deflection was better than 0.1 pixels ($< 2.25 \mu rad$) [11].

6.6 Discussion

Fig. 6.9 shows a comparison of the integrated electric field measured by (a) electron holography and (b) pixelated DPC, over the same field of view and with similar sampling. Note, the holography plot has been deliberately undersampled to match the DPC plot.

This comparison may seem limited as the fields of view imaged by the two techniques only have a few data points in common. However, the two techniques show excellent agreement, albeit there is a difference in measured peak values (see line profile for the magnitude field in (c)). This could be due to two reasons. Firstly, the long-range field

[1] This was checked by analysing disk correlation values

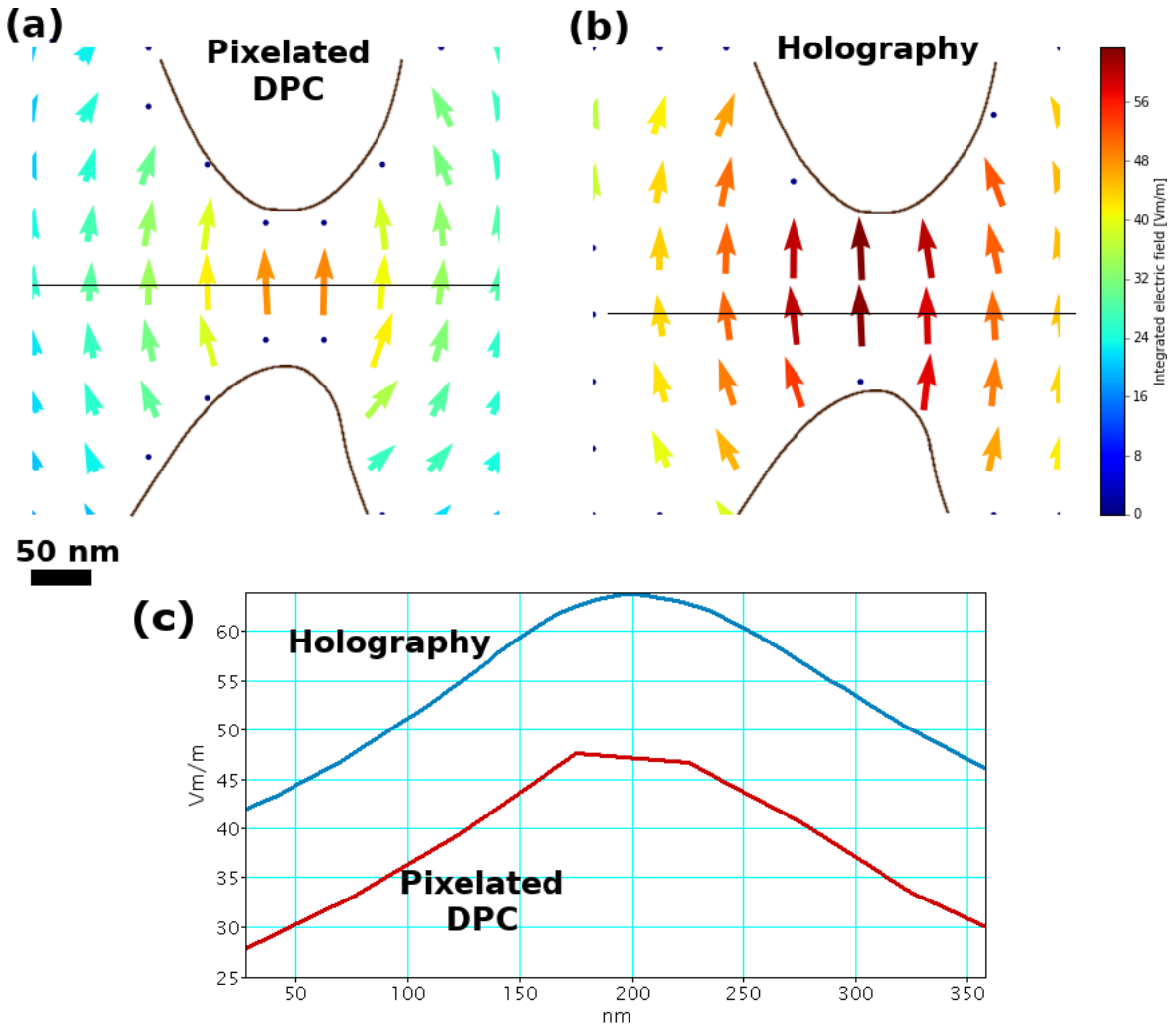

Fig. 6.9 *A comparison of the integrated field plot for (a) scanning diffraction and (b) holography after correction for image rotations and mapping exactly the same field of view in both cases. (c) shows a comparison of a line profile for black lines in (a) and (b), which shows a constant offset of otherwise excellent agreement between the methods. The offset can be present due to two reasons: 1. leakage of the electric field into reference wave area for electron holography, and 2. offset in pixelated DPC due to not precise 0V reference (which was unlikely given the analysis in Figs 6.6 and 6.7). The approximate outline of the needles are shown in fine black lines*

can affect the reference wave in holography (CTEM) and secondly, the difference can be attributed to the beam shift between the reference $0\,V/m$ scan and the $20\,V/m$ scan in pixelated differential phase contrast (STEM). The pixelated DPC measurement was analysed and symmetry of the electric field was used to find the shift of the beam. The shifts will only result in a constant offset from the true field values, therefore the pixelated DPC is still quantitatively comparable with holographic mapping of integrated potentials. Unfortunately, only a single pixel was present directly between the needles, however this was the best dataset available for the analysis.

In this particular experiment, the number of probe position images in pixelated STEM was limited by the software architecture used for the acquisition (2 GB limit per single data file) which essentially allowed only 20x20 data points per image. This was not optimal but it shows the possibility of such analysis. A 100x100 pixel image would require about $\sim 20\,GB$ of memory, given that the resolution of the CCD camera used was 1000x1000 pix and data was acquired with a 16-bit depth of information.

This experiment confirms the simple interpretation of electron holography of electric fields in free space as mapping electric potentials. It will be always likely that holography datasets will contain many more pixels than scanned diffraction datasets due to memory limitations. Therefore, electron holography will always be more practical for mapping areas using fine sampling, however the interpretation of pixelated DPC can be much less problematic for imaging more complex fields within materials [10]. It was also shown in Chap. 4 and in [11], that pixelated DPC can offer additional options to filter diffraction contrast from the material. In electron holography, such problematic contrast sources have to be treated carefully, either by imaging the structure above and under Curie temperature (for magnetic imaging) or by using different accelerating voltages of the microscope [18–20]. Both approaches then require subtraction of images acquired in different conditions, this can also cause issues with registration. The resolution of the two techniques can be enhanced by switching the objective lens on. The pixelated DPC was reported to be sensitive to the deflection of the beam down to 0.02 pix in Chap. 4. The resolution of long-range electric field DPC imaging will be then effectively limited by the largest aperture for which the shifts of the beam are detectable.

DPC was used to acquire images of atomic potentials in [6, 21, 22], however, the complexity of the interactions at such a level requires advanced analysis and simulation. Electron holography can also offer atomic resolution [23–25], however, again very careful measures have to be taken to use such a technique.

6.7 Conclusions

In this chapter, the electric field distribution around two needles was studied. The tips of the needles were placed $100\,nm$ apart and a $20\,V$ potential difference was applied to them. Measurements by electron holography and pixelated DPC were compared and it was established that the two techniques are complementary in electron microscopy. Off-axis electron holography was used to reconstruct the potential distribution around the needles, which was then numerically differentiated to find the integrated electric field. This is easily interpretable as the imaging was conducted in free space. Pixelated differential phase contrast was used in the same microscope with exactly the same sample configuration.

The potential difference between the needles was measured by registering the STEM disk deflections due to the integrated electric field. It is clear that the two techniques produce comparable results, however there are some differences. In electron holography this is possibly due to a perturbed reference wave (due to long range electric fields) or because of a shift in the beam between the scans for pixelated DPC (the position of 0V reference was not stable between the two scans - i.e. beam has drifted). It was shown that the latter can be corrected by analysis of the symmetry in the bivariate histogram of the field components for the given experiment.

References

[1] M. R. McCartney and D. J. Smith, "Electron holography: phase imaging with nanometer resolution," *Annu. Rev. Mater. Res.*, vol. 37, pp. 729–767, 2007.

[2] A. Twitchett, R. Dunin-Borkowski, R. Broom, and P. Midgley, "Quantitative electron holography of biased semiconductor devices," *Journal of Physics: Condensed Matter*, vol. 16, no. 2, p. S181, 2003.

[3] P. Somodi, A. Twitchett-Harrison, P. Midgley, B. Kardynał, C. Barnes, and R. Dunin-Borkowski, "Finite element simulations of electrostatic dopant potentials in thin semiconductor specimens for electron holography," *Ultramicroscopy*, vol. 134, pp. 160–166, 2013.

[4] V. Migunov, A. London, M. Farle, and R. Dunin-Borkowski, "Model-independent measurement of the charge density distribution along an Fe atom probe needle using off-axis electron holography without mean inner potential effects," *Journal of applied physics*, vol. 117, no. 13, p. 134301, 2015.

[5] M. Lohr, R. Schregle, M. Jetter, C. Wächter, T. Wunderer, F. Scholz, and J. Zweck, "Differential phase contrast 2.0—Opening new "fields" for an established technique," *Ultramicroscopy*, vol. 117, pp. 7–14, 2012.

[6] N. Shibata, S. D. Findlay, Y. Kohno, H. Sawada, Y. Kondo, and Y. Ikuhara, "Differential phase-contrast microscopy at atomic resolution," *Nature Physics*, vol. 8, pp. 611–615, Aug. 2012.

[7] N. Shibata, S. D. Findlay, H. Sasaki, T. Matsumoto, H. Sawada, Y. Kohno, S. Otomo, R. Minato, and Y. Ikuhara, "Imaging of built-in electric field at a pn junction by scanning transmission electron microscopy," *Scientific reports*, vol. 5, 2015.

[8] K. Müller-Caspary, F. F. Krause, T. Grieb, S. Löffler, M. Schowalter, A. Béché, V. Galioit, D. Marquardt, J. Zweck, P. Schattschneider, *et al.*, "Measurement of atomic electric fields and charge densities from average momentum transfers using scanning transmission electron microscopy," *Ultramicroscopy*, 2016.

[9] D. Taplin, N. Shibata, M. Weyland, and S. Findlay, "Low magnification differential phase contrast imaging of electric fields in crystals with fine electron probes," *Ultramicroscopy*, vol. 169, pp. 69–79, 2016.

[10] I. MacLaren, L. Wang, D. McGrouther, A. J. Craven, S. McVitie, R. Schierholz, A. Kovács, J. Barthel, and R. E. Dunin-Borkowski, "On the origin of differential phase contrast at a locally charged and globally charge-compensated domain boundary in a polar-ordered material," *Ultramicroscopy*, vol. 154, pp. 57–63, 2015.

[11] M. Krajnak, D. McGrouther, D. Maneuski, V. O'Shea, and S. McVitie, "Pixelated detectors and improved efficiency for magnetic imaging in STEM differential phase contrast," *Ultramicroscopy*, vol. 165, pp. 42–50, 2016.

[12] D. Shindo and Y. Murakami, "Electron holography study of electric field variations," *Journal of electron microscopy*, vol. 60, no. suppl 1, pp. S225–S237, 2011.

[13] M. Beleggia, T. Kasama, R. E. Dunin-Borkowski, S. Hofmann, and G. Pozzi, "Direct measurement of the charge distribution along a biased carbon nanotube bundle using electron holography," *Applied physics letters*, vol. 98, no. 24, p. 243101, 2011.

References

[14] M. Beleggia, T. Kasama, D. Larson, T. Kelly, R. Dunin-Borkowski, and G. Pozzi, "Towards quantitative off-axis electron holographic mapping of the electric field around the tip of a sharp biased metallic needle," *Journal of Applied Physics*, vol. 116, no. 2, p. 024305, 2014.

[15] G. Möllenstedt and H. Düker, "Fresnelscher interferenzversuch mit einem biprisma für Elektronenwellen," *Naturwissenschaften*, vol. 42, no. 2, pp. 41–41, 1955.

[16] A. H. Tavabi, V. Migunov, C. Dwyer, R. E. Dunin-Borkowski, and G. Pozzi, "Tunable caustic phenomena in electron wavefields," *Ultramicroscopy*, vol. 157, pp. 57–64, 2015.

[17] T. C. Arnoldussen and L. L. Nunnelley, *Noise in digital magnetic recording*. World Scientific, 1992.

[18] R. J. Harrison, R. E. Dunin-Borkowski, and A. Putnis, "Direct imaging of nanoscale magnetic interactions in minerals," *Proceedings of the National Academy of Sciences*, vol. 99, no. 26, pp. 16556–16561, 2002.

[19] J. C. Loudon, N. D. Mathur, and P. A. Midgley, "Charge-ordered ferromagnetic phase in La0. 5Ca0. 5MnO3," *Nature*, vol. 420, no. 6917, pp. 797–800, 2002.

[20] F. A. M. Ramírez, *Holography: Different Fields of Application*. InTech, 2011.

[21] K. Müller, F. F. Krause, A. Béché, M. Schowalter, V. Galioit, S. Löffler, J. Verbeeck, J. Zweck, P. Schattschneider, and A. Rosenauer, "Atomic electric fields revealed by a quantum mechanical approach to electron picodiffraction," *Nature communications*, vol. 5, 2014.

[22] A. Lubk and J. Zweck, "Differential phase contrast: An integral perspective," *Physical Review A*, vol. 91, no. 2, p. 023805, 2015.

[23] M. Linck, B. Freitag, S. Kujawa, M. Lehmann, and T. Niermann, "State of the art in atomic resolution off-axis electron holography," *Ultramicroscopy*, vol. 116, pp. 13–23, 2012.

[24] F. Genz, T. Niermann, B. Buijsse, B. Freitag, and M. Lehmann, "Advanced double-biprism holography with atomic resolution," *Ultramicroscopy*, vol. 147, pp. 33–43, 2014.

[25] T. Akashi, Y. Takahashi, T. Tanigaki, T. Shimakura, T. Kawasaki, T. Furutsu, H. Shinada, H. Müller, M. Haider, N. Osakabe, *et al.*, "Aberration corrected 1.2-MV cold field-emission transmission electron microscope with a sub-50-pm resolution," *Applied Physics Letters*, vol. 106, no. 7, p. 074101, 2015.

CHAPTER 7

Summary and outlook

Summary

In this thesis, a novel approach to differential phase contrast in scanning transmission electron microscopy was introduced. Using a pixelated detector to acquire a full image of the central diffraction disk, the information transfer for magnetic materials was enhanced. This was provided by advanced computer vision algorithms, with which 4D datasets were analysed after the experiment. Pixelated DPC was used to image a magnetic domain wall in a polycrystalline thin film; skyrmions in chiral magnets and; to measure an electric field in free space.

In Chapter 3, a simulation of differential phase contrast was introduced, where an artificial 4D dataset was created and analysed by three proposed algorithms. The three algorithms were: segmented detection, centre of mass and cross-correlation. They were used to find the deflection of the central diffraction disk in STEM. The characteristics of each of the algorithms was shown for the simulation of a simplified polycrystalline sample. It was shown that if there is a change in the bright field intensity of the beam, the segmented detection does not give an exact measure of DPC in a simulated, polycrystalline like sample. The centre of mass algorithm can overcome this problem, however it does not provide a good separation of spatial frequencies from the crystallites and magnetic induction. That problem was addressed by the cross-correlation algorithm, which filters crystallite like contrast and was shown to obtain a low noise image of the integrated magnetic induction of the sample.

In Chapter 4, an experimental confirmation of pixelated detection in DPC STEM was shown. A CCD camera was used for the preliminary work, where the pixelated DPC method was tested and the principle was proved to be exceptionally successful for the suppression of the diffraction contrast in a polycrystalline sample. It was shown that the integrated magnetic induction can be measured with even pixel by pixel precision using the cross-correlation algorithm.

The enhanced detection method was tested on a 20 nm thick polycrystalline sample of $Py_{95}Pt_5$, where even a single line trace was enough to accurately measure the width of the domain wall. This is a promising achievement which can be used in the measurements of smaller localised magnetic structures, like vortices or skyrmions, where pixel by pixel sensitivity is the key to successful measurements.

By the introduction of the direct electron detector Medipix3, practical acquisition times for large enough datasets were achieved. In the particular example given in Chapter 4, the 256x256 probe position dataset was acquired in two minutes. This dataset was 8 GB in size which takes about two minutes to analyse by a GPU accelerated code based on C++ and ArrayFire matrix processing software. It was shown that even subpixel deflections can be measured using the enhanced edge generating algorithm. This provided precision better than 0.05 px in a free space scan. Such precision is important if the deflection due to the in-plane electromagnetic field is small or if a large aperture is used, to achieve high spatial resolution (a probe size below 1 nm was used in the chapter).

In Chapter 5, the imaging of a skyrmion in a skyrmion lattice with 1 nm resolution in the *FeGe* chiral magnet was shown. Images show a detailed structure of in-plane magnetic induction of single skyrmions in a skyrmion lattice. It was argued that this structure has similarities with a 3Q model and with 3Q with an additional harmonic, however both models differ from experimental images. It is possible that skyrmions in a skyrmion lattice contain a divergent component of the magnetisation. This component can be present because of various reasons, i.e. the surface states and/or because of domain wall like signal variations in a skyrmion lattice. A comparison with a simple 3Q model was presented and it was shown that a pure 3Q model can be altered by the addition of a third harmonic (3Q+) to simulate skyrmions with a hexagonal structure of in-plane field in the bivariate histogram. However, neither 3Q nor 3Q+ give the full answer to the structure of the skyrmion, which seems to be somewhere inbetween. The structure of a field of skyrmions within a skyrmion lattice was shown to vary significantly. This means that the averaging of signals from many skyrmions should be done with care.

Electron holography and pixelated differential phase contrast were shown to be comparable, quantitative techniques in Chapter 6. Their differences were discussed for the imaging of the electrostatic field in free space. It was shown that electron holography can offer a high sampling but that great care is needed in placing the reference wave, which should pass through a field free area. Pixelated differential phase contrast was provided in a very limited sense (20x20 point dataset), however even with such a small number of points, an integrated electric field was successfully measured. Both techniques were presented and their advantages and disadvantages discussed.

Outlook

This work has opened up exciting opportunities in the analysis of scanning diffraction datasets. It could be applied to the analysis of thin magnetic specimens as one of the leading methods in Lorentz microscopy. The problematic imaging of polycrystalline samples has been enhanced, therefore characterisations of the smallest structures are now more accessible. This work allows for easy measurement of magnetic vortex core sizes (by filtering the diffraction contrast). This is of interest as a direct measure of the Dzyaloshinskii-Moriya interaction [Butenko, et al., Phys. Rev. B, 80.13, 2009, 134410]. Similarly, work investigating the structure of skyrmions and imaging of chiral magnets can be enhanced (i.e. temperature studies, single skyrmion imaging, helicoid imaging) and compared with simulations.

A significant part of future efforts in pixelated STEM will be in data handling and computing, as the datasets rapidly scaled to gigabyte sizes. In this work, a great effort was taken to maximise the speed of analysis, which has shown potential to be developed for live imaging. This will be a necessity for very weak magnetic structures, where the localisation of regions of interest may not be possible with the current, faster methods (i.e. segmented detector).

The development of direct electron detection will enable the simultaneous acquisition of more types of data. It is now possible to use computer vision style algorithms for the analysis of CBED patterns for a whole STEM dataset, previously this was not easily accessible. Measures of strains and other effects are also possible.

Cross-correlation can be also used to compute the quality of the edge of the disk, given as the maximum of a cross-correlation pattern. This gives the exciting option to image only the highest spatial frequencies present at the edge of the beam and relates to the established annular bright field imaging technique. Here we can even compute a directional version of annular bright field imaging. The directional (asymmetric) changes at the edge of the beam were discussed in the simulations in Chap. 3 and were also shown for atomic scale imaging simulations [Müller-Caspary, et al., Ultramicroscopy, 2016].

.

.....let's pixelate!